Université de Montréal

THE SEARCH FOR NEW RESONANCES IN STRONG SYMMETRY BREAKING SCENARIOS WITH THE ATLAS DETECTOR

par
Merlin Davies

Département de physique
Faculté des arts et des sciences

Thèse présentée à la Faculté des études supérieures
en vue de l'obtention du grade de Philosophiæ Doctor (Ph.D.)
en physique

August, 2013

Université de Montréal
Faculté des études supérieures

Cette thèse intitulée:

THE SEARCH FOR NEW RESONANCES IN STRONG SYMMETRY BREAKING SCENARIOS WITH THE ATLAS DETECTOR

présentée par:

Merlin Davies

a été évaluée par un jury composé des personnes suivantes:

Claude Leroy,	président-rapporteur
Georges Azuelos,	directeur de recherche
Jean-François Arguin,	membre du jury
Matt Dobbs,	examinateur externe
Claude Leroy,	représentant du doyen de la FES

Thèse acceptée le: . . . .

RÉSUMÉ

Utilisant les plus récentes données recueillies par le détecteur ATLAS lors de collisions pp à 7 et 8 TeV au LHC, cette thèse établira des contraintes sévères sur une multitude de modèles allant au-delà du modèle standard (MS) de la physique des particules. Plus particulièrement, deux types de particules hypothétiques, existant dans divers modèles théoriques et qui ne sont pas présentes dans le MS, seront étudiés et sondés.

Le premier type étudié sera les *quarks-vectoriels* (QV) produits lors de collisions pp par l'entremise de couplages électrofaibles avec les quarks légers u et d. On recherchera ces QV lorsqu'ils se désintègrent en un boson W ou Z, et un quark léger. Des arguments théoriques établissent que sous certaines conditions raisonnables la production simple dominerait la production en paires des QV. La topologie particulière des évènements en production simple des QV permettra alors la mise en oeuvre de techniques d'optimisation efficaces pour leur extraction des bruits de fond électrofaibles.

Le deuxième type de particules recherché sera celles qui se désintègrent en WZ lorsque ces bosons de jauges W, et Z se désintègrent leptoniquement. Les états finaux détectés par ATLAS seront par conséquent des évènements ayant trois leptons et de l'énergie transverse manquante. La distribution de la masse invariante de ces objets sera alors examinée pour déterminer la présence ou non de nouvelles résonances qui se manifesterait par un excès localisé.

Malgré le fait qu'à première vue ces deux nouveaux types de particules n'ont que très peu en commun, ils ont en réalité tous deux un lien étroit avec la brisure de symétrie électrofaible. Dans plusieurs modèles théoriques, l'existence hypothétique des QV est proposé pour annuler les contributions du quark *top* aux corrections radiatives de la masse du Higgs du MS. Parallèlement, d'autres modèles prédisent quant à eux des résonances en WZ tout en suggérant que le Higgs est une particule composite, chambardant ainsi tout le sector Higgs du MS. Ainsi, les deux analyses présentées dans cette thèse ont un lien fondamental avec la nature même du Higgs, élargissant par le fait même nos connaissances sur l'origine de la masse intrinsèque des particules.

En fin de compte, les deux analyses n'ont pas observé d'excès significatif dans leurs

régions de signal respectives, ce qui permet d'établir des limites sur la section efficace de production en fonction de la masse des résonances.

Mots clés : ATLAS, LHC, collisionneur, quarks vectoriels, diboson, resonance, technicouleur, analyse, Higgs composite.

ABSTRACT

Using the most recent data collected by the ATLAS detector in pp collisions delivered by the LHC at 7 and 8 TeV, this thesis shall establish severe constraints on a variety of models going beyond the Standard Model (SM) of particle physics. More particularly, two types of hypothetical particles, existing in various theoretical models shall be studied and probed.

The first type will be the search for vector-like quarks (VLQ) produced in pp collisions through electroweak couplings with the u and d quarks. The quest for these particles will be made as they decay into either $W(\ell\nu)$+jet or $Z(\ell\ell)$+jet. There exist theoretical arguments that establish that, under certain reasonable conditions, single production of VLQ dominates over production in pairs. The particular topology of such events enables the implementation of effective techniques to extract signal over electroweak background.

The second type is the search for resonant particles decaying to WZ when the gauge bosons W and Z decay leptonically. The final states detected by ATLAS therefore contain three leptons (e, or μ) and missing transverse energy. The distribution of the invariant mass of these objects will then be examined to determine the presence or absence of new resonances that manifest themselves as localized excesses in $m(WZ)$.

Despite the fact that, at first glance, these two new types of particles have very little in common, they are in fact both closely linked to electroweak symmetry breaking. In many theoretical models, the hypothetical existence of VLQ is put forward to counteract the top quark's contribution to radiative loop corrections of the Higgs mass, a calculation which assumes that the Higgs is an elementary particle. Concurrently, other models foretelling the existence WZ resonances alternatively suggest that the Higgs is a composite particle, completely rewriting the whole Higgs sector of the SM. In this perspective, the two analyses presented in this thesis have a fundamental link with the very nature of the Higgs, thereby extending our knowledge of the origin of particle masses.

Ultimately, the two analyses did not observe any significant excess in their respective signal regions, paving the way for the computations of limits on the production cross

section as a function of the mass of the resonances.

Keywords: ATLAS, LHC, collider, vector-like quarks, diboson, resonance, technicolor, analysis, composite Higgs.

CONTENTS

LIST OF TABLES

LIST OF FIGURES

xxii

xxxiv

LIST OF APPENDICES

LIST OF ABBREVIATIONS

AdS	Anti-de Sitter
ALEPH	Apparatus for LEP Physics at CERN
ATLAS	A Large LHC ApparatuS
BC	Bunch Crossing
BDT	Boosted Decision Tree
BESS	Balloon-borne Experiment with Superconducting Spectrometer
BSM	Beyond the Standard Model
CB	Crystal Ball
CC	Charge Current
CFT	Conformal Field Theory
CHM	Composite Higgs Models
CKM	Cabibbo–Kobayashi–Maskawa
CMS	Compact Muon Spectrometer
CP	Charge-Parity *or* Cluster Processor
CPU	Central Processing Unit
CR	Control Region
CSC	Cathode Strip Chambers
CTP	Central Trigger Processor
DAQ	Data Acquisition system
DELPHI	DEtector with Lepton, Photon and Hadron Identification
DM	Dark Matter
DSB	Dynamical Symmetry Breaking
ECAL	Electromagnetic Calorimeter

EER	Electron Energy Resolution
EES	Electron Energy Scale
EF	Event Filter
EGM	Extended Gauge Model
ETC	Extended Technicolor
EM	Electromagnetic
EMEC	Electromagnetic End-Cap
EW	Electroweak
EWPM	Electroweak Precision Measurements
EWSB	Electroweak Symmetry Breaking
FATRAS	Fast Track Simulation
FCAL	Forward Calorimeter
FCNC	Flavor Neutral Current Current
FR	Fake Rate
FSR	Final State Radiation
GALLEX	Gallium Experiment
GB	Goldstone Bosons
GCW	Global Cluster Weighting
GNO	Gallium Neutrino Observatory
GRL	Good Runs List
GUT	Grand Unified Theory
HEC	Hadronic End-cap Calorimeter
HEP	High Energy Physics
HF	Heavy Flavour
HLT	High-Level Tigger
ICHEP	International Conference on High Energy Physics

ID	Inner Detector
IP	Interaction Point
IR	Infrared
ISR	Initial State Radiation
JEP	Jet/Energy-sum Processor
JES	Jet Energy Scale
JER	Jet Energy Resolution
JVF	Jet Vertex Fraction
KK	Kaluza-Klein
L1(2)	Level 1(2) trigger
L1Calo	Level 1 Calorimeter Trigger
LAr	Liquid Argon
LB	Luminosity Block
LCW	Local Cluster Weighting
LER	Lepton Energy Resolution
LES	Lepton Energy Scale
LH	Little Higgs OR Left-Handed
LHC	Large Hadron Collider
LLR	Log-Likelihood Ratio
LSTC	Low-Scale Technicolor
MC	Monte-Carlo
MCP	Muon Combined Performance
MDT	Monitored Drift Tubes
MES	Muon Energy Scale
MG	Muon Girl
MIP	Mininum Ionizing Particle

MJ	Multijet
MOND	Modified Newtonian Dynamics
MS	Muon Spectrometer
MSSM	Minimal Supersymmetric Model
mSUGRA	Minimal Supergravity
MWT	Minimal Walking technicolor
NC	Neutral Current
NBG	Numbu-Goldstone Boson
NLO	Next-to-Leading Order
NNLO	Next-to-Next-to-Leading Order
OPAL	Omni-Purpose Apparatus for LEP
PDF	Parton Distribution Function
PGB	Pseudo-Goldstone Boson
PMNS	Pontecorvo–Maki–Nakagawa–Sakata
PMT	Photomultiplier Tube
PRW	Pile-up Reweighting
PTP	p-Terphenyl
PV	Primary Vertex
QCD	Quantum Chromodynamics
QED	Quantum Electrodynamics
QFT	Quantum Field Theory
RDO	Raw Data Object
RF	Radiofrequency
RG	Renormalization Group
RH	Right-Handed
RoI	Region of Interest

RMS	Root Mean Square
RPC	Resistive Plate Chambers
S1(2,3)	Sampling 1, 2, or 3
SCT	Semiconducting Tracker
SF	Scale Factor
SM	Standard Model
SNO	Sudbury Neutrino Observatory
SPS	Super Proton Synchrotron
SR	Signal Region
SSB	Spontaneous Symmetry Breaking
SSM	Sequential Standard Model
SST	Supernova Search Team
SUSY	Supersymmetry
TC^2	Topcolor-Assisted Technicolor
TC	Technicolor
TCSM	Technicolor Strawman Model
TGC	Thin Gap Chambers
TMVA	Tools for Multivariate Analysis
TR	Transition Radiation
TRT	Transition Radiation Tracker
TTC	Timing, Trigger, and Control system
UED	Universal Extra Dimension
UV	Ultraviolet
VBF	Vector Boson Fusion
VEV	Vacuum Expectation Value
VLQ	Vector-Like Quark

WIMP	Weakly Interacting Massive Particle
WLCG	Worldwide LHC Computing Grid
WZW	Wess-Zumino-Witten

For my parents,

To me there has never been a higher source of earthly honor or distinction than that connected with advances in science.

- Isaac Newton

ACKNOWLEDGMENTS

STATEMENT OF PERSONAL CONTRIBUTIONS

The ATLAS experiment, being the largest particle physics experiment alongside CMS, is a huge collaboration in which thousands of people have made significant contributions. From its conception to the understanding of its performance, a vast variety of expertise and manpower is needed to carry through fruition the complex particle hunting endeavours the ATLAS detector has the capacity to achieve. Therefore, it goes without saying that the results presented in this thesis have required the help and support of not only the ATLAS collaborators as a whole, but also of many colleagues with whom I had the privilege to work and to bring to conclusion the search for vector-like quarks and WZ resonances.

This being said, I would like to point out here my own contributions to these analysis efforts.

In my first year as a member of ATLAS, I worked on the event overlay project [1], whose goal was to develop a tool for superimposing simulated signal events onto zero-bias data [1]. This in turn would provide analyzers a way to model background noise or pile-up collisions more accurately given that such backgrounds are ordinarily modelled with Monte Carlo simulation. The overlay procedure required GEANT 4 [2] simulation in hits format of a signal process, to be superimposed to the zero-bias data, in digitized raw data objects (RDO), One of the main difficulties in the project concerned the need to *unfold* the data's pulse shapes back into what would have been the deposited energy, all of this while understanding the intricacies of each subdetectors' pulse shape mechanics and the conditions database, including the geometry database. Once in hand, the deposited energies from simulation and data can then be safely added and subsequently used to compute the overlaid total pulse shape.

Unfortunately, in the prospect of a very high luminosity Large Hadron Collider (LHC), it may become difficult if not impossible to fully simulate statistically significant samples with GEANT 4. It may then be necessary to rely on *fast* simulation techniques. ATLFAST and ATLFAST II [3] offer this possibility. However, unlike GEANT 4, very

---

1. Events upon which no trigger was applied.

important electron and muon tracking information are not simulated and hence not available for analysis. To remedy this, the *FAst TRacking* ATLAS *Simulation* known as FATRAS [4, 5] was developed. My assignment was to help in the development of making possible the overlay of zero-bias events with events simulated with FATRAS instead of GEANT 4. This contribution of mine shall not be described in the present thesis, but is summarized in the ATLAS note [1].

As is expected for most ATLAS collaboration members, I dedicated time to perform shifts in the ATLAS control room. I did two types of shifts, one which consisted of looking over the performance and operation of the Liquid Argon detectors, and the other which consisted of looking over the overall data acquisition quality of all subsystems. Furthermore, in my formative years, I made generator level studies involving CompHep [6] and CalcHep [7] to understand how models, such a Little Higgs (which predict vector-like quarks), could yield potential LHC signatures. From there, I worked my way into the Exotics group where I began to work on the search for vector-like quarks coupling to light quarks. In parallel to that, I also began working within the diboson subgroup on WZ resonances.

Within these two working groups, I touched on almost all aspects of the analyses. It began with the generation and validation of the vector-like quark and WZ resonance signals. It then went on to the involved tasks of checking the modelling of background predictions in the control regions and signal regions. It also included various systematics studies as well as acceptance times efficiency studies upon trigger, p_T , and isolation variables to name just a few. The systematics studies involved understanding the shape uncertainties in our final predicted distribution along with, for example, the understanding of jet energy scale uncertainties after optimization of the signal over background in the signal region.

A large portion of our time was dedicated to verify and counter-verify the consistency of each of our analysis selections (colloquially known as *cut-flow* exercises). This was to ensure that our independently written analyses codes produced identical outcomes, thereby confirming and certifying our results. Moreover, to have the analyses approved by the collaboration, I presented on numerous occasions the status of the analyses to

ATLAS internal exotics subgroups, whose task is to make certain all necessary cross checks have been made as well as help guide the analysis towards a result that does not impinge on other similar analyses to make ATLAS results as consistent as possible. Finally, I participated in the elaboration of the ATLAS internal technical notes along with the publicly available conference notes [8, 9] and published papers [10, 11].

An important aspect of the VLQ search is the optimization of the signal versus backgrounds yields in the signal regions. Using the statistical software tools provided by *Toolkit for Multivariate Data Analysis* [12] (TMVA) with ROOT [13], I optimized the signal cuts upon angular variables between the final state objects.

In the WZ resonance search, an interpolation of the signals was necessary to cover the whole WZ mass spectrum with potential signal. Utilizing the tools offered by RooFit [14], I developed the method to construct such signal templates taking into account all possible shape and normalization uncertainties. I also worked on the extraction of the LSTC limits, which was the primary motivation for the search.

Hence, in both ATLAS searches presented in this thesis, I have made significant contributions that have enabled these searches to come to fruition.

CHAPTER 1

INTRODUCTION

We have no right to assume that any physical laws exist, or if they have existed up to now, that they will continue to exist in a similar manner in the future.

Max Planck

As the Large Hadron Collider (LHC) continues to take vast amounts of data, it is without doubt an extremely exciting period in human history to be a particle physicist and to participate in the adventure of understanding the foundations of reality.

We are hopefully beginning to peek into what lies beyond the Standard Model (SM) of particle physics [15], a model that has proven to be astonishingly accurate ever since its inception [1]. This is especially evident when focusing on one piece of the SM, quantum electrodynamics (QED), whose predictions of the electron's anomalous magnetic moment, and the Lamb shift of hydrogen's energy levels are both examples of how incredibly accurate the theory can be. The SM also has the ability to explain other surprisingly complex processes, such as numerous particle lifetimes and decay widths, and predict particle interaction cross sections. A simple glance through the *Review of Particle Physics* from the *Particle Data Group* [16] is quite convincing, not to mention the recent discovery of a Higgs particle [17, 18] which was the last building block of the SM that had yet to be detected. It is a model entrenched in the theory of quantum fields, mixing both classical quantum theory and special relativity, a facet of the theory we shall examine more deeply in chapter 2 along with its group theory based principles. The model however is heavily dependent on the measurement of 19 free parameters [15] that do not stem from any widely accepted theory. Some of these parameters are related to the SM's particle content, but whose structure remains completely mysterious. The SM

---

1. Despite some recently observed inadequacies; A lot more on this a bit further and in chapter 2.

also suffers from the *fine-tuning* or *hierarchy* problem to which a section in chapter 2 will be dedicated. Finally, the model falls short of explaining many experimental facts obtained over the past few decades about the Universe and its inner workings. These discoveries on the other hand will certainly help us guide our way towards a more profound understanding of nature.

In the last two decades, new insights from various experimental measurements have thankfully emerged giving us the very first few hints as to the reality of nature at energies beyond the electroweak (EW) scale. In parallel, theorists have created a great number of models knowing from the very beginning (since the 1970s) that, based purely on theoretical grounds, the SM cannot be the whole picture. But despite the numerous theoretical propositions, no grander theory has been able to gain support of the entire physics community. It is therefore quite natural to expect that experiments will continue to lead and guide our way in the near future. It is in fact something we have already been witnessing given the recent results from neutrino [19], supernovae [20], and LHC experiments. These observations, detailed in section 2.5.1, along with many others can also be used to synthesize or organize the way in which we think of the deficiencies of the SM and perhaps gain vision into how it might be surpassed.

After presenting the SM at the beginning of chapter 2, I will then go through a list of experimental and theoretical issues that continue to plague it while briefly describing some of the candidate theories that claim to solve some, if not all, of these plaguing issues. The main experimental facts that are incompatible with the SM that shall be discussed are 1) neutrino oscillations, 2) the apparent matter/antimatter asymmetry, and 3) the lack of understanding of the nature of the energy content of the Universe. Alongside these problematic experimental facts, the SM also presents inherent theoretical concerns. The most obvious of these pertains to the fact that the SM does not include gravity as a fundamental force, and in connection to this, if the SM were the final story, there would be an unexplained void of particles for energies between those of the weak scale and the Planck scale. This in turn would require the parameters of the SM to be fine-tuned up to some 30 orders of magnitude for the Higgs mass to be in the electroweak range, a difficult pill to swallow. This theoretical thorn in the SM is of utmost importance as it

links all new theoretical propositions discussed in this thesis, and consequently, a section in chapter 2 shall be dedicated to it. Another issue afflicting the SM is, as mentioned previously, that it has 19 free parameters, most of which dictate the mass of the quarks and leptons. In other words, the SM remains totally silent as to why the top quark, for example, is $\sim 10^6$ orders of magnitude more massive than the electron. The SM also offers no reason as to why the strong force does not break Charge-Parity (CP) conjugation. All renormalizable terms (given the SM particle content) are present in the SM, except for the one term that would give rise to CP-violation in the strong sector (more on this in chapter 2). Accompanying these puzzling features, is a lack of an explanation for the existence of three, and not more [2], fermion generations. Finally, the fact that the weak force breaks parity maximally is yet another mysterious facet of the SM that still eludes a convincing theoretical explanation.

Altogether, the experimental and theoretical questions raised by these facts beg for a new enveloping theory that would at the very least resolve some of these points. To this end, the ATLAS experiment and the LHC program were designed to undertand the nature of electroweak symmetry breaking (EWSB), the cornerstone of the SM, which, via the Higgs mechanism and the value of the electroweak coupling parameters, produces the correct ratio of W to Z boson masses. This mechanism however, as explained in chapter 2, does not in of itself resolve any of the aforementioned problems. In fact, the SM extensions that shall be discussed and considered in chapters 4 and 6 will all have a deep connection to the Higgs sector, either by the addition of new particle states to cure the hierarchy problem, or by hypothesizing that the Higgs be a composite particle, and that EWSB occurs dynamically. All such theories as a result also predict the existence of new resonances in distinct production and decay channels.

Hence, motivated by these general ideas about the inadequacies of the SM and the theories that purport to resolve some of them, I will present in this thesis the results of two ATLASsearches [8, 9] that try to identify whether or not new phenomena or new particles emerge in two specific resonance channels. Such resonances are of course not

---

2. Recent LHC searches [21] along with the Higgs cross section measurements [22] leave no room for 4$^{\text{th}}$ generation chiral quarks.

present in the SM and their existence (and even non-existence) would therefore guide us towards a more fundamental theory.

The two searches that shall be presented in this thesis can be detailed as follows:

- 1) The search for singly produced vector-like quarks (VLQ) coupling to 1st generation quarks. A tree level diagram of such processes can be seen in figure 1.1.

$$qq \to Dq' \to Wuq'$$
$$qq \to Uq' \to Zuq'$$

- 2) The search for $WZ \to l\nu ll$ resonances, where $l = e, \mu$ and $\nu = \nu_e, \nu_\mu$. The Feynman diagram for this resonance is found in figure 1.2.

$$qq \to W' \to WZ$$
$$qq \to \rho_T, a_T \to WZ$$
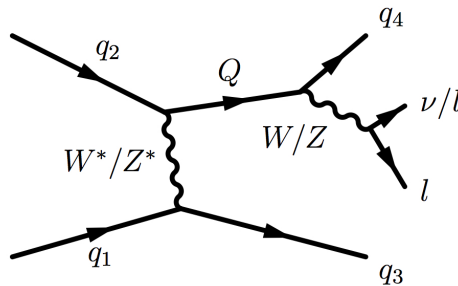
Figure 1.1: t-channel diagram showing the single production of a VLQ Q coupling to light generations (u, d).
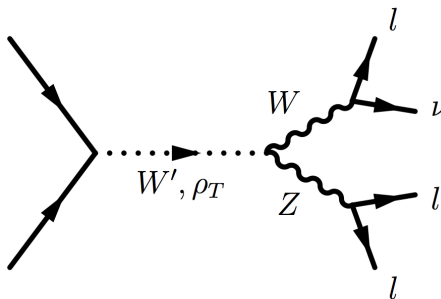
Figure 1.2: Feynman diagram of a s-channel $WZ \to l\nu ll$ resonance, where the possible resonance particles shown are the sequential standard model [23] (SSM) W', and technicolor's ρ_T, although many other possible resonance candidates exist. More on this in chapter 6.

4

In both searches, theoretical models predicting such resonances were used as benchmarks to understand the event structure and topology of such processes as well as understand the detector's search potential. However, despite the use of these underlying models, efforts were made to obtain purely model independent results as shall be shown in chapters 5 and 7.

Moreover, although these two searches seem unrelated, they can both be linked to our understanding of electroweak symmetry breaking (EWSB), itself detailed further in chapter 2. In the context of the newly discovered *Higgs* particle by ATLAS [17] and CMS [18], it may seem as though EWSB is now almost fully understood. It is perhaps correct to state that the particle responsible for it has been found, but many of its properties, its possible compositeness, and how it regularizes its own mass are still very open questions to which both searches above can reveal some answers.

In this context, supersymmetry [24] has been the favorite model of many theorists as it resolves the hierarchy problem, provides a dark-matter candidate, unifies the couplings at the grand unified scale, and explains the breaking of $SU_L(2) \otimes U_Y(1)$, the electroweak gauge group. Extending these ideas to those of general relativity, supergravity has also been a widely studied theory, which, in its minimal form, was dubbed mSUGRA [25] (minimal supergravity). However, there has yet to be experimental evidence thus far for either mSUGRA or MSSM [26] (supersymmetry in its minimal form: minimal supersymmetric model) in spite of extensive searches by LEP, ATLAS and CMS. In this thesis, we shall consider some of the primary alternatives which involve dynamical symmetry breaking scenarios.

In some models invoking the presence of VLQ, such as Little Higgs (LH) models [27] with T-Parity [28], VLQ appear as top-partners that are necessary to cancel the top quark's contribution to the radiative corrections to the Higgs mass [29, 30]. In LH models, which are designed to solve the *little* hierarchy problem[3], a global symmetry whose energy breaking scale is $\sim O(10)$ TeV is hypothesized within which the Higgs is identified as a Pseudo-Goldstone boson [27]. In others, such as in composite

---

3. The little hierarchy problem is used to describe the perceptible tension that exists between the naturalness of the EW scale and the apparent void of new physics up to $\sim O(10)$ TeV.

Higgs models [31], where there exists new strong dynamics, new bound states can be phenomenologically identical to VLQ at energies below the energy scale of this new interaction [31]. Additionally, in universal extra dimensions (UED) models [32, 33], Kaluza-Klein (KK) excitations of a chiral-quark in an odd number of extra dimensions will behave phenomenologically as a VLQ [34]. Finally, within many of the breaking schemes of grand unified theories (GUT), the final result contains a piece identical to the SM, and another containing, among other fermion fields, new up and down type vector-like quarks ($E(6)$ for example only has down-type VLQ [35]). Further details about the role played be VLQ in all of these models will be outlined in chapter 4.

Neutral diboson resonances are also deeply linked to the Higgs' self-coupling as they too have contributing diagrams. WZ resonances however, being of charge ± 1, would seem therefore unrelated. Nonetheless, the theories that do predict such a resonance also have stringent predictions as to the Higgs' properties. For example, technicolor (TC) [36, 37], and its more modern versions such as low-scale technicolor (LSTC) [38] and minimal walking technicolor (MWT) [39], offer new perspectives on the possible ways to achieve EWSB. In analogy to quantum chromodynamics (QCD), it postulates a new force based on $SU(N)_{TC}$ and N_D technifermion doublets making it both confined and asymptotically free. Its energy scale Λ_{TC} however should be around the EW scale $O(100)$ GeV, while its analogue, QCD, is near the ~ 100 MeV scale. In TC, there is no fundamental Higgs, but composite particles such as technipions (Goldstone bosons) that are *eaten* by the electroweak fields to give mass to the W and Z bosons. A detailed account on the EWSB mechanisms produced by the SM scalar doublet Higgs field will be presented in chapter 2, while the one produced by TC and its more modern forms will be presented in chapter 6.

Given these theoretical possibilities, we can understand the connection that exists between these two a priori distinct types of resonances since each predict different phenomenology.

The next chapter will begin by presenting the SM together with an account of the Higgs mechanism before delving primarily into the theoretical problems plaguing it. Following this, chapter 3 will describe the ATLAS detector and the major algorithms

necessary for particle identification and four-momentum measurement. Afterward, the theoretical backgrounds motivating the search for these two aforementioned types of signals will be thoroughly explained in chapters 4 and 6, while their respective AT-LAS searches will be presented in chapter 5 and 7.

CHAPTER 2

THE STANDARD MODEL: ITS ACHIEVEMENTS AND DEFICIENCIES

> *If you can't explain it simply, you*
> *don't understand it well enough*
>
> ———————————————
>
> Albert Einstein

The Standard Model (SM) of particle physics is the framework upon which our understanding of all particle physics is presently based. The present chapter will begin by reviewing the mathematical framework necessary to appropriately describe the SM because some of these aspects will turn out to be important in subsequent chapters. Afterwards, the chapter will briefly go over some of the SM's successes, before concentrating on theoretical questions left unanswered by the SM, to which the theories explained in chapters 4 and chapter 6 propose possible solutions.

Quantum field theory is the mathematical language used to articulate the physical laws put forth by the SM. It also forms the set of rules and building blocks used by the majority of models going beyond the SM. Following primarily the nomenclature of reference [15], but also of [40], the present chapter will now begin by laying down the mathematical foundations of the SM.

2.1 FIELD THEORETIC PRINCIPLES OF THE SM

All quantum operators and states *live* in a tensor product of Hilbert spaces. As such, any operator O can be viewed as the product of operators H_i, that act solely within their respective spaces $O = H_{\mathbf{p}} \otimes H_{SU(2)} \otimes H_{SU(3)} \otimes ... \otimes H_i \otimes ...$ The SM, being a description of the 3 quantized interactions of nature: electromagnetism, the weak and the strong nuclear force, must therefore be a model that describes the interacting Hamiltonian H_{int} as in $H_{\text{total}} = H_{\text{free}} + H_{\text{int}}$. In essence, all of physics may be characterized by the nature of the interacting part of the Hamiltonian. Thankfully, as a very basic guide, many restrictions are to be followed by the interaction Hamiltonian. In fact, several fundamental principles

must be abided by this Hamiltonian if it is to be considered a well-behaved[2] quantum field theory, including of course that of the SM. These principles include:

- 1) Unitarity: The sum of probabilities within an inclusive set of possible outcomes must be equal to 1 and be preserved through time. This requires that the Hamiltonian be hermitian given that the time-evolution operator $U = e^{-iHt}$ must be unitary.

- 2) Cluster decomposition: Physical processes occurring at equal times in different spatial locations are independent. This implies that observables at different spatial locations must commute with one another and that the time-evolution operator must preserve this property.

- 3) Lorentz invariance: The mathematical laws of nature must be invariant under transformations under the Poincaré group. For particle states, this implies that they must be invariant under transformations from the unitary representation of the Poincaré group.

- 4) Stability: The Hamiltonian must be bounded from below. In other words, the vacuum state, or the state with the lowest energy, exists.

- 5) Renormalizability: The physical spectrum at an energy scale Λ must not affect the outcome of physical processes at energies below this scale.

This last principle is perhaps less fundamental than the others if we are content with an approximate theoretical model as many non-renormalizable theories have been put forth to explain, for example, some aspects of neutrino oscillations. But, irrespective of this, if a non-renormalizable theory is needed to explain a given phenomenon, the theory may lose some of its predictive power as infinities often appear while computing basic amplitudes of allowed processes. Therefore, asking for a theory to be renormalizable, as is the SM, is quite natural and expected from a grand unifying theory (GUT).

The SM therefore is a *well-behaved* QFT, as defined above, that attempts to fully describe H_{int}. From here on however, we will write down the SM in the Lagrangian formalism since Lorentz invariance is made more manifest than in the Hamiltonian for-

---

2. The term *well-behaved* means simply those theories which obey the foundational principles detailed further in the text.

malism.

2.2   PARTICLE CONTENT AND FORMAL MATHEMATICAL DESCRIPTION OF THE SM

The SM is founded on the gauge symmetry of the group

$$G_{\text{SM}} = SU_c(3) \otimes SU_L(2) \otimes U_Y(1) \tag{2.1}$$

where $SU_c(3)$ refers to the *color* symmetry of quantum chromodynamics, and where $SU_L(2) \otimes U_Y(1)$ refers to the gauge symmetry of the electroweak force. A Higgs field is introduced as a complex doublet in order to break spontaneously the gauge symmetry via the Higgs mechanism [41], as will be described in section 2.3. In (2.1), L signifies that the symmetry acts upon spinors with left-handed chirality and Y upon particles with hypercharge. These symmetries are immensely important because they inform us about the SM's *local*[3] degrees of freedom. For $SU_c(3)$, the number of degrees of freedom is 8. For $SU_L(2)$, it is 3, and for $U_Y(1)$ it is 1 degree of freedom[4]. Each of these degrees of freedom will be associated to a gauge boson once the theory is gauged by a local symmetry.

Using only the experimentally acquired knowledge of the known fundamental particles and their quantum numbers, and requiring that the theory follow the 5 principles outlined in the previous section, completely defines the possible Lagrangian terms the SM may contain. And quite surprisingly, the SM uses up almost all allowed terms[5]. The particle content and allowed particle interactions of the SM can be summarized loosely by the diagram shown in figure 2.1, where leptons can be seen to interact amongst themselves through the electroweak force (via the γ, $W^\pm$, or Z^0), where quarks are seen to couple via all three forces, and finally where the Higgs field couples to any particle

---

3. Symmetries that exists independently at every point in space and time.

4. The simple unitary group $SU(N)$ has $N^2 - 1$ degrees of freedom.

5. The CP violating gluon-gluon interaction term $\frac{\bar{\theta}}{32\pi^2}\epsilon_{\mu\nu\rho\sigma}F^{a\mu\nu}F^{a\rho\sigma}$ is indeed renormalizable, but experimentally the coupling $\bar{\theta} < 10^{-10}$ [16]. Many theories nonetheless attempt to use a non-zero value for this term to explain some aspects of the matter/antimatter asymmetry of the Universe and possibly also dark matter (DM). A review of these matters can be found in [42].
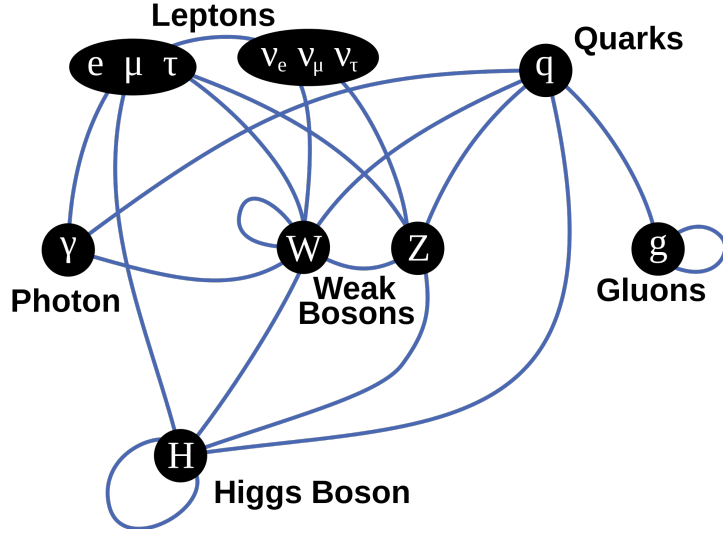
Figure 2.1: Fundamental particles and interactions of the Standard Model [43].

having a non-zero mass.

In terms of spinorial fields, the quark and lepton fields can be denoted by

$$q_{mL} = \begin{pmatrix} u_m \\ d_m \end{pmatrix}_L , \quad u_{mR}, \quad d_{mR} \qquad l_{mL} = \begin{pmatrix} \nu_m \\ e_m \end{pmatrix}_L , \quad e_{mR} \qquad (2.2)$$

where m denotes the quark/lepton generation from 1 to 3, and where q_{mL} (l_{mL}) are spinor doublets of left-handed quarks (leptons) under $SU_L(2)$, and where u_{mR}, d_{mR}, and e_{mR} are singlets again under $SU_L(2)$. Lastly, ν_m and e_m denote the 3 uncharged neutrinos and charged leptons respectively.

Using these known particles as building blocks together with the symmetries of G_{SM} as given in (2.1), one can now move on to fully writing down the SM Lagrangian. Following the nomenclature of reference [40], the SM Lagrangian, in terms of the gauge field-strengths tensors

$$F^i_{\mu\nu} = \partial_\mu G^i_\nu - \partial_\nu G^i_\mu - g_s f_{ijk} G^j_\mu G^k_\nu \rightarrow SU_c(3) \qquad (2.3)$$

$$W^i_{\mu\nu} = \partial_\mu W^i_\nu - \partial_\nu W^i_\mu - g\epsilon_{ijk} W^j_\mu W^k_\nu \rightarrow SU_L(2) \qquad (2.4)$$

$$B_{\mu\nu} = \partial_\mu B_\nu - \partial_\nu B_\mu \rightarrow U_Y(1), \qquad (2.5)$$

11

where W^i_μ, and B_μ are the gauge bosons associated with the local symmetries $SU_L(2)$ and $U_Y(1)$ with structure constants f_{ijk} for $SU_c(3)$ and ϵ_{ijk} for $SU_L(2)$, can be succinctly written in 6 different parts named

$$L_{SM} = L_{SU_c(3)} + L_{SU_L(2)} + L_{U_Y(1)} + L_{\text{Dirac}} + L_\varphi + L_{\text{Yukuwa}}, . \tag{2.6}$$

In terms of the $n_{\text{gen.}} = 3$ generations of quarks and leptons given in equation (2.2), each of these terms can now be expressed as

$$L_{SU_c(3)} = -\frac{1}{4} F^i_{\mu\nu} F^{i\mu\nu} + \sum_r^{\text{flavors}} \bar{q}_{r\alpha} i \slashed{D}^\alpha_\beta q^\beta_r \tag{2.7}$$

$$L_{SU_L(2)} = -\frac{1}{4} W^i_{\mu\nu} W^{i\mu\nu} - \frac{1}{4} B_{\mu\nu} B^{\mu\nu} \tag{2.8}$$

$$L_{\text{Dirac}} = \sum_{m=1}^{n_{\text{gen.}}} \left(\bar{q}_{mL} i \slashed{D} q_{mL} + \bar{l}_{mL} i \slashed{D} l_{mL} + \bar{u}_{mR} i \slashed{D} u_{mR} + \bar{d}_{mR} i \slashed{D} d_{mR} \right.$$
$$\left. + \bar{e}_{mR} i \slashed{D} e_{mR} \right) \tag{2.9}$$

$$L_{\text{Yukawa}} = - \sum_{m,n=1}^{n_{\text{gen.}}} \left(Y^u_{mn} \bar{q}_{mL} \tilde{\varphi} u_{mR} + Y^d_{mn} \bar{q}_{mL} \varphi d_{nR} + Y^e_{mn} \bar{l}_{mL} \varphi e_{nR} \right) \tag{2.10}$$

$$L_\varphi = (D^\mu \varphi)^\dagger D_\mu \varphi - \mu^2 \varphi^\dagger \varphi - \lambda (\varphi^\dagger \varphi)^2. \tag{2.11}$$

In the above equations, the $SU_L(2) \otimes U_Y(1)$ gauge covariant derivatives are

$$\slashed{D} = D_\mu \gamma^\mu = \left(\partial_\mu + i g_L \frac{\sigma^i}{2} W^i_\mu + g_Y \frac{1}{2} B_\mu \right) \gamma^\mu, \tag{2.12}$$

where σ^i are the usual Pauli matrices, whereas the $SU_c(3)$ gauge covariant derivatives $\slashed{D}^\alpha_\beta$ are given by

$$\slashed{D}^\alpha_\beta = D^\alpha_{\mu\beta} \gamma^\mu = \left(\partial_\mu \delta_{\alpha\beta} + \frac{i g_s}{2} G^i_\mu \lambda_i \right) \gamma^\mu, \tag{2.13}$$

where λ_i are the 8 generators of $SU(3)$. The name *covariant* derivative stems from the need to connect one spacetime point with another given these local gauge symmetries. The freedom in choosing any gauge at any spacetime point is analogous to the freedom

of choosing a different coordinate system in vector calculus when computing directional derivatives. The actual value of the derivative remains unchanged irrespective of the choice of basis. The change of basis simply requires the derivative to be transformed under a covariant transformation. In an analogous manner, the choice of gauge and its associated covariant derivatives ensures conservation of the underlying symmetry.

Finally, the structure constants f_{ijk} and ϵ_{ijk} found in equations (2.3) and (2.4) are directly related to the generators of $SU(3)$ and $SU(2)$

$$\left[\lambda^i, \lambda^j\right] = 2if_{ijk}\lambda^k \tag{2.14}$$

$$\left[\sigma^i, \sigma^j\right] = 2i\epsilon_{ijk}\sigma^k \tag{2.15}$$

Equation (2.15) indicates that ϵ_{ijk} is indeed the total antisymmetric symbol.

It is beyond the scope of this thesis to discuss how this quantization procedure arrives at obtaining Feynman rules and computing process amplitudes, but it suffices to say that these procedures are very well established and thoroughly discussed in [44–46] to name just a few.

2.3   THE HIGGS SECTOR

At very high energies, that is above the weak scale, the $SU_L(2) \otimes U_Y(1)$ symmetry of the SM is an unbroken symmetry. During the very early Universe, as the energies dipped below the weak scale (at roughly $t \sim 10^{-11}$ s), the strength of the Higgs field settled to its minimum $\langle\varphi\rangle_0$ and 3 of its degrees of freedom were absorbed , while the 4th became a massive particle known as the Higgs boson. This spontaneous symmetry breaking is vital to the SM as it adequately explains the ratio $\frac{m_W}{m_Z} = \cos\theta_W \simeq 0.92$ between the $W^\pm$ and Z^0 boson masses . Other types of EWSB also achieve the correct ratio such as dynamical symmetry breaking (DSB) as will be discussed in the context of composite Higgs, and technicolor theories in chapter 6, but to fully appreciate the differences, it is important to now go over how the SM's Higgs mechanism operates.

The Higgs sector is defined by terms involving the scalar doublet field [40]

$$\varphi = \begin{pmatrix} \varphi^+ \\ \varphi^0 \end{pmatrix} = \frac{1}{\sqrt{2}} \begin{pmatrix} \varphi_1 - i\varphi_2 \\ \varphi_3 - i\varphi_4 \end{pmatrix} \qquad (2.16)$$

in L_φ and L_{Yukawa} of equation (2.11), and its role is two-fold. The first is to give rise to EWSB and hence break the SM's $SU_L(2) \otimes U_Y(1)$ symmetry. The second is to give a mass to all quarks and leptons [6] through the Yukawa terms given in (2.10). If the μ parameter in the Higgs potential $V(\varphi) = \mu^2 \varphi^\dagger \varphi + \lambda(\varphi^\dagger \varphi)^2$ is imaginary, spontaneous symmetry breaking (SSB) occurs since the minimum of $V(\varphi)$ is at a non-zero value. This potential is the infamous mexican-hat potential as seen in figure 2.2. Without loss
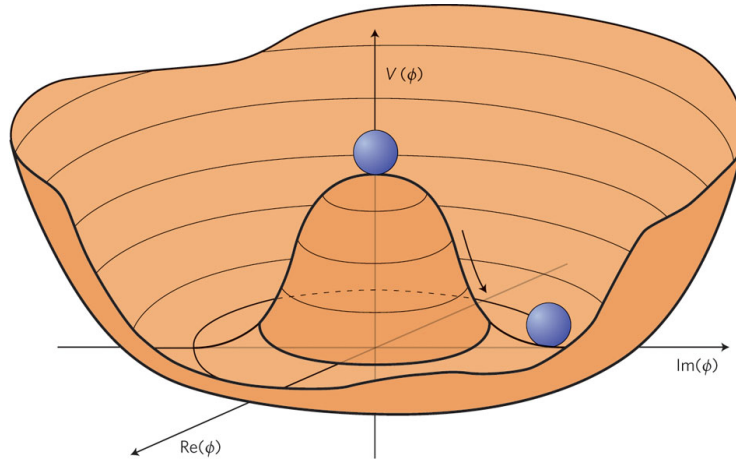
Figure 2.2: Heuristic representation of the Higgs potential acquiring a VEV [49].

of generality, choosing the direction $\langle 0|\varphi_3|0\rangle = v$, where v is the non-zero vacuum expectation value, and leaving $\langle 0|\varphi_i|0\rangle = 0$ for $i = 1, 2, 4$, simplifies the form of the potential, which can be rewritten as

$$V(\langle\varphi\rangle) \longrightarrow V(v) = \frac{1}{2}\mu^2 v^2 + \frac{1}{4}\lambda v^4. \qquad (2.17)$$

---

6. For neutrinos, the relatively recent discovery of flavour oscillations theoretically demands that they have non-zero masses, but the way in which they acquire mass is of theoretical debate. The see-saw mechanism is one possibility [47, 48], but a detailed explanation of such a process goes beyond the scope of this thesis.

Solving for the minima $\frac{dV}{dv} = 0$ yields the solution

$$\frac{dV}{dv} = \mu^2 v + \lambda v^3 = 0 \quad \Rightarrow \quad v = \sqrt{\frac{-\mu^2}{\lambda}}. \tag{2.18}$$

Classically, the case $\mu = 0$ and $\lambda \neq 0$ cannot be treated properly [7], and in fact, together with one-loop corrections, the potential $V(v) = \frac{1}{4}v^4$ also creates spontaneous symmetry breaking [50]. Concentrating however on the case $\mu^2 < 0$, we can first write down the classical solution

$$\varphi|0\rangle_0 = \frac{1}{\sqrt{2}} \begin{pmatrix} 0 \\ v \end{pmatrix}, \tag{2.19}$$

where we have chosen a specific orientation in $SU_L(2)$, and study the quantum field φ around this classical minimum using the unitary gauge transformation

$$\varphi(x) = \varphi_0(x) + \zeta(x), \text{ where } \zeta(x) = \frac{1}{\sqrt{2}} \begin{pmatrix} 0 \\ H \end{pmatrix}. \tag{2.20}$$

$\zeta(x)$ contains the scalar field $H(x)$ which can be correctly associated to the Higgs field. From here, we can express φ in terms of the vacuum expectation value v and the field $H(x)$ with

$$\varphi = \frac{1}{\sqrt{2}} \begin{pmatrix} 0 \\ v + H \end{pmatrix} \tag{2.21}$$

where the explicit choice of direction, equation (2.19), now permits us to rewrite the covariant kinetic terms of L_φ in (2.11) with new this gauge specific φ doublet

$$(D_\mu \varphi)^\dagger D^\mu \varphi = \frac{1}{2} \left[\partial_\mu + i g_L \frac{\sigma^i}{2} W_\mu^i + g_Y \frac{1}{2} \varphi \right]^\dagger \left[\partial^\mu + i g_L \frac{\sigma^i}{2} W^{i\mu} + g_Y \frac{1}{2} B^\mu \varphi \right]$$
$$+ \partial_\mu H \partial^\mu H, \tag{2.22}$$

---

7. The Higgs potential with $\mu = 0$ does not classically give rise to SSB, but once the fields are quantized, SSB does indeed occur as explained in [50].

and with a little algebra, we arrive at

$$(D_\mu\varphi)^\dagger D^\mu\varphi = \frac{v^2}{8}\left(W_\mu^i W^{i\mu} + g_Y B_\mu B^\mu\right) + \frac{1}{8}\left(H^2 W_\mu^i W^{i\mu} + g_Y H^2 B_\mu B^\mu\right)$$
$$+ \partial_\mu H \partial^\mu H. \tag{2.23}$$

With a little foresight, the variable transformations

$$W_\mu^\pm = \frac{1}{\sqrt{2}}(W_\mu^1 \mp i W_\mu^2)$$

$$Z_\mu = -\sin\theta_W B_\mu + \cos\theta_W W_\mu^3$$

$$A_\mu = \cos\theta_W B_\mu + \sin\theta_W W_\mu^3$$

where $\sin\theta_W = g_Y/\sqrt{g_L^2 + g_Y^2}$ and $\cos\theta_W = g_L/\sqrt{g_L^2 + g_Y^2}$, are now used to re-express (2.23) giving

$$(D_\mu\varphi)^\dagger D^\mu\varphi = M_W W_\mu^+ W^{-\mu} + M_Z Z_\mu Z^\mu + \text{Terms with } H. \tag{2.24}$$

In the above equations, θ_W is the Weinberg angle that can be viewed as a measure of the mass splitting that exists between the $W^\pm$ and the Z^0 or the mixing of neutral component of the $SU(2)$ gauge field with the B_μ field. Notice also how the A_μ field, that we can now be promptly associated with the photon, has no mass term, and that the physical $W^\pm$ and Z^0 boson fields have acquired the physical masses

$$M_W = \frac{g_L v}{2} \tag{2.25}$$

$$M_Z = \frac{v\sqrt{g_L^2 + g_Y^2}}{2} \tag{2.26}$$

$$\Rightarrow \frac{M_W}{M_Z} = \cos\theta_W = \frac{g_L}{\sqrt{g_L^2 + g_Y^2}} \tag{2.27}$$

To lowest order, using the known relationships between these couplings and Fermi's constant $G_F/\sqrt{2} \sim g_L^2/8M_W^2$, where $G_F = 1.16639 \times 10^{-5}\text{GeV}^{-2}$, and also that [8]

---

8. Measured via neutral current scattering.

$\sin^2 \theta_W \sim 0.23$, one easily derives the ratio

$$\frac{M_W}{M_Z} \sim \frac{78 \text{ GeV}}{89 \text{ GeV}} \qquad (2.28)$$

Loop corrections raise the masses of both the $W^\pm$ and Z^0 by roughly 2 or 3 GeV, hence reproducing the correct experimentally measured ratio. This prediction is one of the greatest achievements of the SM and electroweak theory in general.

Finally, substituting the φ field of equation (2.21) in the Higgs potential $V(\varphi) = \mu^2 \varphi^\dagger \varphi + \lambda (\varphi^\dagger \varphi)^2$, cubic and quartic Higgs interactions appear [40]

$$V(\varphi) = -\frac{\mu^4}{4\lambda} - \mu^2 H^2 + \lambda v H^3 + \frac{\lambda}{4} H^4. \qquad (2.29)$$

The quadratic term can also be associated to a Higgs mass to first order, yielding a mass of

$$M_H = \sqrt{-2\mu^2} = \sqrt{2\lambda} v \qquad (2.30)$$

where we have used (2.18). Given the recent Higgs mass measurements [17, 18], λ can easily be derived, assuming the discovered particle is the SM Higgs, yielding $\lambda \simeq 0.26$.

The Higgs mechanism within the SM, as just exposed, will be a very useful comparison point while presenting other possible means for EWSB, such as ones that involve more than one Higgs doublet, or ones that are instantiated dynamically via the introduction of possible new forces whose scales are beyond the TeV scale. Both of these prospects and others will be described in chapters 4 and 6.

Simultaneously in Melbourne at the ICHEP conference [51], the bi-annual international conference on high energy physics, and at CERN, the ATLAS and CMS collaborations announced the discovery of a new boson having Higgs-*like* properties. As the collaborations gather more data, the new boson seems to be more and more consistent with the SM Higgs, as its spin and parity have now been measured [52]. However, there still remains to measure its branching fractions into fermions, at which point if the couplings are consistent with those predicted for the SM, the SM shall indeed be consecrated! These important characteristics of the Higgs shall be important to keep in mind

while in chapters 4 and 6, possible extensions to the SM will be discussed.

2.4 EXAMPLES OF EXPERIMENTAL VERIFICATIONS OF THE SM

A vast number of experimental verifications of the SM have been obtained over the past few decades outlining its predictive power at energies up to the TeV scale.

Among collider measurements, the evaluation of the heavy quark (top and bottom) production rates and the determination of the running of the QCD coupling α_s are both examples of the SM's effectiveness in modelling particle physics at energies up to the TeV scale. A summary of all recent results of ATLAS cross section measurements is shown in figure 2.3, compared to SM predictions.

Another example of the SM's predictive prowess that is of particular importance for the search for WZ resonances (chapter 6 and 7), is to understand the WZ production cross section in p-p collisions at 7 and 8 TeV. The latest result from CMS [53] using 19.6 fb^{-1} at 8 TeV produced

$$\sigma_{\text{Experiment}} = 24.61 \pm 0.76 \,(\text{stat.}) \pm 1.13 \,(\text{syst.}) \pm 1.08 \,(\text{lumi.}) \text{ pb}$$

$$\sigma_{\text{Theory}} = 21.91^{+1.17}_{-0.88} \text{ pb at NLO [53]}$$

for a Z boson in the mass range between 71 and 111 GeV. These results validate the theoretical computation of the cross section with the simple Feynman diagrams at next-to-leading order in α_s in both the t-channel and s-channel as shown at leading order in figure 2.4. Figure 2.4(a) derives from the terms in (2.9), whereas figure 2.4(b) is enabled by couplings found in (2.8) and (2.9).

Yet another example involves processes that are very sensitive to new physics: triple and quartic gauge boson couplings. The latter is of special interest because the Higgs field is necessary to unitarize the vector boson scattering cross section at high energies, although no SM measurement of it has yet been possible at the LHC given the present amount of data and the relatively small cross section such SM processes have. As for the triple gauge coupling, the CMS collaboration has recently measured, with 5 fb^{-1} of data
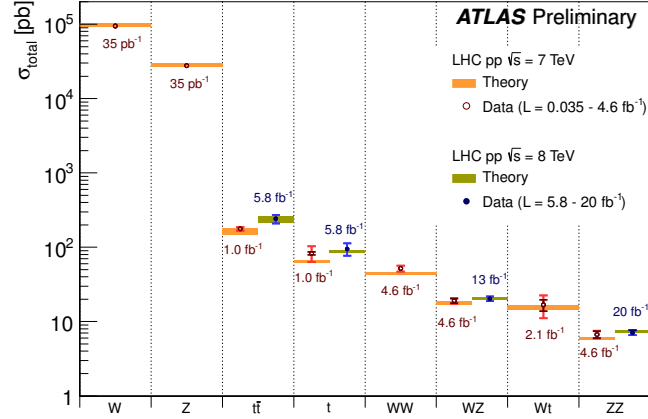
Figure 2.3: Overview of ATLAS' cross section measurements for various processes. The results are all compared to SM predictions, which are in orange for 7 TeV, and green for 8 TeV.

(a) t-channel WZ production

(b) s-channel WZ production
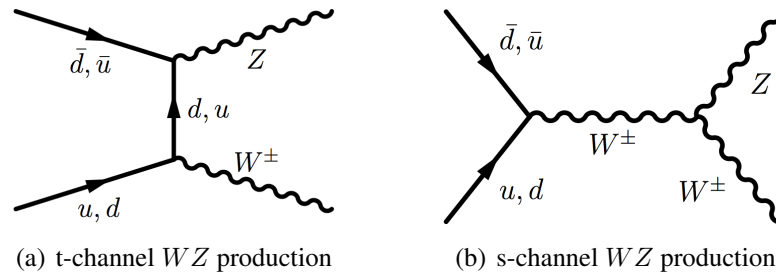
Figure 2.4: Tree level WZ production within the SM. The Lagrangian terms associated to these processes are found in equation (2.8) and (2.9).

at 8 TeV, the cross section of the vector boson fusion (VBF) process $WW \rightarrow Z(ee, \mu\mu)$ to be [54]

$$\sigma_{\text{fiducial}} = 154 \pm 24 \,(\text{stat.}) \pm 52 \,(\text{syst.}) \pm 3 \,(\text{lumi}) \tag{2.31}$$

in agreement with the SM prediction of 166 fb calculated at NLO. The cross section measurement σ_{fiducial} relies on a number of kinematical selections as reported in detail in [54].

Lastly, the processes involving W/Z+jets is of critical importance for VLQ searches in general. It amounts to understanding the shape of the kinematical distributions for W+jet and Z+jet events. Utilizing the low pile-up conditions of the 2010 data, the measured total cross section of the inclusive processes $W \rightarrow \ell\nu_\ell$ and $Z \rightarrow \ell\ell$, where $\ell = e, \mu$, were compared to perturbative QCD calculations at *next-to-next-to-leading-order* (NNLO) and were found to be in good agreement [55]. In a similar study, the ratio of $W^\pm$ to Z^0 production with exactly one jet was performed and again found results compatible with SM predictions [56].

2.5 THEORETICAL WEAKNESSES

As was briefly described in the introduction, the SM faces increasingly problematic experimental facts that it is either unable to explain, or worse, with which it is in plain contradiction.

As of today, we can classify the direct observations that challenge and even contradict the SM into three main categories: *Neutrino Physics*, the *Matter/Antimatter Asymmetry*, and the *Energy Content of the Universe*. This is by no means an exhaustive list, but they are without a doubt some of the most important problems facing modern particle physics. They will also help us shed a broader light upon the ATLAS searches presented in this thesis and fully understand their implications.

Whether it is neutrino oscillations, dark matter, or the matter/antimatter asymmetry, the SM remains completely ill equipped to fully explain these phenomena. But there are also theoretical problems that the SM faces, and that also demand a grander, more enveloping theory to explain satisfactorily. To name just a few, the main theoretical issues

are the origin of fermion generations, their respective mass differences, charge quantization, the left-handedness of the weak force, and the hierarchy problem. In the remaining section of this chapter, we shall focus on the hierarchy problem because it links the two ATLAS resonance searches exhibited in later chapters by the simple fact that the models predicting such resonances also propose solutions to the hierarchy problem.

2.5.1 UNEXPLAINED OBSERVABLES

The first category concerns the SM's neutrino sector. Because neutrinos only carry a weak charge, they couple to matter very weakly and thus make neutrino experiments quite challenging. In the last two decades however, experiments such as Kamiokande (that later became Super-Kamiokande [57]), GALLEX/GNO [58], SNO [59], and many others have together been able to uncover the fact that the flavour states ν_e, ν_μ, and ν_τ are not equivalent to the physical eigenstates. This in turn means that the flavour states must mix or oscillate to produce the observed eigenstates, which is only possible if neutrinos have mass. This feature is completely missing from the SM which only contains massless left-handed ν_L states.

The second category pertains to a quite baffling facet of nature, the matter/antimatter asymmetry of the Universe. Once antimatter was discovered by Carl D. Anderson in 1932 [60], and the Big Bang theory began to gain solid theoretical and experimental footing [61], it did not take long for physicists to wonder why the Universe was totally matter dominated. During the very first moments of the Big Bang, an equal amount of matter and antimatter should have been created, and if the laws of physics are symmetric under the combination of Charge-Parity (CP) conjugation, the simple question arises: Why is there any matter left at all? Some initial explanations invoked the possibility of pockets of antimatter floating around in space awaiting our detection. This was soon laid to rest as antihelium cosmic rays were not to be found [9]. Then perhaps the laws of physics are not symmetric under Charge-Parity conjugation after all, and this proposal proved to be in fact true. Within the mixing of different particle generations through

---

9. Antihelium cosmic rays still today prove to be elusive given the results from the BESS-Polar Spectrometer [62].

the Cabibbo–Kobayashi–Maskawa (CKM) matrix, therein lies the possibility of Charge-Parity (CP) violation. In turn, this conspires to making some matter transitions more probable then their antimatter counterparts. The amount of CP violation is determined by the value of the CP-violating phase of the CKM matrix. It is one the 19 free parameters and has been experimentally measured [16]. Since CP-violation is only possible within the framework of (at least) three quark generations, its discovery [63] predicted the existence of a 3rd generation. Unfortunately, the measured value of the CP-violating phase simply cannot account for the observed baryon asymmetry, measured to be

$$\chi = \frac{n_B - n_{\bar{B}}}{n_\gamma} \simeq 5 \times 10^{-10}. \tag{2.32}$$

where n_B is the number of baryons, $n_{\bar{B}}$ is the number of antibaryons, and n_γ is the number of photons in the Universe today. Within the confines of the SM, one can get a good estimate of the amount of asymmetry created during the early phases of the Big Bang via the measured value of the CP-violating phase [64], and it amounts to $\chi \sim 10^{-18}$ [65], evidently much too small. Hence, the SM is unable to explain the observed matter/antimatter asymmetry despite having mechanisms producing a non-zero asymmetry.

The final category speaks of the matter/energy content of the Universe. Today, physicists face the perhaps embarrassing fact that $\sim 95\%$ of the Universe has no accepted theoretical explanation. Both dark matter (DM) with $\sim 23\%$, and dark energy with $\sim 72\%$ dominate the energy content of the Universe, leaving visible matter with only $\sim 5\%$. These two large unexplained pieces however do lie on convincing observational ground.

At the beginning of the 1970s, Vera Rubin presented measurements she had made of the orbital velocities of stars in the Milky Way [66]. Her findings showed that the orbital velocity of stars hit a plateau as a function of their distance to the galactic center. This conflicted with the calculated gravitational potential produced by visible matter which should have produced a falling orbital velocity distribution going like $v(r) \propto 1/\sqrt{r}$. Other evidence for DM can be seen via the effects of gravitational lensing [67]. By comparing the observed lensing with the one produced by visible matter and predicted

by General Relativity, one sees a clear disagreement. However, if one assumes that matter is surrounded by a massive invisible cloud gravitating near its center, one obtains good agreement with observation [68]. An analysis of the anisotropies in the cosmic microwave background radiation also indicates that the Universe does indeed contain DM [69]. Although there exist alternatives for explaining the orbital velocity and gravitational lensing phenomena just described, such as MOND theory [70], the general view is that these effects are due to the existence of weakly interacting massive particles (WIMP), hypothetical particles that cannot decay into SM particles. If this were indeed the case they could potentially be produced by the LHC and be detected by ATLAS in the coming years [10].

Using Type II supernovae as a standard candle, the redshift measurements from the Supernova Search Team (SST) [20] have shown that galaxies are flying apart from each other at an ever increasing rate. *Dark energy*, as it is colloquially called, permeates all of space-time and acts as a repulsive gravitation force driving afar the galaxies. The cosmological constant found in Einstein's theory field equations [74] can give rise to such a phenomenon, but at the quantum scale, the source of this negative gravitational pressure continues to be mysterious. In fact, one can calculate the vacuum instability pressure from QFT [75], upon which the SM is formulated, and obtain a result over 100 orders of magnitude off the mark given the Higgs field expectation value!

The discussion of these three categories of unexplained phenomena and their relation to the SM was done to illustrate how much is still unknown and why searches at the LHC, through all of its experiments, including of course ATLAS, are crucial to gain a greater understanding and perhaps even elucidate some of these mysteries and go beyond the confines of the SM.

2.5.2 AESTHETICS AND UNNATURALNESS

Pondering about the relative strengths of the four (known) fundamental forces, one quickly comes to wonder why the weak force is 10^{32} times weaker than gravity. Within

---

10. A number of these searches have in fact already been performed by ATLAS [71, 72] and also CMS [73] providing some of the most stringent limits to date.

the SM, this question transforms itself into asking: "why the Higgs mass is so much smaller than the Planck scale, at which point all forces, including gravity, would become unified?" In some sense, the hierarchy problem exists because we take seriously the possibility that the SM is the final theory and that there is nothing else up to Λ_{Planck} [11]. Being careful to restrict ourselves to the SM, one would naturally expect the quadratic corrections to the Higgs mass μ in equation (2.11) be proportional to the ultraviolet (UV) cutoff of the theory

$$\Delta m_H^2 \propto \Lambda_{UV}^2 = \Lambda_{\text{Planck}}^2. \tag{2.33}$$

In the SM, this is equal to the Planck scale, in which case unprecedented cancellations must occur for the Higgs mass to be $\mathcal{O}(100)$ GeV, the scale necessary for producing the correct $W^{\pm}$ and Z^0 masses and unitarizing the vector boson processes $VV \to VV$, where $V = W, Z$. Therefore, to have simultaneously a light Higgs to produce EWSB and a void of particles between the TeV scale up until the Planck scale requires an unnaturally fine ajustement of the parameters to keep the Higgs mass from blowing up to the cutoff scale Λ_{UV}.

More explicitly, take for example, the top-loop contribution to the Higgs propagator as depicted in figure 2.5. Computing its amplitude yields
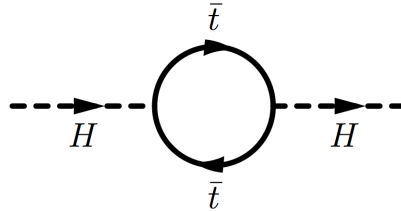
Figure 2.5: Top-loop contribution to the Higgs propagator. The top, being the heaviest known particle, couples significantly to the Higgs.

$$\Pi_{HH}^{\text{top}}(0) = -4\frac{m_{\text{top}}^2}{v} \int \frac{d^4k}{(2\pi)^4} \left[\frac{1}{k^2 - m_{\text{top}}^2} + \frac{2m_{\text{top}}}{(k^2 - m_{\text{top}}^2)^2} \right], \tag{2.34}$$

where $\Pi_{HH}^{\text{top}}(0)$ is the zeroth order loop amplitude. We can see from (2.34) that the 1st

---

11. This idea is further supported by the fact that the SM's couplings are closest to each other at energies of roughly 10^{16} GeV.

term is quadratically divergent, confirming the statement of (2.33).

As it will be shown in chapters 4 and 6, there exists a variety of ways for countering, at least partially, this issue.

Interestingly, the recent Higgs measurements [17, 18] suggest that the electroweak vacuum is *metastable* with a lifetime of $\sim 10^{100}$ years [76, 77]. Figure 2.6 presents, as a function of the top quark and Higgs masses the instability scale Λ_{Inst} in GeV, defined
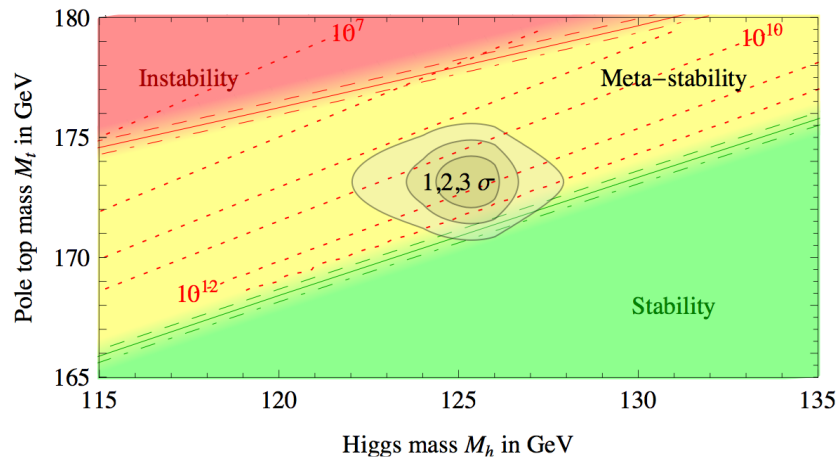
Figure 2.6: The stable (green), metastable (yellow), and unstable (red) regions are drawn as a function of the top quark and Higgs masses. The dashed red lines indicate the instability scale Λ_{Inst} in relation to the top quark and Higgs masses [76].

as the energy where the quartic Higgs coupling, λ in (2.11), turns negative. In other words, beyond Λ_{Inst} the EW vacuum does not have a ground state (see equation (2.17)). If metastable, the lifetime of the EW vacuum is longer than the age of the Universe, thus unaltering the mechanisms of baryogenesis [77].

2.5.3 TRIVIALITY

It has been known for some time that $\lambda\phi^4$ theory (see equation (2.11)), in $D = 4$ spacetime dimensions, has a vanishing of its self-coupling as a function of increasing energy [78, 79]. This in turn suggests that the Higgs field, whose potential (2.17) after EWSB contains a $\lambda\phi^4$ like term, is a long-wavelength approximation and that it may only be valid to lowest order in perturbation theory. With Λ_{UV} denoting the cutoff en-

ergy/momentum of the theory, the $\lambda \phi^4$ coupling grows like

$$\lim_{\Lambda_{UV} \to \infty} \lambda = 0 \tag{2.35}$$

following the renormalization group (RG) equations that lead to the relation between the bare coupling λ_0 and the renormalized coupling λ

$$\frac{1}{\lambda_0} = \frac{1}{\lambda} - \frac{3}{64\pi^2} \log \frac{\Lambda_{UV}}{m_H}, \tag{2.36}$$

where m_H is the Higgs mass which clearly has no relevance in the high energy limit.

This fact along with the previous ones indicate quite convincingly that the Higgs sector of the SM is insufficiently equipped to explain the high energy behaviour of the theory. In consequence, alternatives necessarily need to be considered, some of which shall be exposed in chapters 4 and 6. But first, a thorough description of the ATLAS detector shall follow in order to fully understand how the searches for those alternatives were accomplished.

2.6 MOVING BEYOND THE SM

The pressing question that therefore needs to be answered is whether the recently discovered particle is the SM Higgs or not, and how it fits in a grander picture that elucidates the issues outlined in the previous sections.

Towards this goal, the present thesis shall study processes that have generic predictions of strong EWSB scenarios. Focusing on non-supersymmetric scenarios, this thesis shall therefore probe models such as composite Higgs and technicolor models respectively explained in chapter 4 and 6 and searched for in the analyses of chapters 5 and 7.

CHAPTER 3

THE ATLAS DETECTOR

People who are really serious about software should make their own hardware.

Alan Kay

The ATLAS detector [80, 81] is a multipurpose particle detector designed for particle physics at the TeV scale. Its ingenious design permits it to precisely measure particle 4-momenta with almost 4π in solid angle, and this at extremely high event rates. The detector consists of 3 main sub-detector sections : the inner detector (ID), the calorimeters, and muon detectors, each having a specific role in measuring particle 4-momenta. The multi-purpose design enables it to distinguish between electrons, muons, photons as well as mesons while being able to determine the sign of their electromagnetic charge. In the following sections, I will present in further detail how each of these sub-detectors plays its role in particle detection and introduce the software infrastructure necessary for ATLAS' sub-detectors to work in perfect tandem while recording interesting hard scattering events at frequencies of ~ 400 Hz.

To begin however, a brief addendum about the LHC is in order, because after all, it is the LHC that produces the copious amounts of TeV proton-proton collisions for the ATLAS detector to observe. Therefore, I will begin by discussing the technical aspects of the LHC and the beam conditions it has been able to produce for ATLAS and the other LHC experiments.

3.1 BASICS OF THE LHC [80]

The LHC is a series of two-ringed superconducting magnets constructed in a tunnel originally constructed for the Large Electron Positron (LEP) collider [82]. The tunnel's construction took place between 1984 and 1989 along with instalments of all of the LEP

experiments, ALEPH, DELPHI, OPAL, and L3. Since the dismantlement of LEP, which began in 2001, the construction of the ATLAS cavern began in parallel with those of the other large LHC experiments, namely, CMS, ALICE, and LHCb. The tunnel itself lies between 45m and 170m underground, and at an 1.4% inclination towards lake Geneva (Lac Léman) as seen in figure 3.1. Before entering the LHC ring, packets of protons must first be accelerated in sequence through LINAC 2 (Linear Accelerator), the PS (Proton Synchrotron), and the SPS (Super Proton Synchrotron), thereby acquiring energies of 450 GeV.
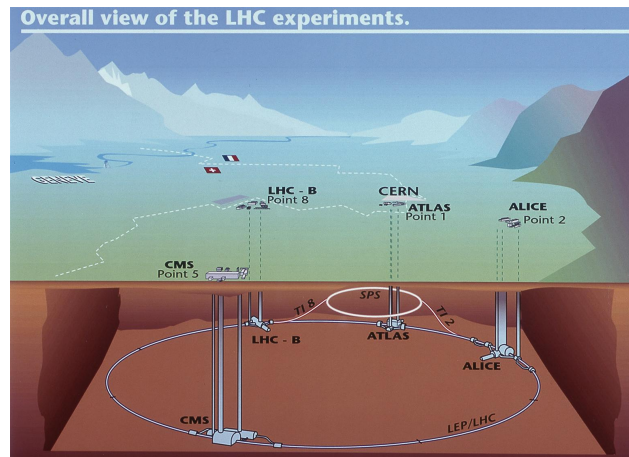
Figure 3.1: Overview of the LHC experiments on the French-Swiss border [83]. Note the location of the Super Proton Synchrotron (SPS) that provides the initial proton acceleration up to 900 GeV.

The LHC's design objective is to produce proton-proton collisions at center-of-mass energies of 14 TeV and at a peak luminosity of 10^{34} cm^{-2}s^{-1}. Unfortunately, due to the 2008 quenching incident [84], the center-of-mass energies had to be lowered to 7 TeV in 2010-2011, and was later raised to 8 TeV in 2012. This was to ensure that the resistance heating between each of the 1232 dipole superconducting magnets, producing a field of 8.33 Tesla (for 7 TeV), would not bring the liquid helium, cooling the magnets, past its boiling point. During this time however, the LHC has been able to deliver ever higher instantaneous luminosities as presented in figure 3.2. In 2012, instantaneous luminosities approaching 0.7×10^{34} where attained using 50 ns bunch spacings. This led to in-time pile-up conditions beyond ATLAS design specifications. Figure 3.3 shows the
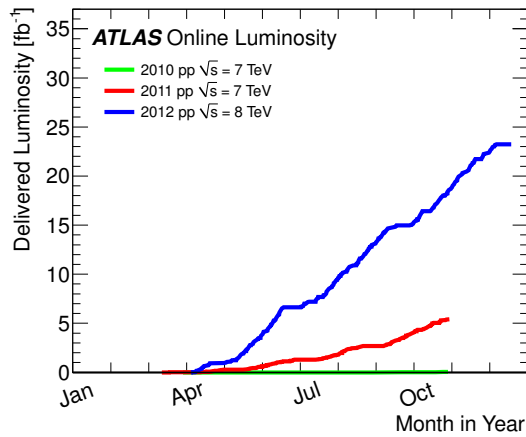
Figure 3.2: Cumulative integrated luminosity obtained in each of the 3 years of data taking [85].

average number of interactions per bunch crossing distribution for both years 2011 and 2012. As discussed in [81], the expected number of minimum-bias [1] events per bunch crossing while running at 10^{34} cm^{-2}s^{-1} and at 25 ns bunch spacing is about $\langle \mu \rangle = 23$. From figure 3.3, we can see that by the second period of the 2012 data-talking run (the center of the second *hump* in the 2012 distribution), the average number of interactions per bunch crossing was approximately $\langle \mu \rangle = 25$. In order to gain a handle on and eliminate the undesirable effects of minimum-bias events, which overlay the more interesting hard scattering events, adequate adjustments to the calculation of missing transverse momentum, in particular, as well as more rigorous criteria for the number of tracks per vertices needed to be implemented, as was done in the analyses put forth in chapters 5 and 7.

The LHC's instantaneous luminosity (from here on, I will speak purely of luminosity when discussing instantaneous luminosity) can be computed with the following equation [80]:

$$L = \frac{N_b^2 n_b f_{rev} \gamma_r}{4\pi \epsilon_n \beta^*} F \qquad (3.1)$$

where

---

1. Minimum-bias events can be defined as those that result from *soft* quark-gluon interactions and that require non-perturbative methods to describe (no color exchange), in contrast to hard scattering events which are well described by perturbative QCD.
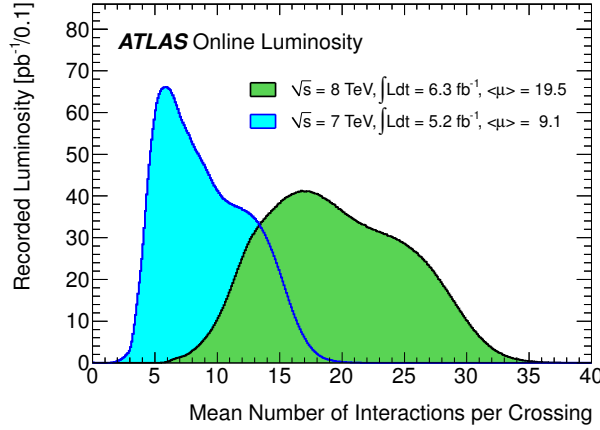
Figure 3.3: Average number of interactions per bunch crossing for the 2011 and 2012 data-taking years.

- N_b is the number of particles per bunch,

- n_b the number of bunches in the beam,

- f_{rev} the revolution frequency,

- γ_r the relativistic Lorentz factor,

- ϵ_n the normalized transverse beam emittance,

- β^* the beta function at collision point, itself related to the emittance as $\sigma_{x,y} = \sqrt{\epsilon_n \beta^*}$, where $\sigma_{x,y}$ is the RMS cross-sectional size of the beam. Finally, where

- $F = \left(1 + \left(\frac{\theta \sigma_z}{2\sigma_{x,y}}\right)^2\right)^{-\frac{1}{2}}$ is the geometrical reduction factor due to the crossing angle at collision point (the beams do not meet exactly head-on). Here, σ_z is the RMS bunch length.

Each of these factors was of course taken into account while designing the LHC. Equivalently, the luminosity can be written more simply as

$$L = \frac{N_1 N_2 f_{rev} n_b}{4\pi \sigma_{x,y}^2} \tag{3.2}$$

where N_1 and N_2 are the number of particles in each colliding bunches. To achieve luminosities of $10^{34}\text{cm}^{-2}\text{s}^{-1}$, one can play around with these equations to see how small β^*, or equivalently $\sigma_{x,y}$ must be. In 2012, the LHC was running with 50 ns bunch spacings,

thus requiring a β^* twice as small as what was thought to be originally achievable by the LHC. After the 2008 quenching incident, many feared the LHC would have trouble achieving its goals, but now it seems like quite the opposite.

The LHC is a formidable machine necessitating around 120 MW while in operation [2]. This energy consumption produces a total beam current of about 0.58 A (7 TeV) corresponding to a total stored energy of roughly 360 MJ. Likewise, the electromagnetic energy stored in the magnets totals approximately 1 GJ.

During a physics run (when there are stable beams and collisions), the luminosity progressively falls as the emittance and intensity of the beams also drop. The primary source for this beam dissipation is not due to radiation losses or Bremsstrahlung, but because of the collisions themselves. The beam lifetime, assuming only losses from collisions, can quantitatively be written down as [80]:

$$\tau_{\text{lifetime}} = \frac{I_0}{L_0 \sigma_{total} n},$$

(3.3)

where I_0 is the beam intensity at a given time t_0, n the number of interaction points (IP) around the ring, σ_{total} the total p-p cross section, and L_0 the luminosity at that time. Knowing the beam lifetime enables to calculate the luminosity as a function of time:

$$L(t) = L_0 e^{-t/\tau_{\text{lifetime}}} \simeq L_0(1 - t/\tau_{\text{lifetime}}) \simeq \frac{L_0}{1 + \frac{t}{\tau_{\text{lifetime}}}}$$

(3.4)

Using the measured total p-p inelastic cross section at 7 TeV by TOTEM [87] of 73.5 mb or $7.35 \times 10^{-26} \text{cm}^2$ and a peak luminosity of $\sim 3.8 \times 10^{33} \text{cm}^{-2}\text{s}^{-1}$ as found in figure 3.4, we find a beam lifetime of $\tau_{\text{lifetime}} \simeq 90$ hours using equation (3.3) and while knowing [3] $n = 2$ and $I_0 = N_{\text{protons}} N_{\text{bunches}} = (1.15 \times 10^{11}) \cdot (1362)$. However, other beam dissipation factors such as residual gas in the beam pipe, intra-beam scattering and RF noise reduce the beam lifetime to roughly 10 hours.

Perhaps one the most important quantities related to collider physics is the integrated

---

2. In comparison, the LHC experiments as a whole consume approximately 22 MW [86]
3. There are two main IP, one for CMS and one for ATLAS. The other LHC experiments run at only a fraction of the full luminosity and therefore contribute negligibly to the beam's dissipation.
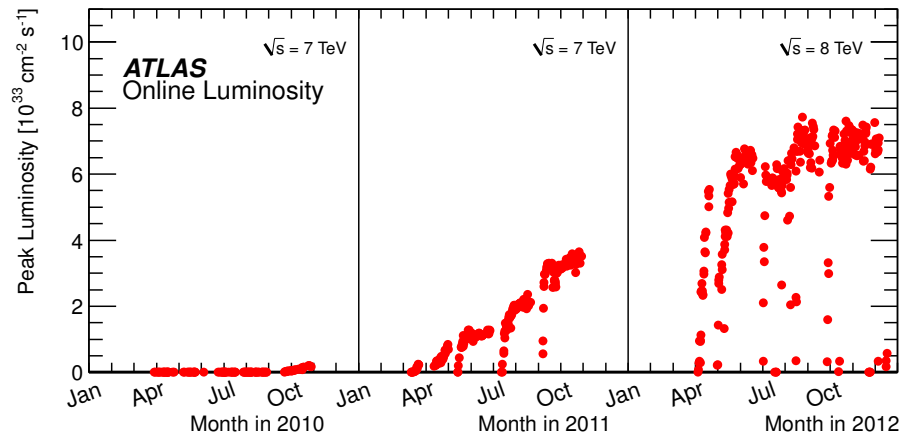
Figure 3.4: Peak luminosity as a function of time obtained during the three years of LHC running [85].

luminosity, defined simply as the time integral of the luminosity: $L_{int} = \int L \, dt$. Associating L_{int} to other quantities just described, we can write

$$L_{int} = L_0 \tau_{\text{lifetime}} \left(1 - e^{-T_{run}/\tau_{\text{lifetime}}} \right) \tag{3.5}$$

assuming τ_{lifetime} is the only contributing factor in beam dissipation, and where T_{run} is the elapsed time of a given run.

Having now seen some of the basic concepts behind the workings of the LHC, we now turn to the discussion of the ATLAS detector, one of the most sophisticated machines ever built.

3.2 OVERVIEW OF THE ATLAS DETECTOR

During the early conception years of the ATLAS detector, physicists realized they needed a thoroughly general-purpose and versatile design in order to cover the rich program of physics of the SM and beyond. This meant that they needed a detector capable of reconstructing many different types of resonances, such as leptonic $W^{\pm}$ and Z^0 bosons as well as J/ψ, Υ, and top quarks among others. The detector also needed to be able to do this via the measured 4-momenta of various objects: electrons, muons, photon, jets,

32

and even neutrinos in the form of missing energy. These basic requirements became the basis upon which the ATLAS detector was designed and the different decay channel searches for the SM Higgs were used as a gauge to determine the performance of each subdetector. A more detailed description of the ATLAS detector and its performance can be found in [80]. The following summarizes the aspects that are important to the particles searches presented in the later chapters.

The multi-purpose nature of the detector grants it the ability to decipher between many different types of background events, such as $t\bar{t}$, W+jets, Z+jets, dibosons, and multijet events, to name just a few, but which are nonetheless the most common backgrounds encountered. One of the main goals for many physics analyses is thus to disentangle such backgrounds from new hypothetical signals. The ATLAS detector's performance in terms of object resolution and reconstruction efficiencies determine by a large measure how well this can be done.

The dimensions of the ATLAS detector are quite impressive: 25m in height, 44m length, and weighing about 7000 tonnes. A visual overview of the detector outlining its principal subdetectors can be found in figure 3.5.
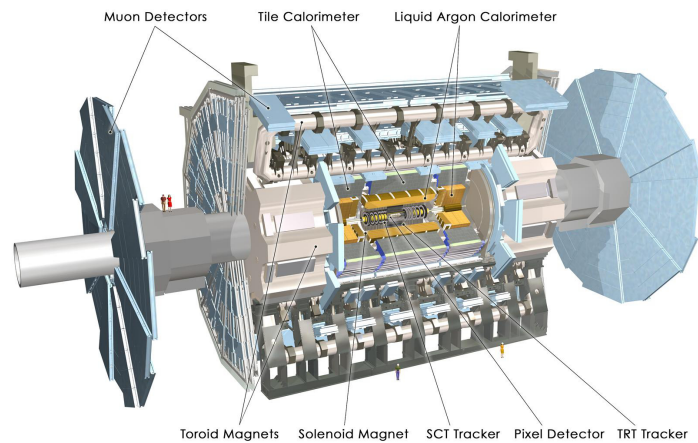
Figure 3.5: View of all major components of the ATLAS detector [83].

The coordinate system used by ATLAS and throughout the next chapters can be summarized as follows. In cartesian coordinates, the z-axis lies along the beam axis while the y-axis points 'up' or is perpendicular to the circle formed by the LHC ring.

The x-axis points towards the center of the LHC ring while the origin of the coordinate system is placed at the nominal IP. A more useful coordinate system for describing particle interactions uses the standard azimuthal ϕ and polar angle θ as well as the pseudo-rapidity $\eta = -\ln\tan(\theta/2)$. The rapidity $y = \frac{1}{2}\ln\left(\frac{E+p_z}{E-p_z}\right)$ and pseudo-rapidity are useful relativistic coordinates since intervals in y remain invariant under boosts along the z-axis for massive objects and η is the geometrical description of y in the limit of $m \to 0$. Lastly, the quantity defined by $\Delta R = \sqrt{\Delta\phi^2 + \Delta\eta^2}$ is often used to quantify the angular separation between two particles trajectories originating from the same IP.

3.3 MAGNET SYSTEMS

One major feature of ATLAS is its superconducting magnet systems. All tracking subdetectors, the ID and MS, along with their reconstruction software (described a little later in section 3.7), utilize the magnetic fields to enhance charged particle recognition capabilities and accurately measure their 4-momenta. The magnets Al-stabilized Nb/Ti/Cu conductors at temperatures below $4.5°$K, immersed in liquid helium cryostats, enable the production of high field strengths while diminishing their thickness. The first system consists of a 2 Tesla solenoidal field surrounding all of the inner detectors. The second is composed of eight air-core toroidal magnets producing a non-uniform field with a maximum strength of 4 Tesla just outside the calorimeters in the barrel region deviating muons that traverse the ID and calorimeters into the muon detector systems. Finally, the end-cap toroidal magnetic system delivers up to 4 Tesla in field strength in the forward region, again primarily for muon deviation. An accurate overall field map is essential for proper object reconstruction, and to this end, a combination of measured and simulated field values for both the solenoidal [88] and toroidal [89] fields have been applied during data-taking.

3.4 THE INNER DETECTOR

The inner detector comprises 3 main subdetectors: the pixel detector, the semiconducting tracker (SCT), and the transition radiation tracker (TRT), all contributing to mea-

suring thousands of particle momenta every bunch crossing while obtaining excellent momentum resolution for tracks within the η range of $|\eta| < 2.5$. A cut-away view of the inner detectors can be seen in figure 3.6. A momentum resolution of
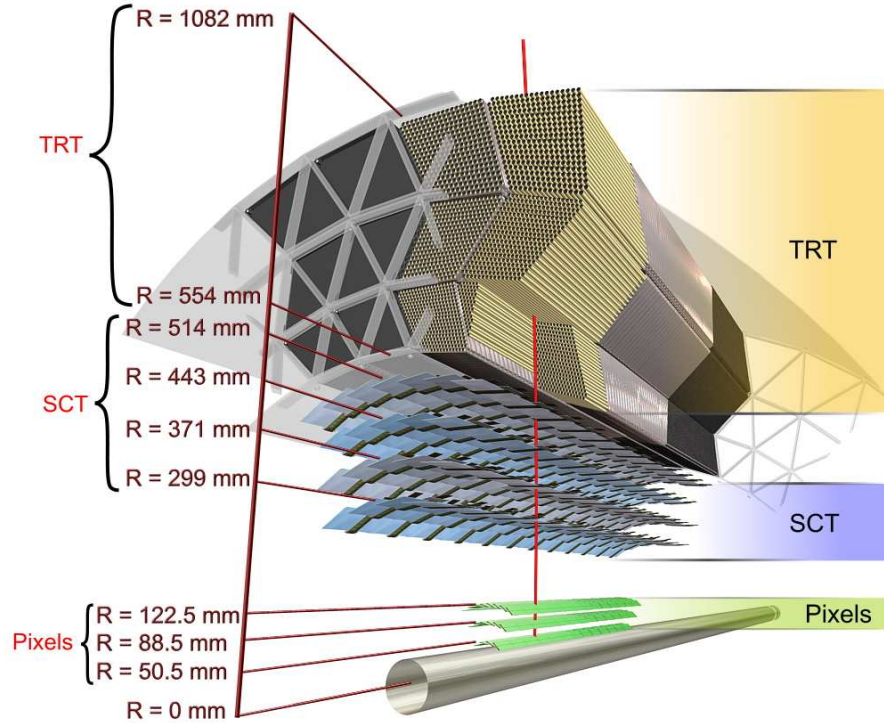
Figure 3.6: Cut-away view of the Pixel, SCT, and TRT detectors showing their respective distances R from the center of the beam pipe. In red is a 10 GeV p_T charged track with an $\eta = 0.3$ successively going through all of the inner detector including the beryllium beam pipe [80].

$$\frac{\sigma_{p_T}}{p_T} = 0.05\% p_T \oplus 1\% \tag{3.6}$$

is achieved for accurate position measurements of the primary and secondary vertices. The ordering of the vertices is calculated based upon the $\sum_{\text{tracks}} p_T{}^2$ of all tracks pointing to it. The vertex with the highest sum thus defines the primary vertex while all others define the secondary vertices. Within high pile-up conditions, the performance of the inner detector is hence indispensable for properly managing the underlying events that overlay the hard scattering processes.

3.4.1 THE PIXEL AND SCT SENSORS

Both the Pixel and the SCT are silicon based semiconducting detectors. They therefore both rely on the same detection principles. An electric field is applied across each of the pixels and each of the SCT silicon *strips*. When a charged particle traverses the silicon, it ionizes the material creating a series of free electrons and holes. The electrons which were in the valence band now find themselves in the conduction band. The applied electric field then pushes these electrons (and the holes in opposite direction) creating a pulse shaped current that is measured by an outside electronic module.

Each pixel sensor is an oxygenated n-type wafer 250 μm thick. Nominally, they operate at a 150 V bias voltage, but this will increase up 600 V as radiation adds impurities to the wafers and changes the semiconductor's properties. There are a total of 1744 pixel sensors each having 47232 square pixels. A 3D overview of the pixel detector can be seen in figure 3.7, where the 3 layer design together with the readout modules on each end are clearly discernable. The standard pixel size is 50×400 μm^2 for about 90% of
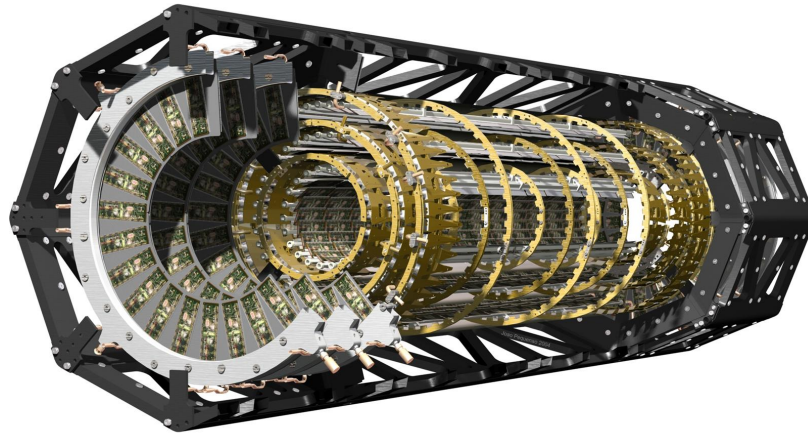
Figure 3.7: 3D view of the Pixel detector [83].

them while the ones near the front-end chip modules are slightly larger.

The SCT is designed as an interwoven silicon strip detector permitting precise ϕ-η position measurements as a particle crosses a series of these strips as seen in figure 3.8. Each strip measures roughly 6 cm in length with a thickness ranging from 270 to 300 μm. Due to restrictions in costs, the SCT's technology was chosen over a larger Pixel

Figure 3.8: View of the SCT before its installation in 2007 [83]

detector. However, such a design, through its use in a number of HEP experiments, has proven to be a very reliable technology. There are 15912 sensors, each operating under a nominal voltage of 150 V, which is expected to reach perhaps 500 V once radiation levels of 3×10^{14} GeV protons/cm^2 [80] are attained.

During the installation of the silicon based detectors, a proper alignment is important to achieve the desired momentum resolutions, although some corrections may be done during offline event reconstruction.

3.4.2 THE PROPORTIONAL DRIFT TUBE TRANSITION RADIATION TRACKER [90]

The process of transition radiation (TR) was first predicted in 1945 by V.L. Ginzburg and I.M. Frank [91] and first observed by P. Goldsmith and J.V. Jelley in 1959 [92]. It occurs when charged particles traverse a boundary between two media of different dielectric constants ϵ. For charged particles with large Lorentz factors $\gamma \gtrsim 1000$, the TR spectrum tends to be in the X-ray range causing the particles to deposit much larger amounts of energy ($\langle dE/dx + \mathrm{TR} \rangle = 14.1$ KeV for electrons) than MIPs would ordinarily do through ionization alone ($\langle dE/dx \rangle = 5.4$ KeV for pions) [93]. Since TR is heavily dependent on the Lorentz factor γ, electrons with energies between 1 and 100 GeV are virtually the only particles that leave significant energy in the TRT. This particularity enables the possibility for differentiating electrons from pions and other hadrons.

In this manner, the objective of the TRT consists of identifying electrons in the range 0.5 to 150 GeV for $|\eta| < 2.0$ (the geometrical limit of the detector).

A gas mixture of Xe, CO_2, and O_2 fills the 350 848 straw tubes of the TRT. The straw tubes themselves consist of polyimide film 25 μm thick having on each of its sides a different set of coatings. The inside is coated with 0.2 μm of aluminum which is itself covered with a 5 to 6 μm of graphite-polyimide. The outside is plated with 5μm polyurethane to thermodynamically isolate it. Figure 3.9 details these straw wall elements.
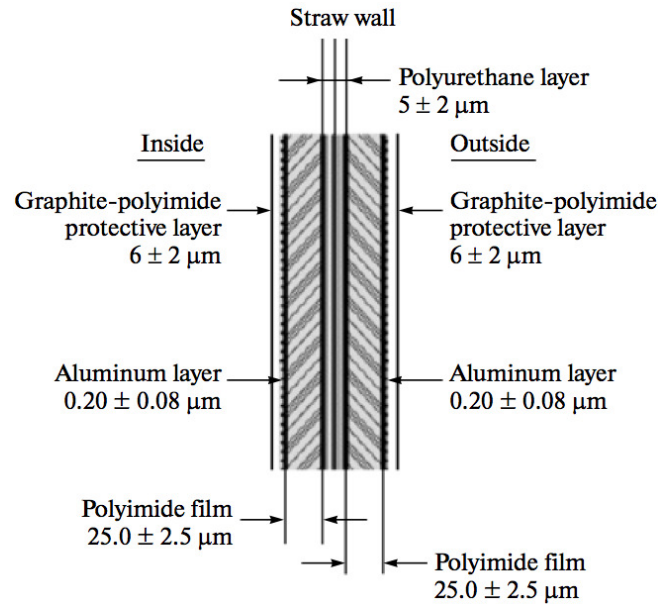
Figure 3.9: Anatomy of the TRT's straw walls [90].

In contrast to the Pixel and SCT, which operate at temperatures between $-5°$C and $-10°$C, the TRT functions at room temperature. Inside each straw tube is a 31 μm diameter tungsten wires coated with about 0.6 μm of gold. A potential difference of 1530 V is applied between the wires (anode) and the tube (cathode) enabling a time of arrival measurement of the pulse shape which achieves resolutions of 130 μm. The way in which these straws operates is visualized in figure 3.10. The coating materials and the gas within the straw have very different dielectric constants which increase dramatically the probability for a charged particle to produce TR as it goes from one medium to the
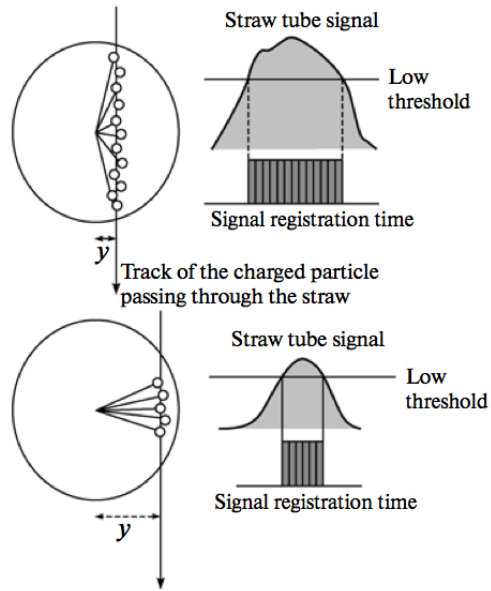
Figure 3.10: Low threshold charge collection from a MIP passing through a TRT straw with varying distance y from the center anode [90]. The different signal registration times permit enhanced resolution capabilities.

next [93]. Two operational modes, low and high threshold, are used to distinguish deposited energy from ionization alone and ionization plus TR photons. When a minimum ionizing particle goes through TR, the absorbed TR photons by the gas admixture create much larger signal amplitudes than those produced from ionization alone, thus enabling a straw-by-straw differentiation between TR produced by electrons and other tracking signals by implementing low and high charge collection thresholds in the front-end electronics. Likelihood distributions constructed from energy deposit yields of electrons and pions are then studied to maximize the electron identification efficiency while simultaneously maximizing the pion rejection rate.

3.5 CALORIMETRY

Depending on whether the goal is to measure accurately the total energy of electromagnetic or hadronic particle showers, different detector materials and designs are needed. The ATLAS detector has three main EM liquid Argon (LAr) calorimeters,

the LAr EM barrel, the LAr EM end-cap (EMEC), and the LAr forward calorimeter (FCAL). The main hadronic calorimeters are the hadronic tile scintillator, and the LAr hadronic end-cap (HEC) calorimeter. Figure 3.11 shows their layout within ATLAS. All calorimeters in ATLAS are *sampling* calorimeters [4], within which we find two different types of materials each having distinct roles. One is to create or enhance the production of particle showers, and the second is to measure the actual deposited energy. Given that some of the energy will be lost in the material that produces the particle showers, only a *sample* of the energy is measured. Careful calibration studies are therefore needed in these types of detectors.
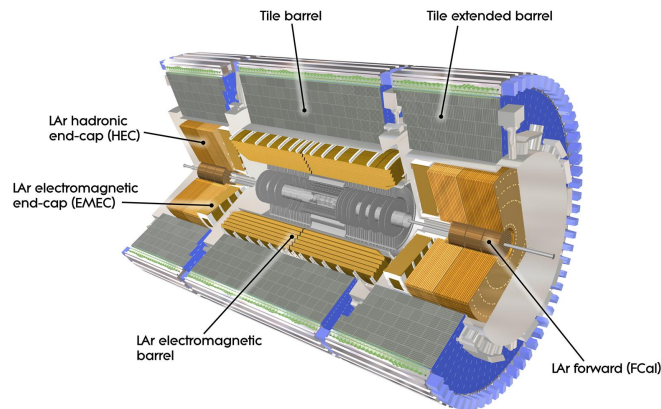
Figure 3.11: Cut-away view of ATLAS' calorimeters [83].

The main principle behind calorimetry is to equate the total number of ionized electrons with a definite amount of energy lost by the particles passing through a particular calorimeter cell. In ATLAS, we have two types of sampling methods. The first uses liquid Argon as the sampling material, and across which is applied a potential difference varying from 250 to 2500 V depending on the subdetector (more on this in the next few sections). Liquid Argon has been chosen for its properties of maintaining a linear relation between the charge collected and the deposited energy as well as for being radiation-hard. The second utilizes polystyrene, a scintillating material found in the tile

---

4. Caveat: The Presampler, which is of the homogeneous type, is used for correcting photon and electron energy losses that occur within the bulk of the calorimeter. It consists of one single LAr layer of 1.1 cm (0.5 cm) thickness in the barrel (end-cap) regions.

calorimeter (see Section 3.5.2.2) in which the production of ultraviolet light is induced by the passing of charged particles via the ionization and then recapturing of electrons.

Furthermore, very important to calorimetry are the related concepts of radiation and nuclear interaction lengths. When an energetic electron losses $1/e$ of its energy (primarily through bremsstrahlung) while passing through a material with atomic number A and charge Z^0, known as the radiation length X_0 of the material in question, and this quantity can be calculated empirically [94]

$$\frac{1}{X_0} = 4\alpha r_e^2 \frac{N_A}{A} \left[Z^2 \left(L_{rad} - f(Z) \right) + Z\, L'_{rad} \right], \tag{3.7}$$

where α is the fine structure constant, N_A is Avogadro's number, r_e is the classical electron radius, L'_{rad} and L_{rad} are empirically determined to be $\ln(1194\, Z^{-2/3})$ and $\ln(184.15\, Z^{-1/3})$ respectively, and finally where $f(Z)$ is also an empirically derived function matching the behaviour of X_0 with respect to varying Z^0 (see [94] or [16] for more details). The radiation length for photons is simply $7/9$ times[5] that for electrons [16].

The characteristic transverse size of an electromagnetic shower within a given material, know as its Molière radius, is also an important property that must be taken into consideration while designing calorimeters. The need for small Molière radii detectors becomes evident when we have, for example, boosted Z^0 bosons that often produce collimated electron decays. In this case, if the detector's characteristic Molière radii are too great, it becomes impossible to disentangle each of the electrons energy as their particle showers overlap. This is a facet we shall reencounter in chapters 5 and 7 while discussing lepton isolation.

For hadrons, a more appropriate characterization of a material is its nuclear interaction length (often simply called interaction length). It is the length necessary to reduce by $1/e$ the number of relativistic charged particles within a given particle shower. Alternatively, we can define it as the mean free path of a particle to undergo a nuclear

---

5. This exact 7/9 conversion factor arrises from the similarities in the Feynman diagrams of pair production and Bremsstrahlung.

interaction. Unlike X_0, nuclear interaction lengths generally have no empirical formula due to the complexities of the nuclear force, but do of course have tabulated values. The total amount of material in units of interaction lengths within ATLAS up until the muon detectors is shown in figure 3.12 as a function of η.
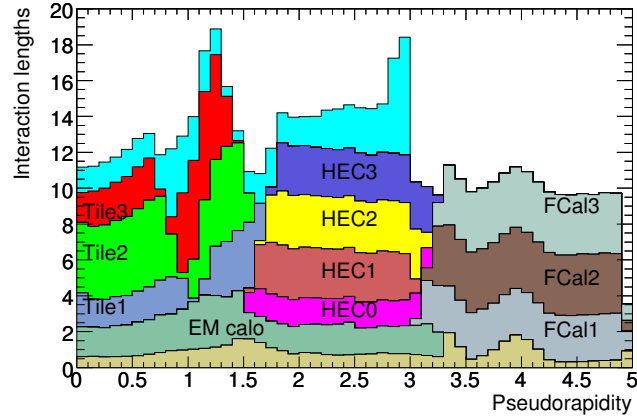
Figure 3.12: Cumulative material in front of the muon systems in units of interaction lengths as a function of $|\eta|$ [80].

3.5.1 ELECTROMAGNETIC CALORIMETRY

Charged lepton momenta, due to the curvature of their paths within the solenoidal magnetic field, can be measured by the ID alone. However, for photons, an EM calorimeter (ECAL) is absolutely essential as they do not leave any tracks, and for electrons, the combined measurements of the ID with the EM calorimeter increases momentum resolution. As an electron's energy increases, its trajectory becomes more and more linear, thus making accurate momentum measurements more difficult using ID tracking alone, and therefore increasing the need for a high performance EM calorimeter to get a better handle on the electron's total energy. The high granularity of the EM calorimeter within $|\eta| < 2.5$, which matches the ID coverage, fullfils these precision physics requirements, including a good missing transverse energy measurement which is particularly important for both the VLQ search in the charged-current decay mode (chapter 5), and the WZ resonance search (chapter 7). Table I.I in appendix I summarizes the $\Delta\eta \times \Delta\phi$ granularity

of the EM calorimeter as well as those of the hadronic calorimeter, discussed in the following section. In short, one barrel ($|\eta| < 1.475$), one end-cap ($1.375 < |\eta| < 3.2$), and one forward ($3.15 < |\eta| < 4.83$) EM calorimeter segmentations are used to fully cover the η range and hence gain in E_T^{miss} measurement capabilities.

The Barrel LAr EM calorimeter has Pb-absorbers and Kapton[6] electrodes in an accordion type design (figure 3.13) permitting azimuthal uniformity, high radial segmentation, and fast charge transfer times [95]. The EM end-cap calorimeter (EMEC) is a pair of co-axial wheels, one on each side of the detector. Each wheel measures 63 cm thick ranging 1.375 to 3.2 in η and azimuthally sliced into 8 separate modules. However, as is the case of the barrel, the end-cap's accordion type design does not bring about any azimuthal discontinuity. The LAr drift gap between absorbers in the barrel is 2.1 mm,
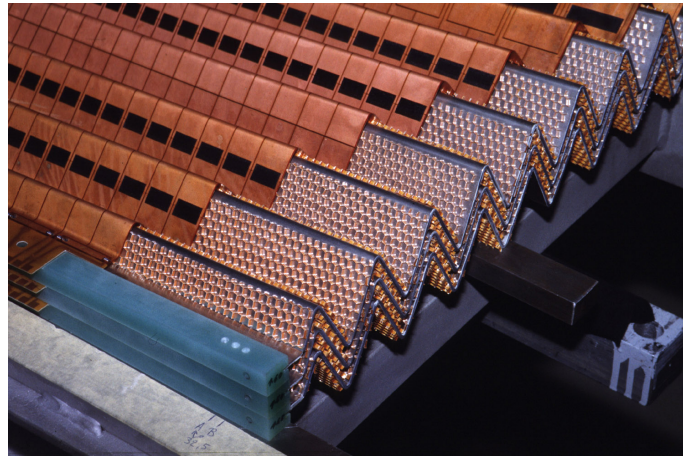
Figure 3.13: Segment of the Barrel EM calorimeter featuring the accordion design providing full azimuthal coverage [83].

corresponding to a 450 ns drift time while operating at 2000 V. The extracted pulse shape is sampled every 25 ns and fitted knowing that the induced current by a charge q drifting towards the electrodes is [81]

$$I = \frac{q \, v_{\mathrm{drift}} \, E_{\mathrm{local}}}{V},\tag{3.8}$$

where E_{local} is the local electric field, v_{drift} is the drift velocity of the electron and V is

6. Kapton is a polyimide that remains stable within a wide range of temperatures: $-270°C$ to $\sim 400°C$.

the applied potential. In the plane regions (i.e. not in the kinks of the accordion), the electric field is roughly $\sim 10\,\text{kV/cm}$ [81]. In the kinks, the electric field is numerically obtained using Poisson's equation. Knowing lead's absorption properties, and LAr's ionization energies, one can extract the total deposited energy with a precision equal or better than [81]

$$\frac{\sigma_E}{E} = \frac{10\%}{\sqrt{E}} \oplus 0.7\%. \tag{3.9}$$

Contrary to the barrel EM calorimeter, EMEC's drift gap varies from 0.9 to 3.1 mm depending on its radial distance from the beam pipe.

The forward region of the detector ($|\eta| > 3.2$) is a radiation intense environment and therefore requires radiation-hard detector materials designed for a successful and continuous operation while the LHC delivers over 100 fb^{-1} of data. The EM FCal (FCal1) has relatively small sampling cells with respect to its copper shielding as illustrated in figure 3.14. Inside each LAr filled tube resides a copper rod playing the dual role of absorber and electrode. Surrounding the liquid argon is another copper tube electrode itself coated with radiation-hard plastic fiber to insulate it from the main absorption matrix. This tube-like design and the use of copper enables greater resolution and heat transfer
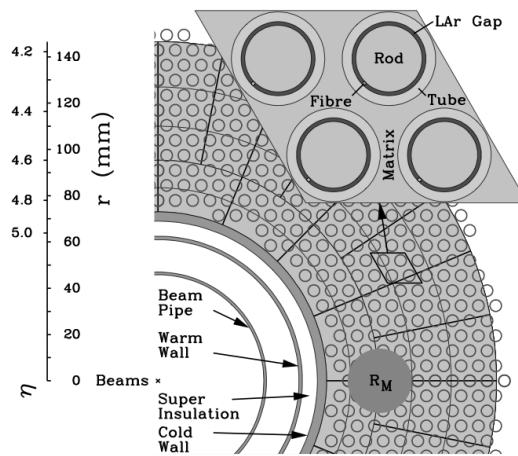
Figure 3.14: Slice of the FCal showing the [96]

capabilities. With 12260 electrodes and 1008 readout channels, the EM FCal is 45 cm thick (total length of each co-axial copper tubes) and operates at a nominal potential of 250 V. Finally, with a typical drift time of 60 ns, the EM FCal makes a pulse shape

measurement every 25 ns and provides excellent $\eta \times \phi$ resolution that will turn out to be crucial during the analysis of VLQ in chapter 5.

3.5.2 HADRONIC CALORIMETRY

The copious amounts of jets produced by the LHC, especially under the 2012 pile-up conditions (see figure 3.3), renders the measurement of jet energies a challenging task. The LAr and tile calorimeters using different types of detector technologies arrive nonetheless at energy resolutions for single jets similar or better than the original design objectives [80]:

$$\frac{\sigma_E}{E} = \frac{50\%}{\sqrt{E}} \oplus 3\% \tag{3.10}$$

for the barrel and end-cap regions ($|\eta| < 3.2$) and

$$\frac{\sigma_E}{E} = \frac{100\%}{\sqrt{E}} \oplus 10\% \tag{3.11}$$

for the forward region ($3.1 < |\eta| < 4.9$). Various resolutions and jet energy scale studies using the 2010 and 2011 data suggest that these objectives have been achieved or surpassed [97–99]. The tile calorimeter is a sampling detector using polystyrene as active scintillating material and steel as its absorber. The hadronic end-cap calorimeter on the other hand utilizes LAr as active material and copper as its absorber. The forward hadronic calorimeters (FCAL2 and FCAL3) uses once again LAr as active material, but as tungsten as its primary absorption material.

In the end-cap region, figure 3.15 shows the placement of each of these subdetectors in relation to one another. For further details on detector operating regions, consult once more Table I.I.

3.5.2.1 THE LIQUID ARGON DETECTORS

The hadronic LAr detectors, the hadronic end-cap calorimeter (HEC) situated within $1.5 < |\eta| < 3.2$, and the forward calorimeters (FCAL2 and FCAL3) covering $3.1 < |\eta| < 4.9$ utilize two different detector technologies depending on the radiation environ-
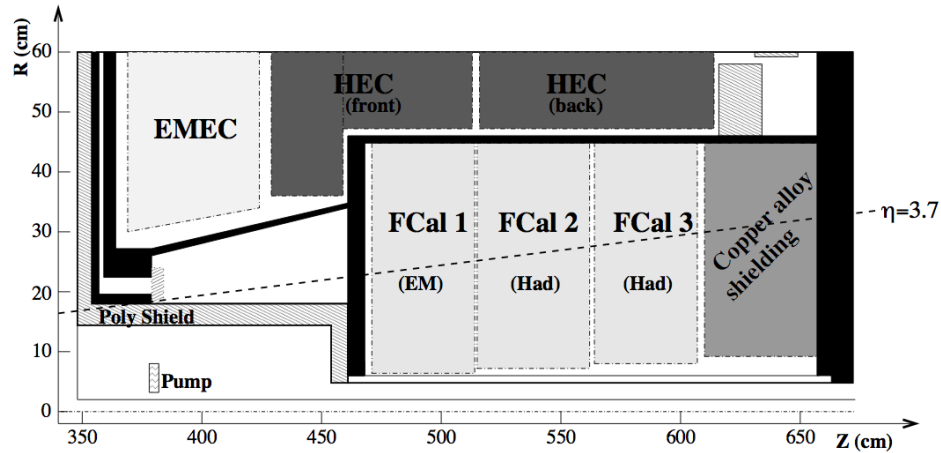
Figure 3.15: Schema of the detector placement in the forward region. An $\eta = 3.7$ line is drawn for illustrative purposes [96].

ment they encounter.

The HEC is a standard sampling detector with copper as absorber. It is divided into two wheels (HEC1 and HEC2) on each side of the IP, themselves divided into 32 identical modules sliced in ϕ. The front wheel samplers have 25 mm thick 24 copper plates, while the HEC2 only has 16 50mm thick ones. The measured deposited energy in the samplers with respect to the initial particle's total energy for the HEC1 and HEC2 are 4.4%, and 2.2% respectively [80]. A little known fact about the HEC is its ability to measure muon radiative energy losses. This provides additional information for the muon algorithms to improve their combination of tracks from the ID and the MDT (see section 3.8.2).

As does the EM FCal (FCal1), the hadronic FCal (FCal2 and FCal3) have relatively small sampling cells with respect to its tungsten shielding as illustrated in figure 3.14. Contrary to the FCal1, the FCal2 and FCal3 have Tungsten both inside and outside the LAr gap electrodes [96]. This was to maximize the absorption lengths and by the same token increase energy resolution for high momentum objects.

As a last note, all of the LAr detectors were designed together with the integration of liquid N_2 cryostats. The placements of these cryostats were in each case chosen such that their impact on particle 4-momenta resolution would be minimized while of course

ensuring that low temperatures pervade throughout the LAr calorimeters.

3.5.2.2 THE TILE SCINTILLATING DETECTORS

The scintillating tile calorimeter [100] surrounds the barrel EM calorimeter and is divided into three sections in the region $|\eta| < 1.7$. A central barrel measuring 5.8 meters in length and two extended barrels of 2.6 meters, each lie at a radial distance of 2.28 meters from the beam pipe. The scintillator itself has a total interaction length of roughly 7.4λ [80], where λ is average interaction length of mesons. The $\sim 460,000$ polystyrene scintillating tiles come in eleven different sizes depending on their radial position, therefore creating a tower of eleven tiles ranging from 97 mm to 187 mm in radial depth. As seen in figure 3.16, each scintillating tile is interceded with 5 mm thick steel plates and connected to wavelength-shifting optical fibers. Plastic sleeves cover and protect the scintillating medium while providing high reflectivity of 95%. The optical
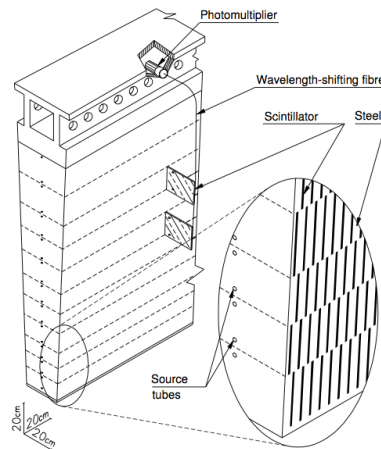
Figure 3.16:

fibers are coated with aluminum mirrors themselves having a reflectivity of 75 ± 7 %. The polystyrene is doped with two fluors (PTP and POPOP) to shift the UV scintillating light into the visible spectrum [101]. The fibers further shift the light with an attenuation length of 325 cm down to the desired wavelength of 430 nm with a final optical spread of roughly 3% [102]. From there, groupings of readout fibers transmit their light into

photomultiplier tubes (PMT), where the fiber groupings are done in such a way as to produce an approximate projective geometry (equal $\Delta\eta$ and $\Delta\phi$) as given in table I.I.

A high performing tile calorimeter is essential for reducing the foreseen jet energy scale uncertainties that we shall encounter during the search for VLQ in chapter 5. To that end, an understanding of the average tile cell energies from minimum bias events (for example), as shown in figure 3.17, is paramount. Similarly, the observed light pulse
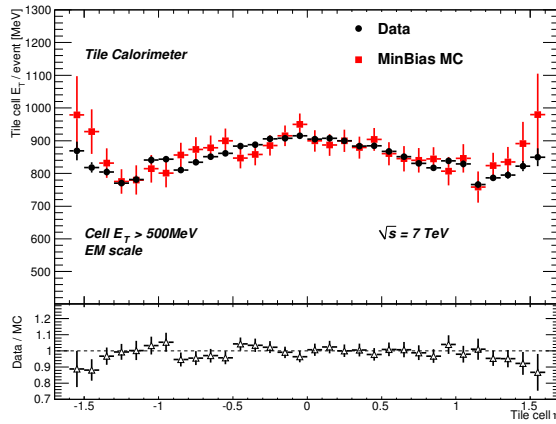
Figure 3.17: Average summed transverse energy of tile calorimeter cells as a function of η with cells having $E_T > 500$ MeV [103]. Overlaid with the data points are non-diffraction MC minimum bias events.

shape passing an optical filter algorithm [104] must also be well known. The comparison between a reference high grain pulse shape and an observed pulse shape is given in figure 3.18.

3.6 THE MUON SPECTROMETER

From the Bethe equation shown below [16], which describes the mean rate of energy loss of moderately relativistic ($0.1 \gtrsim \beta\gamma \gtrsim 1000$) charged heavy particles (not electrons), one can calculate within a few percent the energy loss of a muon as it passes through the detector before arriving at the muon spectrometer (MS):

$$-\left\langle \frac{dE}{dx} \right\rangle = Kz^2 \frac{Z}{A} \frac{1}{\beta^2} \left[\frac{1}{2} \ln \frac{2m_e c^2 \beta^2 \gamma^2 T_{\max}}{I^2} - \beta^2 - \frac{\delta(\beta\gamma)}{2} \right]. \qquad (3.12)$$
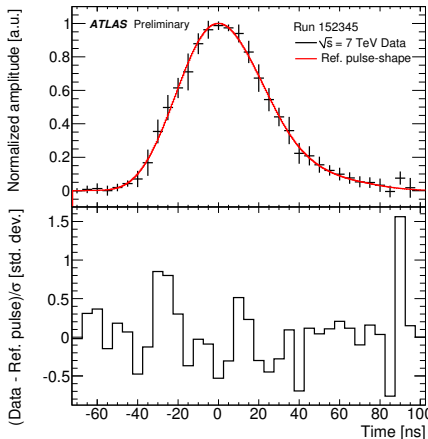
Figure 3.18: Top: Pulse shape differences between a reference pulse-shape, used for reconstruction, and the data pulse shape. Bottom: Their difference divided by the variance is shown below. The reference pulse-shape was obtained from the optical filter algorithm [103].

Here, T_{max} is the maximum kinetic energy that can be bestowed upon a free electron in a single collision, I is the mean excitation of the material of charge Z and atomic number A, $\delta(\beta\gamma)$ is the density effect correction to ionization energy loss, $K = 4\pi N_A r_e^2 m_e c^2$, and finally where z is the charge of the incident particle, which in the case of the muon is 1. For a 100 GeV muon traversing for example lead, having a density of 11.34 g cm^{-3}, $\langle dE/dx \rangle \simeq 1.8$ MeV g^{-1} cm^2. In other words, even if the ATLAS detector had been made entirely of lead up until the MS, which for the barrel region is located at 5 m from the IP, the muon would only have lost approximately 10% of its initial energy. Therefore, the only way to measure accurately muon 4-momentum is through tracking detectors utilizing powerful magnets that bend the muon's trajectory. Unlike all other particles capable of being detected by ATLAS, muons are the only ones that rely solely on tracking reconstruction for their measurement.

ATLAS' muon systems are instrumented with separate tracking and triggering detectors (see figure 3.19 for an overview). The monitored drift tubes (MDT) and cathode strip chambers (CSC) offer high resolution tracking and utilize the large air-core toroid magnets in the region $|\eta| < 1.0$, the smaller end-cap magnets in the region $1.4 < |\eta| < 2.7$, and a combination of both magnetic fields in the region $1.0 < |\eta| < 1.4$.

The muon triggering system is guaranteed by the resistive plate chambers (RPC) and the thin gap chambers (TGC). Table I.II in appendix I gives a summary of their respective size and location along with those of the MDT and CSC, each of which are described more fully in the following section.

3.6.1 MUON TRACKING DETECTORS

The MDT [106, 107] and the CSC [108] are both gas filled tracking chambers with anode wiring that aim to achieve $\sim 10\%$ $\Delta p/p$ momentum resolution for 1 TeV p_T muons. Table 3.I enumerates the pertinent specs of the MDT and CSC. The average 0.5 Tesla magnetic field provided by the air-core toroid creates a 500 μm sagitta [7], thus requiring a 50 μm resolution on the sagitta if the resolution goals are to be attained. These resolution objectives therefore demand very precise relative alignments between each of the MDT and CSC modules. Using mechanical-assembly techniques together with optical alignment tools, a precision of 10 μm was achieved. Also, given the sheer size and weight of some of the MDT chamber tubes as shown in figure 3.20, a correction to gravitational sagging must be put into effect.

Inside each 29.970 mm diameter MDT tubes, drift time measurements between the central anode wire and cathode tube enables the determination of the minimum distance $R_{\min}$ at which the traversing muon passes tangentially to the anode wire. This is visually described in figure 3.21.

The CSC must distinguish itself from the MDT due to the much higher counting

---

7. The arc depth of a circle segment s, known as the *sagitta*, can be calculated via $s = r - \sqrt{r^2 - l^2}$, where r is the circle radius and l is the half length between the arc's two endpoints.

Parameter	MDT	CSC
Gas composition	Ar/CO$_2$/H$_2$O (93/7/ $<$ 1000 ppm)	Ar/CO$_2$ (80/20)
Anode wire diameter	50 μm	30 μm
Operating Voltage	3080 V	1900 V
maximum electron drift time	$\sim$ 700 ns	$\sim$ 40 ns

Table 3.I: Muon tracking specs.
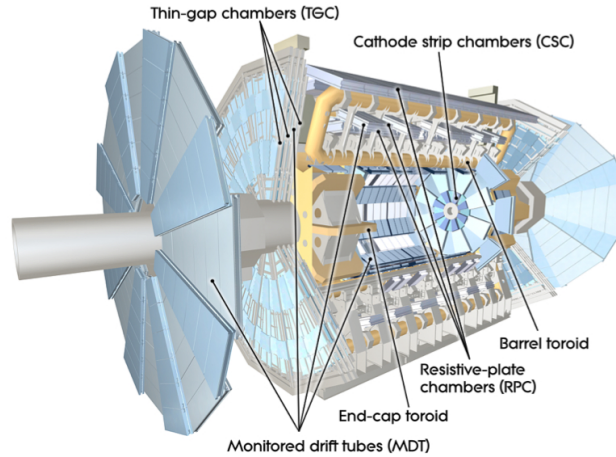
Figure 3.19: Location of each muon detector system within ATLAS [105].
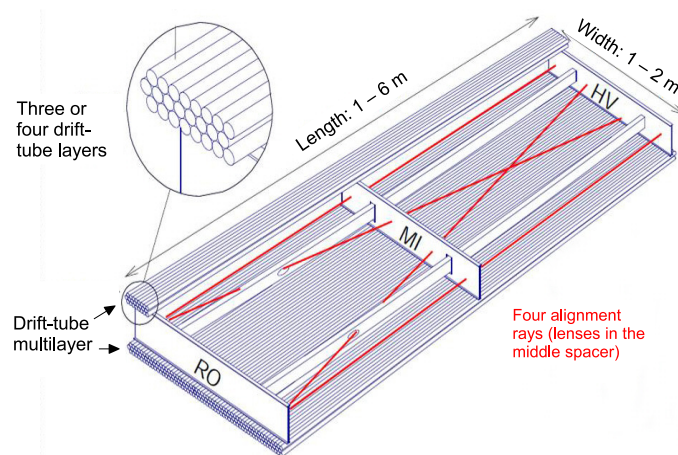
Figure 3.20: Generic internal structure of a MDT chamber [80].

rates it encounters being in the forward region. For this reason, the CSC's radial design, having high spatial and time resolution as well as low neutron sensitivity via the removal of hydrogen in its gas mixture, renders it perfectly adapted to high particle densities one finds in the region $2.0 < |\eta| < 2.7$. The CSC's design contains eight small and large chambers arranged as shown in figure 3.19 while the internal structure of each cathode strip is presented in figure 3.22. There are 250 (402) wires within each cathode strip in the small (large) chambers [109], and all are radially aligned with the beam pipe. High spatial resolution is achieved via the segmentation of the cathode strip into readout strips with widths of 1.519 mm and 1.602 mm in the small and large chambers respectively
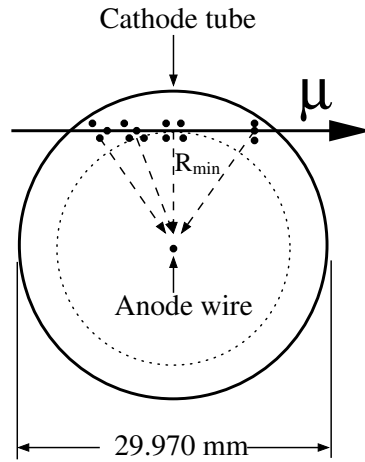
Figure 3.21: Muon distance measurement within a MDT tube [80].
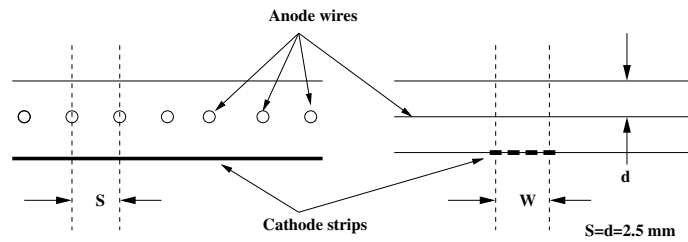
Figure 3.22: Cross-sectional view of each Segmentation widths w of 1.519 mm and 1.602 mm in the small and large chambers respectively [80].

inducing readout pitches [8] of 5.308 mm and 5.567 mm.

Pre-amplifier electronic noise is the primary cause inhibiting accurate spatial resolution measurements. With this in mind, only a limited set of readout strips or channels (generally 3 to 5) are used to compare the location measurement in η.

Although the ID tracking system only extends up to $|\eta| = 2.5$, the CSC remains vitally important for forward region muon events. In fact, the highest WZ invariant mass event has one of its three muons going through the CSC as can be clearly seen in the event display of figure II.8 in appendix II.

---

8. Define readout pitch

3.6.2 MUON TRIGGER SYSTEMS

The primary objective of the two muon triggering subdetectors, the resistive plate chambers (RPC) located in the barrel region and the thin gap chambers (TGC) in the end-cap, is to rapidly identify muon events with p_T thresholds between 6 to 22 GeV (depending on the instantaneous luminosity) such that they can be properly and fully reconstructed by the numerous algorithms involved in muon reconstruction (see section 3.8.2) using the MDT and CSC. Both the RPC and TGC are gas filled chambers, however only the TGC has anode wiring. The RPC is a pure parallel plate detector having three levels, RPC1, RPC2, and RPC3 each having 2 independent detection layers (see figure 3.23). Thus, the combined RPC layers offer 6 independent η-ϕ measurements. For low p_T muons, it is required that a measurement coincidence of at least 3 out of the 4 layers within the RPC1 and RPC2 be recognized. For high p_T muons, together with the coincidence of the 4 layers in the RPC1 and RPC2, at least 1 measurement in one of the two RPC3 layers must also project itself into the same line of flight.
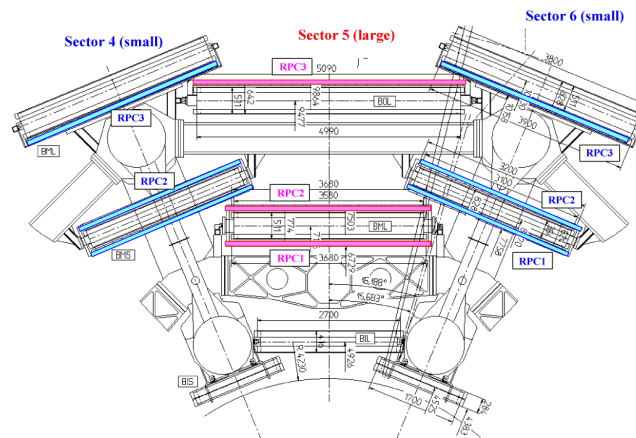
Figure 3.23: The three barrel RPC layers within sectors 4 to 6 of the ATLAS detector [109].

Although it is very similar in concept to the CSC, the TGC has a few distinguishing characteristics. First, its contents are a gas mixture of CO_2 and n-C_5H_{12} (55 % versus 45 %) which suppresses filamentary discharges under almost any operating voltage. Second, the relatively small wire-to-wire distances result in highly accurate time

resolutions. Thirdly, given its precise measurement capabilities, the TGC renders a second ϕ measurement complementing those of the MDT in the region $1.05 < |\eta| < 2.0$, thus improving muon 4-momenta resolution. The geometry of the TGC contains 9 distinct layers of triplet or doublet modules. In the EM big wheel[9], there are a total of 1152 triplet chambers and 1920 doublet chambers. The structure and composition of the chambers are found in figure 3.24.
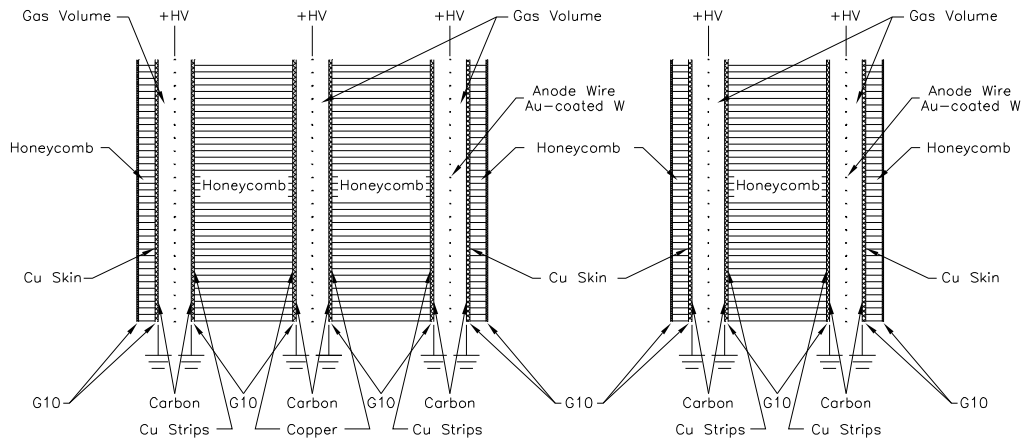
Figure 3.24: Inner structure of the TGC, displaying its two and three layer anatomy [80].

Lastly, table I.III in appendix I offers a comparison between the main operating parameters of the RPC and TGC.

3.7   ONLINE TRIGGERING SYSTEM AND OFFLINE HARDWARE TOOLS

Perhaps the most important feature of the ATLAS detector is its capability to decide extremely rapidly whether an event has *interesting* features or not. These features often, though not exclusively, relate to the measured amount of E_T within a given reconstructed object[10]. The trigger system which performs these tasks and whose functioning shall be explained in some of the following section, is profoundly important to achieve the performance goals the ATLAS experiment has set out for itself.

---

9. Region above (in r) the barrel EM Calorimeter.
10. Some unorthodox trigger variables can be used to trigger on. For example, the number of vertices, the total deposited energy, or perhaps more frequently the E_T^{miss} as it is an important characteristic of many BSM signals, including dark matter candidates.

Additionally, given the variety of particle-detector interactions and particle shower topologies, numerous reconstruction algorithms are necessary to disentangle and properly measure the 4-momenta of all particle types capable of being distinguished by AT-LAS. The details of these algorithms will be discussed in section 3.8.

Finally, in order to match and understand the statistically large data samples produced by the LHC, substantial Monte-Carlo sample generation campaigns are needed, and foreseeing this, the worldwide LHC computing grid (WLCG) was conceived. The basics of its operation will be depicted in section 3.7.2

3.7.1 TRIGGER ALGORITHMS

Given that the maximum rate at which raw data can be written out to tape is roughly 400 events per second (or 1.6 GB per second) and that the LHC produces them at a rate of 20 MHz (with 50 ns bunch-spacing), events must be selected extremely efficiently and quickly based upon a predetermined and limited set of criteria.

To make the decisional process as adaptive as possible, ATLAStriggering system is divided into three distinct levels, each requiring to trigger events at different rates. These are the Level 1 (L1), Level 2 (L2), and event filter (EF) trigger systems. The Level 2 and EF trigger systems together form the High-Level Trigger (HLT). Each trigger level contains a different set of trigger menus [11] that can be modified and adapted to new data taking conditions and new signal searches. Although the L1 decision-making is hardware based while the HLT is software based, perhaps the main difference between the two algorithms is the amount of information each of them uses to make a decision. The L1 algorithms works with reduced granularity in η-ϕ and only with the calorimeters (L1Calo), the RPC and the TGC, whereas the HLT triggers makes use of the full ATLASinformational output along with the more detailed reconstructed objects.

---

11. The trigger menu is a list of items each defining the selection criteria necessary for an event to pass the trigger.

3.7.1.1 LEVEL 1 TRIGGER ALGORITHMS

Despite the fact that the L1 trigger operates on a simplified form of the calorimeters, it is capable nonetheless to make use of basic electromagnetic and/or hadronic calorimeters energies to trigger on high p_T jets, E_T^{miss}, and even τ-leptons. L1 muon triggers, on the other hand, use the coincidence of hits in either the RPC or TGC to trigger events that satisfy a certain set of criteria as described in section 3.6.2.

The digital systems processing the raw detector information are mounted next the detector in order to reduce its trigger decision latency time down to roughly 2.0 μs. The trigger decision, made by the Central Trigger Processor (CTP), is pipelined through optical fibers to the readout systems, located near the detector front-end, using what is known as the Timing, Trigger, and Control system (TTC). It is critically important for the L1 systems to properly identify with certainty which bunch-crossing (or event number) the trigger decision is referring to. To accomplish this, the trigger decision algorithms are coupled to a 40.08 MHz clock tagging each decision precisely enough to be later on compared to the timing of the bunch-crossings and then correctly associated.
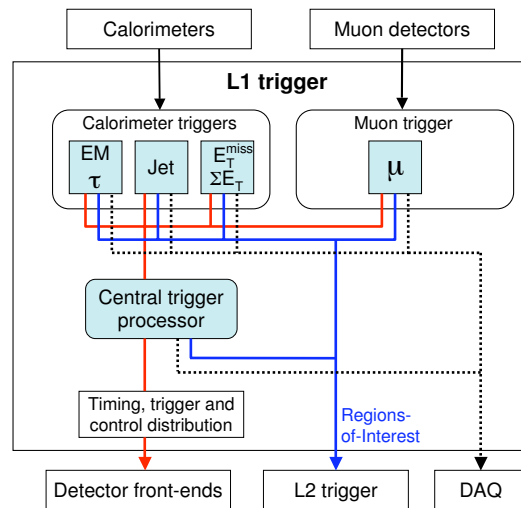
Figure 3.25: Logical flow of ATLAS' L1 trigger systems. The coordinated efforts of the L1 calorimetric and muon triggers pass on to the HLT events that passed their selection criteria together with RoI's that the HLT can use to optimize its own computational tasks [80].

The calorimeter based trigger selection, known as L1Calo (Level 1 Calorimeter trigger), collects deposited energy information from the 7000 analogue trigger towers in predefined sets of cells with a granularity of 0.1×0.1 in $\Delta\eta \times \Delta\phi$ in the central region and a slightly larger granularity in the forward region. Before any trigger decision is made, the detector readout is sent to the service cavern USA15, a region off-detector, where the Cluster Processor (CP) and Jet/Energy-sum Processor (JEP) attempt to identify electrons, photons, and τ-leptons in the case of the CP, and jets and E_T^{miss} in the case of the JEP. Furthermore, both the CP and JEP check whether their objects pass their assigned E_T thresholds and count each object's multiplicity. Once all objects have been processed by the L1Calo, the information is sent back to the CTP.

The electron/photon based L1 trigger algorithm makes use of 2×2 trigger tower clusters as shown in figure 3.26. If one of the possible four 2×1 combinations exceeds a predetermined E_T threshold, then the event passes on to L2.
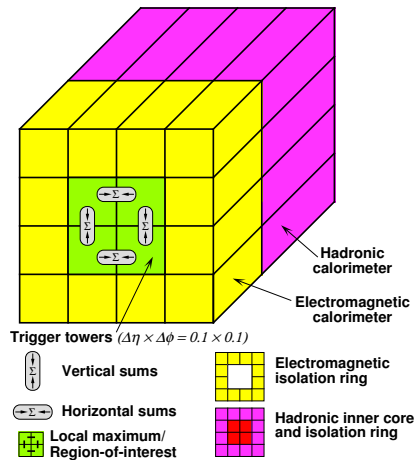
Figure 3.26: Within any 2×2 subsets of L1 $\eta\times\phi$ granularity, the L1 algorithm determines whether any 2×1 or alternatively 1×2 combination passes a predefined transverse energy minimum [110].

The L1 muon trigger system operates within the dedicated RPC and TGC systems. Similar to L1Calo, each trigger decision must be made while being accurately time-stamped to then be unambiguously associated to the correct bunch-crossing. The trigger decisions are based on the coincidence of hits in the deferent layers of the RPC or TGC as described in section 3.6.2. The muon barrel and end-cap trigger decisions are then

merged together before being sent to the CTP. Figure 3.25 shows diagrammatically how the event information is processed and combined before being sent to L2 or the data acquisition system (DAQ), which serves as an event data buffer.

Finally, an important task of the L1 trigger is to define regions of interest (RoI) that are sent and used by the L2 triggers. A RoI is defined with the same 2×2 region used by L1 and that has been triggered on for having objects with high E_T. The 2×2 window iterates in steps of 0.1 (in η or ϕ), therefore overlapping itself with four others. The RoI is chosen such that the energy sum is maximized.

3.7.1.2 HIGH LEVEL TRIGGER ALGORITHMS

The Level 2 and event filter trigger decisions algorithms use information from the entire detector in order to decipher whether a given event contains an *interesting* hard-scatter or not. In parallel to the L2 and EF trigger systems, the DAQ is the interface through which the event data is sent to the central data-recording service. Additionally, since the DAQ and HLT work so closely together, they are often simply referred to as the DAQ/HLT. Among its many tasks, the DAQ/HLT contains the RoI builder [111], which builds upon the RoI defined by the L1 trigger. Other tasks include detector configuration, monitoring, and control, as well as event building and event filtering. A chart showing how the flow of data is handled by the DAQ/HLT is given in figure 3.27. From the diagram 3.27, one can see that the L2 trigger begins with the information output by the RoI builder. The information is then handled by the L2 processing farm designed to bring down the event rate from 75 KHz to 3.5 KHz at which point the event information is sent to the event builder and eventually processed by the event filter. The L2 trigger operates with the full granularity of the detector and is able to build more sophisticated reconstructed objects upon which a flexible (to control rates) E_T or p_T threshold is applied. It also has the capability to combine objects before selection such as a 1 electron plus 1 muon events.

Despite having at its disposal more developed reconstructed objects, the L2 still does not use the full ATLAS event reconstruction algorithms. Such tasks are left to the event builder and the event filter whose goals are respectively to apply the standard reconstruc-
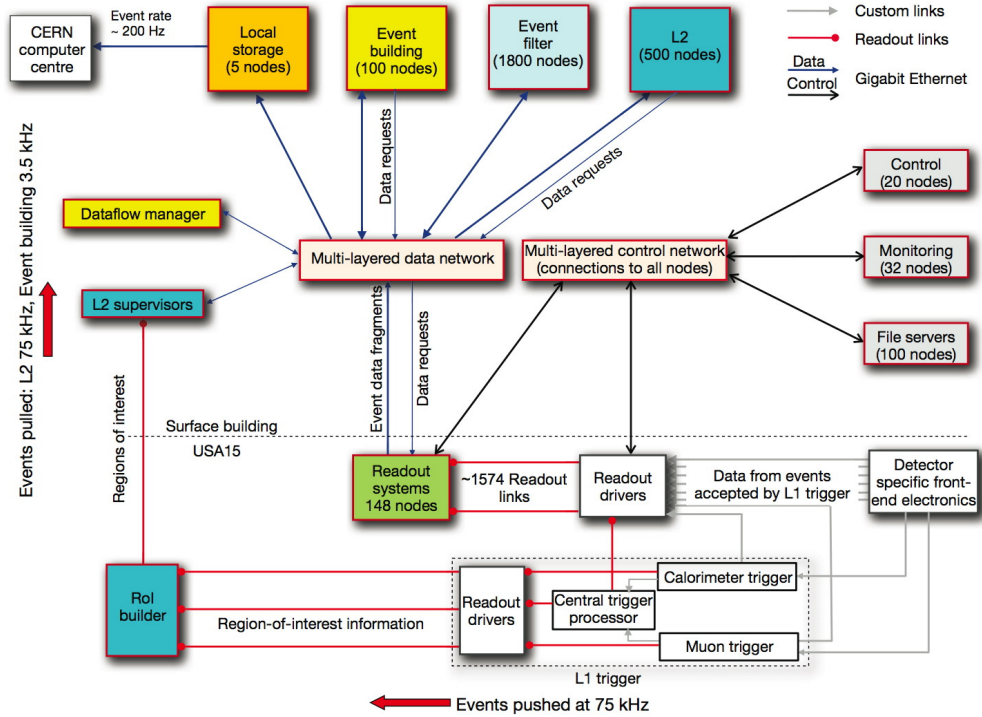
Figure 3.27: Chart of the ATLAS data acquisition and high level trigger systems [80].

tion algorithms and reduce the event rates down to 400 Hz. The EF has in addition the potential to use isolation criteria in order to reduce its p_T thresholds, which were important facets considered in the analyses put forth later in this thesis, where a possible compromise between applying isolation to the trigger items or simply using higher transverse energy/momentum thresholds needed to be made. Performance studies however by the dedicated e/γ and muon combined performance (MCP) teams tend to give precise recommendations on these matters. Using the tag-and-probe method [12] upon $Z \rightarrow e^- e^+$ events, the trigger efficiencies of a number tigger menu items where obtained with the 2010 data [110]. In figure 3.28, the ones referred to in ATLAS as `e15_medium` and

---

12. The tag-and-probe method is a widely used technique to measure various experimental efficiencies with real data. A detailed explanation of this technique will be laid out in chapter 5 and 7 where it will be used to gain an understanding of how frequently jets *fake* the detector signatures of leptons.

e20_loose are given. Such triggers however, if used, would be prescaled [13] in the in-

(a)   (b)
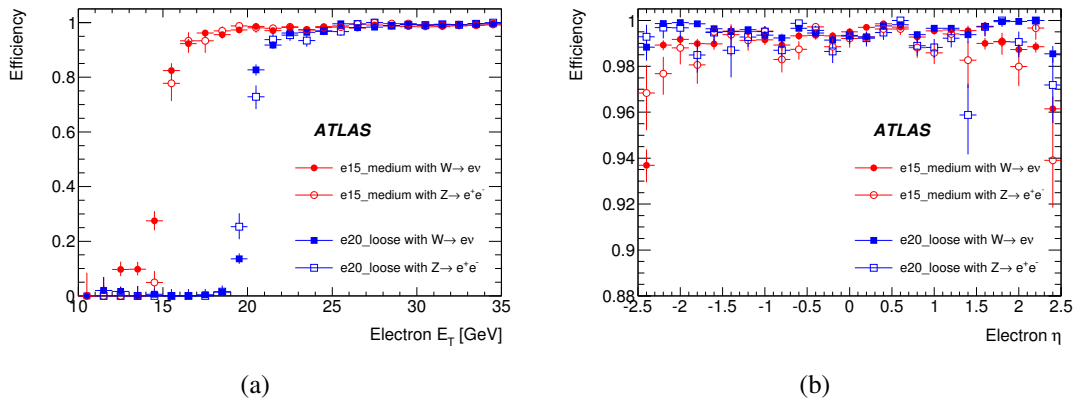
Figure 3.28: Trigger efficiencies measured in $Z \rightarrow e^-e^+$ and $W^{\pm} \rightarrow e^{\pm}\nu$ events as a function of E_T in (a) and $|\eta|$ in (b) for the two trigger menu items: e15_medium and e20_loose, where medium and loose refer to the reconstruction quality of the electron [110]. More on this in section 3.8.1. The efficiencies of each trigger item approach 1 after passing their respective E_T thresholds.

stantaneous luminosity environment of 10^{33} cm^{-2} s^{-1} and beyond delivered by the LHC in 2012. They are shown here purely to demonstrate the expected behaviour of trigger efficiencies.

Finally, the DAQ/HLT must classify events according to ATLAS physics streams [14] which organize events into three general types: e/γ, muon, or jet/E_T^{miss} events, which can subsequently be used more efficiently by various analysis teams.

3.7.2   GRID COMPUTING

In order to store and analyze the vast amounts of data gathered, the WLCG [112] was conceived and assembled in parallel to the construction of the ATLAS detector and the LHC.

The computing grid is an immense CPU framework dedicated for computationally

---

13. Numerical value denoting the fraction of events that pass the trigger, but that cannot be written out to tape given that maximum output rate of 400 Hz.

14. Event data-recording streams are organized according to the on- or off-line state of particular AT-LAS subsystems and the functioning of their associated trigger items.

intensive tasks. Virtually all the data and official Monte-Carlo datasets [15] are either processed, created, or both on the grid. Computing sites are found throughout the world and can all be accessed by any user at any time, providing an incredible tool for dissecting the data and uncovering its secrets.

One of the grid's primary goal is to facilitate the distribution of the data and safeguard it from possible unwanted deletions or hardware failures. A multilayer design was hence developed where different sites, with various level of capabilities, were given different sets of tasks to handle. These levels, named Tier-0, Tier-1, up to Tier-4, each have decreasing responsibility vis-à-vis the amount of tasks and data storage bestowed upon them. All Tiers however are essential for the smooth functioning of the grid as a whole. Figure 3.29 shows how the architecture operates between the different Tier sites and how the data are copied from one level to the next. The ordering of the Tier sites generally reflect the CPU and memory capacities each of the them have.

The computing time that was necessary to complete the particle searches put forth in later chapters goes beyond 10^7 CPU hours. This simple fact clearly demonstrates how vitally important the grid was in performing these analyses which often required multiple iterations with only slightly different parameters. It also demonstrates how the smooth running of all ATLAS physics projects in general are dependent on the good-functioning of the grid.

3.8 PARTICLE RECONSTRUCTION

Using the full versatility of the ATLAS detector, complex reconstruction algorithms were devised to maximize the detector's response and accurately measure particle type, charge, and 4-momenta. A brief description of the main reconstruction algorithms are described here. b-jet and τ-lepton reconstruction were consciously left out as they are not involved in the searches for VLQ and WZ resonances performed in chapter 5 and 7.

---

15. *Official dataset* means those that are and were used for any ATLAS published or public results.
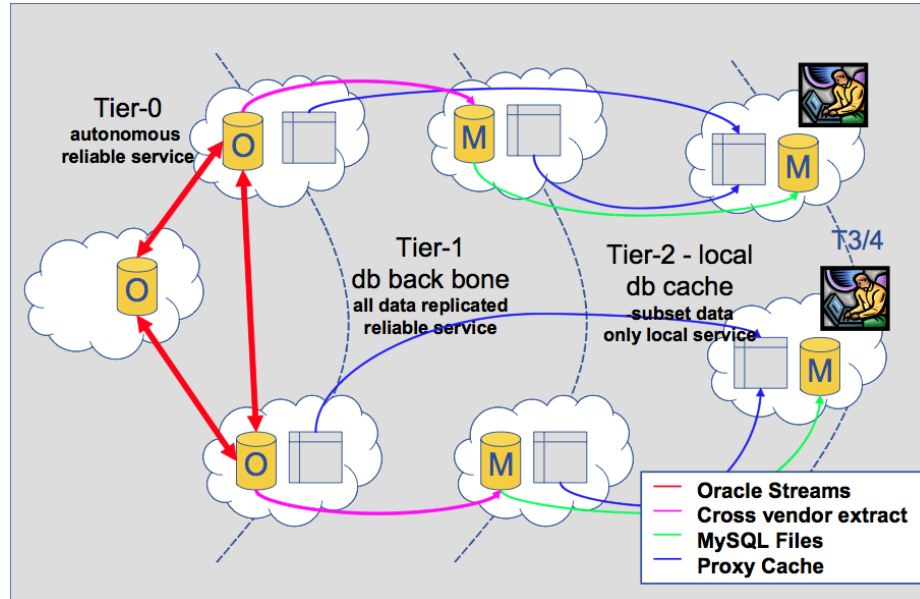
Figure 3.29: Multi-level global architecture of the LHC grid. Tier-0 sites, such as CERN, maintain a full copy of the data and distribute it to all Tier-1 sites. Tier-2 sites possess only a subset of the data and dedicate themselves to more specific computing tasks. Finally Tier-3/4 sites refer to personal computers or local servers upon which simple and generally non-computationally intensive work can be done [112].

3.8.1 ELECTRON AND PHOTON RECONSTRUCTION

The calorimeter based reconstruction of electrons and photons are virtually identical. The obvious difference being that the photon is not associated to any ID track and define themselves by the absence of such tracks. Within the calorimeter, electron and photon candidates are identified using specific shape variables.

For photons, the 4-momentum is fully derived from calorimeter information and the position of the expected primary vertex (PV). After rejecting objects that have tracks pointing to it, optimized shape cuts were put into place to reject isolated π^0 jets. Photon identification is achieved through the use of 9 shower shape variables and can be classified in two main groups: converted and unconverted photons. Converted photons pair-produce $\gamma \rightarrow e^- e^+$ inside the ID, whether it be the beampipe, Pixel, SCT, or TRT. From the point of view of the ECAL, such photons create shower shapes very similar to those of single electrons (see figure 3.30). Unconverted photons on the other hand pair-

produce only once inside the ECAL thereby fathering unique and identifiable shower shapes. The now famous Higgs to $\gamma\gamma$ search relied on these distinctions to increase
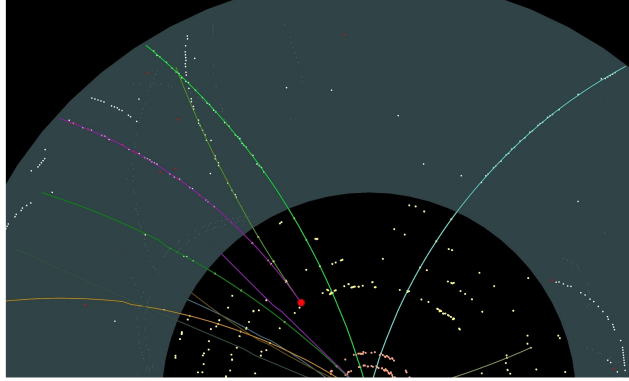
Figure 3.30: Photon conversion (red dot) in the first layer of the SCT. Noticeable bremsstrahlung occurs for one of converted electron (right) in the TRT as its radial curvature decreases and emits other decay products [113].

its sensitivity [17], however given that the searches in the present thesis do not contain photons in the final state, we omit a detailed description.

Electron identification combines the information gathered from both calorimeter shower shapes and from ID reconstructed tracks. Depending on the analysis strategy one wants to deploy and the signal type ones wants to study, various electron efficiency and rejection rates (primarily from pions) need to be defined. To this end, the electron identification algorithms classify electrons in three main quality groups originally called: `loose`, `medium`, and `tight`. As a better understanding of the ATLAS detector evolved, these quality definitions evolved as well. The selections changed to such a degree that they were renamed `loose++`, `medium++`, and `tight++` for the 2012 data-taking campaign. Table 3.II details the variables used by each quality definition. The actual selection or cuts upon these variables strongly depend on the E_T and η of the electron and were optimized using likelihood methods. The optimization involved maximizing the electron reconstruction efficiency while rejecting as much as possible fake sources such as charged pions.

Variable	Definition	`loose++`	`medium++`	`tight++`
E_T	Transverse energy	✓	✓	✓
η	pseudo-rapidity	✓	✓	✓
r_{Had}	E_T leakage into had. calo./E_T	✓	✓	✓
r_{Had1}	E_T leakage into 1st sampling (S1) of had. calo./E_T	✓	✓	✓
R_η	Ratio in η of cell energies in 3×7 in S1 versus 7×7 in sampling 2 (S2)	✓	✓	✓
w_2	3×5 ($\eta \times \phi$) window width	✓	✓	✓
f_1	fraction of energy found in EM S1	✓	✓	✓
ws_{tot}	40-strip shower width	✓	✓	✓
$\Delta E_{\mathrm{max\ S1}}$	Energy of 2nd max. in S1	✓	✓	✓
$\Delta \eta$	$\Delta \eta$ of track extrapolated to calo. S1(2, or 3)	✓	✓	✓
n_{Si}	# of silicon hits on fitted track	✓	✓	✓
n_{Si} Outliers	# of dead (or non-activated) silicon cells along the fitted track	✓	✓	✓
n_{Pixel}	# Pixel track hits	✓	✓	✓
n_{Pixel} Outliers	# dead (or non-activated) pixel cells along the fitted track	✓	✓	✓
f_3	fraction of energy found in EM S3		✓	✓
track d_0	Distance in r of the track to the expected PV		✓	✓
TRT ratio	$\frac{\text{\# high threshold TRT track hits}}{\text{\# of dead (or non-activated) TRT cells along the fitted track}}$		✓	✓
n_{TRT}	# TRT track hits		✓	✓
n_{TRT} Outliers	# of dead (or non-activated) TRT cells along the fitted track		✓	✓
$n_{\mathrm{b\text{-}layer}}$	# b-layer hits		✓	✓
E/p	Tot. calo energy/ID track momentum			✓
conversion bit	conversion unmatching (to reject photons)			✓

Table 3.II: The individual variables selections are heavily dependent on the electron candidate's E_T and η and are determined using Likelihood methods to maximize the efficiency while also maximizing the fake electron rejection rates. In addition, each electron quality definition uses a different set of variables as made explicit by the checkmarks.

The `loose++`, `medium++`, and `tight++` definitions offer different performance advantages. If reducible backgrounds coming from misidentified jets, for example, are dominant, then it should be preferable to require `tight++` electrons as the electron fake rejection rate can be a factor of 10 higher than for `medium++` [114]. A case by case study therefore must be made to choose which electron definition suits best the analysis at hand. Using `tight` (older definition) electrons, figure 3.31 presents the full $m(e^-e^+)$ invariant mass spectrum obtained in 2010 with 40 pb^{-1} of data. Note how the resolution
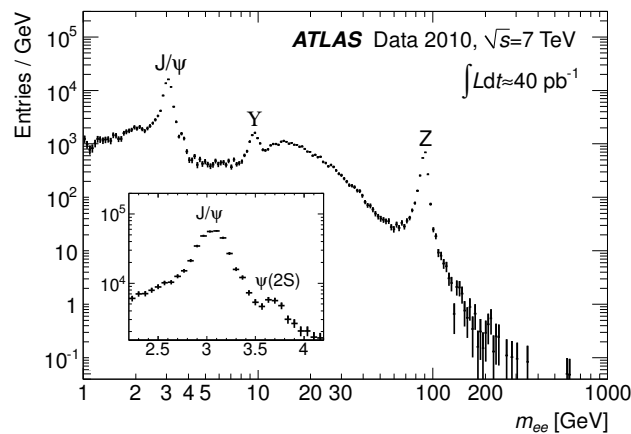
Figure 3.31: Reconstructed dielectron mass distribution of electron candidate pairs passing the tight identification cuts for events selected by low E_T threshold dielectron triggers. The number of events is normalised by the bin width. Errors are statistical only. [115]

decreases as the invariant mass increases, since the 4-momentum resolution decreases with energy (see equation (3.9)).

3.8.2 MUON RECONSTRUCTION

The muon spectrometer in tandem with the ID are capable of measuring muon p_T between 3 to 3000 GeV. Four distinct types of muon reconstruction however are possible [80]:

- **Stand-alone**: Muon 4-momenta utilizing solely the MDT.
- **Segment tag**: ID track reconstruction extrapolated to one segment (no full track) in the MDT.

65

- **Calorimeter tag**: ID track reconstruction extrapolated to energy deposits in the calorimeters.

- **Combined**: 4-momenta reconstruction taking full advantage of complete ID and MDT tracks.

Without a doubt, combined muons offer the best resolution and far greater muon fake rejection rates, but in occasions, in low background environments, stand-alone and segment tag muons do prove to be quite useful because of the higher efficiency such as with $ZZ \to 4\mu$ events [17]. In what shall be presented in the following chapters, only combined muons shall be used, hence the present discussion will concentrate on them.

A great number of muon track matching algorithms have been studied and used in `ATLAS`. Two primary algorithm chains with very similar features, called *Muid* and *Staco* muons, with continuously evolving and improving reconstructions algorithms, compute muon 4-momenta in a slightly different manner. For combined muons, the *Staco* algorithm makes a statistical combination of MS and ID tracks and computes a χ^2 for each combination. The MS and ID tracks independently provide a 4-momentum measurement, however, the track parameters measured in the two subdetectors are averaged by weighting each component with their assigned covariance error matrices. The result of this weighting procedure produces the final *Staco* 4-momentum. The *Muid* algorithm on the other hand, makes a combined track fit of the ID and MS. In both cases, the fit quality must pass a predetermined set of conditions, but if passed, the track thus defines the muon 4-momentum [116].

In most ATLAS searches, *Staco* muons are chosen over *Muid* for the simple reason that it was found to be slightly more efficient, which is also why the VLQ and WZ resonance searches presented later use *Staco* muons.

Figure 3.32 shows the full dimuon mass spectrum in with 40 pb^{-1} 2010 data. In comparison with figure 3.31, which shows the same dilepton invariant mass distribution for electrons, one quickly notices how muon resolution is far better than electron resolution at low mass (by noticing the difference in width between the J/ψ and ψ' resonance peaks in each of the distributions), but that this advantage dissipates for higher masses (the Z^0 peaks are roughly the same in 3.31 and 3.32). In fact, for very high reconstructed
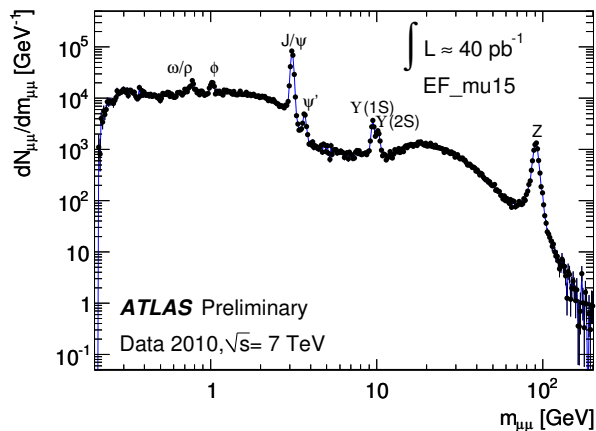
Figure 3.32: Dimuon invariant mass spectrum observed in 2010 with 40 pb^{-1} of 7 TeV data using fully reconstucted combined muons [117].

objects producing high p_T muons or electrons, there is a trade-off, muons have a higher efficiency, but electrons have better resolution.

3.8.3   JET RECONSTRUCTION

For both particle searches presented in chapters 5 and 7, high jet reconstruction efficiencies as well as high jet p_T resolutions are fundamental. For the vector-like quark search in particular, very high p_T jets need to be handled and understood properly to appropriately study high resonance mass regions and put a finger on their uncertainties.

The ATLAS jet reconstruction algorithms use raw calorimeter cell energy information and divide themselves into main types: towers and topological clusters.

Towers are, as the name indicates, a towered energy sum (in r) of nearby cells within a square $\Delta\eta \times \Delta\phi = 0.1 \times 0.1$ grid. Towers therefore neglect possible shower shape differences because all cells within this $\Delta\eta \times \Delta\phi$ region are summed regardless of their energy, which can be negative. In fact, while negative energy towers are possible due to noise, they are recombined until the net sum becomes positive. Once this is achieved, this operation defines by construction a 4-vector that will used by more sophisticated jet algorithms further down the algorithm chain. The simplicity of towers however remain very useful in high luminosity environments to quickly grasp whether a particular event

has interesting jet features or not (i.e. does it have high p_T jets or large jets with possible substructure).

Topological clusters, contrary to towers, perform a three-dimensional reconstruction of calorimeter cell energy deposits. Any cell with

$$|E_{\text{seed cell}}| > 4\,\sigma_{\text{seed cell}}, \tag{3.13}$$

where $\sigma_{\text{seed cell}}$ is the one standard deviation positive fluctuation around the total pileup and electronic noise, can be used as a seeding cell with which adjacent cell energies are added. Then, if these neighbouring cells satisfy

$$|E_{\text{adjacent cell}}| > 2\,\sigma_{\text{adjacent cell}}, \tag{3.14}$$

then in turn their respective adjacent cells are added as well. The summation of neighbouring cells continues until a cell fails equation (3.14). From such a cell, its neighbouring cells are nonetheless summed if

$$|E_{\text{adjacent cell}}| > 0, \,^{16} \tag{3.15}$$

but the cell iteration ends there. An important feature of topological clusters is that its algorithm naturally suppresses noise since it is unlikely for noisy cells to satisfy one of the three conditions (3.13), (3.14), or (3.15), and they are therefore not included in the sum.

Starting from these two basic types of jet reconstruction, more involved and computationally demanding algorithms are employed. These include the *Cone*-type algorithms [118–120], and the sequential clustering or successive recombination algorithms such as the Cambridge/Aachen [121, 122], k_T [123] and anti-k_T algorithms [124]. Figure 3.33 diagrammatically shows the reconstruction chain of ATLAS jets starting from the basic cell energies up until the refined and calibrated jet objects. It is assumed that not all towers and topological cluster are fully reconstructed in this manner as not all jets

---

16. This value varies depending on the calibration of each individual cell.

pass the necessary selection criteria, such as having too low p_T or not having fired the L1 or L2 triggers (assuming nothing else of interest happened in the event).
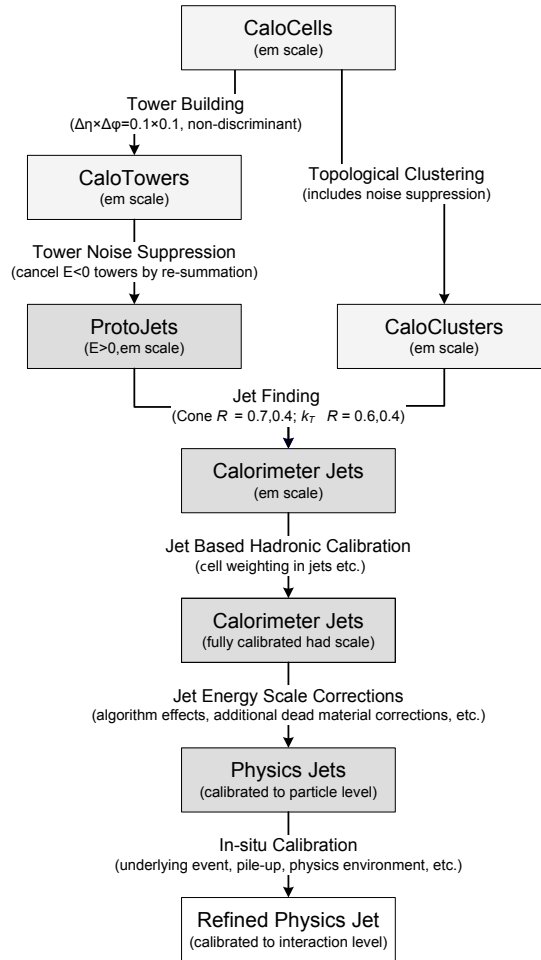
Figure 3.33: The diagram shown here establishes the main steps involved in jet reconstruction in ATLAS [80].

Generally, theorists tend to disfavour cone-type algorithms and prefer sequential clustering since the former are often not infrared-safe [17] (notable exception: SISCone [125]), and also not collinear-safe [18] . In the following therefore, we shall focus on the sequential clustering algorithm anti-k_T [124] as it is the most widely used jet reconstruction algorithm in ATLAS and the one used in the analyses presented in this thesis.

---

17. Infrared-safe: Jets reconstruction insensitive to soft parton emissions.
18. Collinear-safe: Jets reconstruction insensitive to collinear parton splitting.

The class of sequential clustering algorithms, to which the anti-k_T algorithm belongs, can all be grouped together via the parametrization of the power of the energy scale in the distance measure d_{ij}, where i and j refer to particles or pseudojets within a predefined jet radius R. The distance measure itself is defined as [124]

$$d_{ij} = \min \left(k_{Ti}^{2b}, k_{Tj}^{2b} \right) \frac{\Delta_{ij}^2}{R^2}, \tag{3.16}$$

where $k_{T(i,j)}$ is the transverse momentum of objects i or j, and where

$$\Delta_{ij}^2 = (y_i - y_j)^2 + (\phi_i - \phi_j)^2 \tag{3.17}$$

is the squared distance between the two objects with rapidity y and azimuthal angle ϕ. In equation (3.16), The value of the exponent b in this equation (3.16) defines the type of sequential clustering algorithm under consideration. With $b = 1$, one fully recovers the ordinary k_T algorithm. For $b = 0$, one obtains the Cambridge/Aachen algorithm [121, 122]. It is now perhaps obvious that the name anti-k_T is appropriately defined for negative b values. Concentrating on the value $b = -1$, one produces the core definition of the anti-k_T algorithm used in ATLAS. Sequential clustering algorithms however need another distance measure:

$$d_{iB} = k_{Ti}^{2b}, \tag{3.18}$$

or more simply, the momentum k_T^{2b} of the object i. Using $b = -1$, the anti-k_T algorithm can be explained as follows. Within a cone of radius R, the algorithm proceeds by successively combining the objects i and j that have the smallest distance measure as defined in (3.16). The recombination of objects or group of calorimeter cells continues until the smallest measure found is

$$d_{iB} = \frac{1}{k_{Ti}^2}, \tag{3.19}$$

at which point the algorithm simply defines i as a jet. The procedure then repeats using

the objects that were not previously combined into a jet.

An important particularity of the anti-k_T algorithm is that the resulting jet is always conical. To understand this, consider one hard p_T particle and a set j of soft particles. The distance measures between the hard particle and the soft ones are

$$d_{hj} = \min\left(\frac{1}{k_{Th}^2}, \frac{1}{k_{Tj}^2}\right)\frac{\Delta_{hj}^2}{R}, \tag{3.20}$$

where the hard particle is indexed h. This quantity will be determined by the hard jet and therefore, the soft particles will always cluster or be combined with the hard particle before they cluster amongst themselves. It is this characteristic of the algorithm that in turn also produces conical jets. The main advantage of anti-k_T versus k_T is that anti-k_T behaves like an idealized cone algorithm, i.e. being perfectly conical (which k_T is not), as well as being infrared and collinear safe. It is hence not surprising that in almost all ATLAS results, including the ones presented in subsequent chapters, anti-k_T has been the preferred choice.

Another very important aspect to jet 4-momentum reconstruction is energy calibration. Using either towers or topological clusters, calorimeter cell energies are re-summed using the function [80]

$$P_\mu^{\mathrm{reco}} = \sum_i^{\mathrm{n\ cells}} w(\rho_i, \vec{X}_i)P_\mu^i \tag{3.21}$$

where $P_0^{\mathrm{reco}} = E^{\mathrm{reco}}$ and where the calibration factor w depends on the individual cell energy densities $\rho_i = E_i/V_i$ and their respective location $\vec{X}$. The calibration factors were originally exclusively determined using simulated dijet events [80], but have since seen refinements using real data via the inclusion of actual detector data-taking conditions and alignments. From these recalibration cell energies, a number of other calibrations are performed upon fully reconstructed jet objects such as anti-k_T jets. The first of which necessitates the rescaling of EM to hadronic energy scales while employing when possible the hadronic calorimeters (see section 3.5.2). In-situ approaches utilize γ+jet(s) and Z+jet(s) events to disentangle as much as possible the EM and hadronic deposited energies within jets. These techniques and many others have been able to achieve jet

energy resolutions well within design goals (see equations (3.10) and (3.11)).

3.8.4 E_T^{MISS} RECONSTRUCTION

E_T^{miss} reconstruction is perhaps the most delicate and refined reconstruction algorithm in ATLAS simply because every reconstructed object and/or every calorimeter cell is involved in its calculation. E_T^{miss} resolution, in fact, with its various sources is among the leading uncertainties in the WZ search (chapter 7).

Two main avenues for computing E_T^{miss} are considered. The first bases its calculation purely on the calibrated calorimeter cell energies, where the calibration is carried out as in the previous section 3.8.3. In this manner, without making use of refined calorimeter based reconstructed objects, the E_T^{miss} referred to as `MET_LocHadTopo` uses topological clusters and scales each of them independently to compute the negative vector of total transverse energy. Under low pile-up conditions, its performance is comparable to the second E_T^{miss} type referred to as `MET_RefFinal`. It vectorially adds the transverse energy of reconstructed objects before applying a number of pile-up corrections, which are continuously evolving and improving with the accumulation of data. In both methods however, reconstructed muon tracks must be added for a proper E_T^{miss} measurement.

In the case of `MET_RefFinal`, the objects used in the E_T^{miss} reconstruction are:

- Default `medium` reconstructed electrons.
- `tight` photons at the EM scale.
- `tight` taus using the local cluster weighting [19] (LCW) calibration scheme.
- anti-k_T jets with $R = 0.4$ and $p_T > 20$ GeV using the LCW+JES calibration scheme.
- anti-k_T jets with $R = 0.4$ with $p_T > 10$ GeV, but with $p_T < 20$ using the LCW scheme and not applying JES.
- Calorimeter cells not summed in any of the reconstructed objects listed above and that have been matched nonetheless to tracks (using with what is known as the

---

19. Two different types of cluster calibrations exist: local cluster weighting (LCW) and global cluster weighting (GCW). These two types of calibrations have varying performance qualities that depend strongly on the event type, however LCW is generally preferred.

track-matching algorithm) are calibrated with the LCW scheme and added to the E_T^{miss}

- Combined and segment-tagged muons (depending on the $|\eta|$ region) that are reconstructed with the *Staco* algorithm.

Figure 3.34 displays the relationship between E_T^{miss} resolution and the type of events analysed such as $W^\pm$ and Z^0 events decaying leptonically. In the search for VLQ and WZ resonances, E_T^{miss} resolution played an important role in our choice of selections. Therefore, it is essential to properly understand how well E_T^{miss} is modelled by simula-
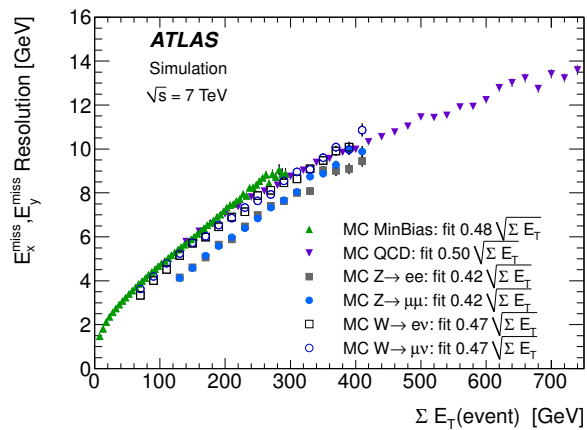
Figure 3.34: E_T^{miss} resolution using `MET_RefFinal` for each of the x and y components obtained via 7 TeV simulation. The distribution for each event type are fitted with a squared root function $a\sqrt{E_T^{\mathrm{miss}}}$ with the resulting a value given in the plot legend [126].

tion. Shown in figure 3.35 is the E_T^{miss} distribution after imposing selections to obtain primarily $W \to e\nu$ events [126]. The selection details are not important to the discussion here, just simply the behaviour seen in the ratio Data/MC for the E_T^{miss}. Such discrepancies between simulation and data for the E_T^{miss} are in fact seen very frequently, highlighting the difficulties in modelling E_T^{miss} reconstruction.

Finally, another often crucial aspect of missing transverse momentum are its fake sources, which can be from cavern backgrounds, beam halo, hot, dead, or noisy cells and from objects (primarily muons) that fall outside the detector's fiducial region. There are also corrections associated to detector defects including, for example, the cryostat regions for which the E_T^{miss} algorithm makes corrections.
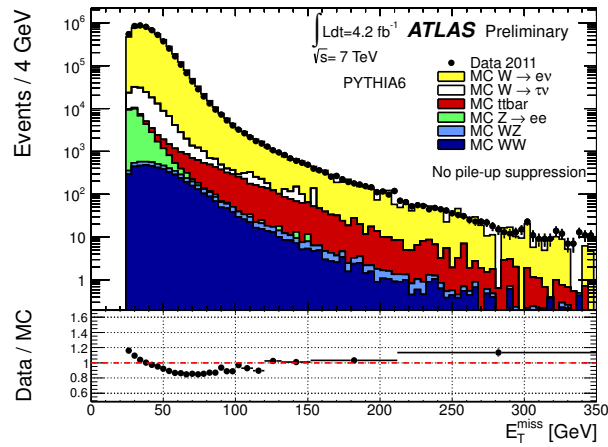
Figure 3.35: Missing transverse momentum distribution in $W \rightarrow e\nu$ events with 4.2 fb^{-1} of 2011 data. The Monte Carlo simulation of the events were done with PYTHIA 6 [127]. The lower half of the plot shows the ratio data/MC [126].

3.9   FINAL THOUGHTS ON THE ATLAS DETECTOR

In conclusion to this chapter, the ATLAS detector is without a doubt one of the most sophisticated piece of technology ever built by man, offering unique opportunities for discovering perhaps the next revolution in particle physics. The next chapter along with chapter 6 will now develop theoretical ideas extending the SM to which the ATLAS detector can provide great insight.

CHAPTER 4

THE SEARCH FOR HEAVY VECTOR-LIKE QUARKS

> *Elementary particles are terribly boring, which is one reason why we're so interested in them.*
>
> ———————————————
> Steven Weinberg

In this chapter, I will present the main theoretical models that conjecture the existence of vector-like quarks after briefly outlining their main properties. This in turn will motivate the experimental search for vector-like quarks (VLQ) presented in the following chapter.

First, the Little Higgs and Composite Higgs models shall be described, motivating the model-independent search for VLQ whose theoretical ground work shall be described in section 4.3.

4.1 THEORETICAL BASICS

Given the observation of a new boson with Higgs-like properties by both the AT-LAS [17] and CMS [18] experiments, interest has grown on the theoretical side for the possible existence of vector-like quarks. These particles would exhibit properties unlike any known fundamental particle of the Standard Model, their main characteristic being that their right and left handed components couple identically under the weak force. More explicitly, this means that chiral quarks couple via terms proportional to

$$\sim W_\mu \bar{\psi}_q \gamma^\mu (1 - \gamma_5) \psi_q \quad \longrightarrow \quad \text{chiral coupling} \tag{4.1}$$

reflecting what was found in equation (2.9) in chapter 2, whereas vector-like quarks, if added to the SM Lagrangian, by definition imply the existence of terms proportional to

$$\sim W_\mu \bar{\psi}_Q \gamma^\mu \psi_Q \quad \longrightarrow \quad \text{vector-}like \text{ coupling,} \tag{4.2}$$

where q and Q denote chiral and vector-like quarks respectively. The *-like* in vector-like simply means that their spinors behave *like* vectors under $SU_L(2)$.

The vast majority of theories going beyond the Standard Model (BSM) offer solutions to the hierarchy problem (see section 2.5.2) which states that if only SM particles exist, extremely fine-tuned parameters are necessarily implied for the Higgs mass to be light, which is *unnatural*.

In supersymmetric scenarios, superpartners differing by one-half spin with respect to their SM counterparts perfectly cancel the SM contributions to the Higgs propagator. Of course, this perfect cancellation would only occur if the symmetry were unbroken, which is evidently not the case given the fact that particles of identical mass to those of the SM have not been detected. The literature is full of ways to break this symmetry while keeping the Higgs mass light, but this goes beyond the scope of this thesis. Suffice it to say that in minimal supersymmetric models and many other variations and extensions of supersymmetry (SUSY), the existence of VLQ are generally not hypothesized. However, there are supersymmetric models with extensions that do include VLQ [128] , and in such models, the VLQ alleviates the tension between having a light Higgs and a broken supersymmetry with superpartners in the $\mathcal{O}(1)$ TeV mass range.

In fact, VLQ very often play the role of mitigating (or even totally cancelling) the quadratic divergences associated to the Higgs propagator in a number of BSM theories, and is the reason behind the heightened interest in them in recent years. Because they are vector-like, their contribution to the Higgs propagator is of opposite sign to those of regular quarks. The simple Feynman diagram shown in figure 4.1 illustrates their individual contribution to the Higgs propagator. Adding such a diagram to those of the SM, and in particular to that of the top quark (figure 2.5), can potentially cure the hierarchy problem if the couplings within the BSM theory are of the correct magnitude. Note that VLQ have no Yukawa terms (hence no 3-point interaction terms) unless both singlets and doublets exist which together can form an $SU_L(2)$ invariant term. Conversely, if only singlets or doublets exist, such VLQ have no effect on $gg \rightarrow H$ production unlike 4th generation chiral quarks.
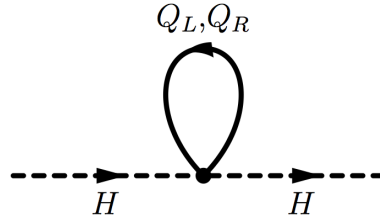
Figure 4.1: The right and left handed components of the VLQ Q couple to the Higgs at the same vertex. Notice the 4-point interaction between the H, Q_L, and Q_R which is to be compared to the 3-point interactions as in figure 2.5.

4.2 MODELS PREDICTING THE EXISTENCE OF VLQ

A wide variety of theoretical models contain vector-like quarks within their framework [129, 130]. In brief, these models include the

- *Little Higgs models*: An $SU(5)$ global symmetry breaking occurs around the TeV scale, thus producing a naturally appearing Higgs as a pseudo-goldstone boson. The VLQ present in this model plays the role of SM fermion partner to cancel the top quark's contribution to the Higgs propagator [131–133].

- *Composite Higgs models*: A new force (or new strong dynamics) exists along with its new set of particles that carry its new charge [31, 34, 134–136]. These include, but are not restricted to, technicolor models (see chapter 6).

- *Extra-dimension models*: Universal extra-dimensions can produce under certain conditions Kaluza-Klein excitations whose characteristics are once again phenomenologically very similar to VLQ [137].

- *Composite top models*: A top quark condensate procures EWSB through the addition of new color-triplet states with vector-like couplings [138].

- *GUT models built upon large groups (E_6, $SO(10)$ for example)*: Within the numerous breaking scales of these large groups, one remaining piece contains SM particles, while others contain exotic particles that include VLQ [139, 140].

- *Gauging of the flavour group*: VLQ need to exist in order to procure anomaly cancellations and play a role in the mechanisms of quark mass generation [141–143].

- **Beautiful Mirrors**: VLQ are postulated to explain the measured top/antitop quark production asymmetries at the Tevatron [144]. The *bottom*-like VLQ in these nicknamed *Beautiful mirrors* models couple slightly to the Z which in turn affects the decays $t \to W^+ b$ and $\bar{t} \to W^- \bar{b}$ in an asymmetric manner [145, 146].

Within this non-exhaustive list, we shall now focus on describing in more detail the first three models since their phenomenological consequences at the LHC are of greater importance in the context of the model-independent searches presented in the next chapter.

The VLQ in all of these models can be classified with respect to their representation under $SU_L(2) \otimes U_Y(1)$ [129, 130] . Table 4.I presents their respective hypercharges and potential Yukawa couplings.   In addition, vector-like quarks forming doublets under

Representation	Naming	Isospin I_3	Hypercharge $Y = (Q_c - I_3)$	Charge	Allowed Yukawa terms L_Y
singlets	(U) (D)	0	$2/3$ $-1/3$	$2/3$ $-1/3$	$-\lambda_u^i \bar{q}_L^i \varphi D_R$
doublets	$\begin{pmatrix} U \\ D \end{pmatrix}$ $\begin{pmatrix} T \\ U \end{pmatrix}$ $\begin{pmatrix} D \\ Y \end{pmatrix}$	$\begin{pmatrix} 1/2 \\ -1/2 \end{pmatrix}$	$1/6$ $7/6$ $-5/6$	$2/3$ $-1/3$ $5/3$ $2/3$ $-1/3$ $-4/3$	$-\lambda_u^i \bar{Q}_L \varphi u_R$ $-\lambda_u^i \bar{Q}_L \varphi d_R$
triplets	$\begin{pmatrix} X \\ U \\ D \end{pmatrix}$ $\begin{pmatrix} U \\ D \\ Y \end{pmatrix}$	$\begin{pmatrix} 1 \\ 0 \\ -1 \end{pmatrix}$	$2/3$ $-1/3$	$5/3$ $2/3$ $-1/3$ $2/3$ $-1/3$ $-4/3$	$-\lambda_i \bar{q}_L^i \tau^a \varphi Q_R^a$

Table 4.I: Classification of the allowed VLQ representations under $SU_L(2) \otimes U_Y(1)$. Presented are their respective hypercharges and foreseen Yukawa coupling terms where Q is the VLQ spinorial field, and φ the Higgs doublet field [130].

$SU_L(2) \otimes U_Y(1)$ can have gauge invariant bare mass terms such as

$$L_{\text{mass}} = m_Q \bar{Q} Q \tag{4.3}$$

where $Q = T, U, D, Y$, giving further freedom to BSM theories to include such terms and avoid experimental constraints. Hence, VLQ masses are not generated through the Higgs mechanism. This classification in singlet, doublet and triplet VLQ fields displays concretely the types of allowed VLQ within a model-independent perspective. In parallel to these ideas relating VLQ to EWSB, VLQ are the simplest addition to the SM that produces tree-level flavour changing neutral currents (FCNC) [147], hence their addition must take into account existing FCNC constraints [16]. More interestingly, VLQ can also induce CP violation [148, 149], an appealing feature given the known matter/antimatter asymmetry conundrum (briefly described in section 2.5.1).

4.2.1 THE LITTLE HIGGS MODELS

The development of Little Higgs (LH) models [131, 132, 150, 151] began at the turn of the century and they remain the smallest extension to the SM that stabilises the Higgs mass up to a new physics scale of $\Lambda_{\mathrm{LH}} \sim 10$ TeV [132] where new UV dynamics should appear. Their key features can be summarized as follows [133]:

- A global breaking occurs at a scale Λ_{LH} producing Goldstone bosons (GB), of which one can be associated to the Higgs.

- Through a second symmetry breaking at the electroweak scale Λ_{weak}, the Higgs acquires a mass and becomes a pseudo-Goldstone boson.

- The Higgs scalar field remains light (with respect to scales beyond Λ_{LH}) due to the nature of the approximate global symmetry and is free from 1-loop corrections to its mass, i.e. the sum of all 1-loop contributions cancel identically.

To achieve this last point, Little Higgs models introduce a new copied set of SM gauge bosons and pairs of VLQ $\tilde{Q}$ and $\tilde{Q}'^{c}$ [1] whose mixings with SM particles will cancel each other's contributions to the Higgs propagator. Additionally, through their mixings with SM chiral fermions, the physical states of the top quark, for example, shall appear alongside VLQ T states. Note that the cancellations occur between particles of identical statistics, unlike SUSY for example, and is a consequence of how the theory is protected

---

1. With quantum numbers $(\mathbf{3}, \mathbf{1})_{Y_i}$.

under its global symmetry. The Higgs is therefore only weakly coupled up to energies of order Λ_{LH}.

To illustrate these features more concretely, a coarse outline of the simplest Little Higgs model, dubbed the *Littlest Higgs Model* [132], shall now ensue.

At a scale $\Lambda_{\text{LH}} \sim 4\pi f$, a VEV f breaks a hypothesized *global* symmetry $SU(5)$ down to $SO(5)$, producing 14 Goldstone bosons. In parallel to this, the local symmetry group $[SU(2) \otimes U(1)] \otimes [SU(2) \otimes U(1)]$ is broken down to its diagonal subgroup $SU_L(2) \otimes U_Y(1)$ which we naturally associate to the electroweak symmetry of the SM. The 14 Goldstone bosons produced by this symmetry breaking, under $SU_L(2) \otimes U_Y(1)$, transform as one real singlet $\mathbf{1}_0$, a real triplet $\mathbf{3}_0$, a complex doublet $\mathbf{2}_{\pm\frac{1}{2}}$, and a complex triplet $\mathbf{3}_{\pm 1}$. The complex doublet plays the role of the SM Higgs field. The neutral component acquires a VEV, v, triggering EWSB as seen in chapter (2). The gauge bosons associated to the broken gauge groups acquire mass of order Λ_{LH} after *eating* the real singlet and triplet fields, yielding heavy $W_H^{\pm}$, Z_H, and γ_H. The remaining 10 Goldstone bosons (complex triplet and Higgs field) will then acquire mass through the existence of gauge and Yukawa couplings which break the global SO(5) symmetry.

The new vector-like quark fields $\tilde{Q}$ and $\tilde{Q}'^c$ are Weyl fermions, and can have mass terms as indicated in equation (4.3), but in the Littlest Higgs model, their masses are simply *chosen* to be of order f, a fact necessary for the LH theory to be natural while still providing some cure to the hierarchy problem. Following the nomenclature of Ref. [133], the effective field theory of the previously mentioned 14 Goldstone bosons can be modelled by a non-linear sigma model

$$L_\Sigma = \frac{f^2}{8}\text{Tr}|D_\mu \Sigma_{5\times 5}|^2 \tag{4.4}$$

with the $SU(5)$ invariant field Σ. The covariant derivative in (4.4), spanning over the two sets of bosons, preserves the full $[SU(2) \otimes U(1)]^2$ symmetry:

$$D_\mu \Sigma = \partial \Sigma - i \sum_{n=1}^{2} \left(g_n(W_n\Sigma + \Sigma W_n^T) + g_n'(B_n\Sigma + \Sigma B_n^T) \right). \tag{4.5}$$

To understand the various couplings and how EWSB comes about, the Σ field can be expanded around its VEV Σ_0 (occurring at the Λ_{LH} scale), resulting in

$$\Sigma = \Sigma_0 + \frac{2i}{f} \begin{pmatrix} \phi^\dagger & \frac{h^\dagger}{\sqrt{2}} & \mathbf{0}_{2\times 2} \\ \frac{h^*}{\sqrt{2}} & 0 & \frac{h}{\sqrt{2}} \\ \mathbf{0}_{2\times 2} & \frac{h^T}{\sqrt{2}} & \phi \end{pmatrix} + \mathcal{O}\left(\frac{1}{f^2}\right) \tag{4.6}$$

where Σ_0 is chosen to point in

$$\Sigma_0 \propto \begin{pmatrix} & & \mathbf{1}_{2\times 2} \\ & 1 & \\ \mathbf{1}_{2\times 2} & & \end{pmatrix}, \tag{4.7}$$

and where the fields h and ϕ are respectively doublets and triplets under $SU_L(2)$. These are written as

$$h = (h^+, h^0), \quad \text{and} \quad \phi = \begin{pmatrix} \phi^{++} & \frac{\phi^+}{\sqrt{2}} \\ \frac{\phi^+}{\sqrt{2}} & \phi^0 \end{pmatrix} \tag{4.8}$$

Naturally, the h^0 field shall be associated to the SM Higgs field H of chapter 2. Using (4.7) and (4.5), the fields W_1, W_2, B_1, and B_2 can be combined yielding the mass eigenstates

$$W = \frac{g_2}{\sqrt{g_1^2 + g_2^2}} W_1 + \frac{g_1}{\sqrt{g_1^2 + g_2^2}} W_2 = sW_1 + cW_2, \tag{4.9}$$

$$B = \frac{g_2'}{\sqrt{g_1'^2 + g_2'^2}} B_1 + \frac{g_1'}{\sqrt{g_1'^2 + g_2'^2}} B_2 = s'B_1 + c'B_2, \tag{4.10}$$

$$W' = -cW_1 + W_2, \quad \text{and} \tag{4.11}$$

$$B' = -c'B_1 + s'B_2, \tag{4.12}$$

where the massless W and B field are recognized as the SM electroweak fields with couplings

$$g_Y = \frac{g_1 g_2}{\sqrt{g_1^2 + g_2^2}}, \quad \text{and} \quad g_L = \frac{g_1' g_2'}{\sqrt{g_1'^2 + g_2'^2}}, \tag{4.13}$$

81

and where the W' and B' gauge bosons shall acquire mass of $\mathcal{O}(1)$ TeV, as mentioned above, by absorbing the real singlet $\mathbf{1}_0$ and real triplet $\mathbf{3}_0$. These heavy GB's lead to the important feature that the sum of the amplitudes for four-point interactions between the primed and unprimed bosons with the PGB Higgs exactly cancel at the 1-loop level, where the opposite sign between the fields stems from the gauge symmetry breaking scheme [132, 150].

For the fermionic cancellations between the top and vector-like quarks at the 1-loop level, the relevant terms are the Yukawa couplings between these Σ fields, the top quark and the vector-like quarks. After expanding Σ to first order using equation (4.6), and keeping only terms proportional to h along with bare mass terms, the Yukawa couplings become [132, 133]

$$L_Y = \lambda_2 f \tilde{Q}\tilde{Q}'^c - i\sqrt{2}\lambda_1 b_3 h^+ u_3'^c - i\sqrt{2}\lambda_1 t_3 h^0 u_3'^c + if\tilde{Q}u_3'^c + \text{ h.c.} \qquad (4.14)$$

where $t = (t_3, b_3)$ and $u_3'^c$ are respectively the 3$^{\text{rd}}$ generation weak doublet and weak singlet. Hence, in LH models, as made explicit in this Littlest Higgs model, the standard Yukawa couplings of 3$^{\text{rd}}$ generation quarks are modified. Moreover, the fact that these couplings are small up to a cutoff scale of $\mathcal{O}(10)$ TeV greatly reduces their quadratic contributions to the Higgs mass. This is how LH models *resolve* the hierarchy problem, in essence rescaling the issue to the $\mathcal{O}(10)$ TeV scale. The t_3, b_3 and u'^c fields together with the new vector-like quark fields $\tilde{Q}$ and $\tilde{Q}'^c$ shall mix, giving rise to the mass eigenstates

$$m_{\text{top}} = \frac{iv\lambda_1\lambda_2}{\sqrt{\lambda_1^2 + \lambda_2^2}}\left(1 - \frac{v^2}{f^2}\left[\frac{1}{3} - \frac{v'f}{v^2} - \frac{\lambda_1^2}{2(\lambda_1^2 + \lambda_2^2)}\left[1 - \frac{\lambda_1^2}{\lambda_1^2 + \lambda_2^2}\right]\right]\right) \qquad (4.15)$$

$$m_T = f\sqrt{\lambda_1^2 + \lambda_2^2}\left[1 + \mathcal{O}\left(\frac{v^2}{f^2}\right)\right] \qquad (4.16)$$

These physical states are naturally associated to the top quark, and the VLQ T mentioned at the beginning of this section. The known top quark mass places constraints upon the couplings $\lambda_{1,2}$ limiting them to obey the approximate relation (derived from

equation (4.15))

$$\frac{v^2}{m_{\text{top}}^2} = \left[\frac{1}{\lambda_1^2} + \frac{1}{\lambda_2^2}\right] \cdot \left[1 - \mathcal{O}\left(\frac{v^3}{m_{\text{top}}f^2}\right)\right] \tag{4.17}$$

Although there is perhaps no need to implement the same formalism for couplings with first and second generation quarks, given that their quadratic corrections remain natural below the scale $\mathcal{O}(10)$ TeV, nothing prevents the inclusion of a new set of VLQ just as the $\tilde{Q}$ and $\tilde{Q}'^c$ ones which couple and mix with first and/or second generation quarks. It must also be emphasized that mixings with light quarks are not excluded given that cancellations among the new heavy quarks can occur [152, 152, 153] giving rise to sizeable couplings between VLQ and light quarks. This should be kept in mind when discussing the model-independent search presented next, but first, here are other relevant BSM models for such VLQ searches.

4.2.2 LITTLE HIGGS WITH T-PARITY

Unfortunately, a detailed study of processes involving primarily heavy gauge boson exchange have shown that the symmetry breaking scale f in the Littlest Higgs model is bounded by $f \geq 3.5$ TeV in order to satisfy constraints from precision electroweak data [154, 155]. This implies that a significant amount of fine-tuning is required for the Higgs to remain light. Gladly, an appealing solution to this problem exists through the introduction of the concept of T-parity [156, 157]. This new discrete symmetry essentially enforces the gauge couplings, g_n and g'_n in equation (4.5), to be equal [158]. In other words, interchanging the two copies of the gauge group $SU(2) \otimes U(1)$ leaves the Lagrangian invariant. As a consequence, and in analogy to R-parity in SUSY, the SM doublet fermions are T-even including the Higgs, while the heavy gauge bosons, γ_H, $W_H^\pm$ and B_H (the W' and B' in (4.11) and (4.12) after acquiring a mass though the Higgs mechanism) are T-odd. For consistency, a complete set of T-odd VLQ are partnered to each SM fermion. The single exception is the T VLQ introduced earlier which is T-even [2].

Studies of electroweak precision measurement constraints on the parameters of the

---

2. The top quark also has a additional partner T' which is T-odd just like all other SM fermions.

Littlest Higgs model with T-parity (LHT) have shown that f as low as 500 GeV are allowed, thereby removing the fine-tuning previously necessary for the Higgs to remain light [159]. However, as nothing comes easy in the world of BSM theory building, quantum anomalies appear at low energy due to Wess-Zumino-Witten (WZW) interaction terms [3] which break T-parity [160, 161]. Fortunately, either by

- Dropping the assumption that the theory has condensing fermions at $\mathcal{O}(10)$ TeV, or

- Constructing the theory upon anomaly-free groups such as $SO(N)$ [162]

removes these WZW interactions terms and maintains T-parity as an exact symmetry. If preserved, T-parity conservation leads to a lightest T-odd particle (LTP) which cannot decay into SM particles. The LTP is typically the *heavy photon* γ_H, and is a potential dark matter candidate [163].

Finally, the PGB nature of the Higgs in LH models can be incorporated in larger frameworks having as general feature a composite Higgs.

4.2.3 COMPOSITE HIGGS MODELS

In the literature, composite Higgs models (CHM) generically refer to models with a new strong interaction, yielding composite states which can be fermions (VLQ), vector bosons (W', Z'), or scalars (Higgs). The model however is often described in terms of extra dimensions whose strong sector acts within a $5D$ anti-de Sitter spacetime (AdS), using the AdS/CFT correspondence. The Higgs in such models is a composite state, just as VLQ, whose behaviours at low energy are phenomenologically indistinguishable to the SM Higgs and *fundamental* VLQ [31, 34, 134, 135].

An elegant way to explain EWSB is through the existence of a new strongly interacting sector, just as in technicolor models (more on technicolor in chapter 6). However, primitive technicolor models (without *walking* couplings) fail to predict S and T electroweak parameter [4] values within experimental bounds [165]. In CHM [134, 136, 166],

---

3. In QCD for example, WZW interaction terms allow for decays of the form $K\bar{K} \to \pi\pi\pi$. Such terms hence describe the anomalous low-energy effective physics in terms of PGB (the pions/kaons in QCD) and gauge fields.

4. The Peskin–Takeuchi parameters S, T and U [164] indicate the degree to which new phenomena,

and in particular the minimal composite Higgs model (MCHM) [34], the idea of an extra strongly coupled sector is retained but within the context of $5D$ Anti-de Sitter spacetime (AdS). The conjectured AdS/CFT correspondence then permits strongly coupled $4D$ theories to be weakly coupled $5D$ theories for which model calculations can be performed. The new strong interaction enables the possibility that the Higgs be a composite pseudo-Goldstone boson (PGB).

In the MCHM [34], the holographic PGB (Higgs) arises as the product of the breaking of the global symmetry $SO(5) \otimes U_{B-L}(1)$. This is the smallest symmetry group integrating the SM electroweak group along with producing a PGB Higgs. Moreover, the Higgs potential in such a scenario can be determined from the contributions arising from 1-loop diagrams of SM particles. Interestingly, within this model, the Higgs remains light, i.e. ≤ 140 GeV [34].

As mentioned before, although the Higgs (if composite) is protected from self-coupling corrections, VLQ are often introduced to mitigate the UV sensitivity to the top quark [31, 135]. For example, following the approach of Ref. [135] where a $SO(5)$ global symmetry is hypothesized to spontaneously break to $SO(4)$ at a scale F, this can give rise to a Higgs doublet constructed out of the original $SO(5)$ symmetry. In this model, the quark sector is also extended to include the new fields [135]

$$\psi_L = (q, X, T)_L, \, t_R, b_R, X_R, T_R. \tag{4.18}$$

where ϕ_L is a vector under $SO(5)$, $q_L = (t_L, b_L)$, and where the VLQ fields $X_{L,R}$ and $T_{L,R}$ are respectively doublets and singlets under $SU_L(2)$. These new VLQ fields alleviate the UV sensitivity of the Higgs mass to the top quark loop by introducing Yukawa terms similar to those found in (4.14).

Similarly, through the AdS/CFT correspondence, warped extra-dimensions can alternatively be viewed as a theory of partial compositeness [167, 168], which typically extends or includes the ideas of composite Higgs models. Partial compositeness posits

---

or new physics are influenced by electroweak radiative corrections due to new massive particles in loops. By definition, they are zero in the SM.

that the SM particle fields couple to a new particle sector such that the heaviest particles of the SM, namely the top quark, mix sizeably to this new sector. Naturally, such models have constraints on their respective mixing angles [135], but credible models have been devised [169] and include VLQ.

4.3 THE SEARCH OF VLQ COUPLING TO LIGHT GENERATIONS - THEORETICAL UNDERPINNINGS

The BSM models just described all contain VLQ. However their respective cross sections at the LHC are heavily dependent on the model considered. Therefore, a model-independent approach, parametrizing their couplings to SM particles is a manageable way to go about investing their potential existence. From there, limits on the couplings can be reinterpreted in all proposed models to determine whether there remain sizeable parameter regions where such models are still valid and concur with experiment.

The search therefore presented in the next chapter focuses on VLQ coupling to first generation quarks. Ordinarily, VLQ are expected to couple to the third generation to alleviate the quadratic divergences of the Higgs mass due to the top quark, but as we have seen, this is not the exclusive case. Couplings to the first generation, however, exhibit features cancelling out their observable effects on EW constraints [152, 153, 170]. This is the case, for example, for two degenerate (before EWSB) doublet VLQ (see table 4.I) that have Yukawa couplings only to the up type sector and that have the following charge assignments [171]

$$Q_T = \frac{5}{3}, \quad Q_U = \frac{2}{3}, \quad Q_D = -\frac{1}{3}, \quad Q_Y = -\frac{4}{3}. \tag{4.19}$$

This occurs naturally in extra dimensional models with the $Zb\bar{b}$ coupling protected. With these, one can now write down their allowed EW couplings to first generation right-

handed (RH) quarks as [172]

$$L = \frac{g_L}{\sqrt{2}} \left\{ W_\mu^+ \left[\kappa_{uD} \bar{u}_R \gamma^\mu D_R + \kappa_{dY} \bar{d}_R \gamma^\mu Y_R \right] + W_\mu^- \left[\kappa_{uT} \bar{u}_R \gamma^\mu T_R + \kappa_{dU} \bar{d}_R \gamma^\mu U_R \right] \right.$$

$$\left. + \frac{Z_\mu}{\sqrt{2} c_W} \left[\kappa_{uU} \bar{u}_R \gamma^\mu U_R + \kappa_{dD} \bar{d}_R \gamma^\mu D_R \right] \right\} \tag{4.20}$$

$$+ \Gamma_{uQ} \bar{u}_R \varphi U_L + \Gamma_{dD} \bar{d}_R \varphi D_L \tag{4.21}$$

$$+ m_U \bar{U}_L U_R + m_D \bar{D}_L D_R + m_T \bar{T}_L T_R + m_Y \bar{Y}_L Y_R + \text{ h.c.} \tag{4.22}$$

where the electroweak couplings κ_{qQ} and Yukawa couplings Γ_{qQ} parameterize all of the model dependence. Only RH couplings are shown for brevity, although equivalent couplings to LH quarks should also be considered. From a collider perspective, the Yukawa terms could be relevant for searches of the type

$$gg \to H \to \bar{q}Q \to \bar{q}Vq', \tag{4.23}$$

where the Higgs H is produced through gluon fusion and subsequently decaying into a light quark q and VLQ Q which itself decays to an electroweak boson $V = W, Z$ and another light quark q'. Alternatively, the VLQ could be searched for through its decay into a Higgs as in the single production process

$$q_1 q_2' \to q_3 Q \to q_3 H q_4, \tag{4.24}$$

where q_i for $i = 1, 2, 3,$ and 4 are light quarks. Such searches, however, have yet to be performed, although several search proposals have been put forward [173].

Focusing on the discovery potential of the *Dirac* terms, electroweak precision measurements have already constrained the couplings κ_{qQ} to ~ 0.01 [172] in the absence of cancellations between the mixings of heavy quarks. However, in relatively simple mod-

els such as the one with degenerate doublets (not the parametrization given above) [171]

$$Q_{L,R} = \begin{pmatrix} U_{L,R} \\ D_{L,R} \end{pmatrix}_{Y=\frac{1}{6}}, \text{ and } X = \begin{pmatrix} \chi_{L,R} \\ \chi_{L,R} \end{pmatrix}_{Y=\frac{7}{6}}, \tag{4.25}$$

have Yukawa terms mixing the heavy quarks with the up quark[5] are given by [171]

$$L = \lambda_{u1}\bar{q}_L \tilde{\varphi} u_R + \lambda_{u2} \left(\bar{Q}_L \tilde{\varphi} + \bar{X}_L \varphi \right) u_R, \tag{4.26}$$

with the relevant Yukawa couplings $\lambda_{u1,u2}$. From there, it has been shown that corrections to the up quark mass follows [171]

$$m_{\text{up}} = \lambda_{u1} v \left[1 - \lambda_{u2}^2 \left(\frac{v}{m_Q} \right)^2 + \mathcal{O} \left(\frac{v}{m_Q} \right)^4 \right] \tag{4.27}$$

while the mass of the VLQ U reads

$$m_U = m_Q \left[1 + \lambda_{u2}^2 \left(\frac{v}{m_Q} \right)^2 + \mathcal{O} \left(\frac{v}{m_Q} \right)^4 \right]. \tag{4.28}$$

Hence, to reproduce the up quark mass, λ_{u1} must be below $\sim 10^{-5}$, but λ_{u2} can even be order unity with the new quarks have mass much greater than $v = 174$ GeV. It is shown in [171] that $\mathcal{O}(1)$ coupling κ_{qQ} is compatible with electroweak and flavour constraints. Under such conditions, not only do they avoid precision electroweak constraints, the couplings κ_{qQ} can be appreciably large. On the other hand, the existence of these new particles would have an effect upon the oblique parameters. In the two VLQ doublet model just outlined, the dependence of the oblique parameter S on the coupling κ_{uU} is presented in figure 4.2. Therefore, couplings of $\kappa_{uU} \lesssim 0.7$ remain experimentally allowed and are one of the focuses of the search presented in the next chapter.

---

5. The same would be true for the couplings to the down quark.
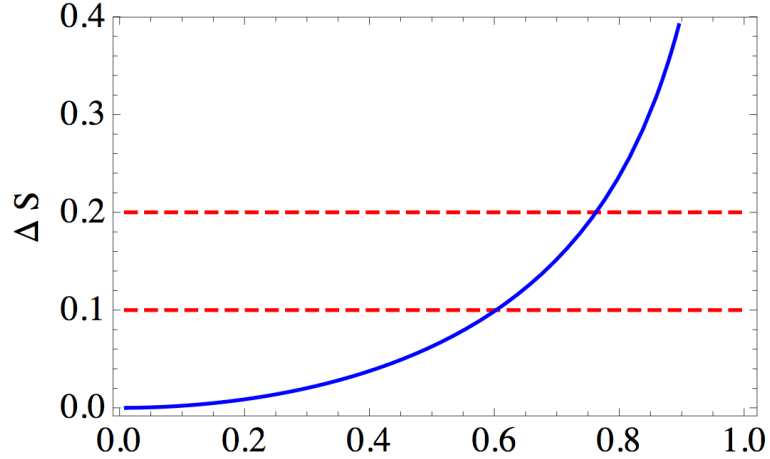
Figure 4.2: Contributions to the S parameter as a function of the coupling κ_{uU} and the two VLQ doublet model with hypercharge assignments of $1/6$ and $7/6$. Present 95% C.L. exclusion bands upon S [16] roughly lie between $S = 0.1$ and $S = 0.2$ (red dotted lines) [171].

4.3.1 PRODUCTION MECHANISMS

There are two main production mechanisms for VLQ in a pp collider. Strong pair production via

$$gg \to Q\bar{Q} \tag{4.29}$$

and weak single production

$$q_1 q_2 \to q_3 Q q_4 \tag{4.30}$$

as shown in figure 1.1. Generally, given the ordinarily small electroweak couplings, pair production dominates over single production, as is the case for the top quark for example, whose pair production cross section at the LHC is roughly an order of magnitude greater than its single production (see figure 2.3). Yet, the fact that the couplings κ_{qQ} can be relatively large, as we have just seen, single production in such conditions can dominate over pair production. And this advantage increases as a function of the VLQ's mass due to simple kinematics. Figure 4.3 presents, as a function of m_Q, the mass of the VLQ, the cross sections σ times $\tilde{\kappa}_{qQ}^{-2}$, where

$$\tilde{\kappa}_{qQ} = \frac{m_Q}{v} \kappa_{qQ}, \tag{4.31}$$

89

for pair and single production in the charged current channel ($pp \to jU$ or $j\bar{U}$). Parameterizing as a function of $\tilde{\kappa}_{qQ}$ shall prove useful given the relation (4.28). Of course, the
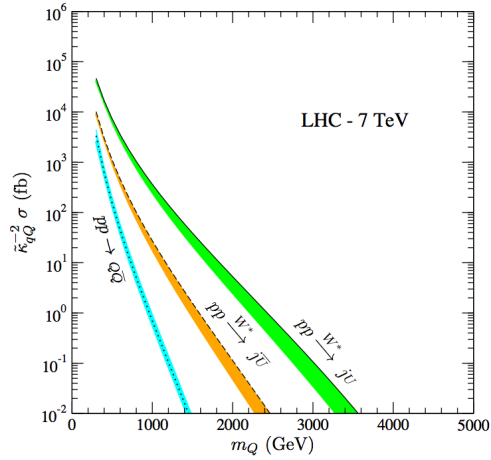
Figure 4.3: Single versus pair production cross section after dividing out the dependence on $\tilde{\kappa}_{qQ}$ at LO. The colored bands indicate the renormalization scale dependance from m_W to m_Q [172]. Note that pair production is independent of $\tilde{\kappa}_{qQ}$

situation is virtually identical at $\sqrt{s} = 8$ TeV.

These final facts set the stage for the presentation of the search for VLQ coupling to light quarks. The abundance of theories postulating the existence of VLQ along with the potentially loose constraints upon the couplings to first generation have greatly motivated and guided the search described in chapter 5.

CHAPTER 5

RESULTS ON THE SEARCH FOR HEAVY VECTOR-LIKE QUARKS

An expert is someone who knows some of the worst mistakes that can be made in his subject, and how to avoid them.

Werner Heisenberg

This chapter shall feature the details of the search for singly produced vector-like quarks (VLQ) coupling to light quarks. The main results presented here are reported in Ref. [8] [1] which is an improved and updated version of the analysis published in Ref. [10]. This former analysis is discussed in appendix IV.

5.1 ANALYSIS OUTLINE AND STRATEGIES

The search aims to explore the potential presence of neutral and charged current resonances of the type

- $q_1 q_2 \to D q_3 q_4 \to W u \, q_3 q_4 \Leftrightarrow$ *Charged Current* (CC), and
- $q_1 q_2 \to U q_3 q_4 \to Z u \, q_3 q_4 \Leftrightarrow$ *Neutral Current* (NC)

where the up-type U and down-type D VLQ form an $SU_L(2)$ doublet as portrayed in section 4.3 with hypercharge assignments $Y = 1/6$ and $Y = 7/6$ respectively. They can be produced in either the t-channel or s-channel as shown in figure 5.1, although the t-channel processes heavily dominate over the s-channel ones.

Using the model-independent approach elaborated previously in section 4.3, resonances in the final states $\ell\nu$+jet (CC) and $\ell\ell$+jet (NC) shall be examined and (if no such resonance is found) limits upon their respective cross sections and couplings to light quarks, parameterized by

$$\kappa_{qQ} = \frac{v}{m_Q} \tilde{\kappa}_{qQ} \tag{5.1}$$

---

1. For ATLAS members, the supporting documentation can be found in Ref. [174].

(a) t-channel VLQ production   (b) s-channel VLQ production
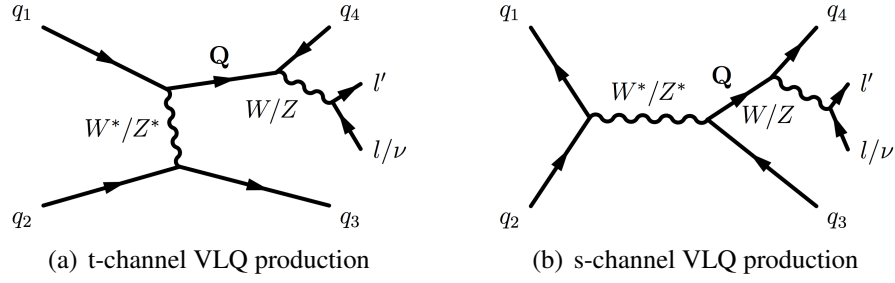
Figure 5.1: Single production of VLQ coupling to light quarks q_i for $i = 1, 2, 3, 4$.

to reiterate equation (4.31), shall be computed.

For there to be cancellations among the VLQ mixings to light quarks, a necessary component to circumvent constraint from precision measurements, equation (4.27) indicates that the mass of the VLQ must be appreciably larger than $v = 174$ GeV. In this analysis, however, we shall concentrate on investigating resonance masses greater than or equal to 400 GeV.

Taking advantage of the fact that the t-channel dominates, one expects there to be, along with a high p_T jet (product of the VLQ decay), a second jet in the high η or forward region of the detector. This jet shall be designated the *associated* jet and can be identified as the product of the hadronization of the quark q_3 in 5.1(a).

In both the CC and NC channels, the *invariant* mass of the final states shall be used as the distinguishing or discriminant variable. For the CC channel, given that the total momentum transfer of the hard scatters are unknown quantities, the missing energy along the beam line is unmeasurable. However, assuming the event produced a W boson decaying to leptons $W \to \ell\nu$ where $\ell = e, \mu$, the neutrino p_z can be inferred through the simple relativistic equations

$$m_W^2 = E_{\text{total}}^2 - \mathbf{P}_{\text{total}}^2 = (E_\ell + E_\nu)^2 - (\mathbf{P}_\ell + \mathbf{P}_\nu)^2 \text{, and} \qquad (5.2)$$

$$E_\nu = \sqrt{p_T^2(\nu) + p_z^2(\nu)}. \qquad (5.3)$$

Fixing $m_W = 80.4$ GeV [16], which assumes the W is exactly on shell, is a very good approximation given the detector's resolution. Then, isolating the unknown $p_z(\nu)$ yields

$$p_z(\nu) = \frac{A p_z(\ell) \pm \sqrt{A^2 p_z^2(\ell) + \left[4E_\ell^2 - p_z^2(\ell)\right]\left[A^2 - 4E_\ell^2 p_T^2(\nu)\right]}}{4E_\ell^2 - p_z^2(\ell)}, \qquad (5.4)$$

where $A = m_W^2 + 2\mathbf{p}_T(\ell) \cdot \mathbf{p}_T(\nu)$. The right-hand side of equation (5.4) are all experimentally measurable quantities assuming $p_T(\nu) = E_T^{\text{miss}}$, yielding a concrete value for $p_z(\nu)$, apart from the uncertainty associated to the $\pm$ sign. The method used to choose either the *plus* or *minus* $p_z(\nu)$ solution shall be exposed in section 5.4 with the general object selections and shall depend on the event topology.

The EW vector-boson and $t\bar{t}$ backgrounds, being the dominant backgrounds for this search, must be very well modelled beyond LO to provide an accurate prediction of the VLQ mass distribution. Learning from the 1 fb^{-1} search [10] however (presented in appendix IV), it is clear that the EW vector-boson simulated with ALPGEN overestimates the background slope in the vector boson p_T distribution as seen in figures IV.1 (CC) and IV.2 (NC) when translated to the $m(\text{VLQ})$ spectrum. Other generators such as SHERPA [175] were found to produce the same overestimation. As a consequence, a bump hunting approach in conjunction with a functional fit to the background was deemed ideal under these circumstances. In other words, because absolute event yield predictions are unnecessary for a pure resonance search (we are not making a SM measurement), a simple fit to the background (while excluding a window for the hypothesized signal) is sufficiently adequate and does not hinder on the possibility to compute limits. This method shall be explained in detail in section 5.9.2.

The MC background modelling however shall remain important in validating the signal optimization scheme laid out in section 5.7. There, multivariate (MV) techniques shall be used to optimize the sensitivity $S/\sqrt{S + B}$.

5.2 THE 2011 DATASET

This analysis uses the full 2011 analysis ready dataset, which tallied 4.65 fb^{-1} at a center of mass energy of $\sqrt{s} = 7$ TeV. The LHC total delivered luminosity was 5.6 fb^{-1} with a peak luminosity of 3.6×10^{33} cm^{-2}s^{-1} [176]. Given that all components of the detector are required to be functioning properly, for E_T^{miss} reconstruction for example, 83% of LHC delivered data are analysis ready. Dedicated analysis groups provided *good runs list* (GRL) specifying the runs and luminosity blocks (LB) where the ATLAS detector was in stable operation. The uncertainty on the integrated luminosity stands at 1.8% [176].

The data were collected from March to December in 10 distinct data-taking conditions [2] labelled by the run periods *D* to *M*. The middle plot in figure 3.2 illustrates how the instantaneous luminosity increased during these periods, and as a consequence, the pile-up conditions changed considerably. The in-time pile-up, driven by the average number of interactions per bunch crossing (BC) $\langle\mu\rangle$, grew from a mean of roughly 6 to 13 interactions per BC, as seen in figure 3.3, due to the increased amount of protons per bunch.

Despite the incremental increases in the total number of bunches in the collider, out-of-time pile-up was not significantly altered given the standard 50 ns bunch spacing used within the *trains* of bunches (for the majority of the dataset starting from period F). By December, the proton bunches were organized in sets of triple trains, each train separated by 225 ns and containing 36 bunches at the standard separation of 50 ns. The maximum number of bunches attained in 2011 was 1331 [176].

5.2.1 TRIGGER SELECTIONS

The increasing instantaneous luminosity between run periods *D* and *M* forced the p_T threshold upon the lowest unprescaled single and double lepton triggers to increase accordingly. Table 5.I and 5.II present the triggers used in the electron and muon channels

---

2. These *conditions* are a reflection of the LHC proton bunch configurations and on ATLAS online reconstruction software such as the constantly evolving trigger menus. For example, period F is where 50 ns bunch spacings began and period G is where pile-up suppression was initiated at HLT.

respectively as a function of the run periods and the luminosity they represent.

Run Period	CC channel	NC channel	Integrated Lumi. (% of total)
D-J	`e20_medium`	`2e12_medium`	1.66 fb^{-1} (35.8)
K	`e22_medium`	`2e12T_medium`	0.58 fb^{-1} (12.5)
L-M	`e22vh_medium1`	`2e12Tvh_medium`	2.40 fb^{-1}

Table 5.I: Electron trigger menu items used to trigger on electronic decays of the EW vector-bosons. The trigger item nomenclature indicates the electron quality through the `medium` tagged-name which is similar to the `medium` electron quality definition given by table 3.II but at a coarser level. `medium1` indicates that the electron must also be isolated. Finally, the `vh` signifies that some hadronic background suppression selections were applied.

Run Period	CC/NC channel	Integrated Lumi. (% of total)
D-I	`mu18_MG`	1.45 fb^{-1} (31.3)
J-M	`mu18_MG_medium`	3.19 fb^{-1} (69.7)

Table 5.II: Muon triggers items utilized to select both $W \to \mu\nu$ and $Z \to \mu\mu$ events using the Muon Girl (MG) reconstruction algorithm. The nomenclature follows the same conventions as for the electron. `medium` reflects the fact that quality selections upon the muon tracks were required to keep the unprescaled threshold at 18 GeV for period J and onwards.

In MC, because the trigger items changed over time, a luminosity-weighted random period generator was used to account for possible trigger efficiency variability.

5.3 MONTE-CARLO SAMPLE GENERATION

5.3.1 VLQ SIGNAL SIMULATION

Using the MADGRAPH generator [177], the VLQ model described in section 4.3 was implemented such that resonances of the type shown in figure 5.1 can be readily produceable and simulated. The model incorporated the Lagrangian of Ref. [172] in which the two VLQ doublets, as given in equation (4.25), couple to light quarks [3].

---

3. Great thanks to the authors of Ref. [172] for implementing the model in MADGRAPH.

Two signal types were produced. The CC single production process $D \to Wu$, and the NC one $U \to Zu$ for masses ranging from 225 to 2000 GeV in steps of 100 GeV beginning at 300 GeV. As mentioned previously however, we shall only consider the cases with $m_Q \geq 400$ GeV. Focusing on the model of Ref. [171] (see equation (4.25)), the processes giving rise to $U \to Wd$ and $D \to Zd$ are simply not present and were hence neglected (see equation (21) in Ref. [172]). For both the CC and NC, the EW vector-bosons that are the product of the VLQ decay are forced to decay leptonically. The cross sections for these resonances were calculated assuming $\tilde{\kappa} = 1$ (see equation (5.1)) and a 100% branching ratio of the VLQ to first generation quarks. In a sense, because the analysis is to be model-independent, each VLQ is considered independently. Details on these VLQ signals, including their cross sections as a function of mass, which range from $\mathcal{O}(1)$ picobarn at 400 GeV to $\mathcal{O}(1)$ femtobarn at 2 TeV, are reported in appendix VI.1. No generator level selections [4] were applied on the angular distributions of the final state lepton or on jet p_T.

Given our focus on couplings to the up quark, there is the additional possibility that it mixes to the other VLQ doublets parametrized through the Lagrangian (4.22), namely the charged $+5/3\ T$ quark. Now, since the $T^{5/3}$ quark couples only to up quarks (charge conservation), its production cross section in a pp collider may be considerable. Under the assumption $\tilde{\kappa}_{uT} = 1$, its production cross sections as a function of mass are given in table VI.II in appendix VI.

Instead of fully simulating $T^{5/3}$ events as it was done for the U and D type VLQ, demonstrating that the main kinematical variables of the $T^{5/3}$ are very similar to those of the D quark would thus permit us to use the U MC samples to measure the signal strength of the $T^{5/3}$ quark. Hence, for a mass of 600 GeV, various kinematical distributions are compared between the $D \to Wu$ and $T \to Wu$ in appendix VI. The adequate agreement between the two provides us with the means to interpret the limits in terms of κ_{uT}.

---

4. Parton level selections upon the final state particles before any hadronization and/or detector effects.

5.3.2 BACKGROUND SIMULATION

The dominant background in both the CC and NC channels are EW vector-boson production in conjunction with 2 or more jets where the vector-boson decays leptonically. Therefore, by necessity, a simulation that goes beyond LO is required given the presence of multiple final state jets. For both $W \rightarrow \ell\nu+$ jets and $Z \rightarrow \ell\ell+$jets, samples were simulated with ALPGEN [178] given its ability to generate events with fixed number of final state partons, interfaced with HERWIG [179] for parton shower and fragmentation processes and along with JIMMY [180] for underlying event simulation. Tables VI.III and VI.IV present the main parameter of the samples used in this analysis for $W(\ell\nu)$+jets and $Z(\ell\ell)$+jets respectively. For each lepton decay channel, six separate samples were produced as a function of the number of final state partons (0 to 5) with the appropriate matrix element versus parton showering jet matching techniques to avoid double counting identical events. In this case, the MLM scheme was used [178]. Naturally, the samples with 2 final state partons were of capital interest. The effective luminosity for these samples were roughly 8.4 fb^{-1} in the CC channels and 40 fb^{-1} in NC channel.

The secondary backgrounds include the diboson, top quark (in pair and single production), and multijet production. The first two were simulated with MC@NLO [181], the details of which can be found in table VI.V of appendix VI. The multijet background on the other hand, due to the known difficulty in correctly modelling the small rate at which jets fake the signatures of leptons[5], and this with sufficient statistics, the multijet background was estimated through a *data-driven* approach that shall be discussed in section 5.6.

Beforehand however, an exposition of the object selections is in order.

5.4 OBJECT SELECTIONS

The core ATLAS reconstruction algorithms presented in section 3.8 provide the basis upon which individual analyses build on to enhance their sensitivity. In addition,

---

5. Also known as mis-identified jets

ATLAS performance teams also provide reconstruction re-calibrations or corrections tools as well modelling correction factors that need to be applied to Monte-Carlo simulations. These tools are summarized here below (with in parentheses the ATLAS tool name and version for ATLAS internal information purposes only).

Pile-up Reweighting (PRW) (PileupReweighting-00-02-01)

    The $\langle \mu \rangle$ distribution in MC is reweighted event-by-event to match the data.

Jet Calibration (ApplyJetCalibration-00-01-06)

    Correct JES calibration.

    Compute JES/JER uncertainties.

Jet Resolution Smearing (ApplyJetResolutionSmearing-00-00-03)

    Modify MC jet resolution to match the data.

E/γ Calibration (egammaAnalysisUtils-00-03-25)

    Recalibrate electron energy scale (EES).

    Modify MC electron energy resolution (EER) to match the data.

    Compute electron reconstruction efficiency scale factors (SF) to be applied to MC.

    Calculate uncertainties related to EES, EER, and electron reconstruction efficiency scale factors.

E_T^{miss} Calibration (MissingETUtility-01-00-06)

    Recompute the missing E_T using only the analysis specific objects.

    Calculate E_T^{miss} uncertainties due to pile-up and soft terms [6].

Muon Reconstruction Efficiency (MuonEfficiencyCorrections-02-01-00)

    Compute muon reconstruction SF that are applied to MC to match the data.

Muon Calibration (MuonMomentumCorrections-00-06-06)

    Correct muon energies

    Compute uncertainties related to muon 4-momentum.

Lepton Trigger Efficiency (TrigMuonEfficiency-00-02-03)

    Obtain and apply to MC lepton trigger efficiency SF.

    Compute uncertainties related to lepton trigger efficiencies.

---

6. The cell energy deposits that do not enter into the computation of any fully reconstructed object.

The above tools are essential to compute systematic uncertainties, details of which shall be given in section 5.8. Because the simulation campaigns for the backgrounds and signals needed to begin before the data were acquired, a very rough estimate of the $\langle \mu \rangle$ distribution had to be assumed and used to randomize the number of interactions per bunch crossing (alternatively be described by the number of reconstructed vertices). The reweighting procedure thus used the information from the combined N_{vertex} and $\langle \mu \rangle$ distribution to compute a weight for a given MC event.

We can separate the object selections in two main classes. The first encompasses all selection criteria that quantitatively affect our handle on the objects identity (electron, photon, jet, etc.) and/or on the object's 4-momentum resolution. These include some of the selections appearing in table 3.II characterizing electron quality definitions, such as the number of silicon hits on fitted track or conversion unmatching to reject photons. These types of selections also include isolation criterium which as we shall see plays a critical role in signal efficiency for high mass signals. The second are simple kinematic ones that define a selected region within the object's 4-momentum phase space and include selections such p_T thresholds, η ranges for example. Viewing the selections in these two different classes permits a clearer understanding of their relation to the final results which, if we neglect uncertainties of all kinds, only depend on the phase space selections of the second class.

5.4.1 ELECTRON DEFINITION

The candidate electrons are required to have $p_T > 25$ GeV, the point at which all previously mentioned triggers reach their efficiency plateau. The candidates must also fall within $|\eta| < 2.47$ while excluding the crack region $1.37 < |\eta| < 1.52$ where the barrel and end-cap regions of the detector meet. They are additionally required to be reconstructed either from a cluster-based algorithm, or by both track- and cluster-based algorithms. Lastly, all candidate electrons must be isolated. Concretely, in this analysis, this signifies that the transverse energy within a cone of radius $R = 0.2$ that was *not* included in the calculation of the candidate's E_T must not be greater than 10% of the final candidate's E_T.

In the NC channel, both final state electrons must pass the `medium++` selection criteria (see section 3.8.1).

In the CC channel, the single final state electron is required to satisfy the `tight++` selection criteria.

5.4.2 MUON DEFINITION

Selecting the *Staco* muon reconstruction algorithm (refer to section 3.8.2 for details), combined[7] muons are required to have $p_T > 25$ GeV within the range $\eta < 2.4$. Similar to electrons, muon candidates are only required to be isolated within a cone of $R = 0.2$ such that the transverse momentum within this cone that is *not* associated to the final muon p_T be less than 10% of the latter. In addition, to suppress possible cosmic muon events, muon tracks must point within 1 mm in z of the PV, and satisfy $\sigma_{d_0}/d_0 < 3$ where d_0 is the radial distance of the track to the PV and σ_{d_0} its uncertainty. Finally, a number of track quality requirements were imposed. These are summarized in table 5.III.

Variable(s) to be selected on	Selection
B-layer hits	> 0 if expected
Number of Pixel hits + crossed dead Pixels	> 1
Number of SCT hits + crossed dead SCT sensors	> 5
Number of Pixel Holes + SCT Holes	< 3
TRT Hits requirement $N_{\mathrm{TRT}} = $ TRT Hits + TRT Outliers	If $|\eta| < 1.9$, $N_{\mathrm{TRT}} > 5$ and TRT Outliers $< 0.9 N_{\mathrm{TRT}}$ If $|\eta| \geq 1.9$ and $N_{\mathrm{TRT}} > 5$, require TRT Outliers $< 0.9 N_{\mathrm{TRT}}$

Table 5.III: Muon track quality requirements as prescribed by the ATLAS muon performance team.

5.4.3 JET DEFINITION

Jets are reconstructed using the anti-k_T algorithm [124] with radius parameter $R = 0.4$. As described in section 3.8.3, this top-level algorithm uses topological clusters as

---

7. Combining track information from both the ID and MS.

inputs to compute the jets 4-momentum. Once the reconstruction complete, jets are required to have $p_T > 25$ GeV and $|\eta| < 4.5$. The associated jet, being the *associated* product of a t-channel VLQ production, is expected to be in the forward region, hence the importance to use the largest possible fiducial region. Furthermore, a set of quality selections is imposed to reduce jets that are the product of calorimeter noise or cosmic rays. Jets that fail such criteria are deemed *bad* jets. Additionally, if a jet passes the kinematic selections but fails these quality selections, the event itself is rejected to ensure that the missing transverse momentum is well-measured. A least 75% of the tracks pointing to the reconstructed calorimeter cone must also point to the PV. This is known as the jets vertex fraction (JVF). Lastly, jets are rejected if they are within a distance $\Delta R \leq 0.3$ to a well-reconstructed electron or muon as defined in the last two sections.

5.4.4 E_T^{MISS} DEFINITION

The missing transverse momentum is defined as the negative vectorial sum of all fully calibrated objects including electrons, muons and jets within $|\eta| < 4.5$. The actual E_T selection will depend upon the control/signal region at hand.

Table 5.IV presents an overview of the selections imposed on the 4 main objects in this analysis.

Selection	Electrons	Muons	Jets	E_T^{miss}
Transverse momentum	> 25 GeV	> 25 GeV	> 25 GeV	N.A.
Pseudo-rapidity	$|\eta| < 2.47$ remove $1.37 < |\eta| < 1.52$	$|\eta| < 2.4$	$|\eta| < 4.5$	Using cells up to $|\eta| < 4.5$
Quality	`medium++` NC channel `tight++` CC channel	Track Quality*	Not *bad* JVF > 0.75	No *bad* jets present
Isolation	$\frac{E_T^{\not{e}}}{E_T^{e}} < 0.1$ in $\Delta R \leq 0.2$	$\frac{\not{\mu}}{p_T^{\mu}} < 0.1$ in $\Delta R \leq 0.2$	N.A.	N.A.

* See table 5.III for details.

Table 5.IV: Synthesis of the object selections.

5.4.5　MALFUNCTIONING CRATE IN THE LAr EM CALORIMETER

A crate controller dedicated to outputting cell voltage measurements in the region defined by $0 < \eta < 1.4$ and $-0.8 < \phi < -0.5$ malfunctioned during a portion of the 2011 data. If a jet fell within this region with a p_T greater than 25 GeV in MC or $25\frac{1-c_{\mathrm{JET}}}{1-c_{\mathrm{CELL}}}$ in data, the event was vetoed. c_{JET} and c_{CELL} are calibration correction factors at jet and cell level respectively. For MC, a random run number generator simulated this on the appropriate portion of integrated luminosity.

5.5　EVENT SELECTIONS AND CONTROL REGION DEFINITION

5.5.1　MISSING p_z DEFINITION

As equation (5.4) demonstrates, the missing p_z of an event with a leptonically decaying W boson can be determined up to a sign. Several methods can be used to choose this undetermined sign, however two simple choices were tested to see which one outperformed the other. The two choices being the solution that minimized either

1. $|p_z|$, or

2. $\Delta\eta(W, j_{\mathrm{lead}})$,

where j_{lead} is the highest p_T jet. Using the D-type VLQ signal samples listed in table VI.II, the Root Mean Square (RMS) of the (Truth $-$ Reconstructed) VLQ mass in GeV is presented in table 5.V. Lastly, in the case the solution is imaginary, only the real part is kept.

Truth here refers simply to the VLQ mass at generator level. What can be easily deduced from the table is that, for all masses, the RMS of (Truth $-$ Reconstructed) using $\min(\Delta\eta(W, j_{\mathrm{lead}}))$ performs better than $\min(|p_z|)$ and shall therefore be used throughout.

5.5.2　BASELINE CC CHANNEL EVENT SELECTION

Prior to any sensitivity optimization, the following selections were applied upon events with at least one well-reconstructed electron.

1. $E_T^{\mathrm{miss}} > 50\,\mathrm{GeV}$

Signal Mass GeV	RMS of Truth - Reconstruction $m(\text{VLQ})$	
	$\min(\lvert p_z \rvert)$ solution	$\min(\Delta\eta(W, j_{\text{lead}}))$ solution
400	166.7 ± 3.1	166.6 ± 3.1
500	129.0 ± 2.1	128.5 ± 2.1
600	120.1 ± 1.8	117.8 ± 1.8
700	122.7 ± 1.8	121.9 ± 1.7
800	119.4 ± 1.7	117.5 ± 1.6
900	133.2 ± 1.8	129.7 ± 1.7
1000	132.2 ± 1.8	130.0 ± 1.7
1100	151.2 ± 2.0	148.6 ± 1.9
1200	161.6 ± 2.1	158.3 ± 2.0
1300	175.0 ± 2.2	172.9 ± 2.2
1400	188.4 ± 2.4	186.2 ± 2.4
1500	194.4 ± 2.5	191.0 ± 2.4
1600	211.9 ± 2.7	208.4 ± 2.6
1700	210.1 ± 2.6	207.8 ± 2.6
1800	230.7 ± 2.9	229.1 ± 2.9
1900	230.4 ± 2.9	228.4 ± 2.9
2000	246.8 ± 3.1	245.2 ± 3.1

Table 5.V: Comparison of the RMS of $(\text{Truth} - \text{Reconstructed})$ VLQ mass using either the missing p_z solution that minimizes $\lvert p_z \rvert$ or $\Delta\eta(W, j_{\text{lead}})$.

2. $N_{\text{jets}} > 2$

3. $m_T(\ell, \nu) > 40 \text{ GeV}$

4. $p_T(\text{leading jet}) > 60 \text{ GeV}$

5. $\lvert \Delta\eta(\ell, \nu) \rvert < 2.5$

Each of these selections serves a purpose in diminishing some of the background contributions. An E_T^{miss} greater than 50 GeV greatly reduces the contribution from the multijet background although an exact measure of how much shall be determined in section 5.6. The same goes for a transverse mass of the candidate W, which if reconstructed by lepton fakes and mis-measured E_T^{miss} will less likely produce values near the mass of the W. The minimum 60 GeV selection upon the leading jet p_T effectively reduces contributions

from the dominant background W+jets. Finally, the angular selection on the $\Delta\eta(\ell, \nu)$ in essence requires the W to be slightly boosted, again reducing the W+jet contribution.

All of these selections were chosen qualitatively after verifying that the signal efficiencies remained high (above 90% for a 600 GeV signal), except for the W transverse mass selection which was recommended by the EW vector-boson ATLAS working group [182] (ATLAS internal).

5.5.3 BASELINE NC CHANNEL EVENT SELECTION

Prior once again to any sensitivity optimization, the following selections were assigned to events with exactly 2 oppositely charged same flavour electrons or muons

1. $|m_Z - m_{(\ell, \ell)}| < 25$ GeV, and

2. $N_{\text{jets}} > 2$.

Having such a candidate Z boson significantly reduces most backgrounds except the irreducible Z+jets and reducible diboson backgrounds.

5.5.4 PILE-UP REWEIGHTING

An essential aspect needed to be verified is the pile-up reweighting of the MC backgrounds to match the pile-up conditions found in the data. The two distributions of interest are therefore $\langle\mu\rangle$ and N_{vertex}, and are given in figure 5.2. The systematics uncertainties given by the yellow bands in figure 5.2 are dominated by JES uncertainties (more on this in section 5.8), while the multijet background was estimated by means of data-driven techniques as explained in the next section.

5.6 MULTIJET BACKGROUND ESTIMATION

The multijet background is of critical importance in the CC channel due to its extremely large cross section and its potential to fake lepton signatures. However, given the relatively tight selection criteria on electrons and muons, such mis-identified jets occur infrequently and in turn render their modelling very difficult. Therefore, data-driven
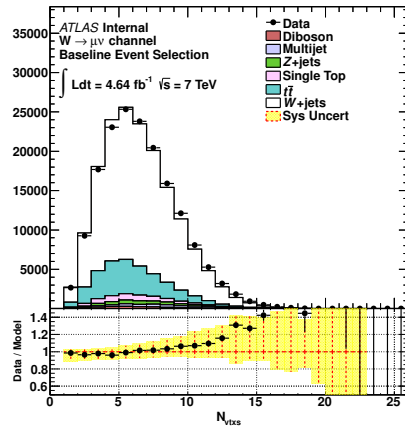
(a) N_{vertex} in CC channel
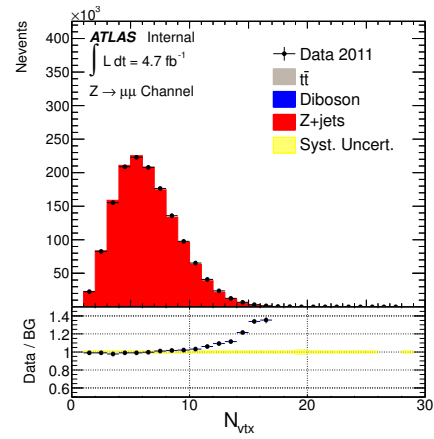
(b) N_{vertex} in NC channel
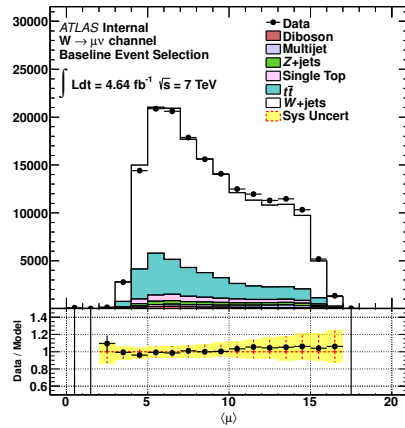
(c) $\langle \mu \rangle$ in CC channel
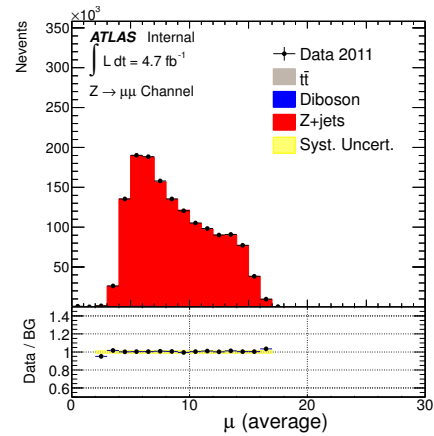
(d) $\langle \mu \rangle$ in NC channel

Figure 5.2: After pile-up reweighting (Procedure explained in the text), the $\langle \mu \rangle$ and N_{vertex} distributions in MC are compared to the data. The multijet background was computed as explained in section 5.6. The good agreement provides confidence in the handling of data pile-up conditions.

techniques are necessary to estimate the multijet background contributions. In the case of $W \to e\nu$ events, light-flavour hadron sources, such as charged pions, are expected to be the dominant source of fake electrons with heavy-flavour decays contributing significantly less. This being the case, the construction of a multijet template from data is done by reducing the quality requirement upon the electron. Such electrons are therefore required to pass the `medium++` but **not** `tight++` quality definitions (to produce a sample completely orthogonal to our nominal event selection as defined in 5.5.2). Requiring $m_T(W) > 40$ GeV, the three E_T^{miss} distributions constructed with

1. Data $\to$ `tight++` electrons

2. Data multijet template $\to$ `medium++` and **not** `tight++` electrons (Data Template)

3. MC background $\to$ `tight++` electrons in simulated W+jets, $t\bar{t}$, Z+jets, dibosons, and single top quark events. (Real Background Lepton)

are fitted in the range $5 < E_T^{\text{miss}} < 100$ GeV with two floating parameters: the normalization of the multijet template, and the normalization of the MC background. These two distributions, (2) and (3), are fitted to the data distribution (1) by minimizing the standard χ^2 value. In the electron channel, the fit is executed in 4 distinct selection regions. Motivated by the fact that the pile-up conditions are different in the EM barrel versus the EM end-cap calorimeters, the two η regions $|\eta| < 1.9$ and $|\eta| \geq 1.9$ are considered. Additionally, the two regions defined by $N_{\text{jets}} = 2$ and $N_{\text{jets}} \geq 3$ are examined separately. Once the fits completed in each of these regions, the fraction of multijet events can be extracted and are given in figures 5.3. This fraction is directly related to the overall normalization w_{multijet} used to appropriately scale the multijet templates and is given by

$$w_{\text{multijet}} = \frac{f N_{\text{data}}}{N_{\text{multijet}}}, \tag{5.5}$$

where N_{multijet} and N_{data} are the integrated number of events in the multijet template and the data respectively. The resulting f is shown in figure 5.3.

(a) 3 jets : $|\eta_e| < 1.9$

(b) 2 jets : $|\eta_e| < 1.9$

(c) 3 jets : $|\eta_e| \geq 1.9$

(d) 2 jets : $|\eta_e| \geq 1.9$
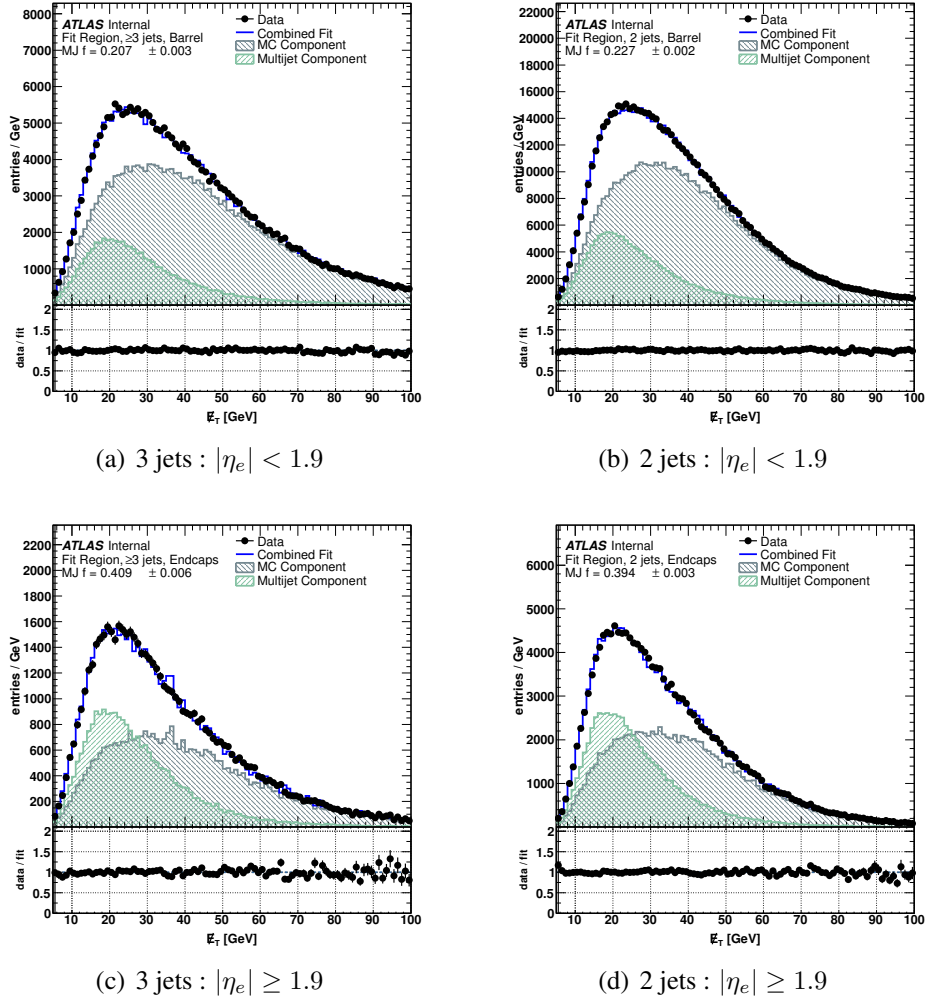
Figure 5.3: E_T^{miss} distribution comparisons between the data and the combined fit of the MC component and multijet (or QCD) component in the electron channel as explained in the text. The fraction of multijet events, *MJ f*, are listed the legends. The fits are performed in four distinct regions, defined by their number of jets, 2 or ≥ 3, and whether the electron in the event was reconstructed in the EM barrel ($|\eta| < 1.9$) or in the EM end-cap ($|\eta| \geq 1.9$).

In the muon channel, the multijet template is built by reversing the isolation requirement. Hence, the requirement becomes

$$0.1 < \frac{p_T^{\not\mu}}{p_T^\mu} < 0.2. \tag{5.6}$$

In this case, and contrary to the electron channel, heavy-flavour decays are expected to be the dominant source of muon fakes. Processes such as $b \to W^*(\mu\nu)c$ produce real muons, and in some sense form an irreducible background. These are different from W+jets events because heavy-decays do not produce on-shell W. Once the necessary distributions are at hand, the fitting procedure proceeds identically as in the electron channel and minimizes the χ^2 value in the two regions with $N_{\text{jets}} = 2$ and $N_{\text{jets}} \geq 3$. The results of the fitting and the extracted multijet fraction f are presented in figure 5.4.

(a) 2 jets   (b) 3 jets
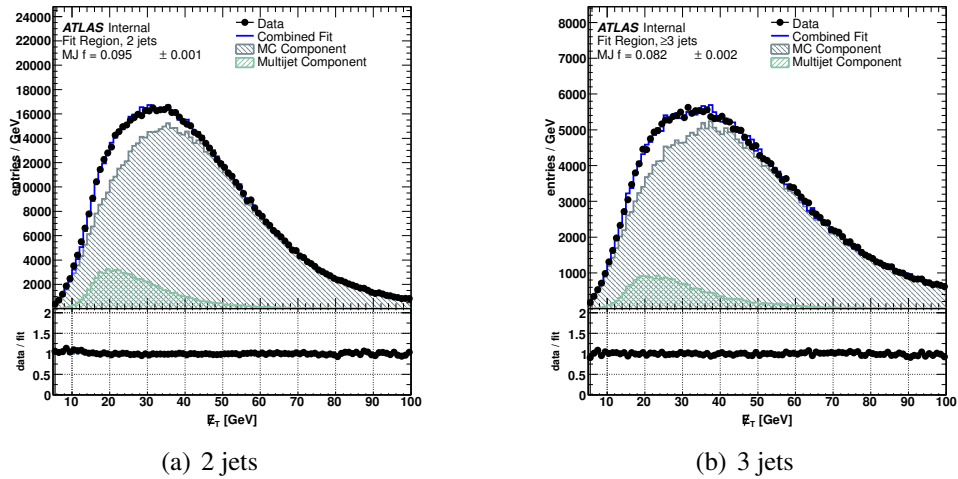
Figure 5.4: E_T^{miss} distribution comparisons between the data and the combined fit of the MC component and multijet (or QCD) component in the muon channel as explained in the text. The fraction of multijet events, *MJ f*, are listed the legends. The fits are performed in two distinct regions, one with exactly 2, and the other with 3 or more jets.

These multijet templates with their obtained scalings shall be used in predicting the contributions from mis-identified jets in the CR and SR. Note however that they shall not be used in the signal optimization procedure outlined in the next section where the main objective was to enhance the sensitivity with respect to the W/Z+jet background.

5.7 SIGNAL TOPOLOGY AND EXTRACTION

The single production of VLQ creates prominent signal characteristics which are drawn schematically in figure 5.5. These features include back-to-back EW vector-
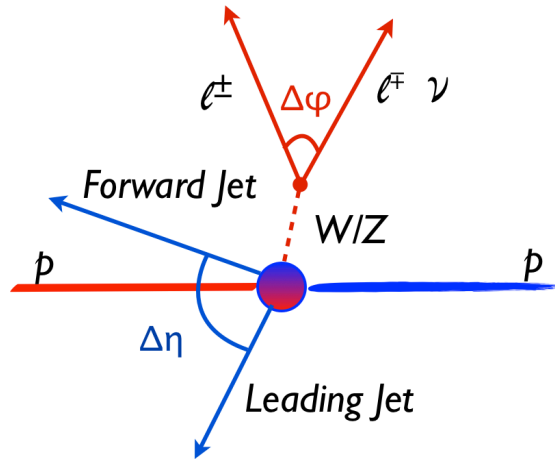
Figure 5.5: Heuristic view of a typical signal event that includes a high p_T EW vector-bosons with opposite to it, a hard p_T leading jet, and also a forward jet in the relatively high $|\eta|$ region of the detector. The $\Delta\eta$ and $\Delta\phi$ are examples of the angular variables chosen in the optimization process.

bosons with large p_T jets, and the presence of a forward jet with relatively high $|\eta|$.

Two distinct optimization techniques were probed in an attempt to increase the sensitivity by determining which one outperformed the other in extracting signal from background. The ROOT based analysis toolkit called TMVA [12] (Toolkit for Multivariate Data Analysis with ROOT) was used to execute these tasks.

The first optimization technique included the use of boosted decision trees (BDT) that provides a single variable to select upon, called the *classifier*. In brief, it is a series of interdependent square selections, and depending on where a given event ends up in the tree, a single classifier value is assigned to it. Figure 5.6 displays how this BDT technique operates. At each node (or each step), a single variable selection separates the *tree* into two distinct regions, after which the subsequent selections become completely and intently independent. In additions, at each step the variable with greatest

separation power [8] is chosen. Knowing the original input type, signal or background,
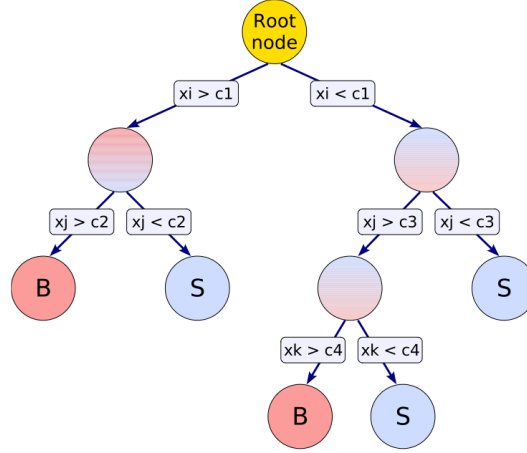
Figure 5.6: A three variable example of the inner-workings of a BDT. At the first step (node), variable xi is selected on : $xi <$ or $> c1$. Then, at step 2, variable xj is selected upon with selection values that differ depending on the outcome of the first selection [12].

the training of the BDT proceeds by assigning weights to events that were incorrectly separated. This re-shapes or *boosts* the input variable distributions which in turn modifies and ideally optimizes the selection values. Although demonstrably inferior to neural network techniques in performance, BDT have the advantage of requiring little tuning for it to perform optimally. Furthermore, neural networks offer no insight as to how they arrive at extracting the signal (black box) whereas with BDT, it is possible to trace back the selections that a given event either passed or failed. This is of consequence when propagating systematics.

The second technique evaluated was a simple optimization of rectangular selections or *cuts*. For a given signal efficiency, the selections were optimized by maximizing the background rejection rate, a procedure that was repeated for all signal efficiencies in steps of 0.01. Knowing the signal cross section then enables one to select the signal efficiency that optimizes $S/\sqrt{S + B}$.

In order to avoid as much as possible the use of variables that are very correlated to the VLQ invariant mass, only angular variables were used as they are generally less

8. Quantitatively, the **separation** $\langle S \rangle^2$ of a variable x is given by $\langle S \rangle^2 = \int \frac{(S(x) - B(x))^2}{S(x) + B(x)} dx$ [12].

correlated with $m(\text{VLQ})$. Variables such as the p_T of the leading jet, for example, are heavily correlated to the VLQ mass and would therefore be of little help in separating signal from background.

The chosen angular variables were therefore, in the CC channel:

CC.1 $\Delta\eta(W, j_{\text{lead.}})$

CC.2 $\Delta\eta(W, j_{\text{ass.}})$

CC.3 $\Delta\phi(\ell, E_T^{\text{miss}})$

CC.4 $\Delta\phi(W, j_{\text{lead.}})$

CC.5 $\Delta\eta(j_{\text{lead.}}, j_{\text{ass.}})$,

and for the NC channel they were:

NC.1 $\Delta\phi(\ell\ell)$

NC.2 $\Delta\eta(\ell\ell)$

NC.3 $\Delta\phi(Z, j_{\text{lead.}})$

NC.4 $\Delta\eta(Z, j_{\text{lead.}})$

NC.5 $\Delta\eta(Z, j_{\text{ass.}})$

NC.6 $\Delta\eta(j_{\text{lead.}}, j_{\text{ass.}})$,

where the associated jet $j_{ass.}$ is defined as the one farthest from the leading jet in η.

Before the training of the two optimizations can proceed, two facts need to be verified. First, the angular variables amongst themselves must not be too correlated in background events, otherwise their simultaneous use is counterproductive yielding no extra separation power. Second, and more importantly, the MC simulations of the EW backgrounds must adequately model what is found in the data after the baseline selections of section 5.5.2 and 5.5.3.

5.7.0.1 ANGULAR VARIABLE MODELLING

The angular variables CC.1 to CC.5 and NC.1 to NC.6 are known to be difficult to model given their sensitive dependence on higher order effects. In fact, we do not expect the MC to model the background perfectly given that our dominant background is modelled by ALPGEN, a multi-leg leading order LO* generator (with multiple final state partons, but no loop diagrams). However, adequate modelling is enough to motivate

and validate the training and use of MVA techniques because the final results shall be interpreted through a bump hunting method that is independent of MC background modelling. In other words, a perfect modelling of the background would improve the signal sensitivity (as it is fed through the multivariate analysis) and prediction thereof.

Figures 5.7 and 5.8 exhibit the CC channel's distributions in the electron and muon channel for each of the 5 angular variables.

(a) $\Delta\eta(j_{\text{lead}}, j_{\text{ass.}})$ (b) $\Delta\eta(W, j_{\text{ass.}})$ (c) $\Delta\eta(W, j_{\text{lead}})$

(d) $\Delta\phi(\ell, E_T^{\text{miss}})$ (e) $\Delta\phi(W, j_{\text{lead}})$
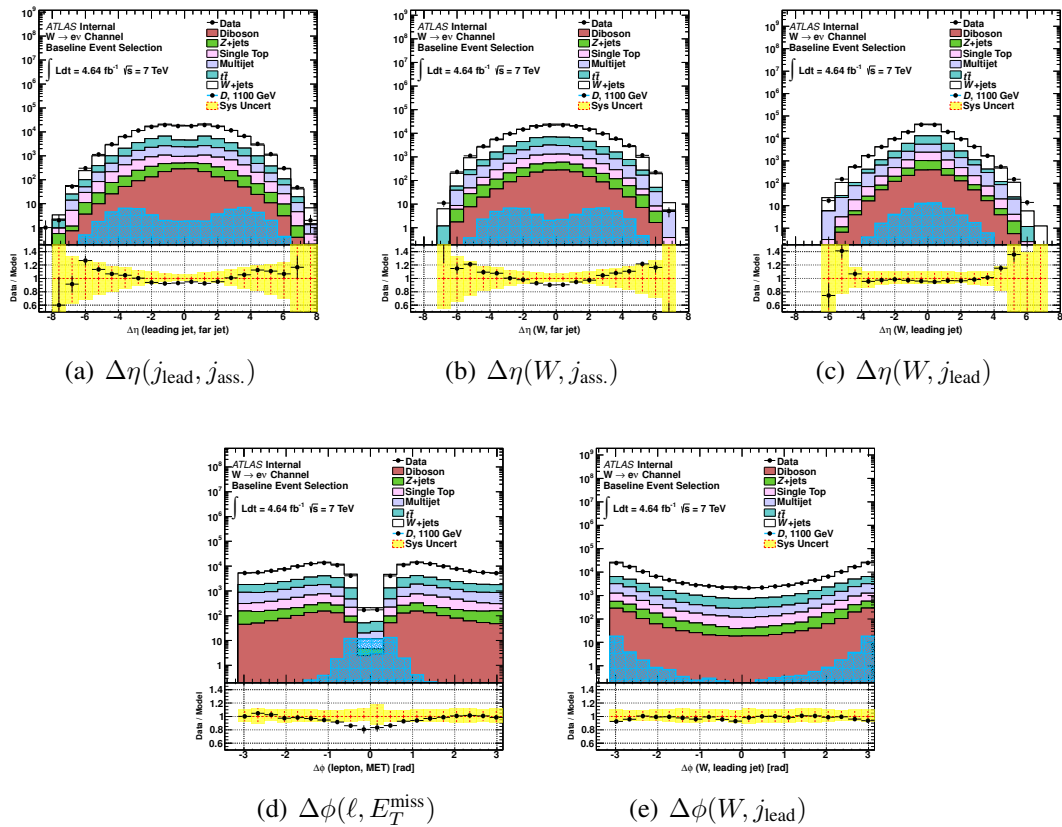
Figure 5.7: Data versus MC comparison of the angular variables used in the CC electron channel. Yellow bands are the combined statistical and systematic uncertainties of the MC.

Similarly, figures 5.9 and 5.10 show the data versus MC distribution for the 6 angular variables used for the signal selection optimization in the NC channel.

Each of the angular distributions show reasonable agreement between data and MC, at least within statistical and systematic uncertainties shown by the yellow bands.

112

(a) $\Delta\eta(j_{\text{lead}}, j_{\text{ass.}})$ (b) $\Delta\eta(W, j_{\text{ass.}})$ (c) $\Delta\eta(W, j_{\text{lead}})$

(d) $\Delta\phi(\ell, E_T^{\text{miss}})$ (e) $\Delta\phi(W, j_{\text{lead}})$
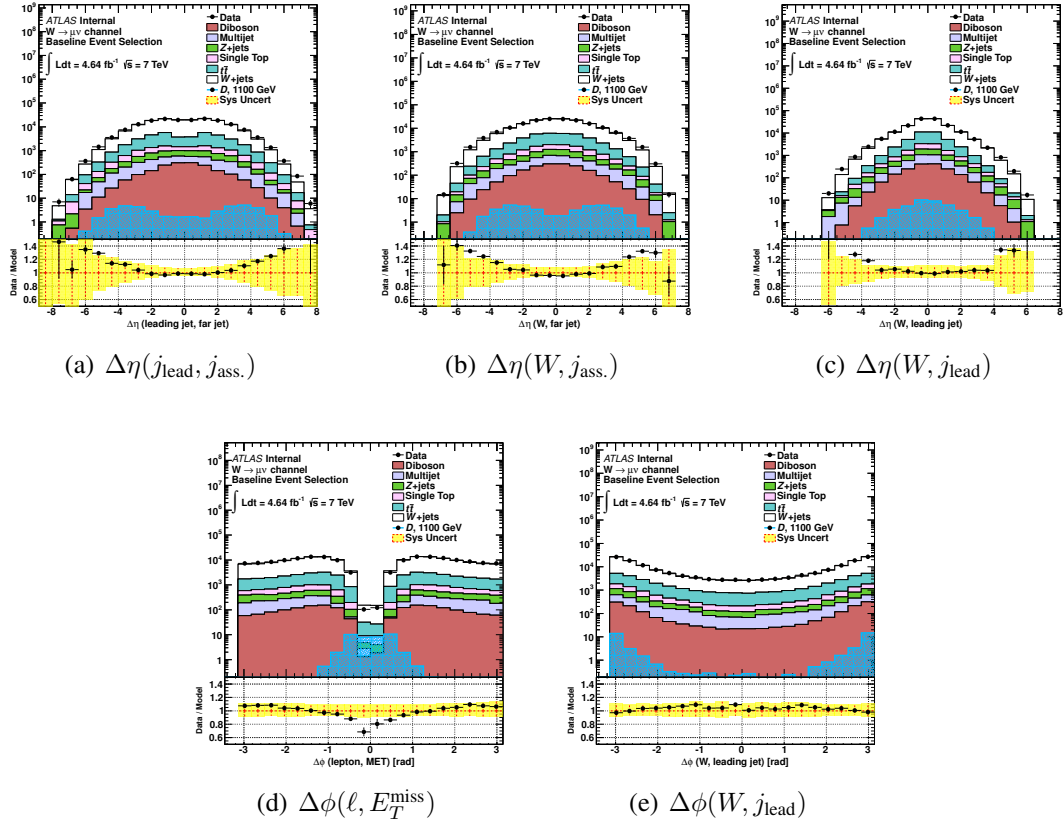
Figure 5.8: Data versus MC comparison of the angular variables used in the CC muon channel. Yellow bands are the combined statistical and systematic uncertainties of the MC.

5.7.0.2 ANGULAR VARIABLE CORRELATIONS

The use of correlated variables in a cut optimization procedure can easily lead to an inefficient optimization. Therefore, it is important to verify that the correlations that do exist between the angular variables are not significant such that they can be safely used as inputs to the selection optimization. The linear correlation matrices are presented for the input variables in the CC and NC channels in figure 5.11 and 5.12, where we find that, at least to leading order, the correlations in the background, which include W/Z+jets, $t\bar{t}$, diboson, and single top quark, are not substantial, that is below 0.35. Expectedly however, in signal, the correlations are more significant. Of course, there may be important hidden non-linear correlations, but such effects can safely be neglected

(a) $\Delta\eta(j_{\text{lead}}, j_{\text{ass.}})$ (b) $\Delta\eta(\ell, \ell)$ (c) $\Delta\eta(Z, j_{\text{lead}})$

(d) $\Delta\eta(Z, j_{\text{ass.}})$ (e) $\Delta\phi(\ell, \ell)$ (f) $\Delta\phi(Z, j_{\text{lead}})$
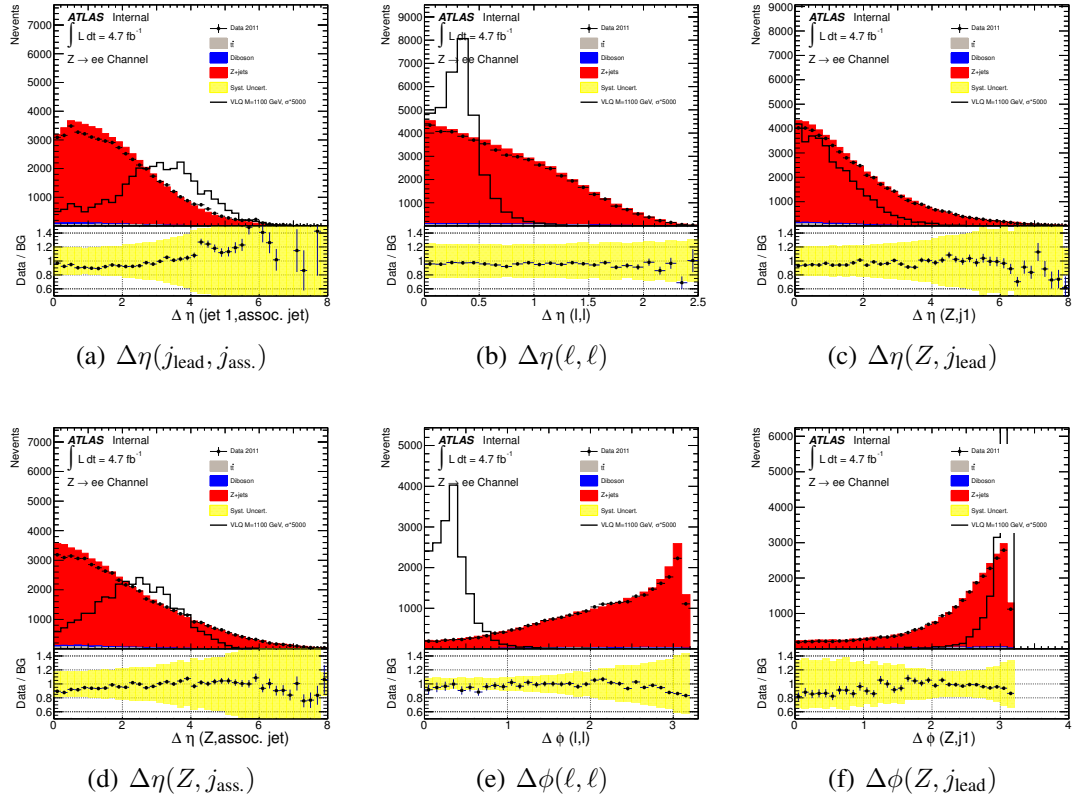
Figure 5.9: Data versus MC comparison of the angular variables used in the NC electron channel. Yellow bands are the combined statistical and systematic uncertainties of the MC.

as long as the BDT is not overtrained.

Overtraining of the BDT is a known issue that is often overlooked. It occurs when the BDT becomes sensitive to statistical fluctuations within the signal and backgrounds samples. To make certain this was not the case, the distributions before and after were verified to be comparable, thus indicating overtraining was avoided.

5.7.1 MULTIVARIATE ANALYSIS RESULTS

The BDT was trained in three different signal mass regions: low, medium and high mass. The mass ranges were $[400, 800]$, $[900, 1200]$, and $[1200, \infty[$ GeV, such that the 400, 900, and 1200 GeV mass points were selected for the training of the BDT and
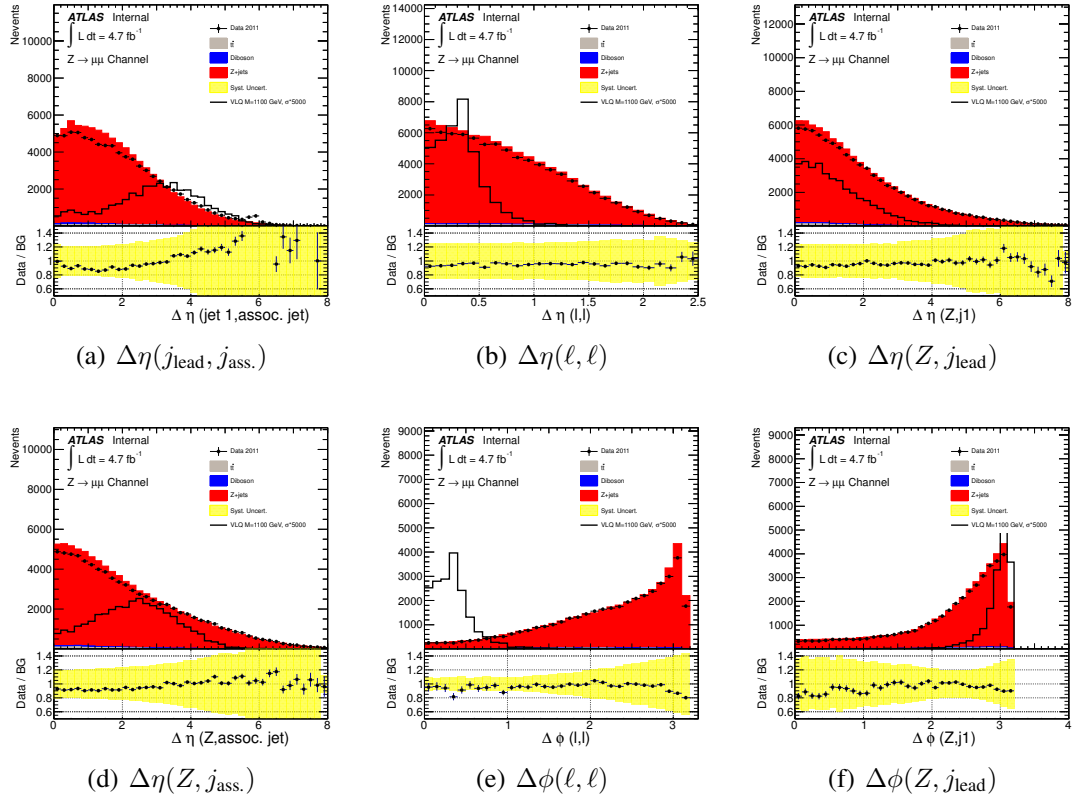
Figure 5.10: Data versus MC comparison of the angular variables used in the NC muon channel. Yellow bands are the combined statistical and systematic uncertainties of the MC.

produced the selections for the mass ranges above them. The mass ranges were chosen in anticipation of the VLQ mass limit and to simplify the analysis.

Furthermore, both techniques, the BDT and rectangular cuts were tested using the same mass ranges. The obtained sensitivity $S/\sqrt{S+B}$ for each of these methods are summarized in Table 5.VI. When comparing the sensitivity achieved with the BDT selection to rectangular selections optimized for the sensitivity $S/\sqrt{S+B}$ using the TMVA rectangular cut optimization method in the CC channel, it was found that the sensitivities attained were roughly equal.

In addition, when evaluating the expected sensitivity in these signal regions it was found that there was no large gain in sensitivity at high mass using the optimization with a 900 or a 1200 GeV signal versus a 400 GeV signal. With this in mind, the final

(a) Signal
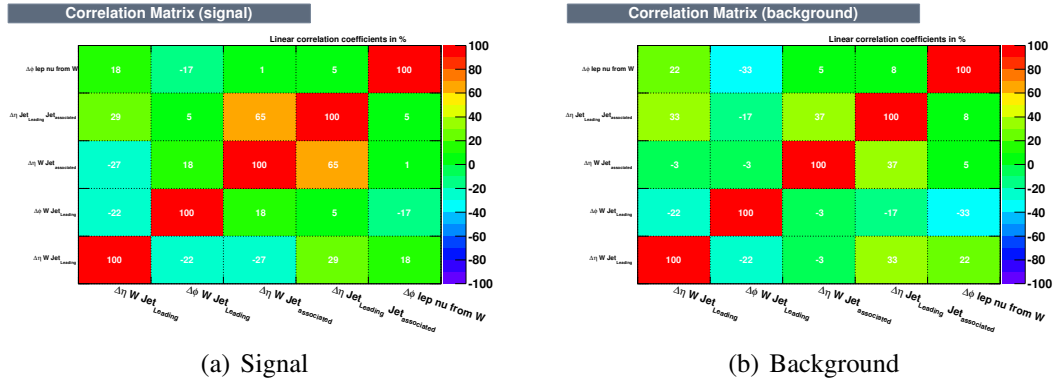
(b) Background

Figure 5.11: After applying the baseline selections, presented here are the linear correlations between the angular variables in signal and background in the CC channel. Expectedly, the correlation are greater in signal than in background. Values obtained with TMVA [12].

Training Mass	Signal Points [GeV]	BDT Significance	Rectangular Cuts Significance
400	400-800	25.1	25.0
900	900-1100	5.2	5.8
1200	1200-2000	2.5	2.6

Table 5.VI: Signal significance calculated by counting events of signal and background and comparing $S/\sqrt{S+B}$ in the SR for each of the training masses in the low, medium, and high mass signal regions.

selections were chosen to be a set of 5 (6) rectangular cuts in the CC (NC) channels, optimized using only the 400 GeV signal.

This simplifies the analysis dramatically without hindering on its reach. In the CC channel, after the baseline selections, the following SR selections were thus obtained:

- $\Delta\eta(W, j_{\text{lead.}}) < 2.3$
- $\Delta\eta(W, j_{\text{ass.}}) > 1.6$
- $\Delta\phi(\ell, E_T^{\text{miss}}) < 1.3$ rad
- $\Delta\phi(W, j_{\text{lead.}}) > 2.1$ rad
- $\Delta\eta(j_{\text{lead.}}, j_{\text{ass.}}) > 1.3$,

and for the NC channel they were:

(a) Signal
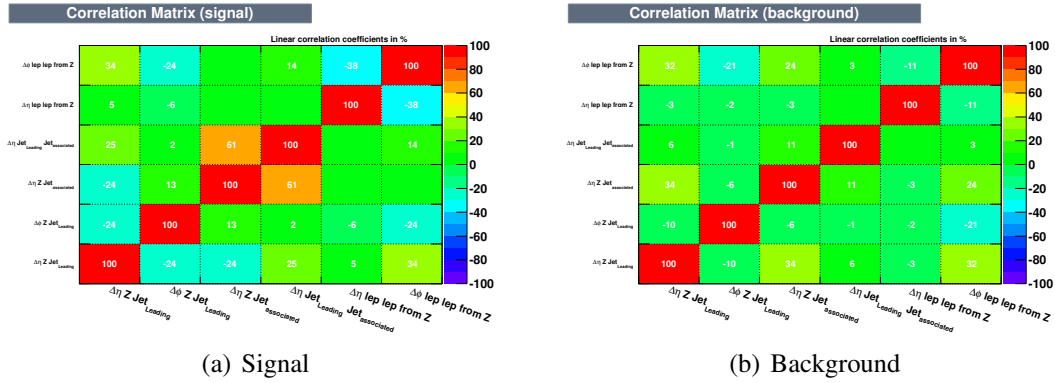
(b) Background

Figure 5.12: Linear correlations between the angular variables in signal and background after the baseline selections in the NC channel. Again expectedly, the correlation are greater in signal than in background. Values obtained with TMVA [12].

- $\Delta\phi(\ell\ell) < 1.5$ rad
- $\Delta\eta(\ell\ell) < 1.6$
- $\Delta\phi(Z, j_{\text{lead.}}) > 2.1$ rad
- $\Delta\eta(Z, j_{\text{lead.}}) < 1.1$
- $\Delta\eta(Z, j_{\text{ass.}}) > 0.9$
- $\Delta\eta(j_{\text{lead.}}, j_{\text{ass.}}) > 0.9$.

5.7.2 CONTROL REGIONS

Inverting the SR $\Delta\phi(\ell, E_T^{\text{miss}})$ selection:

- $\Delta\phi(\ell, E_T^{\text{miss}}) \geq 1.3$ rad

defines an orthogonal region of phase space that is shown in figure 5.13.

Very similarly, by inverting the $\Delta\phi(\ell, \ell)$ selection in the NC channel:

- $\Delta\phi(\ell, \ell) \geq 1.5$ rad

procures a CR for backgrounds in the NC channels. These are presented in figure 5.14.

Despite the acceptable agreement between data and MC, one must keep in mind that the SR shall be interpreted through the use of a functional form fitting the background and not by the combined use of MC and DD predictions of the background.

(a) electron   (b) muon
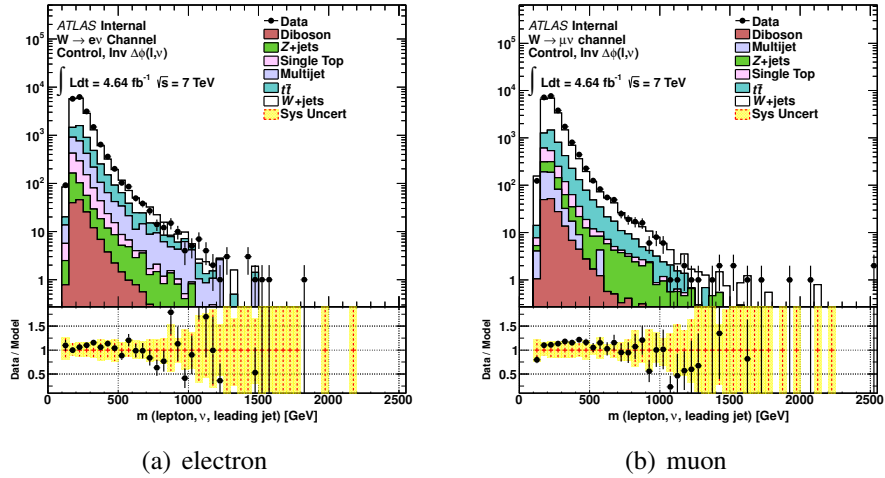
Figure 5.13: Reconstructed VLQ mass in the CC channel control region as defined in the text for both the electron (left) and muon (right) channels. The yellow bands indicate the combined statistical and systematic uncertainties.

(a) electron   (b) muon
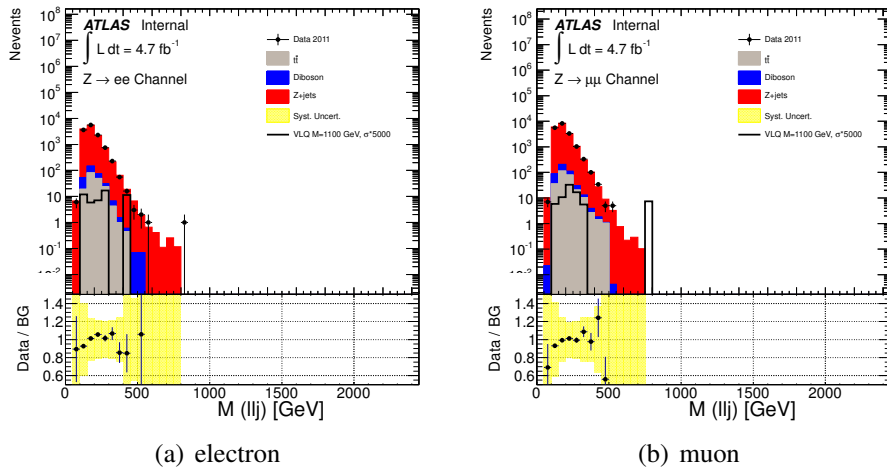
Figure 5.14: Reconstructed VLQ mass in the NC channel control region as defined in the text for both the electron (left) and muon (right) channels. The yellow bands indicate the combined statistical and systematic uncertainties.

5.8 SYSTEMATIC UNCERTAINTIES

The systematic uncertainties affecting the backgrounds are of second order in importance given our bump hunting search strategy. Therefore, systematic uncertainties from MC signal VLQ shall be the focus of this section.

Beginning with object and trigger systematics provided by the performance tools listed in section 5.4, these are tabulated in 5.VII for the electron channel and 5.VIII for the muon channel for a selected set of signal masses.

The tables illustrate that statistical uncertainties are on par with the dominant systematic JES. Trigger efficiency is very near one with negligible uncertainty in the NC channel. Lepton energy resolution is important in the CC channel, but not in the NC channel because in the CC channel, the missing p_z measurement is very sensitive to lepton resolution on a same footing as LES. Figures 5.15 and 5.16 present along with the normalization uncertainties, the visible shape uncertainties associated to the dominant systematics in the CC and NC channels respectively. The statistical uncertainties are shown by the yellow bands in 5.15.   These figures illustrate the relatively large

(a) electron   (b) muon
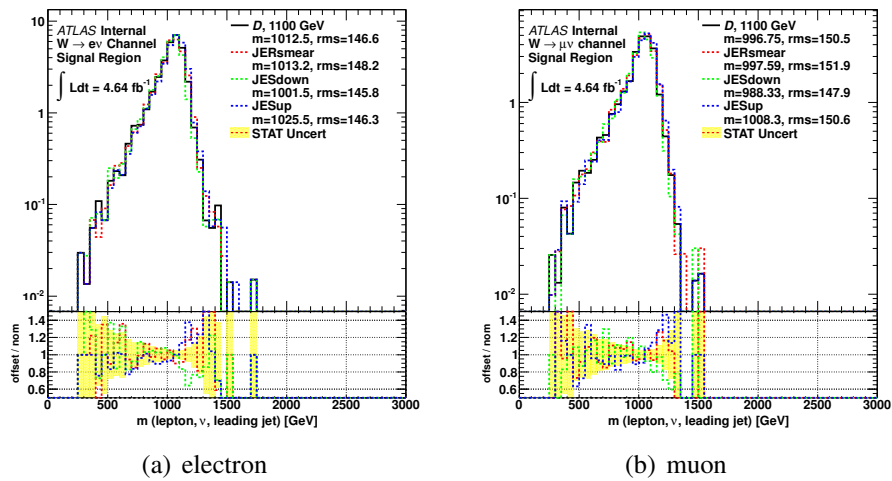
Figure 5.15: Nominal signal hypothesis (CC) of a 1.1 TeV VLQ compared with its JES and JER systematic variations. The yellow bands in the ratio plots indicate statistical uncertainties only.

shape alterations induced by variations in JES. The shape differences are handled as

Charged-Current Channel

Signal Mass	Total Expected Yield ± Combined Uncertainty	Statistics	JES	JER	EES	EER	Reconstruction Efficiency
400	1584 ± 94	±45	±79	±12	±1.7	±5.4	±18
700	258 ± 10	±5.8	±7.9	±0.79	±0.17	±0.52	±2.5
900	88.9 ± 3.6	±2.9	±0.21	±0.18	±0.079	±0.52	±1.1
1200	21.43 ± 0.84	±0.44	±0.66	±0.026	±0.12	±0.12	±0.22
1800	1.685 ± 0.074	±0.034	±0.063	±0.0056	±0.0065	±0.0065	±0.0098

Neutral-Current Channel

Signal Mass	Total Expected Yield ± Combined Uncertainty	Statistics	JES	JER	EES	Reconstruction Efficiency
400	381 ± 23	±17	±15	±1.9	±0.8	±4
700	82.0 ± 4.5	±3.3	±2.9	±0.1	±0.04	±0.8
900	25.0 ± 1.4	±1.0	±0.9	±0.1	±0.02	±0.2
1200	3.20 ± 0.19	±0.14	±0.12	±0.003	±0.005	±0.03
1800	0.140 ± 0.009	±0.006	±0.006	±0.0005	±0.0004	±0.0015

Table 5.VII: Signal systematic uncertainties in the CC and NC channels as a function of mass that are involved in the electron decay channel $Q \to W(e\nu)/Z(ee)$+jet in terms of event counts in the SR.

Charged-Current Channel

Signal Mass	Total Expected Yield ± Combined Uncertainty	Statistics	JES	JER	MES	Reconstruction Efficiency
400	1484 ± 77	±43	±58	±2	±4	±2
700	224 ± 12	±5	±9	±4	±0.4	±0.3
900	69.4 ± 3.9	±1.6	±3.1	±1.1	±0.07	±0.15
1200	15.1 ± 0.7	±0.4	±0.6	±0.17	±0.08	±0.02
1800	1.13 ± 0.06	±0.03	±0.05	±0.004	±0.003	±0.0004

Neutral-Current Channel

Signal Mass	Total Expected Yield ± Combined Uncertainty	Statistics	JES	JER	MES	Reconstruction Efficiency
400	447 ± 28	±21	±18	±5	±0.6	±1.9
700	91.6 ± 4.8	±3.6	±3.2	±0.3	±0.13	±0.3
900	25.8 ± 1.4	±1.1	±0.9	±0.1	±0.008	±0.08
1200	3.08 ± 0.16	±0.12	±0.11	±0.015	±0.006	±0.008
1800	0.180 ± 0.011	±0.008	±0.007	±0.0016	±0.0006	±0.0003

Table 5.VIII: Signal systematic uncertainties in terms of event counts the CC and NC channels as a function of mass that are involved in the muon decay channel $Q \to W(\mu\nu)/Z(\mu\mu)$+jet.

(a) electron   (b) muon
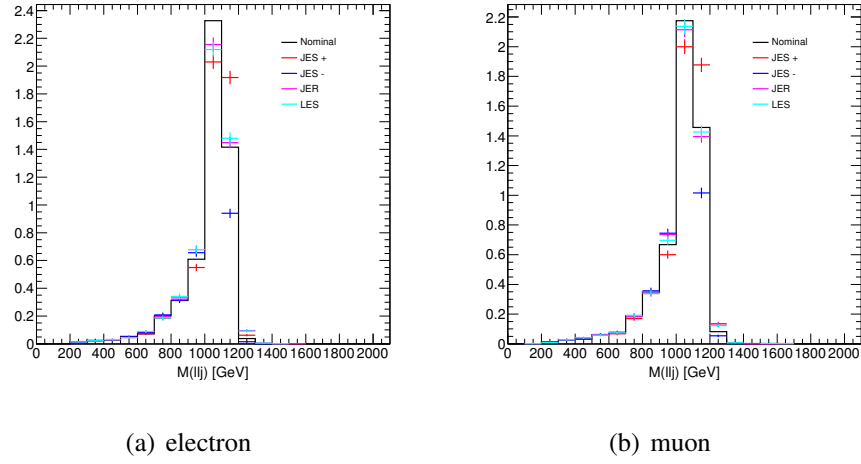
Figure 5.16: Nominal signal hypothesis (NC) of a 1.1 TeV VLQ compared with its JES, JER and LES systematic variations. The uncertainties upon the data points indicate purely statistical uncertainties.

bin-dependent nuisance parameters as explained in III.3.

5.8.1 SIGNAL PDF UNCERTAINTIES

The default parton distribution function (PDF) used in MADGRAPH [177] for simulating the VLQ signals is CTEQ6L1. Unfortunately, the error matrix is not available for this PDF set. To estimate the error on the signal cross section, signals were generated in MADGRAPH with the PDF set CTEQ66 [183] whose Hessian error matrix is known. There are 45 distinct orthogonal PDF eigenvector parameters, each of which is independently fluctuated up and down by one standard deviation leaving all others to their nominal value. We therefore obtain 90 *alternate* cross section values and the total upper (lower) uncertainty is evaluated by adding in quadrature those that increase (decrease) the cross section with respect to the nominal value. In the CC channel, the total uncertainties for a sample of mass points are given in table 5.IX. The calculation required at least one parton with $p_T > 50$ GeV. Likewise, the NC channel PDF uncertainties are summarized in table 5.X. The uncertainties in the CC and NC channels are

PDF set	σ [pb] per signal mass [GeV]				
	300	600	1000	1400	2000
CTEQ66	$16.5^{+0.4}_{-0.5}$	$1.10^{+0.03}_{-0.04}$	$0.0987^{+0.0038}_{0.0045}$	$0.0145^{+0.0007}_{-0.0011}$	$0.00118^{+0.00013}_{-0.00015}$
CTEQ6L1	15.4	1.07	0.101	0.0154	0.00132

Table 5.IX: Uncertainties on the cross section computed using the error matrix of the CTEQ66 [183] PDF. The cross sections include the BR of the VLQ to $D \to \ell\nu u$.

PDF set	σ [pb] per signal mass [GeV]				
	300	600	1000	1400	2000
CTEQ66	$2.46^{+0.09}_{-0.05}$	$0.182^{+0.08}_{-0.004}$	$0.018^{+0.0008}_{-0.0005}$	$0.00292^{+0.00013}_{-0.00012}$	$0.000266^{+0.000013}_{-0.000017}$
CTEQ6L1	2.28	0.178	0.0186	0.00314	0.00031

Table 5.X: Uncertainties on the cross section calculated using the CTEQ66 [183] PDF error matrix. The cross sections include the BR of the VLQ to $U \to \ell\ell u$.

parametrized quadratically by

$$\sigma^{+\left(3.459-(3.827\times10^{-3})m+(3.754\times10^{-6})m^2\right)\%}_{-\left(3.121-(1.156\times10^{-3})m+(2.985\times10^{-6})m^2\right)\%} \quad (CC) \tag{5.7}$$

$$\sigma^{+\left(3.459+(1.190\times10^{-3})m+(2.64\times10^{-7})m^2\right)\%}_{-\left(2.012-(4.539\times10^{-4})m+(1.33\times10^{-6})m^2\right)\%} \quad (NC) \tag{5.8}$$

where m is the signal mass. This error shall be included in the theory cross section curves but shall *not* come into the calculation of the expected or observed limits.

Lastly, possible shape uncertainties are evaluated by comparing the signal shapes of CTEQ66 and CTEQ6L1. Figure 5.17 illustrates the results, showing that the shape differences are negligible. These were therefore ignored during the cross section limit calculations.

5.8.2 INITIAL AND FINAL STATE RADIATION UNCERTAINTIES

Initial and final state radiation (ISR and FSR) uncertainties are of potential significance as they can affect the signal's kinematics thereby affecting the signal's acceptance. To estimate them, a set of PYTHIA parameters, which are listed in table 5.XI, are modified.

(a) 600 GeV VLQ   (b) 1000 GeV VLQ
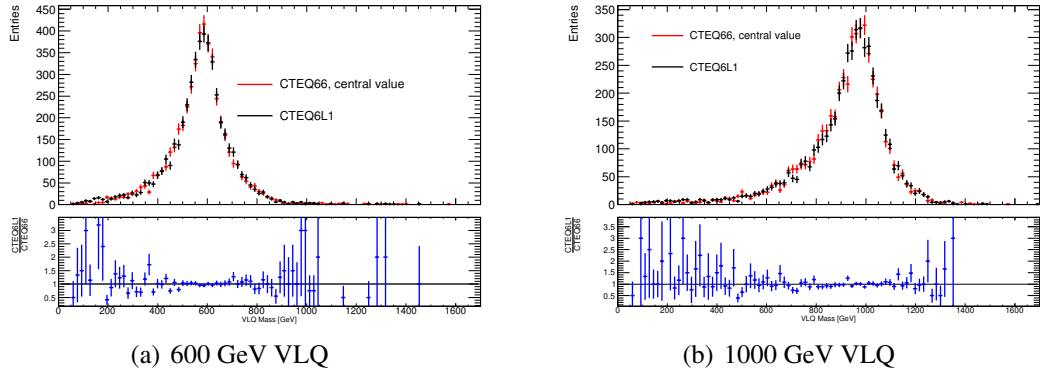
Figure 5.17: Shape comparisons between the PDF CTEQ6L1 and CTEQ66 (generated with ATLAS Fast Simulation) in the CC channel for the 600 and 1000 GeV signal masses. Similar results are found for other mass points and in the NC channel. Both signals are normalized to an identical (arbitrary) number of entries.

Parameter Description	Value		
	Nominal	ISR up	ISR down
Modifies ISR α_s evolution scale	1	0.25	4
Is the maximum parton virtuality within ISR showers	4	6	0.5
Parameter Description	Nominal	FSR up	FSR down
Controls the running of α_s in the parton shower	0.192	0.384	0.0196
IR cut-off scale in FSR parton branching	1	0.5	2

Table 5.XI: Set of PYTHIA parameters [127] used to estimate ISR and FSR uncertainties.

The acceptances were then compared and were found to be of order $\sim 1\%$. The differences in shape however were found to be negligible as seen in figure 5.18 for the two mass points 600 and 1000 GeV in the CC channel. A similar behaviour is observed in the NC channel as well as for all other signal resonance masses.

5.8.3 QCD SCALE UNCERTAINTY

Factorization and renormalization (F&R) scale uncertainties were computed by varying the F&R scale μ around its nominal value. The customary procedure of dividing and multiplying μ by 2 was used to estimate this uncertainty and the obtained variations in the cross sections are tabulated in 5.XII. The QCD scale uncertainty is evidently mass

(a) ISR 600 GeV VLQ   (b) ISR 1000 GeV VLQ

(c) FSR 600 GeV VLQ   (d) FSR 1000 GeV VLQ
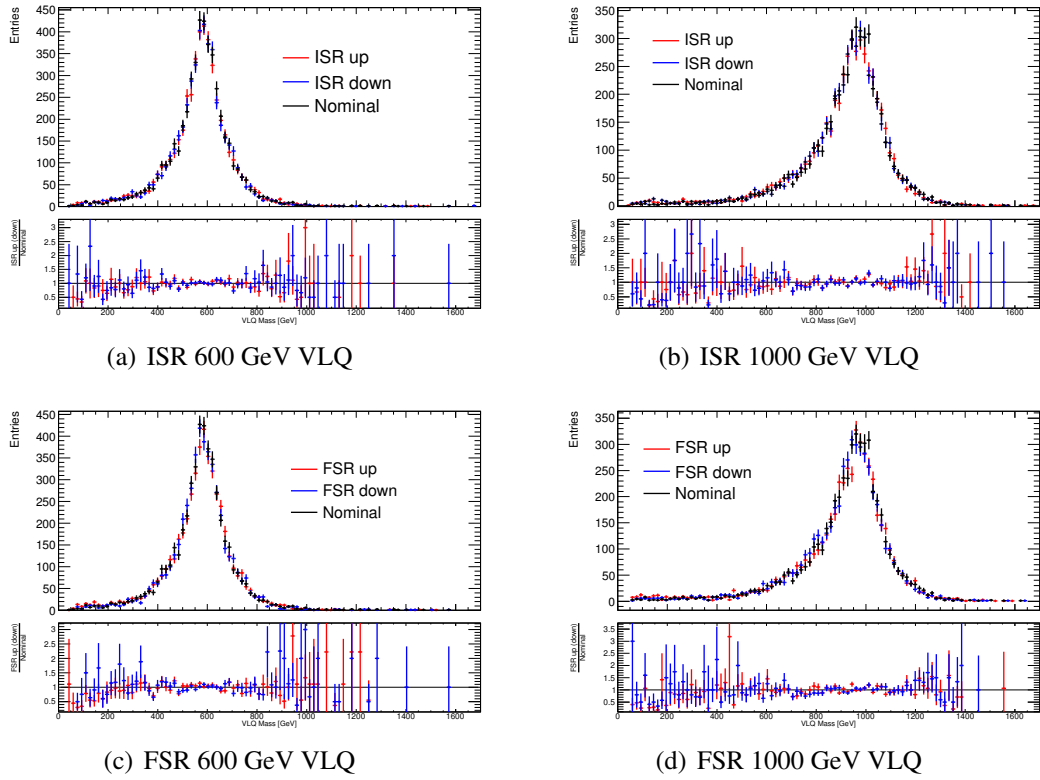
Figure 5.18: Shape comparisons in the CC channel for upwards and downwards fluctuations of ISR and FSR as detailed in table 5.XI for the 600 and 1000 GeV signals. The acceptance differences are removed (setting the yields to an arbitrary number) to highlight the shape differences.

dependent, and thus requires a mass dependent parametrization as was the case for the PDF uncertainty 7.X. The end result being a quadratic parametrization of the uncertainty on the cross section:

$$\sigma\,{}^{+\left(2.128-0.001553m+(2.565\times10^{-6})m^2\right)\%}_{-\left(1.958-0.00113m+(1.918\times10^{-6})m^2\right)\%} \tag{5.9}$$

where m is the signal mass in GeV.

5.8.4 LAr EM Calorimeter Crate

As explained in section 5.4.5, the LAr EM calorimeter had a malfunctioning crate that required a specific set of event and jet removals to render the jet, electron, and E_T^{miss} measurements more reliable in the region where the data information was lost.

mass [GeV]	CC channel σ [fb]			NC channel σ [fb]		
	$\mu/2$	μ	2μ	$\mu/2$	μ	2μ
300	17300	16400	15700	2630	2470	2350
600	1210	1100	1000	204	185	169
1000	113	98.5	86.9	21.3	18.5	16.4
1400	17.1	14.4	12.4	3.55	3.00	2.59
2000	1.47	1.18	0.979	0.338	0.276	0.229

Table 5.XII: Signal cross section in the CC and NC channels with varying factorization/renormalization scales nominally set to $\mu = m_{\mathrm{VLQ}}$.

A systematic uncertainty was therefore derived by varying by 20% the MC jet p_T threshold. The change in the number of events passing our selections was found to be small ($< 0.1\%$) given that it only affected a relatively small portion of the whole dataset ($\sim 15\%$).

5.9 RESULTS

5.9.1 DATA VERSUS EXPECTATION - SIGNAL REGIONS (SR)

Before executing the bump hunting methodology on the data distribution in the SR, it is informative to compare the data to MC expectation as shown in figure 5.19 and 5.20 for the CC and NC channels respectively. Both figures illustrate the similar behaviour that the MC expectation progressively overestimates the yields with increasing VLQ invariant mass. This was foreseen given the results of the 1.04 fb^{-1} search (appendix IV), where the MC background required a linear correction. Using the full 2011 dataset, we can conclude once again that the MC simulation of W/Z+jets through ALPGEN is unable to reproduce the correct behaviour in the tails of the $m(V + j_{\mathrm{lead}})$ distribution. Hence, a functional fit to the observed background is appropriate as it shall provide a more accurate description of the variable of interest.
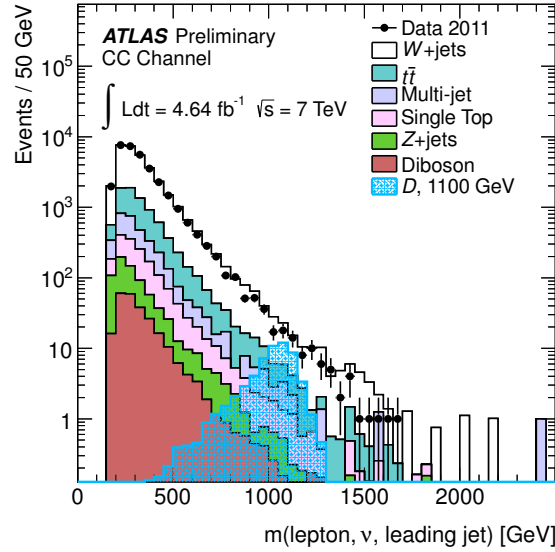
Figure 5.19: Monte Carlo estimates and the data in the combined electron and muon channels in the CC are compared. A 1.1 TeV VLQ signal has been overlaid and normalized to the nominal VLQ cross section assuming a coupling of $\kappa_{qQ} = \frac{m_Q}{v} = \kappa_{qQ} = 1$ and 100% branching fraction $Q \rightarrow Wq$, where q is a light quark.

5.9.2 BACKGROUND ESTIMATION THROUGH A FUNCTIONAL FIT

The background-only hypothesis is hence modelled through the functional form given by

$$f(m; p_{0,1,2,3}) = \frac{p_0 \left(1 - \frac{m}{\sqrt{s}}\right)^{p_1}}{x^{p_2 + p_3 \ln\left(\frac{m}{\sqrt{s}}\right)}}, \tag{5.10}$$

where m is the VLQ mass m_{VLQ}, $p_{0,1,2,3}$ are the fit parameters, and $\sqrt{s} = 7$ TeV. The function approximates a parabola in log-log scale with the $(1 - \frac{m}{\sqrt{s}})$ term forcing it to be zero at $m = \sqrt{s}$. The usefulness of this function stems from its ability to fit a wide range of falling SM backgrounds and its *inability* to fit resonance peaks. It has been used across a number of experiments and searches [184–186]. Therefore, the *goodness* of the fit, defined by its χ^2 p-value, shall provide a quantifiable measure of whether the background is entirely smooth or contains *bumps* or excesses in a localized region in m_{VLQ}.

126
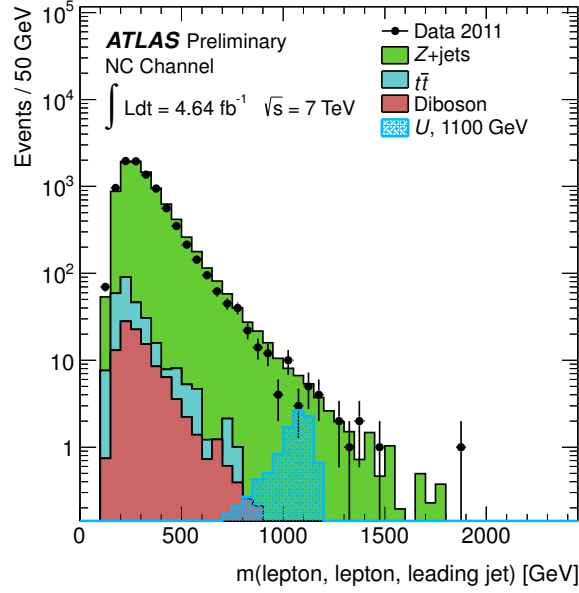
Figure 5.20: Monte Carlo estimates and the data in the combined electron and muon channels in the NC are compared. A 1.1 TeV VLQ signal has been overlaid and normalized to the nominal VLQ cross section assuming a coupling of $\kappa_{qQ} = \frac{m_Q}{v} = \kappa_{qQ} = 1$ and 100% branching fraction $Q \to Wq$, where q is a light quark.

The fit itself maximizes the likelihood function

$$L(D|B) = \prod_{i=1}^{N_{\text{bins}}} \frac{B_i^{D_i}}{D_i!} e^{-D_i},$$ (5.11)

where

$$B_i = \int_{m_i^{\text{low}}}^{m_i^{\text{up}}} f(m; p_{0,1,2,3}) \, dm.$$ (5.12)

and follows the BUMPHUNTERmethods detailed in appendix III.5. The integral delimiters m_i^{up} and m_i^{low} are the upper and lower edges of bin i. If the fit is performed over the entire VLQ mass spectrum, it is natural to wonder whether a signal can be absorbed in the fit. This is avoided by the exclusion of a region in the VLQ mass spectrum if the fit quality drops below

$$p\text{-value} \leq 0.01.$$ (5.13)

If the p-value fails this condition, then selected regions, as described in III.5 of the spec-

trum are incrementally excluded from the fit until condition (5.13) is satisfied. The obtained fit then serves as the background model upon which possible excesses shall be examined. To determine the robustness of the method, a number of tests were performed.

5.9.2.1 TEST 1: FIT TO MC BACKGROUND

The first test to determine the proficiency of equation (5.10) to correctly model the background was done using a series of pseudo-experiments generated around the nominal MC background expectation. Each pseudo-experiment thus provided a *new* background shape to which the fit could be tested. Figure 5.21 shows the fit to the nominal MC background in each of the relevant decay channels with its uncertainty given by the red bands. This uncertainty is evaluated from the distribution of fits to the pseudo-experiments and ranges from $\sim 5\%$ at 500 GeV to $\sim 20\%$ at 1500 GeV. Figure **??** shows the negative log-likelihood distribution of the fit *qualities* where the likelihood is computed using (5.11) for each pseudo-experiment. In each of the histograms, the red arrow indicates the nominal $-\log(L)$ value with which one can define a p-value by computing the fraction of pseudo-experiments having larger $-\log(L)$ than the nominal fit. This p-value does not go below 1% giving confidence in the fits to such background shapes in general.

5.9.2.2 TEST 2: VERSATILITY OF THE FUNCTIONAL FORM VERSUS JES AND BACKGROUND COMPOSITION

For the second test, the function's ability to model various background shapes was tested by shifting the JES up and down before generating pseudo-experiments around these distributions. The resulting negative log-likelihoods are shown in figures 5.23 and 5.24 in the CC and NC channels respectively.

The fit quality was also evaluated after changing the background composition. The non-EW backgrounds (multijets, $t\bar{t}$, diboson, and single top quark) were scaled up and down by 50% while leaving the EW background normalizations unchanged. With the newly obtained distributions, the procedure of generating pseudo-experiments and com-

(a) CC electron channel

(b) CC muon channel

(c) NC electron channel

(d) NC muon channel
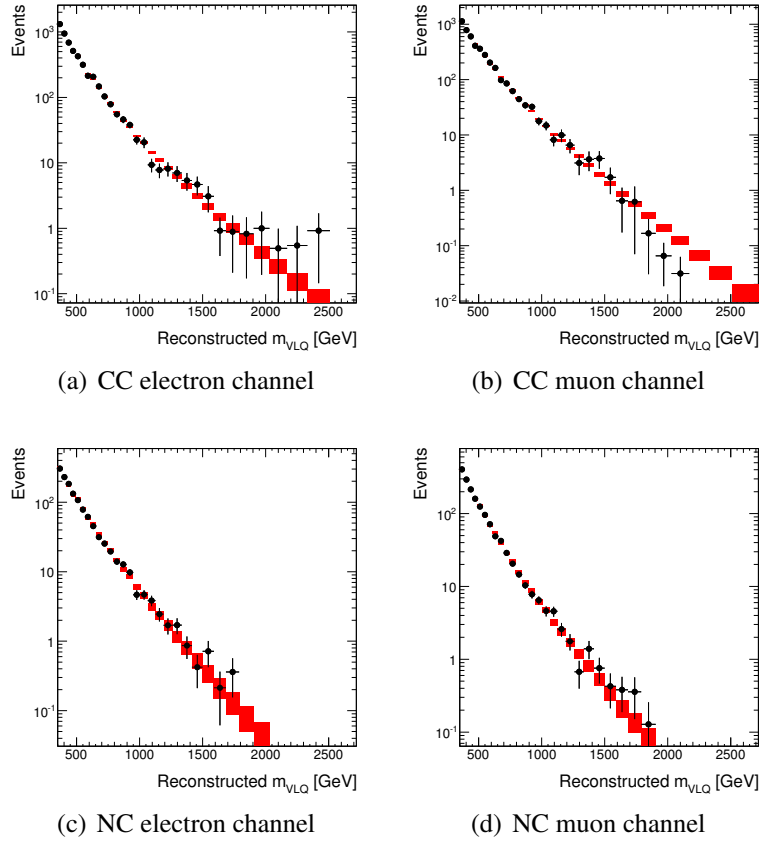
Figure 5.21: Fits to the MC background shape (data points) with estimated systematic uncertainty on the fit given by the red bands. The uncertainties varies from $\sim 5\%$ near $m(\text{VLQ}) = 500$ GeV to 20% around $m(\text{VLQ}) = 1500$ GeV. The fit uncertainty is estimated bin-by-bin though the distribution of fit values obtained from pseudo-experiments.

puting the negative log-likelihood was repeated. The results are presented in figure 5.25.

5.9.2.3 TEST 3: MASS EXCLUSION WINDOW

If signal there is, BUMPHUNTERmust be able to seek out such excesses and efficiently exclude them in the background fit. While incrementally injecting a 900 GeV NC channel VLQ signal, a set of pseudo-experiments were generated around the nominal background plus signal hypothesis to obtain the proportion of times the fit to the background would exclude a window containing the 900 GeV VLQ invariant mass. The

(a) CC electron channel　　　　　　(b) CC muon channel

(c) NC electron channel　　　　　　(d) NC muon channel
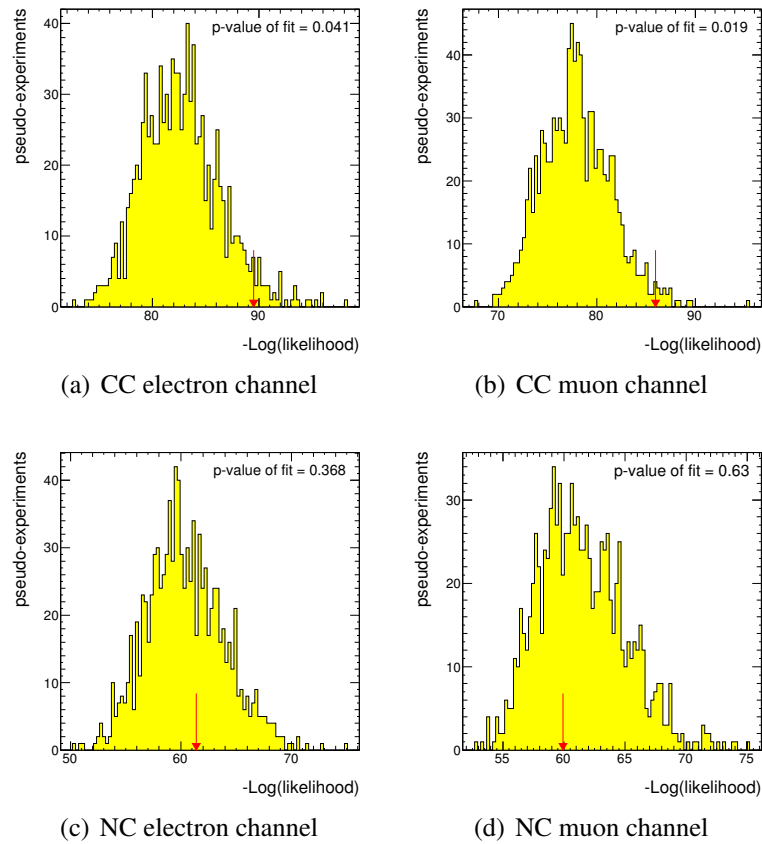
Figure 5.22: Negative log-likelihood distributions of the fits to pseudo-experiments generated from the nominal MC background. The red arrow points to log-likelihood value obtained from the fit to the nominal distribution with its corresponding p-value.

full results are tabulated in 5.XIII for given sets of injected signal. Based on these results, we can conclude that the background fitting procedure correctly excludes regions that contain signal when a sufficient number of signal events are present.

5.9.2.4　TEST 4: MEASURING SIGNAL STRENGTH

The previous study demonstrates that the BUMPHUNTER, although sensitive to the presence of signal, may swallow a portion of it and have a non-negligible effect on its fit parameters. To quantify this effect, two alternate methods were devised. In both cases however, 900 and 1300 GeV signals are progressively injected and pseudo-experiments are generated around their respective yield predictions.

(a) JES $+1\sigma$ electron channel

(b) JES -1σ electron channel

(c) JES $+1\sigma$ muon channel

(d) JES -1σ muon channel
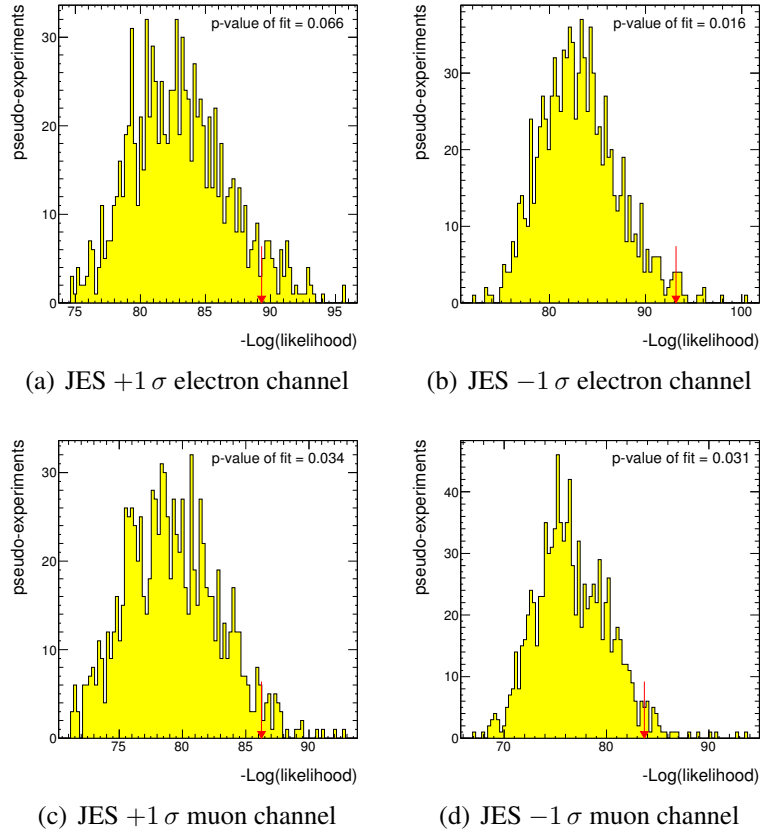
Figure 5.23: Charged-current channel negative log-likelihood distributions of the fits to pseudo-experiments generated from shifted MC backgrounds by $\pm1\sigma$ in JES. The red arrow points to log-likelihood value obtained from the fit to the nominal ($\pm1\sigma$ in JES) distribution with its corresponding p-value.

The first one attempts to fit these background + signal distributions using the background-only function (5.10) while excluding regions if the fit p-value falls below 0.01. The number of signal events is then defined as the number of events above the background prediction around the signal mass. The measured mean number of signal events S are then plotted versus the number of injected signal N in figure 5.26 in the CC electron channel for brevity (Very similar behaviours are observed in the other channels). We find that the proportion of swallowed events varies from $\sim 10\%$ to $\sim 30\%$, which is a rather poor performance. Gladly, this uses the background-only hypothesis, and is *not* how signal strengths shall be measured.

(a) JES $+1\,\sigma$ electron channel

(b) JES $-1\,\sigma$ electron channel

(c) JES $+1\,\sigma$ muon channel

(d) JES $-1\,\sigma$ muon channel
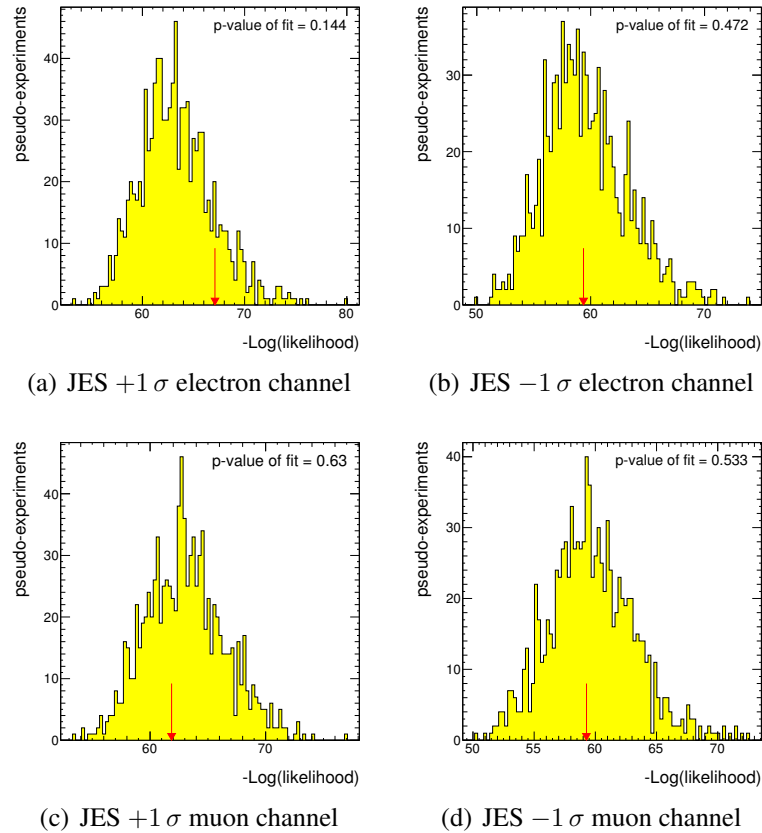
Figure 5.24: Neutral-current channel negative log-likelihood distributions of the fits to pseudo-experiments generated from shifted MC backgrounds by $\pm1\sigma$ in JES. The red arrow points to log-likelihood value obtained from the fit to the nominal ($\pm1\sigma$ in JES) distribution with its corresponding p-value.

The second way in which signals will be measured shall adhere to the following procedure. A *simultaneous* fit of background + signal where the background is again modelled through (5.10), but where an additional fit parameter representing the signal normalization is included. The much improved measure of signal events are presented in figure 5.27 for the NC muon channel for conciseness. Assuming the BUMPHUNTERfinds no excess, the limit procedure then in essence follows a very similar procedure as this one.

(a) CC electron channel

(b) CC muon channel:

(c) NC electron channel

(d) NC muon channel
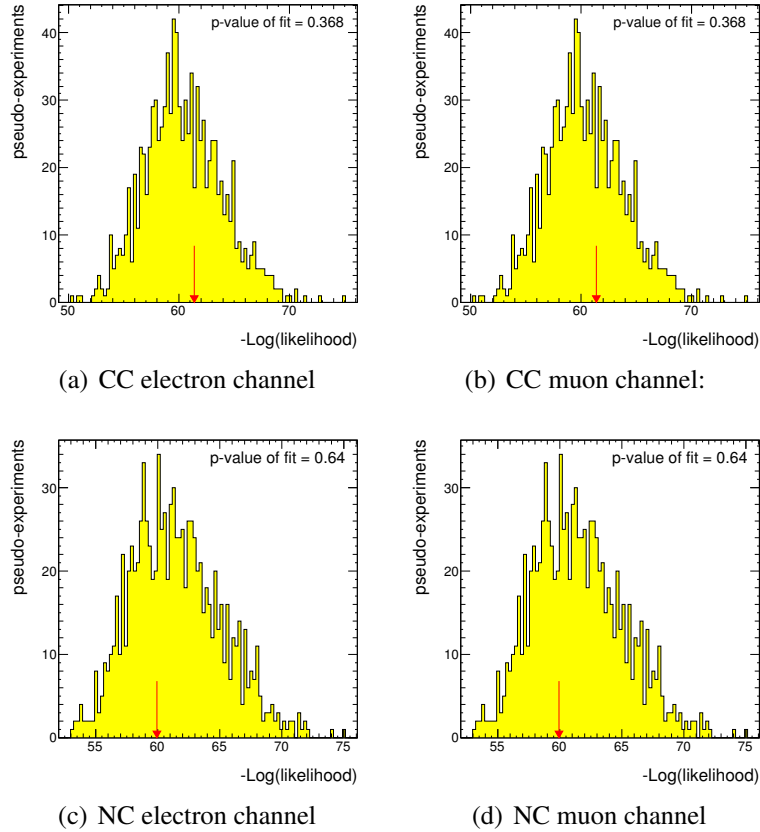
Figure 5.25: Negative log-likelihood distributions of the fits to pseudo-experiments generated from altered MC background compositions. The non-EW backgrounds were scaled by $\pm 50\%$. The red arrow points to log-likelihood value obtained from the fit to the nominal distribution with its corresponding p-value.

# Of Injected Signal Events	No Mass Region Excluded	Correct Mass Region Excluded
0-30	99.5%	0.5%
30-60	98.7%	1.3%
60-100	31.8%	68.2%

Table 5.XIII: Percentage of pseudo-experiments with a given number of injected signal events that contained a mass region excluded by the BUMPHUNTER. The injected events were that of a 900 GeV NC channel signal.

(a) 900 GeV Injected Signal

(b) 1300 GeV Injected Signal
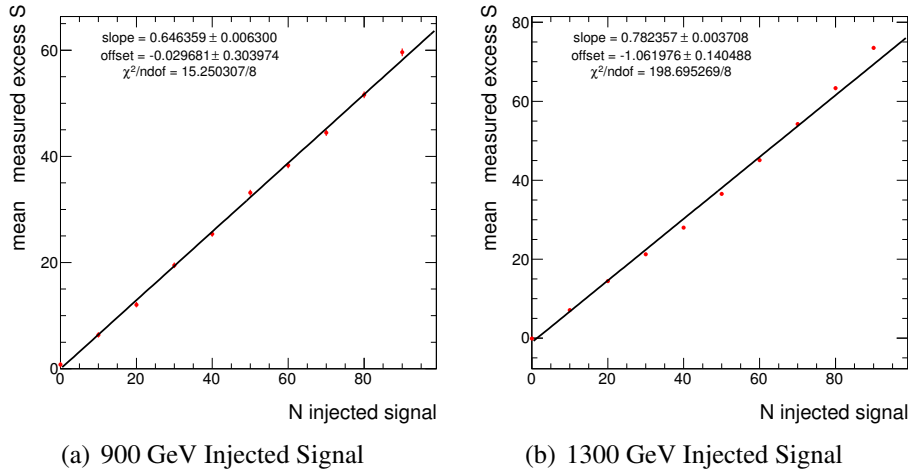
Figure 5.26: Mean measured excess as a function of the actual number of injected 900 GeV (a) and 1300 GeV (b) signal events. The background + signal distributions are fitted with the background-only function (5.10) as described in more detail in the text. Roughly 35% (22%) of the 900 (1300) GeV signal events are *swallowed* by the fitting function.

5.9.3 RESULTS ON SR DATA

Having confidence in the bump hunting method and background modelling procedure of the previous section, the procedure is now applied to the data distribution found in figures 5.19 and 5.20 when the data were compared to MC prediction. The resulting fit results are presented in figure 5.28 and 5.29 for the CC and NC channels respectively. The smallest p-values found are given in table 5.XIV. We therefore find that the data fits well with the background-only hypothesis as no significant excess is found over the entire CC and NC $m(\text{VLQ})$ distributions.

	CC	NC
Smallest p-value	0.56 ± 0.02	0.91 ± 0.01
Mass range [GeV]	1065-1500	1005-1090
Number of Bins	6	3

Table 5.XIV: Characteristics of the binned regions in $m(\text{VLQ})$ with the smallest p-values found during the bump hunter search in the CC and NC channels.

(a) 900 GeV Injected Signal   (b) 1300 GeV Injected Signal
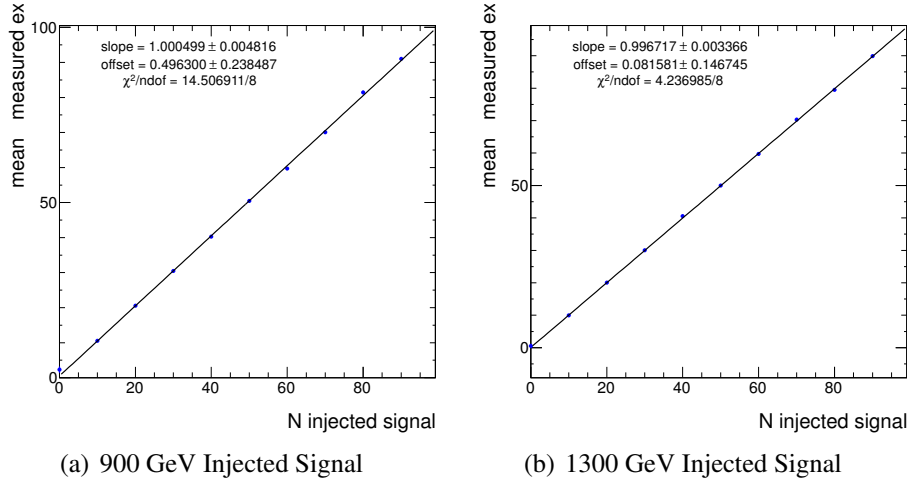
Figure 5.27: Mean measured excess as a function of the actual number of injected 900 GeV (a) and 1300 GeV (b) signal events. The background + signal distributions are fitted simultaneously with the background-only function (5.10) plus a signal hypothesis as detailed in the text. Virtually none of the 900 (1300) GeV signal events are *swallowed* by this fitting procedure.

5.9.4 CROSS SECTION LIMITS

Given the observed smoothness of the data for $m(\text{VLQ})$ in the SR, we can move onto computing limits within the model-independent approach of section 4.3. Bayesian limits [9] are calculated on

$$\sigma(pp \to Dq) \times BR(D \to Wu)(CC)$$
$$\sigma(pp \to Tq) \times BR(T \to Wu)(CC)$$
$$\sigma(pp \to Uq) \times BR(U \to Zu)(NC) \tag{5.14}$$

assuming $\tilde{\kappa}_{uD} = \tilde{\kappa}_{uT} = \tilde{\kappa}_{uU} = 1$. As a function of VLQ mass, the expected and observed limits are exposed in figure 5.30(a) for the CC channel, and figure 5.30(b) for the NC channel after combining the electron and muon channels.

Because the cross section is proportional to $\tilde{\kappa}_{qQ}^2$, the results can be re-interpeted in terms of limits on the coupling $\tilde{\kappa}_{qQ}$. Given (5.14), limits on $\tilde{\kappa}_{uD}$, $\tilde{\kappa}_{uT}$, and $\tilde{\kappa}_{uU} = 1$ were

---

9. With prior following a flat distribution on the expected number of signal events.
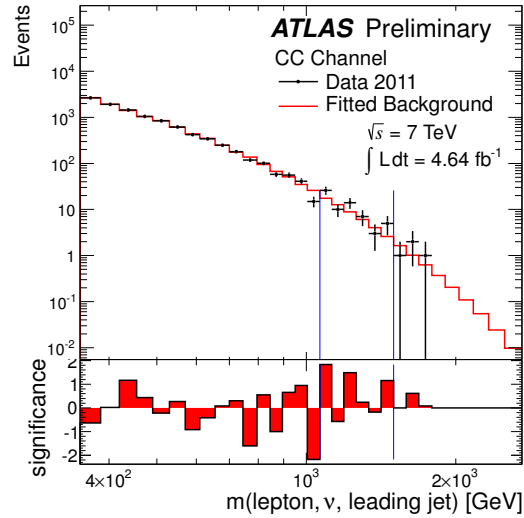
Figure 5.28: Functional form fit to the observed 2011 data in the CC channel with its bin-by-bin statistical significance. The binned region with the smallest p-value of 0.56 is delimited by blue lines.
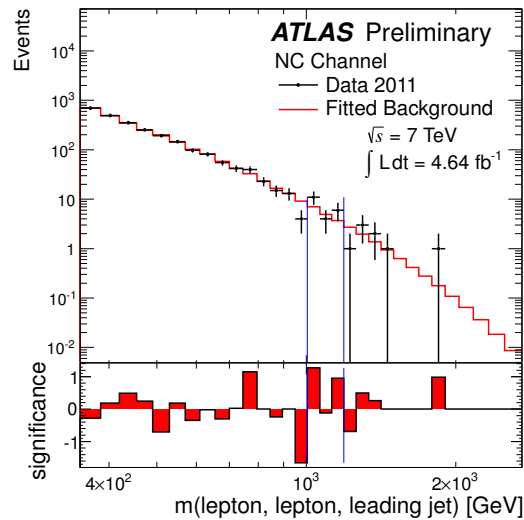
Figure 5.29: Functional form fit to the observed 2011 data in the NC channel with its bin-by-bin statistical significance. The binned region with the smallest p-value of 0.91 is delimited by blue lines.

computed as function of m_Q and drawn in figure 5.31.

Lastly, in the CC, selecting negatively charged leptons has the potential to increase the sensitivity of the search for high mass VLQ. This is due to the fact that in pp collisions, it is expected that roughly 2/3 of the total W+jets background be positively charged while signal D-quark production is expected to produce primarily negatively charged W simply because u-quarks are more abundant than $\bar{u}$-quarks from a PDF perspective. Hence, once the selection is applied, the limits machinery was put in action producing the results presented in figure 5.32. The observed (expected) mass limit upon the U-type, D-type (using the negatively charged lepton selection), and T-type VLQ within the confines of their model independent representation [172], are respectively 1080 (1090) GeV, 1180 (1360) GeV, and 1420 (1570) GeV. Table 5.XV summarizes the cross section limits results along with limits upon the couplings $\tilde{\kappa}_{uU}$, $\tilde{\kappa}_{uD}$, and $\tilde{\kappa}_{uT}$ as a function of VLQ mass.

Lastly, appendix II presents ATLAS event displays of the highest $m(W/Z + \text{jet})$ invariant mass events for both lepton decay modes in each of the CC and NC channels.

Mass [GeV]	CC $\sigma \times$ BR [pb]	NC $\sigma \times$ BR [pb]	$\tilde{\kappa}^2_{uD}$	$\tilde{\kappa}^2_{uX}$	$\tilde{\kappa}^2_{uU}$	CC$^-$ $\sigma \times$ BR [pb]
400	3.0	1.9	0.12	0.082	0.15	2.6
500	2.2	0.81	0.20	0.14	0.15	1.1
600	0.87	0.54	0.17	0.11	0.20	0.89
700	0.64	0.41	0.25	0.15	0.29	0.51
800	0.38	0.44	0.27	0.15	0.57	0.21
900	0.36	0.21	0.45	0.25	0.47	0.26
1000	0.29	0.15	0.62	0.32	0.55	0.30
1100	0.26	0.19	0.91	0.45	1.1	0.25
1200	0.26	0.14	1.5	0.72	1.3	0.18
1300	0.20	0.14	1.8	0.83	1.9	0.14
1400	0.16	0.12	2.2	0.97	2.6	0.10
1500	0.13	0.081	2.7	1.2	2.6	0.068
1600	0.10	0.061	3.3	1.4	2.9	0.048
1700	0.081	0.056	3.9	1.6	4.0	0.037
1800	0.058	0.059	4.2	1.6	6.1	0.033
1900	0.045	0.062	4.9	1.8	9.4	0.031
2000	0.035	0.073	5.6	2.0	16	0.029

Table 5.XV: Observed upper limits at 95% C.L. on the VLQ production cross section times branching ratio $\sigma(pp \to Qq) \times \text{BR}(Q \to Vq)$ as a function of its mass and the corresponding upper limit on a model-independent couplings to the u-quark. The last column shows the limits on the CC process after selecting negatively charged leptons.
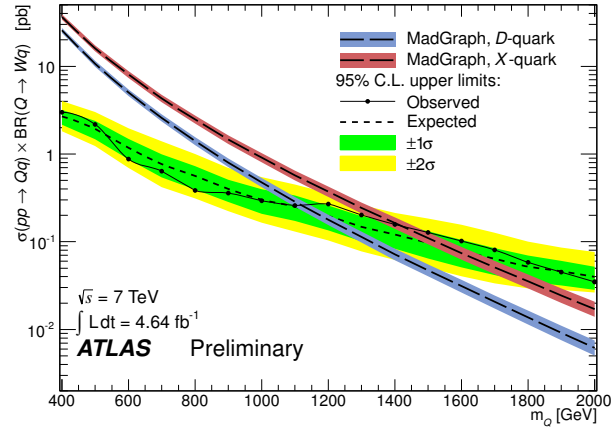
(a) CC channel limits
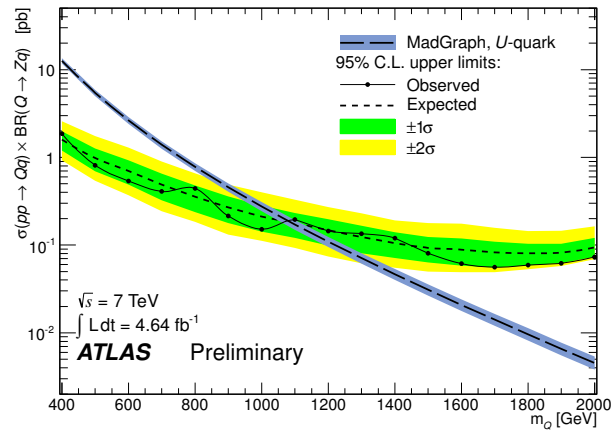
(b) NC channel limits

Figure 5.30: Electron and muon combined limits on the production of D- or T-quarks (top) and U-quarks (bottom). The theoretical uncertainties associated to the signal cross sections are represented by the coloured blue and red bands.

(a) uD coupling

(b) uU coupling
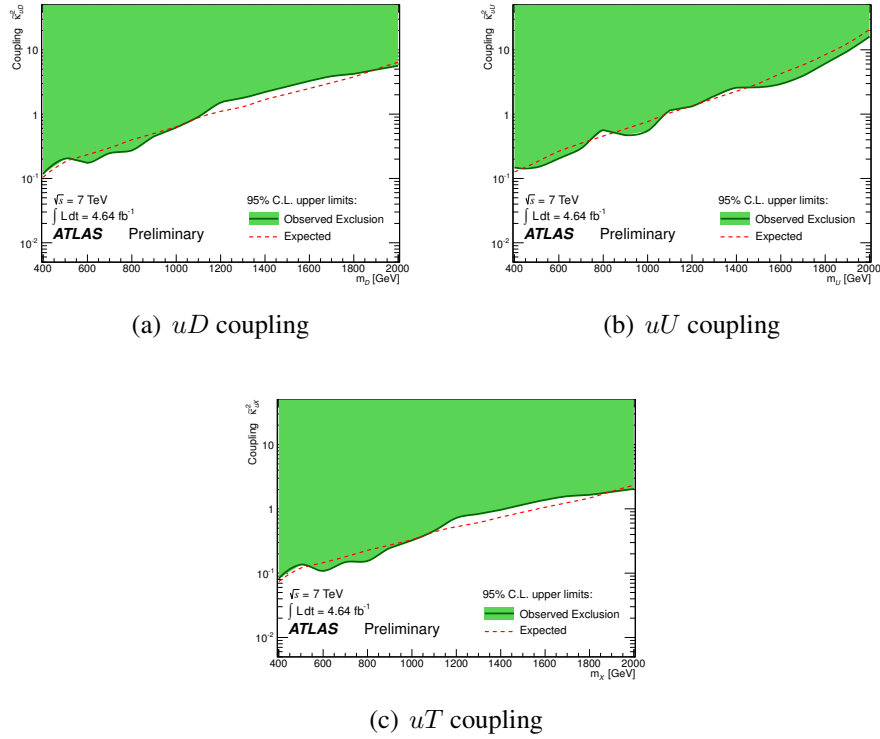
(c) uT coupling

Figure 5.31: Reinterpretation of the expected and observed limits on $\sigma(pp \to Qq) \times$ BR$(Q \to Vq)$ in terms of the couplings $\tilde{\kappa}_{uD}$, $\tilde{\kappa}_{uU}$, and $\tilde{\kappa}_{uT}$ ($T \equiv X$ in the figure) squared.
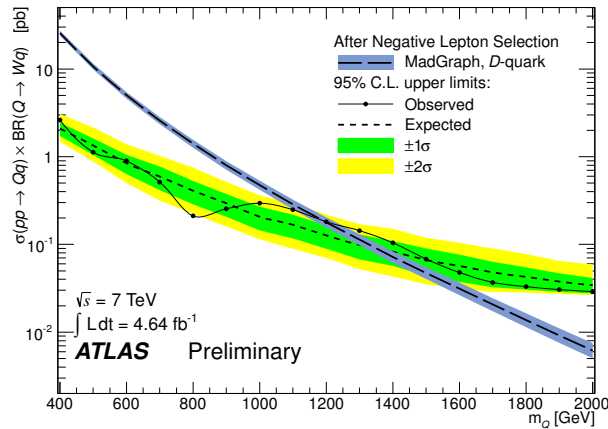
Figure 5.32: Limits on $\sigma(pp \to Qq) \times$ BR$(Q \to Wq)$ after selecting negatively charged leptons. The theoretical uncertainty on the signal cross section is represented by the coloured blue band.

CHAPTER 6

TECHNICOLOR: PRESENT STATUS

> *Your theory is crazy, but it's not crazy enough to be true.*

Niels Bohr

On the theoretical side, one particularly compelling proposal for explaining EWSB is Technicolor (TC), which can be briefly described as a *copy* of QCD, mimicking its general features, but whose fundamental energy scale lies near or at the electroweak scale Λ_{weak}. A description of how TC achieves EWSB is given in section 6.1.

Building on those ideas, further developments led to an extended form of technicolor called extended Technicolor (ETC), which provided a way to generate fermion masses (except for the top quark mass [1]). This shall be discussed in section 6.2. Unfortunately, ETC was thought entirely dead given the electroweak precision measurement (EWPM) results obtained by LEP, and the ETC predictions concerning flavour-changing neutral current (FCNC) processes which are not sufficiently suppressed when reasonable fermion and *technifermion* masses are to be explained. However, with the advent of *walking* Technicolor (WTC) and its contemporary models, TC models have since regained attention among the theoretical community and also within the ATLAScollaboration because WTC allows for higher fermion masses even at very large ETC scales. The EWPM cannot be compared directly with predictions of WTC since many energy scales are involved. Therefore, WTC along with a description of the problems it was invented to resolve or avoid, including TC's influence on the *oblique* parameters [2], shall be described in section 6.3.

From an experimental perspective, it is desirable to understand the low-energy phenomenology of TC theories in general. In this vein, Low-Scale Technicolor (LSTC), and its straw-man version [188] were developed, and describe, as the name indicates, only

---

1. In this special case, *topcolor* assisted TC provides a way to accomplish this [187].
2. Parameters that are solely influenced by vacuum polarization diagrams.

the most plausible low-energy resonances states that a full theory would produce. This effective theory will be outlined in section 6.4.

Finally, in light of recent experimental developments [17, 189], LSTC in the form presented in [188] seems to be ruled out. However, other TC models, such as MWT as proposed in [39] remain completely possible and credible extensions to the SM given that they do contain a Higgs particle with a phenomenology very similar to that of the SM Higgs, giving further motivation for the WZ resonance search of the following chapter. Along with these, composite Higgs models discussed in chapter 4 in addition to containing a composite Higgs, also contain other heavy bosons that decay through diboson processes. Thus, given this outlook, the minimal walking technicolor (MWT) model will be expanded on in section 6.5 as models of its type abide by all present experimental constraints. Interestingly, newly conceived MWT models also contain DM candidates [190–192].

6.1 EWSB WITHOUT A FUNDAMENTAL SCALAR

Since the onset of the well known hierarchy problem (see chapter 2.5.2), a number of solutions have been proposed. A simple solution is to do without fundamental scalars entirely and attempt to arrive at EWSB dynamically. In fact, a particularity of QCD is that it too produces the correct ratio of $W^{\pm}$ and Z^0 masses as does the Higgs mechanism (see section 2.3).

In the limit of massless quarks, the $SU_c(3)$ part of the SM Lagrangian as taken from equation (2.7) is

$$L_{SU_c(3)} = -\frac{1}{4}F^i_{\mu\nu}F^{i\mu\nu} + \sum_r \bar{q}_{r\alpha} i {\not{D}}^\alpha_\beta q^\beta_r. \tag{6.1}$$

The indices r refer to the quark generations, while α and β are color indices. Applying the transformations

$$q \to e^{i\theta_i \frac{\tau^i}{2}}q, \quad \text{and} \quad q \to e^{i\theta_i \frac{\tau^i}{2}\gamma_5}q, \tag{6.2}$$

where τ^i are Pauli matrices, upon the spinors q, we arrive at the conclusion that QCD

respects chiral symmetry

$$SU_L(2r) \otimes SU_R(2r), \tag{6.3}$$

where r is the number of quark generations [37]. The symmetry has $8r^2 - 2$ independent components. In parallel to this, we know (at least experimentally) that the quark condensate operator $\bar{q}q$ must have a non-zero expectation value because of its confining properties. Explicitly, this operator is proportional to

$$\langle \bar{q}_{r\alpha} q_{s\beta} \rangle \sim \delta_{rs} \delta_{\alpha\beta} f_\pi^3, \tag{6.4}$$

where $f_\pi = 93$ MeV is the pion's decay constant since $\bar{q}q \sim \bar{q}_L q_R + \bar{q}_R q_L$. In other words, the ground state of QCD breaks the chiral symmetry of equation (6.1) leaving only the symmetries of isospin intact corresponding to the diagonal group of (6.3), itself having $4r^2 - 1$ independent components. The fact that the ground state breaks the symmetries of its very own Lagrangian translates to the fact that the symmetry was broken in a *dynamical* way. This is the essence of dynamical symmetry breaking (DSB). By Goldstone's theorem [193, 194], a set of $4r^2 - 1$ Nambu-Goldstone bosons (NGB), or more specifically in this case pseudoscalar mesons, must emerge from the breaking of such continuous symmetries. Considering only one generation, these are the known pions π^-, π^0, and π^+.

Turning on the $SU_L(2) \otimes U_Y(1)$ part of the SM Lagrangian, the polarization tensor of the $W^\pm$ and Z^0 bosons thus necessarily contain these meson states, albeit primarily first generation pions (given the weak decays of the 2nd and 3rd generation quark) as shown in figure 6.1. The one-loop polarization tensor terms for these are therefore [37, 44]

$$\Pi_{\mu\nu}^{ab}(q) = (q_\mu q_\nu - q^2 g_{\mu\nu}) \left(\frac{g_a g_b r f_\pi^2}{4q^2} \right), \tag{6.5}$$

when q^2 approaches [3] 0, where the indices a, $b = 0, 1, 2, 3$, and the couplings $g_0 = g_Y$ while $g_{1,2,3} = -g_L$. A direct consequence of this is that the $W^\pm$ and Z^0 have acquired

---

3. The pions are for now pure NGB, that is, they are considered massless.
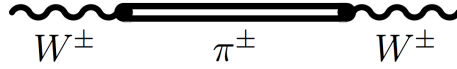
Figure 6.1: Meson states appear as poles in the vector boson polarization tensor. A very similar process occurs in LSTC for the production of the techni-ρ.

masses equal to [37]

$$M_W = \frac{g_Y \sqrt{r} f_\pi}{2}, \text{ and} \tag{6.6}$$

$$M_Z = \frac{\sqrt{g_L^2 + g_Y^2} \sqrt{r} f_\pi}{2}. \tag{6.7}$$

These are to be compared to equations (2.25) and (2.27), where it was the Higgs mechanism that produced the $W^\pm$ and Z^0 masses. Notice that making the substitution

$$\sqrt{r} f_\pi \to v \tag{6.8}$$

divulges the fundamental equivalency between the two symmetry breaking schemes, implying that both symmetry breaking mechanisms predict the same ratio of masses between the $W^\pm$ and Z^0. Noticeably however, QCD's energy scale is 3 orders of magnitude too small, yielding masses for the $W^\pm$ and Z^0 of $m_W \simeq 53$ MeV and $m_Z \simeq 60$ MeV [37]. The idea behind TC therefore becomes clear. It postulates the existence a new force built upon the symmetries of $SU(N_{\text{TC}})$, where $N_{\text{TC}} \geq 3$, together with the desired properties of asymptotic freedom and confinement whose lowest energy bound states, namely technipions π_T, appear in the polarization tensors of the weak vector bosons, but this at the electroweak scale Λ_{weak}. In particular, the technipion's decay constant must be

$$F_{\pi_T} \simeq v, \tag{6.9}$$

the minimum of the Higgs potential, by definition equivalent to the weak scale.

The minimal TC model [37, 195] has one doublet of technifermions, $(U, D)_{L,R}$ which forms condensates, such as $\langle \bar{U}_L U_R \rangle$ and $\langle \bar{D}_L D_R \rangle$ near the weak scale assuming once again the gauge structure $SU(N_{TC})$, thus breaking technifermion chiral symmetry

as well as $SU_L(2) \otimes U_Y(1)$. In complete analogy with QCD, the spin-1 isotriplet vector mesons ρ_T, its axial-vector partner a_T, and the isosinglet ω_T form, along with spin-0 technipions π_T, the lowest energy bound states to be searched for at the LHC. Their rich phenomenology will be detailed in section 6.4 in the context of LSTC.

6.2 EXTENDED TECHNICOLOR

Minimal TC as just outlined procures the correct $W^{\pm}$ and Z^0 masses in a purely dynamical fashion. The question then arises as to whether an *extended* form of TC can also generate masses for the fermions while keeping intact the SM gauge group $G_{SM} = SU_c(3) \otimes SU_L(2) \otimes U_Y(1)$, remembering that the SM Yukawa terms (equation (2.10)), which previously generated fermionic masses, involved couplings to the Higgs doublet. The first attempts at building such models [196, 197] laid the foundation for the various extended technicolor (ETC) models that were later developed [198, 199]. In these models, ETC is also needed to provide possible decays of techniquarks into light SM quarks, otherwise they would be stable and quickly come into conflict with experimental data.

The way such a model achieves mass generation for SM fermions goes as follows. It classifies all fermionic fields (including those of technicolor) into a large irreducible representation of a gauge group G_{ETC}, which at a some large energy scale $\Lambda_{ETC} \gg \Lambda_{TC}$, breaks into

$$G_{ETC} \underset{\Lambda_{ETC}}{\longrightarrow} G_{TC} \otimes G_{SM} \underset{\Lambda_{TC} \sim \Lambda_{weak}}{\longrightarrow} G_{TC} \otimes SU_c(3) \otimes U_{EM}(1), \qquad (6.10)$$

where $G_{SM} = SU_c(3) \otimes SU_L(2) \otimes U_Y(1)$ is the recognizable SM gauge group. Namely, it is the chiral symmetry breaking of G_{TC} that breaks G_{SM} at Λ_{TC}. The breaking of G_{ETC} produces new heavy gauge bosons B with masses equivalent to

$$m_B \sim \alpha_{ETC} \Lambda_{ETC} \qquad (6.11)$$

where α_{ETC} is their coupling strength and Λ_{ETC} is the scale at which ETC undergoes sym-

metry breaking. The exact nature or origin of the ETC symmetry breaking shall remain superfluous, and in some sense irrelevant in the context of LHC energies, and hence, for the time being, the important fact is that this grand breaking scheme procures radiative corrections to the SM fermions, thus generating their mass, the end result being [37]

$$m_f(\Lambda_{\text{ETC}}) \simeq \frac{\langle \bar{F}F \rangle_{\Lambda_{\text{ETC}}}}{\Lambda_{\text{ETC}}} \simeq \frac{\alpha_{\text{ETC}}^2}{m_B^2} \langle \bar{F}F \rangle_{\Lambda_{\text{ETC}}} \tag{6.12}$$

where the F are part of techniquark doublets, and where the condensate $\langle \bar{F}F \rangle_{\Lambda_{\text{ETC}}}$ is renormalized at the Λ_{ETC} scale. The relevant diagram for such a correction can be viewed in 6.2. Rescaling it to the Λ_{TC} scale produces the renormalization equation

$$\langle \bar{F}F \rangle_{\Lambda_{\text{ETC}}} \longrightarrow \langle \bar{F}F \rangle_{\Lambda_{\text{TC}}} \cdot \exp\left(\int_{\Lambda_{\text{TC}}}^{\Lambda_{\text{ETC}}} \frac{d\mu}{\mu} \left[\frac{3C_2(R)}{2\pi} \alpha_{\text{TC}}(\mu) + \mathcal{O}(\alpha_{\text{TC}}^2) \right] \right), \tag{6.13}$$

where $C_2(R)$ is the quadratic Casimir invariant[4] of the group G_{TC} with representation R. From equation (6.13), one can compute the generated SM quark masses simply by postulating a form for the group G_{TC}, which ordinarily, is taken to be $SU(N_{\text{TC}})$. With the additional assumption that the coupling α_{TC} becomes small beyond Λ_{TC}, which is quite natural if technicolor is indeed asymptotically free, and combining equations (6.12) and (6.13), one arrives at an estimate for this new scale Λ_{ETC} in relation to the produced SM fermion masses. This yields [37]

$$\Lambda_{\text{ETC}} \simeq \sqrt{\frac{4\pi F_{\pi_T}^3}{m_f N_D^{\frac{3}{2}}}}, \tag{6.14}$$

where N_D is the number of technicolor doublets and m_f is the mass of any SM fermion. Using the plausible relations $F_{\pi_T} \sim 246$ GeV, $N_D = 4$, while isolating m_f gives

$$m_f \sim \frac{0.023[\text{TeV}]^3}{\Lambda_{\text{ETC}}^2}. \tag{6.15}$$

---

4. Let G_a be the generators of the group G under some representation R. The quadratic Casimir operator then becomes $\sum_a G_a G^a = C_2(R)\mathbb{1}$
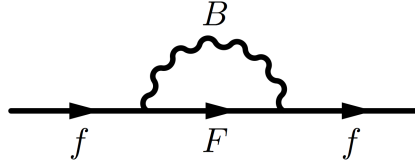
Figure 6.2: Radiative loop corrections to SM fermions q via an ETC gauge sector with heavy gauge bosons B and technifermions Q.

For quarks and leptons in the MeV to a few GeV range, Λ_{ETC} can therefore be set to an energy scale well beyond $\Lambda_{\text{ETC}} \gg \Lambda_{\text{TC}}$. However, as we shall see in section 6.3, this shall be insufficient to avoid FCNC. An even deeper problem arises if ETC should give rise to the top quark mass. Plugging in $m_f = m_{\text{top}} = 173.1$ GeV [16] into equation (6.15) suggests that Λ_{ETC} be $\mathcal{O}(1)$ TeV which is by no means much greater than $\Lambda_{\text{TC}} \sim \Lambda_{\text{weak}}$, a prerequisite of ETC. Consequently, the top-quark mass must be generated through a mechanism not present in ETC.

6.2.1 TOPCOLOR-ASSISTED TECHNICOLOR

The formalism behind the addition of the new breaking scale Λ_{ETC} at which point the all encompassing gauge group G_{ETC} breaks is capable of generating masses for all known fermions except the top-quark. This inability stems from the fact that the quark mass is of the same order as the weak scale itself. Combining the ideas of topcolor [138] and ETC enables to construct a model where all SM fermion masses emerge naturally through radiative corrections, and not via Yukawa like terms. This model was dubbed topcolor-assisted technicolor (TC^2) [187, 200].

Topcolor on its own was devised to be the minimal dynamical scheme though which EWSB could occur while producing a large top mass [138]. The top-quark condensate $\langle \bar{t}t \rangle$ forms through a new $SU(3) \otimes U(1)$ strong interaction at a high energy scale $\Lambda_{\text{topcolor}}$, where the $U(1)$ symmetry is invoked to suppress the $\langle \bar{b}b \rangle$ condensate [201] in favor of the $\langle \bar{t}t \rangle$ condensate. Topcolor hypothesizes the gauge group structure

$$G_{\text{topcolor}} = SU_2(3) \otimes U_2(1) \otimes SU_1(3) \otimes U_1(1) \xrightarrow[\Lambda_{\text{weak}}]{} SU_c(3) \otimes U_Y(1) \qquad (6.16)$$

where 3rd generation quarks couple to $SU_1(3) \otimes U_1(1)$ (topcolor) while the first two generations couple to $SU_2(3) \otimes U_2(1)$. The breaking of G_{topcolor} into its diagonal group at the weak scale produces the correct gauge structure of the SM. Unfortunately, the model suffers from some of the same issues as the Higgs mechanism, that is, it requires fine-tuning as the energy scale required to reproduce the SM masses is $\Lambda_{\text{topcolor}} \sim 10^{15}$ GeV. Through the combination of topcolor and ETC ideas emerges a model where this last issue resolves itself while retaining a dynamical mechanism for top quark mass generation.

In the TC^2 model proposed in [202], all desired features are present:

- Dynamical mass generation for all SM quarks and leptons
- Flavor mixing between the heavy (3rd) and light (1st and 2nd) generation (not present in standard topcolor) is produced by ETC operators.
- The breaking of $U_1(1) \otimes U_2(1) \rightarrow U_Y(1)$ occurs at a higher energy than EW breaking $SU_L(2) \otimes U_Y(1) \rightarrow U_{\text{EM}}(1)$.
- EWSB occurs via the breaking of G_{TC}, the technicolor gauge group.

This model and further developments of TC^2 have therefore over time proven to be an important contender for explaining the origin of both fermionic masses and EWSB. There have unfortunately been, of course, a few setbacks.

6.3 SOLVING THE FCNC AND OBLIQUE PARAMETER DISCORDANCES

A number of experimental constraints upon ETC and TC^2 model building must be imposed. ETC must be asymptotically free with no gauge anomalies. The theory must also allow weak CP-violation, but without strong CP-violation. These conditions can be met relatively easily [37], however, the requirement that FCNC must be small is a more difficult condition for ETC to circumvent. The reason being that [201] the new PNGB bosons produced through the breaking of G_{ETC} makes possible transitions of the type shown in figure 6.3. At low energies, that is for $E \ll \Lambda_{\text{ETC}}$, ETC interactions can be approximated by contact interactions. The interesting (from a phenomenological
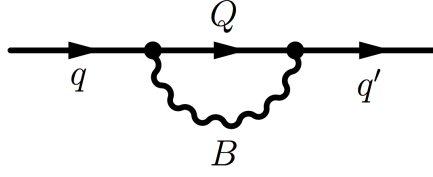
Figure 6.3: Flavour-Changing Neutral Currents (FCNC) as permitted by ETC. In ETC, the additional techniquarks Q couple to the ordinary quark q and q' providing corrections to their propagator (as shown in figure 6.2). Very similar processes however, like the one shown here, make possible FCNC which are heavily constrained by experiment [16].

perspective) interactions can in turn be summarized by [5] [201]

$$\alpha_{ab}\frac{\bar{Q}B^aQ\bar{Q}B^bQ}{\Lambda_{\text{ETC}}^2} + \beta_{ab}\frac{\bar{Q}_LB^aQ_R\bar{\psi}_RB^b\psi_L}{\Lambda_{\text{ETC}}^2} + \gamma_{ab}\frac{\bar{\psi}_LB^a\psi_R\bar{\psi}_RB^b\psi_L}{\Lambda_{\text{ETC}}^2}, \qquad (6.17)$$

where the B^a are the generators of the group G_{ETC} times chiral factors such as $(1-\gamma_5)/2$, and the coefficients α_{ab}, β_{ab}, and γ_{ab} contain information about the strength of the interactions which depend heavily on the chosen structure of G_{ETC}. The ψ spinors are SM fermions (quarks or leptons), while Q are the ETC techniquarks. The terms proportional to α_{ab} generally elevate the masses of the PNGB of the theory into experimentally acceptable ranges. The β_{ab} permit the decay of techniparticles into SM particles, while sadly the term proportional to γ_{ab} permits FCNC of SM particles, which again, are considerably constrained by experiment. Under such conditions, Λ_{ETC} would have to be so high ($\mathcal{O}(10^3)$ TeV [201]) that the fermion masses would be too low. In fact, using equation (6.15) and setting $m_f = 1$ GeV, we find that $\Lambda_{\text{ETC}} \simeq 4.8$ TeV, which is seemingly high for a viable ETC theory, but it is not high enough to evade FCNC contraints [201].

Before discussing a possible solution to this issue, another argument against ETC relates to the oblique parameters S, U, and T, defined by [203] $S = \frac{4e^2}{\alpha}\left[\Pi'_{33}(0) - \Pi'_{3Q}(0)\right]$, $T = \frac{e^2}{\alpha s_W^2 c_W^2 m_Z^2}\left[\Pi_{11}(0) - \Pi_{33}(0)\right]$, and $U = \frac{4e^2}{\alpha}\left[\Pi'_{11}(0) = \Pi'_{33}(0)\right]$, where $s_W = \sin\theta_W$ and $c_W = \cos\theta_W$, and where the vacuum polarizations Π are related through [203]

$$ig^{\mu\nu}\Pi_{XY}(q^2) + (q^\mu q^\nu \text{ terms}) = \int d^4x\, e^{-iqx}\langle J_X^\mu(x)J_Y^\nu(0)\rangle \qquad (6.18)$$

---

5. Loosely following the notation of [201]

149

to $J_i^\mu(0)$, with $i = 1, 2, 3$, the isospin current vectors and J_Q^μ the electromagnetic current, which couple to the W and Z gauge bosons (after combining (2.9) and (2.12), and assuming only SM contributions). Experimentally, the values are $S = 0.00^{+0.11}_{-0.10}$, $T = 0.02^{+0.11}_{-0.12}$, and $U = 0.08 \pm 0.11$ [16], all consistent with zero given the Higgs boson mass near its measured value of ~ 126 GeV. Now, since U is only affected by precision measurements on m_W, in most cases, it can safely be set to zero as it is also predicted to be two orders of magnitude smaller than T. Hence, with $U \sim 0$, S can be viewed as the total size of the new particle sector, and T by how much this new sector breaks weak-isospin. The various sources of constraints upon S and T can be viewed in figure 6.4.
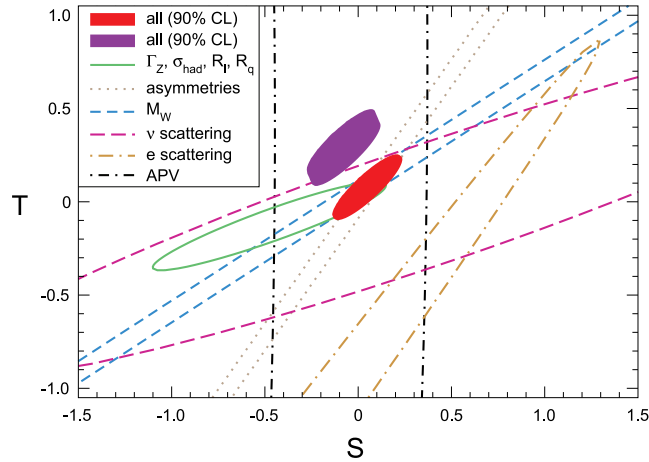
Figure 6.4: 1 σ constraints from various sources (as indicated in the legend) in the S versus T parameter plane. The red blob is the inclusive 90% C.L. region assuming a Higgs mass between 115.5 GeV and 127 GeV, while the violet blob indicates the 90% C.L. region for $0.6 < M_H < 1$ TeV. Both these colored regions also include constraints from measurements of m_Z and were computed assuming $U = 0$ [16].

Within radiative corrections, the W and Z propagator masses can be modified by the presence of new states/particles in one-loop (and higher order) diagrams. In the case of ETC, these new contributions modify the S and T depending on the chosen TC group G_{TC}. Despite the numerous choices for G_{TC}, N_{TC} and N_D, the S and T parameter values fall into regions outside the red blob of figure 6.4 [201, 203]. Using the narrow-resonance

approximation [6], the authors of [203] obtain the result

$$S = 4\pi \left[1 + \frac{m_{\rho_T}^2}{m_{a_T}^2} \right] \frac{F_{\pi_T}^2}{m_{\rho_T}^2}, \tag{6.19}$$

where the m_{ρ_T} and m_{a_T} are the techni-ρ and techni-a masses which are the assumed dominating low-lying states contributing to the polarization tensors of (6.18) (more on these technimesons in section 6.4). Hence, with the additional reasonable assumptions that $m_{\rho_T} = 800$ GeV, $m_{a_T} = 880$ GeV [7], and that the rescaling of (6.9) is appropriate, one arrives at

$$S \simeq 2.2. \tag{6.20}$$

Clearly, such scenarios are excluded given the EW precision measurements shown in figure 6.4.

6.3.1 WALKING TECHNICOLOR

Fortunately, the issues plaguing ETC as just described can all be mitigated by dropping one important assumption on the behaviour of the coupling α_{TC}. If the TC couplings are asymptotically free as they are in QCD, the should fall off like $\alpha_{\text{TC}} \sim \frac{1}{\ln E}$ for energies E beyond Λ_{TC}. However, no fundamental principle demands this to be the case. In fact, $\alpha(E)$ can be imagined to be approximately flat for energies $\Lambda_{\text{TC}} < E < \Lambda_{\text{ETC}}$. Studies of QCD-like theories have shown that the UV and IR behaviour of their couplings are heavily dependent on the number of flavours [204] and the chosen Yang-Mills theory gauge group. Estimating the number of flavours N_f^c at which point the coupling becomes fixed is a difficult task however. For QCD-like theories, i.e. based on $SU(3)$, table 6.I presents the expected short and long range behaviour of a coupling α with respect to the number of flavours. Authors of reference [204] estimate N_f^c to be $8 < N_f^c < 12$. These studies among many others suggest that a near constant coupling for ETC between energies $\Lambda_{\text{TC}} < E < \Lambda_{\text{ETC}}$ is feasible and even quite realistic. It simply depends on the number of

---

6. The states appear as poles (δ-functions) in the polarization tensors.

7. The reason for such a choice of masses will become apparent in the following chapter where one type of signal studied has $m_{\rho_T} = 1.1\, m_{a_T}$.

	UV	IR
$N_f < N_f^c$	$\alpha \to 0$	$\alpha \to \infty$
$N_f^c < N_f < 16.5$	$\alpha \to 0$	$\alpha \to \text{Const.}$
$N_f > 16.5$	$\alpha \to \infty$	$\alpha \to 0$

Table 6.I: Short (UV) and long (IR) distance behaviour of an SU(3) Yang-Mills theory as a function of the number of flavours N_f [204].

flavours and the gauge group. Such TC theories where the coupling approaches a fixed point for a range of energies (not up until the Planck scale) were denominated *walking technicolor* (WTC) [37].

A walking coupling α_{TC} procures a number of desired properties. It would enhance both the α_{ab} and β_{ab} terms of equation (6.17) while not altering the FCNC γ_{ab} term, alleviating considerably the FCNC tensions [205–207].

Additionally, conventional techniques for estimating the oblique parameters have been shown to be inapplicable for WTC [37]. For WTC, the anomalous coupling

$$\gamma_m(E) \simeq \frac{3C_2(R)}{2\pi}\alpha_{\text{TC}}(E) \tag{6.21}$$

is no longer valid. This is because it assumed $\gamma_m(E) \ll 1$, which in the walking technicolor regime may no longer be true. In fact, $\gamma_m(E)$ is expected to near 1 under constant α_{TC}. Hence, the perturbative methods used for obtaining the oblique parameters are no longer valid. Likewise, spectral function studies [208, 209] of the vector and axial-vector WTC states indicate that if [188]

$$M_{\rho_{Ti}} \simeq M_{a_{Ti}}, \quad \text{and} \quad g_{\rho_{Ti}} \simeq g_{a_{Ti}}, \tag{6.22}$$

where $g_{\rho_{Ti}}$ and $g_{a_{Ti}}$ are the couplings of the vectors ρ_{Ti} and axial-vectors a_{Ti} (more on these possible *towers* of states in the following section), the S parameter may be small or even negative.

In brief, *walking* extended technicolor theories continue to be an interesting candidate for BSM phenomenology at the LHC while also being the only candidate that attempts to explains both EWSB and fermion mass generation.

6.4   Low-Scale Technicolor and its Phenomenology

Up until now, we have considered two technicolor scales, Λ_{TC} and Λ_{ETC}, the first being the scale at which the gauge group g_{TC} forms condensates that break the EW symmetry $SU_L(2) \otimes U_Y(1) \to U_{\text{EM}}$, and the second being the one that, through its own breaking, generates fermionic masses, and provides a decay chain route for TC particles into SM particles. One can imagine a series of N scales

$$G_{\text{ETC}_N} \to G_{\text{ETC}_{N-1}} \to ... \to G_{\text{ETC}_1} \to G_{\text{TC}} \otimes SU_c(3) \otimes U_{\text{EM}}(1) \qquad (6.23)$$

each contributing dynamically to the weak scale. This idea is known as multi-scale technicolor [201, 210, 211] and has an interesting phenomenology of importance for the following chapter.

For there to be walking TC, either there needs to be a large number of technifermion doublets N_D in the fundamental representation $G_{\text{TC}} = SU(N_{\text{TC}})$ or a few doublets in higher-dimensional representations [210] such as those in (6.23). However, even in the higher-dimensional case, it has been shown that due to the constraints on ETC representations as detailed in the previous section, there will necessarily be technifermions in the fundamental representation [188]. Therefore, this situation implies that there must be *low-scale* states such as the ρ_T, π_T, ω_T, a_T, η_T, and etc. re-using the QCD nomenclature with the important caveat that their respective mass relations may very well be entirely different.

The technicolor straw-man model (TCSM) [38, 212, 213] assumes these basic ideas about WTC models in general and casts these ideas into a simple phenomenologically testable model. Closely following the details found in [188], the fundamental TCSM parameters and well-motivated assumptions are

1. The lightest doublet of technifermions (U, D) do not carry color charge.

2. The lightest of the technipions, π_{T1} has decay constant $F_{\pi_{T1}} = F_{\pi_T} \sin \chi$, where $F_{\pi_T} = 246$ GeV as in (6.9) and where χ entails the amount of EWSB produced by the first generation of technipions in a potentially multi-scale paradigm of WTC.

3. Isospin breaking produced by the technidoublet (U, D) must be small.

4. The lightest technimesons are the techni-isospin

   (a) Vectors: $\rho_T^{\pm,0}$ with isospin-1, and ω_T with isospin-0.

   (b) Pseudovectors: $a_T^{\pm,0}$ with isospin-1, and f_T with isospin-0.

   (c) Pseudoscalars: $\pi_{T\,1}^{\pm,0}$ with isospin-1, $\pi_{T\,1}^{\prime 0}$ with isospin-0, and η_T with isospin-0.

5. The longitudinal component of the electroweak bosons V_L ($V_L = W_L^\pm$, Z_L^0) are the superposition of all technipions (from all higher-dimensional representations):

$$|V_L\rangle = \sum_i a_i |\pi_{Ti}\rangle \tag{6.24}$$

   where $\sum_i a_i^2 = 1$. Hence, the π_{Ti} are not mass eigenstates, and the *mixing* angle χ can be defined as

$$|\pi_{T1}\rangle = \sin\chi |V_L\rangle + \cos\chi |\pi_T\rangle, \tag{6.25}$$

   where π_T is lowest *mass* eigenstate of the π_{Ti} states.

6. The low lying states π, ρ_T, a_T, ω_T, and the η_T are decoupled from higher-mass states. Therefore, LSTC together with this assumption simplifies drastically the phenomenological consequences. For isospin symmetry to be approximately exact, one expects:

$$M_{\rho_T} \simeq M_{\omega_T}, \text{ and} \tag{6.26}$$

$$M_{a_T} \simeq M_{f_T} \tag{6.27}$$

7. The TCSM states influence the polarization tensor of the γ and the transverse components of the gauge bosons $V_\perp$, thereby enabling the production processes $\bar{q}q \to \gamma, Z^0 \to \rho_T, a_T, \omega_T$ or $\bar{q}q' \to W \to \rho_T, a_T, \omega_T$, where the latter case shall be one of the studied production processes in the search for WZ resonances.

8. The π_T couplings are expected to be Higgs-like with respect to fermions. Because the π_T couplings to SM fermions are governed by ETC, they are expected to couple

to them in proportion to their mass. Note however, that no such couplings exist for processes of the type $\pi_T \nrightarrow \gamma\gamma$ or $\pi_T \nrightarrow ZZ$ since π_T is a pseudoscalar.

These guidelines were used by the authors of [188] to construct an effective Lagrangian that would describe the collider phenomenology as seen by the LHC experiments. A number of processes are of interest for the LHC, but those that are of particular interest for the searches involving WZ resonances, concern the $\rho_T^\pm$ and $a_T^\mp$ whose possible decay chains are presented in table 6.II. In light of the fact that the TCSM eigenstate π_{T1} is an admixture of the longitudinal bosons V_L and the mass eigenstate π_T (see equation (6.25)), the decay amplitudes can be used to compute the amplitudes for the processes $\rho_T^\pm, a_T \rightarrow W^\pm Z^0$ as shown in figure 6.5 with the coupling constant K as provided
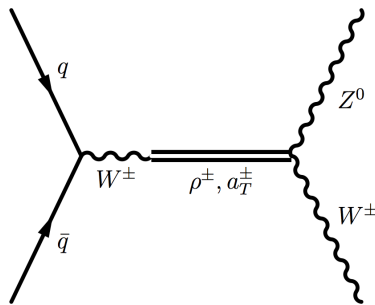
Figure 6.5: The production and decay of the charged ρ_T and a_T with their subsequent decay to WZ. As indicated in table 6.II, this is not the only possible decay process for these technimesons and this fact shall be taken into account in the following chapter.

in table 6.II. These expected technicolor processes formed the primary motivation behind the search for WZ resonances as outlined in the following chapter.

6.4.1 RECENT ATLAS AND CMS RESULTS

The recent discovery of a boson decaying to both $\gamma\gamma$ *and* ZZ^* cannot be accounted for in the TCSM model. The TCSM techni-η, being a pseudoscalar with zero charge may provide at first glance a possible signature mimicking those of the SM Higgs. However, the branching ratios of the techni-η to ZZ^* and WW^* are highly suppressed [214], due in part to its negative parity, whereas its possible decay to $\gamma\gamma$ can reproduce the current experimental measurements [17, 18]. Furthermore, recent measurements have

Decay process	Coupling strength
$\rho_T^\pm \to W_\perp^\pm Z_L^0$	$\mp \sin\chi/2\sin\theta_W$
$\rho_T^\pm \to W_\perp^\pm \pi_T^0$	$\mp \cos\chi/2\sin\theta_W$
$a_T^\pm \to W_\perp^\pm \pi_T^0$	$\pm \cos\chi/2\sin\theta_W$
$a_T^\pm \to W_\perp^\pm Z_L^0$	$\pm \sin\chi/2\sin\theta_W$
$a_T^\pm \to W_L^\pm Z_\perp^0$	$\mp \sin\chi\cot2\theta_W$

Table 6.II: Important decay processes for the $\rho_T^\pm$ and $a_T^\pm$ in TCSM [188, 213].

also confirmed that the discovered boson is of positive parity and spin-0 [52], which are therefore consistent with the SM Higgs hypothesis.

In parallel to these LHC results, the CDF collaboration have updated their Wjj analysis reexamining the contribution from the multijet background [189] resulting in a nullification of the previously observed dijet anomaly [215]. This was a further blow to LSTC as it had promulgated an explanation for this excess [216].

The combination of these results from all three collaborations have put a serious clamp upon TCSM's future prospects. In spite of the fact that it is virtually excluded by experiment, the TCSM can still prove useful because other WTC models, as we shall see in the following section, do contain scalar particles with couplings very similar to those of the SM Higgs.

Perhaps it is possible to revise some of the assumptions enumerated in 6.4 such that the phenomenology of the low-lying states can account for a $I^{PC} = 0^{++}$ particle coupling to mass, although, such a study shall be left to the theorists. For now, we shall complete our motivation for the search for TC particles via the avenues proposed by the so-called minimal walking technicolor models [39, 217].

6.5 MINIMAL WALKING TECHNICOLOR: A PERSPECTIVE

Besides the need for a WTC model with a SM Higgs-like particle, an additional motivation for continuing the search for dynamical symmetry breaking theories relates to another issue plaguing many models with elementary scalar fields (and in fact many BSM theories), that is, they offer no insight into the origin of flavour physics, while TC on the other hand, as just described, not only renders a dynamical mechanism for EWSB, but also provides, through ETC, a possible source for flavour symmetry breaking, as in TC^2.

As was done in the case of LSTC, the authors of [39] wrote down an effective theory describing the phenomenology of minimal walking technicolor (MWT) as potentially seen at the LHC that passes electroweak precision measurements [217].

The following will outline the main aspects of the model and expose its features that are its composite Higgs particle and its PGB bosons, some of which are at the origin of dynamical symmetry breaking, while other particles can decay to WZ, for example. We shall see that it is the global symmetry $SU(4)$ which breaks dynamically down $SO(4)$, its diagonal subgroup.

Using the nomenclature of [39], the theory is based on an $SU(2)$ technicolor gauge group with technifermions in their *adjoint* representation

$$Q_L^a = \begin{pmatrix} U^a \\ D^a \end{pmatrix}_L, \; U_R^a, \; D_R^a, \tag{6.28}$$

where the fields Q_L^a have color index $a = 1, 2, 3$. This was found to be the minimal model which yields conformal (walking) technicolor which is at the same time in accord with the S parameter [218]. In other fermion representations, in order to have a conformal theory depends on the number of technicolors $N = N_{\text{TC}}$ and flavors N_f as depicted in figure 6.6. To make the theory anomaly free [219], one must add the weakly interacting
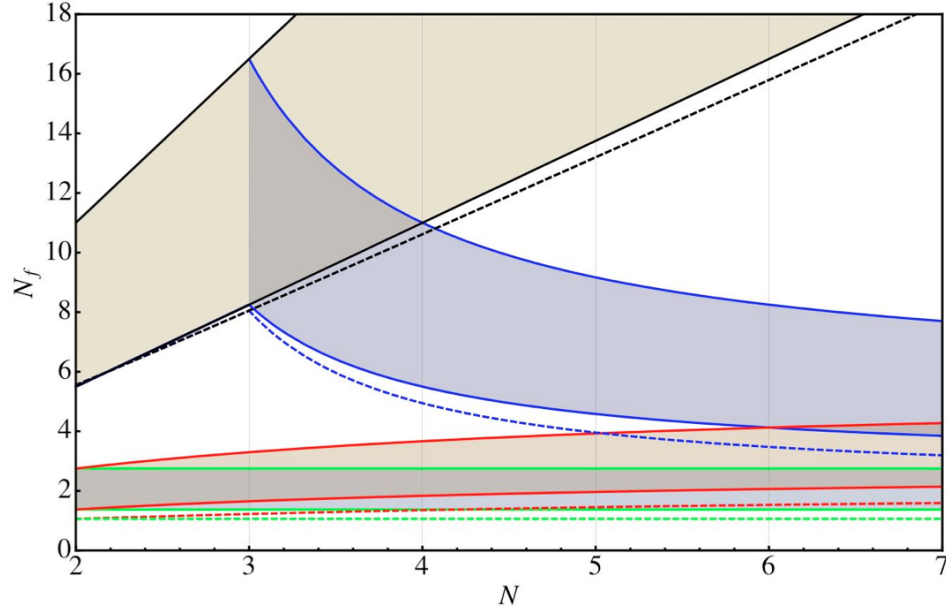
Figure 6.6: As a function of the number of techniflavour N_f and the number of technicolors N, ETC theories are expected to have a conformal fixed point within the solid curves if the fermions are in the fundamental representation (black), the two-index antisymmetric representation (blue), the two-index symmetric representation (red), or the adjoint representation (green) as the minimal model detailed in the main text [218].

technicolor singlet fields

$$L_L = \begin{pmatrix} N \\ E \end{pmatrix}_L, \quad N_R, E_R, \tag{6.29}$$

with appropriate hypercharge assignments [39].

The Lagrangian, as defined in the SM by equation (2.11), can now be rewritten as

$$L_{\mathrm{MWT}} = -\frac{1}{4} F_{\mu\nu}^a F^{a\mu\nu} + i\bar{Q}_L \slashed{D} Q_L + i\bar{U}_R \slashed{D} U_R + i\bar{D}_R \slashed{D}_R \tag{6.30}$$

$$+ i\bar{L}_L \slashed{D} L_L + i\bar{N}_R \slashed{D} N_R + i\bar{E}_R \slashed{E}_R, \tag{6.31}$$

where $F_{\mu\nu}^2 = \partial_\mu A_\nu^a - \partial_\nu A_\mu^a + g_{\mathrm{TC}} \epsilon^{abc} A_\mu^b A_\nu^c$ is the technicolor field strength tensor. The

covariant derivative is define as

$$D_\mu Q_L^a = \left(\delta^{ab} \partial_\mu + g_{\text{TC}} A_\mu^b \epsilon^{abc} - i\frac{g}{2} \mathbf{W}_\mu \cdot \tau \delta^{ab} - i g_Y \frac{1}{2} B_\mu \delta^{ac} \right) Q_L^c, \tag{6.32}$$

where τ are the Pauli matrices and ϵ^{abc} is the antisymmetric tensor.

Moving from the Dirac to the Weyl basis, the technidoublet fields can be written as a tetraplet which transforms under the fundamental representation of $SU(4)$ like

$$Q = \begin{pmatrix} U_L \\ D_L \\ -i\sigma^2 U_R^* \\ -i\sigma^2 D_R^* \end{pmatrix}, \tag{6.33}$$

Assuming the technicolor charged fields form condensates such as

$$\propto \langle \bar{U}_R U_L + \bar{D}_R D_L \rangle, \tag{6.34}$$

these shall break $SU(4) \to SO(4)$ just as QCD breaks $SU_L(2) \otimes SU_R(2) \to SU_V(2)$. This breaking of $SU(4)$ produces 9 Goldstone bosons, 3 of which shall be eaten to give mass to the W and Z.

In constructing the effective theory for the Higgs sector, MWT groups together a composite Higgs σ, its pseudoscalar partner Θ, as well as the nine aforementioned pseudoscalar Goldstone bosons Π with their scalar partners $\tilde{\Pi}$ in the $SU(4)$ invariant matrix [39]

$$M = \left[\frac{\sigma + i\Theta}{2} + \sqrt{2} \left(i\Pi^d + \tilde{\Pi}^d \right) X^d \right] E \tag{6.35}$$

which transforms under $SU(4)$ as $M \to sMs^T$ with $s \in SU(4)$. The X^d for $d = 1$, ..., 9 are the broken generators of $SU(4)$ that leave the vacuum expectation value of M invariant. Three of the nine Goldstone bosons shall become the longitudinal degrees of freedom of the electroweak bosons. The other six shall acquire mass through ETC interactions, but these do not need to be defined further in the context of an effective theory although one could choose to do so.

In the context of searches at the LHC, using an effective theory approach for writing down the MWT Lagrangian has proven to be very useful [220]. From there, the most relevant MWT parameters can be summarized quite succinctly:

- $\tilde{g}$: The coupling strength between the $SU(4)$ vector fields.
- R_1 and R_2: The vector and axial-vector fields (similar to the π_T and ρ_T of LSTC) having masses equal to respectively

$$M_{R_1}^2 = m^2 + \frac{1}{4}\tilde{g}^2(s - r_2)v^2, \text{ and} \tag{6.36}$$

$$M_{R_2}^2 = m^2 + \frac{1}{4}\tilde{g}^2(s + r_2)v^2, \tag{6.37}$$

$$\tag{6.38}$$

where the parameters r_1 (not shown in equation above), r_2, and s parameterize the strength of the interactions between the composite scalars and vectors in units of $\tilde{g}$. v is the EW vacuum expectation value and $m^2 = 12\, M_{\text{Higgs}}^2$.

- Phenomenologically, the ratio $g_L/\tilde{g}$ is of great importance because it controls the amount of mixing amongst the SM+MWT gauge eigenstates and the composite vectors eigenstates. More explicitly,

$$g_{R_{1,2}ff} \sim \frac{g}{\tilde{g}} \tag{6.39}$$

$$g_{R_2WW} \sim \tilde{g} \tag{6.40}$$

$$g_{R_1HZ} \sim \tilde{g} \tag{6.41}$$

where, H is the composite Higgs ($v + H = \sigma$ in (6.35)).

Hence, generically, one can search for MWT successfully in diboson resonances of all types as well as within $\ell\bar{\ell}$ or $\ell\nu$ resonances [220].

In a more precise manner, the phenomenology of MWT at the LHC has been examined in some detail in Ref. [221]. In particular they studied the Drell-Yan process

$$pp \to R_{1,2}^0 \to \ell^+\ell^- \tag{6.42}$$

as well as the charged resonances

$$pp \to R_{1,2}^{\pm} \to \ell^{\pm}\nu \tag{6.43}$$

$$pp \to R_{1,2}^{\pm} \to W^{\pm}Z \tag{6.44}$$

at 14 TeV center-of-mass energies quantifying their respective discovery potential. In this light, using the 2011 data, an ATLAS search [222] for the process (6.42) excluded regions of MWT parameter space in the plane $(M_A, \tilde{g})$, where M_A is the *bare* axial-vector mass [8], the results of which are presented in figure 6.7.
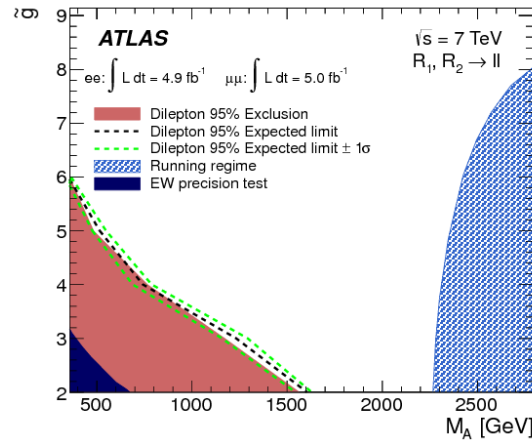
Figure 6.7: Shown here are the observed and expected exclusion regions in the $(M_A, \tilde{g})$ plane at 95% C.L. after combining the ee and $\mu\mu$ dilepton channels. The red area represents the observed exclusion, while the dashed black line indicates the expected exclusion [222].

As a final remark, if we return to the analogy between the phenomenology of QCD and TC, it is important to note that QCD includes a composite scalar, the $f_0(980)$. From there, if we scale its dynamical mass to the EW cut-off scale v under different assumptions of N_{TC}, and include the top-loop contribution evaluated at the cut-off scale v, one obtains a range of values compatible with the experimental measurement of a 125 GeV Higgs. In other words, it is natural to have a scalar in TC [217], and this under a wide range of assumptions.

---

8. In MWT, for a given choice of $\tilde{g}$ and M_{R_1}, M_A and M_{R_2} are uniquely determined.

CHAPTER 7

RESULTS ON THE SEARCH FOR $WZ \to 3\ell\nu$ RESONANCES

> In response to William Gladstone,
> British Chancellor of the Exchequer
> (minister of finance - 1850), who
> asked "what are the practical
> applications of electricity"?
> *One day sir, you may tax it.*
>
> ———————————————
> Michael Faraday

This chapter shall expose and outline the detailed steps that were taken to obtain the results of the search for $WZ \to \ell\nu\ell\ell$ resonances (where $\ell = e, \mu$) found in the conference note [9] on WZ resonances with 13 fb^{-1} of data recorded by ATLAS in 2012 with 8 TeV center-of-mass energy pp colliding beams. These results follow the 2011 publication that used 2011 data at $\sqrt{s} = 7$ TeV [11].

The fully leptonic decay of the $WZ \to \ell\nu\ell\ell$ system provides a unique look into possible resonances that may appear on top of SM WZ production. Unlike $WZ \to \ell\nu jj$ [223] or $WZ \to \ell\ell jj$ production, for example, 4-momentum resolution being substantially better for leptons than for jets improves the sensitivity of the analysis for relatively small $m(WZ)$ (right above its production threshold of $m(Z) + m(W)$) while being competitive at high mass, despite the smaller Z branching fractions to leptons.

7.1 ANALYSIS BLUEPRINT

The theoretical motives for performing this search are generally related to theories with dynamical EWSB, such as technicolor as depicted in the previous chapter, which commonly predict the existence of diboson resonances. Focusing here on WZ resonances, the analysis shall use the following two benchmark models to gauge the presence of a signal:

1. Extended Gauge Model (EGM) W' whose couplings to WZ, $g_{W'WZ}$, follows the relation

$$g_{W'WZ} = g_{WWZ} \left(\frac{m_W}{m_{W'}} \right)^2, \tag{7.1}$$

   where g_{WWZ} is the SM's triple gauge coupling.

2. Low-Scale Technicolor (LSTC) ρ_T together with its axial-vector partner a_T.

In the case of the W', although stringent mass limits have been obtained in the search for $W' \to \ell\nu$, small $W'\ell\nu$ coupling scenarios are plausible thereby rendering the decay process $W' \to WZ$ dominant.

For LSTC, in spite of the known issues already discussed in the context of the recent ATLAS and CMS results concerning the Higgs, the model can still be adopted as a template for other technicolor models such as MWT whose low energy phenomenology can also give rise to WZ resonances [39]. The LSTC parameters used for the signal generation are

- Number of technicolors $N_{\mathrm{TC}} = 4$,
- Charge of the techniquarks U and D are +1 and 0 respectively,
- The mixing angle χ between the electroweak gauge boson W and the technicolor eigenstate Π_T forming the mass eigenstate π_T follows $\sin\chi = 1/3$.

The analysis shall often be divided into its natural four lepton decay channels ($e\nu ee$, $ee\mu\nu$, $e\nu\mu\mu$, and $\mu\nu\mu\mu$) highlighting the different compositions of each, before combining them for the final results.

The *invariant* mass of the 3 lepton plus E_T^{miss} system shall be used as the discriminating variable comparing prediction to observation. Similar to what was done in the CC channel of the vector-like quark search, the missing p_z information is derived assuming the final 3$^{\mathrm{rd}}$ lepton (not the leptons forming the Z) plus the missing transverse momentum have a combined invariant mass equal to $m(W) = 80.4$ GeV. The solution given by equation (5.4) has two solutions, but here we shall pick the smallest one for simplicity if the solution is real, and keep only the real part if the solution is imaginary.

7.2 DATA SELECTION AND MONTE-CARLO SAMPLES

7.2.1 THE 2012 DATASET

The 13.0 fb^{-1} of data collected in 2012 consists of five data-taking periods A to E with slightly differing conditions, those being primarily related to the total number of colliding bunches in the LHC ring. The uncertainty in the total integrated luminosity stands at 3.6%.

A trigger threshold of 24 GeV in E_T (p_T) was used to select electron (muon) events of interest. Their trigger names are respectively `e24i_tight` and `mu24i_tight` for electrons and muons. To recover some of the inefficiencies from the isolation (the `i` in the trigger names) and `tight` quality requirements, the triggers `e60_medium1` (60 GeV E_T threshold) and `mu36_tight` (36 GeV p_T threshold) were also used in tandem with the lower threshold triggers. Together, these formed the nominal trigger selections.

7.2.2 RESONANT SIGNAL GENERATION

The EGM W' and LSTC are implemented in the PYTHIA event generator [127]. Therefore, signal templates for both the W' and ρ_T/a_T were generated with PYTHIA while using the PDF set MRST2007 LO* [224]. Signals with masses of 200 to 2000 GeV in equal steps of 200 GeV were generated for the EGM W'. Similarly, the LSTC ρ_T resonance signals having masses of 250 to 1000 GeV in equal steps of 50 GeV were also produced with LSTC parameters as indicated in section 7.1. Together with other relevant information, table VI.VI in appendix VI lists their cross sections, which range from 1 pb for a 200 GeV W' signal and 0.07 fb for a 2 TeV one. The ρ_T cross sections are roughly 5 to 10 times smaller.

Unfortunately, the PYTHIA implementation of the process $\rho_T/a_T \to WZ$ does not take into account the initial polarization of the ρ_T/a_T resonant state. Therefore, the subsequent leptonic $W \to \ell\nu$ and $Z \to \ell\ell$ decay topologies are slightly askew, in turn affecting the signal acceptances. However, the W' implementation of the decay $W' \to WZ \to \ell\nu\ell\ell$ does fully propagate the polarization information throughout the decay chain. Assuming the technimesons ρ_T and a_T have similar initial polarization

states as those of the W' (a reasonable assumption), the W' signal templates can be used to interpret the LSTC signals simply through a rescaling of their respective cross sections.

7.2.3 BACKGROUND MONTE-CARLO MODELLING

SM WZ production is quite naturally the prominant background for this search, and consequently, accurate MC modelling of it becomes essential. This irreducible background was modelled by POWHEG [225–227], a full NLO QCD event generator in conjunction with PYTHIA for hadronization and the PDF set CT10 [183] containing NLO matrix elements. Detailed information regarding these POWHEG WZ datasets are found in table VI.VII of appendix VI.

Second in importance are the Z+jets backgrounds where the Z decays leptonically and where one of the jets feigns the signature of either an electron or a muon. As mentioned previously, this shall be modelled by virtue of data-driven techniques discussed in section 7.5, however the results shall nonetheless be compared to MC events generated once again by POWHEG. Further information regarding the MC can be found in table VI.VIII, again in appendix VI.

All other backgrounds considered and their MC modelling are summarized in table 7.I.

Background	Generator	PDF set
ZZ	POWHEG [225–227]	CT10 [183]
Z+jets		
WW	MC@NLO [181] for $q\bar{q}$ annihilation gg2WW [228] for gluon fusion	
$Z\gamma$	SHERPA [175]	
$W\gamma$	ALPGEN [178]	
$t\bar{t}$	MC@NLO [181]	CTE6L1 [229]
Single top	ACERMC [230]	

Table 7.I: Generators and PDF sets used to model the tertiary (in importance) backgrounds.

7.3 OBJECT SELECTIONS

The present section discusses how electrons, muons, jets, and E_T^{miss} are defined and handled in this analysis.

7.3.1 ELECTRONS

Electron candidates are selected differently depending on whether they were the deduced product of a Z or W. Table 7.II enumerates the various electron selections.

The isolation selections contain intricate corrections to the energies surrounding the electrons as a function of p_T as well as corrections associated to the effects of pile-up. The energy of the electron is deduced entirely from calorimeter measurements and reconstruction. If the electron track contains at least 4 silicon hits, the track ϕ and η coordinates are used to set the electrons direction of motion, otherwise the calorimeter cluster angular measurements are used.

7.3.2 MUONS

Muon candidates are required to be successfully reconstructed by the *Staco* [116] algorithm combining tracks from both ID and MDT (see section 3.8.2 for details). The selection criteria are presented in table 7.III.

Regarding the isolation criteria, the second arguments after the AND statements only affect muons with p_T < 25 GeV. This selection only applies to a possible fourth muon whose p_T lies between 20 and 25 GeV. Events with such a muon shall be vetoed in order to be orthogonal to other diboson analyses involving 4 final state leptons in the future prospect of combining the results.

7.3.3 JETS AND E_T^{MISS}

Topological clusters recombined with the anti-k_T algorithm with a cone size of $R = 0.4$ form the basic set of jet candidates. Jets are further required to be reconstructed with an $|\eta| < 4.5$ (which uses the maximal fiducial region of the detector of $|\eta| < 4.9$) and

Variable	Selection
Transverse momentum	$p_T > 25$ GeV
Pseudo-rapidity	$|\eta| < 2.47$ excluding the region $1.37 < |\eta| < 1.52$
Quality Definition	`medium++` (for $Z \to ee$) `tight++` (for $W \to e\nu$)
B-layer hit	Required if expected*
PV to reconstructed track distance	$|z_0 \sin\theta| < 0.4$ mm $\frac{d_0}{\sigma_{d_0}} < 3$
Isolation	$\frac{E_T^{\not{e}}}{E_T^e}$ (calo) < 0.16 in $\Delta R \le 0.3$ $\frac{p_T^{\not{e}}}{p_T^e}$ (track) < 0.16 in $\Delta R \le 0.3$

*B-layer only goes up to $|\eta| < 2.0$ and has some dead cells

Table 7.II: Selections imposed to define an electron candidate.

with a $p_T > 25$ GeV. Addition quality selections are imposed to reduce the uncertainties on JES and JER.

Missing transverse energy is calculated as the negative sum of all reconstructed objects up to an $|\eta| < 4.5$.

7.4 EVENT SELECTIONS

The event-by-event selections proceeds as follows:

- Count 3 well-reconstructed[1] leptons (e or μ) with $p_T > 25$ GeV with no extra fourth lepton with $p_T > 20$ GeV.
- Require one pair of opposite sign same flavour leptons to have a combined invariant mass to be within 20 GeV of the Z boson, i.e.

$$|m(\ell^+, \ell^-) - m(Z)| > 20 \text{ GeV}. \tag{7.2}$$

In the advent that two pairs satisfy (7.2), the pair with an invariant mass closest to

---

1. Selections details given in section 7.3.

Variable	Selection
Transverse Momentum	$p_T > 25$ GeV
ID hit requirements	# Pixel Hits + # Traversed Dead pixels > 0
	# SCT hits + # Traversed Dead SCT sensors > 4
	# Traversed Dead Pixels + # Traversed Dead SCT sensors < 3
	TRT hit requirements*
PV to reconstructed track distance	$\left\| z_0 \sin \theta \right\| < 1$ mm
	$\left\| \frac{d_0}{\sigma_{d_0}} \right\| < 3$
Isolation	$\frac{E_T^{\ell}}{E_T^e}$ (calo) < 0.2 AND $0.014 \times p_T - 0.15$ in $\Delta R \leq 0.3$
	$\frac{p_T^{\ell}}{p_T^e}$ (track) < 0.15 AND $0.01 \times p_T - 0.10$ in $\Delta R \leq 0.3$

*See 5.III for the particulars.

Table 7.III: Selection criteria used to defined a muon candidate.

$m(Z)$ is chosen.

- $E_T^{\mathrm{miss}} > 25$ GeV

- The remaining lepton, that does not reconstruct the Z, together with the missing E_T must have a combined transverse mass less than 100 GeV. Because the signals (either the W' or the ρ_T/a_T) are not expected to produce off-shell W bosons, this selection essentially ensures a reduction in yields of backgrounds caused by mis-reconstructed or mis-measured leptons and E_T^{miss}.

- Taking advantage of the fact that the signal, if heavy, will be produced at rest thereby forcing its decay products, the W and Z bosons, to be more or less back-to-back as heuristically drawn in figure 7.1, the selections

$$|\Delta y(W, Z)| < 1.8, \text{ AND} \tag{7.3}$$

$$|\Delta \phi(W, Z)| > 2.6 \tag{7.4}$$

are imposed. Figures 7.2 presents the MC only distributions of these variables for the sum of all backgrounds and the W' signal (the same is observed for the ρ_T/a_T signal).
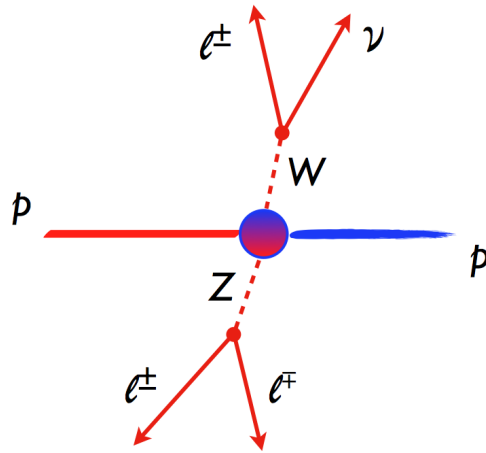
Figure 7.1: Schematic view of the decay products stemming from the hypothetical production of a W' or ρ_T.

(a) $\Delta y(W, Z)$ (b) $\Delta y(W, Z)$
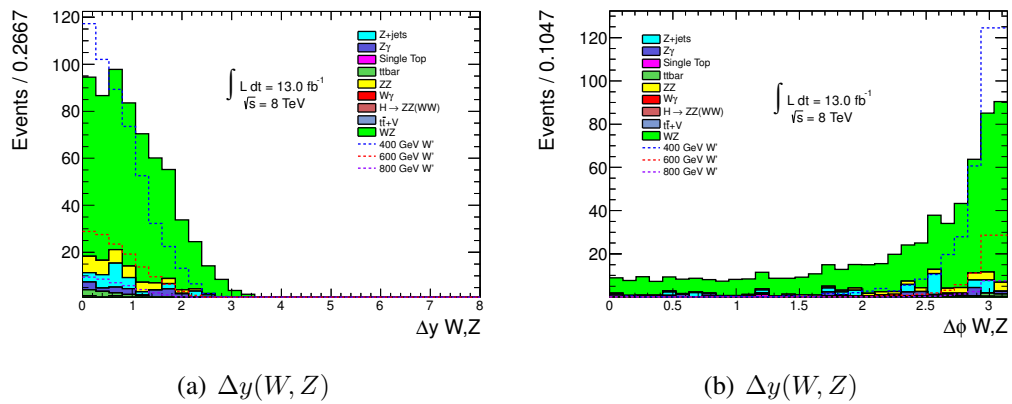
Figure 7.2: Background and signal comparisons in the angular variables $\Delta y(W, Z)$ in (a) and $\Delta\phi(W, Z)$ in (b).

Once the $\Delta y(W, Z)$ and $\Delta \phi(W, Z)$ selections are put into effect along with all the others, this defines the signal region.

Inverting the selections:

$$|\Delta y(W, Z)| > 1.8|, \text{ OR} \tag{7.5}$$

$$|\Delta \phi(W, Z)| < 2.6 \tag{7.6}$$

defines the WZ control region orthogonal to the signal region by construction.

7.4.1 OVERLAPPING OBJECTS: REMOVAL PROCEDURE

In order to avoid double counting objects and improve the jet and lepton identification efficiencies, the following overlap removal procedures were put in place.

1. Remove jets that are within $\Delta R = 0.3$ of an electron.

2. Discard any electron within a $\Delta R = 0.1$ of a muon.

7.4.2 CORRECTIONS AND RE-CALIBRATIONS

As was done in the VLQ analysis, a number of performance tools were used (see beginning of sections 5.4) providing the means through which LES, JES, LER, and missing E_T pile-up uncertainties, to name just a few, were calculated. To reiterate their respective uses, the tools used were (with in parentheses the ATLAS tool name and version for ATLASinternal purposes only):

Pile-up Reweighting (PRW) (PileupReweighting-00-02-08)

The $\langle \mu \rangle$ distribution in MC is reweighted event-by-event to match the distribution in data.

Jet Calibration (ApplyJetCalibration-00-02-09)

Correct JES calibration.

Compute JES/JER uncertainties.

Jet Resolution Smearing (ApplyJetResolutionSmearing-00-00-03)

Modify MC jet resolution to match the data.

E/γ Calibration (egammaAnalysisUtils-00-03-55)

> Recalibrate electron energy scale (EES).

> Modify MC electron energy resolution (EER) to match the data.

> Compute electron reconstruction efficiency scale factors (SF) to be applied to MC.

> Calculate uncertainties related to EES, EER, and electron reconstruction efficiency scale factors.

$E_T^{\textbf{miss}}$ **Calibration** (MissingETUtility-01-01-02)

> Recompute the missing E_T using only the analysis specific objects.

> Calculate E_T^{miss} uncertainties due to pile-up and soft terms [2].

Muon Reconstruction Efficiency (MuonEfficiencyCorrections-02-01-05)

> Compute muon reconstruction SF that are applied to MC to match the data.

Muon Calibration (MuonMomentumCorrections-00-07-01)

> Correct muon energies

> Compute uncertainties related to muon 4-momentum.

Lepton Trigger Efficiency (TrigMuonEfficiency-00-02-17)

> Obtain and apply to MC lepton trigger efficiency SF.

> Compute uncertainties related to lepton trigger efficiencies.

Isolation Efficiency (IsolationScaleFactors-01-02)

> Correct isolation efficiencies of MC as seen in the data.

These tools are of course essential to compute systematic uncertainties, the results of which shall be detailed in section 7.6.

Lepton efficiency scale factors are measured in Z events as a function of E, p_T , η, and ϕ.

7.4.3   EVENT CLEANING

Software developments in 2012 lead to the possibility of restarting the timing, trigger, and control (TTC) subsystems during a collision run thereby enabling the experiment to

---

2. The cell energy deposits that do not enter into the computation of any fully reconstructed object.

continue to gather data without a dumping of the beam. However, during such a restart, for the lumi-block just after the restart, event data may be missing and therefore such events are rejected.

If a jet with p_T greater than 20 GeV fell either into noisy Tile calorimeter cells or in the FCAL region defined by $|\eta| < 3.2$ and $1.6 < \phi < 3.1$ (this applied only to periods C1-C8) were vetoed. This jet cleaning precedure was then also applied to MC to appropriately model its effects.

7.5 ESTIMATING THE $\ell\ell$+JETS BACKGROUND

The relatively high cross section of Z+jets with respect to SM WZ production makes it a difficult background to estimate given the known difficulty in measuring the rate at which jets are mis-identified as leptons. Hence, this rate shall be measured in two separate event types: dijet and Z-tagged events, the results of which shall be compared later on. Both methods aspire to measure precisely the *fake rate* (FR) as a function of lepton p_T , defined by the ratio

$$f(p_T) = \frac{\#\ \text{good}\ leptons}{\#\ \text{bad}\ leptons} \tag{7.7}$$

where *good* and *bad* lepton definitions are found in table 7.IV. The requirement for *good* leptons to fail $\left|\frac{d_0}{\sigma_{d_0}}\right| < 3$ in Z-tagged events is enforced to reduce the contamination of the WZ background in the phase space where the fake rate is measured and increase the proportion of non-prompt muons.

7.5.1 FAKE RATE ESTIMATION IN DIJETS EVENTS

The data used to measure the fake rate in dijet events were selected with the triggers

- `e24vh_loose0` for the selection of *good* electrons,
- `e22vh_loose0` for *bad* electrons,
- `mu24_tight` for *good* muons, and finally
- `mu22_IDTrkNoCut_tight` for *bad* muons.

	Dijet Sample	Z-tagged
Good Electron	Passes all selections listed in sections 7.3.1	Passes all selections listed in section 7.3.1
Good Muon	Passes all selections listed in section 7.3.2	Passes all selections listed in section 7.3.2 **except** fails $\left\|\frac{d_0}{\sigma_{d_0}}\right\| < 3$
Bad Electron	Passes all selections of section 7.3.1 **except** fails `tight++` but passes `medium++`, and fails one of the isolation requirements	Passes all selections of section 7.3.1 **except** fails `tight++` but passes `medium++`, and fails one of the isolation requirements
Bad Muon	Passes all selections listed in section 7.3.2 **except** fails isolation criteria	Passes all selections listed in section 7.3.2 **except** fails $\left\|\frac{d_0}{\sigma_{d_0}}\right\| < 3$ and isolation criteria

Table 7.IV: *Good* and *Bad* lepton definitions depending on whether the fake rate is measured in dijets or Z-tagged events.

The number in each of these trigger names refers to the E_T (p_T) threshold (in GeV) applied upon candidate electrons (muons). For electron candidates, `vh_loose0` signifies that `loose` selection requirements were applied in addition to some hadronic suppression, but without any isolation criteria. For muons, `tight` selections are applied with the exception that for *bad* muons, ID track selections are relaxed. These looser prescaled trigger requirements were chosen to minimize the impact of possible biases of the analysis' nominal triggers. Furthermore, the choice of triggers for the *good* and *bad* leptons stemmed from the need to retain as much statistics as possible (low prescaling) while having relaxed trigger criteria in order to capture all possible sources susceptible of faking lepton signatures.

Dijet events are then collected by imposing the selection criteria:

- $m_T(W(\ell, \nu)) < 40$ GeV
- $E_T^{\text{miss}} > 25$ GeV
- $\Delta\phi(\text{jet}_{\text{tag}}, \text{jet}_{\text{probe}}) > 2.5$ rad

The $\text{jet}_{\text{probe}}$ is the lepton-like jet with which the fake rate or the number of *good* and *bad* leptons are assessed. The jet_{tag} on the other hand must satisfy the selections given in

section 7.3.3 with the additional requirement that its jet vertex fraction [3] JVF > 50% to minimize the effects of pile-up. Requiring low $W(\ell, nu)$ boson transverse mass is necessary to suppress the contamination of $W(\ell, \nu)$+jets events where the final state lepton is *real* while the goal of the method is to measure the rate of *good* and *bad* leptons when both have been mis-identified as leptons. The E_T^{miss} selection is to make the measurement in a region of phase space where the jets total energy have also been potentially mis-measured. Finally, demanding that the lepton (or jet$_{\mathrm{probe}}$) and jet$_{\mathrm{tag}}$ be close to being back-to-back in ϕ increases the probability that the reconstructed lepton in such events are not leptons, but mis-identified jets given the known very high cross section of dijet events.

Once the selections applied, the *good* and *bad* lepton distributions are obtained and shown in figure 7.3.

A number of systematics sources were considered for computing the uncertainties upon $f(p_T)$ [4]. In short, the sources considered were

- Biases associated to the choice of triggers.
- Uncertainties associated to the p_T threshold of the tagged-jet.
- Bias associated with assumption that the jet kinematics and light versus heavy flavour (HF) compositions in the region where the FR is measured are the same as those where it shall be applied.
- The subtraction of MC predicted yields of *real* leptons (from W+jets for example) that contaminate primarily the *good* lepton distributions as seen in figure 7.3.

The uncertainties of each of the sources are assumed to be uncorrelated and their final measured uncertainty is presented in table 7.V along with a brief description of the method used to quantify these systematic uncertainties.

---

3. Fraction of tracks within the jet cone pointing to the PV.

4. A small dependence on η was observed, but was neglected due to lack of statistics, especially in Z-tagged events for which a p_T dependence was neglected as well. The various sources of systematic uncertainties considered shall cover this bias.

(a) *good* electron

(b) *bad* electron

(c) *good* muon

(d) *bad* muon
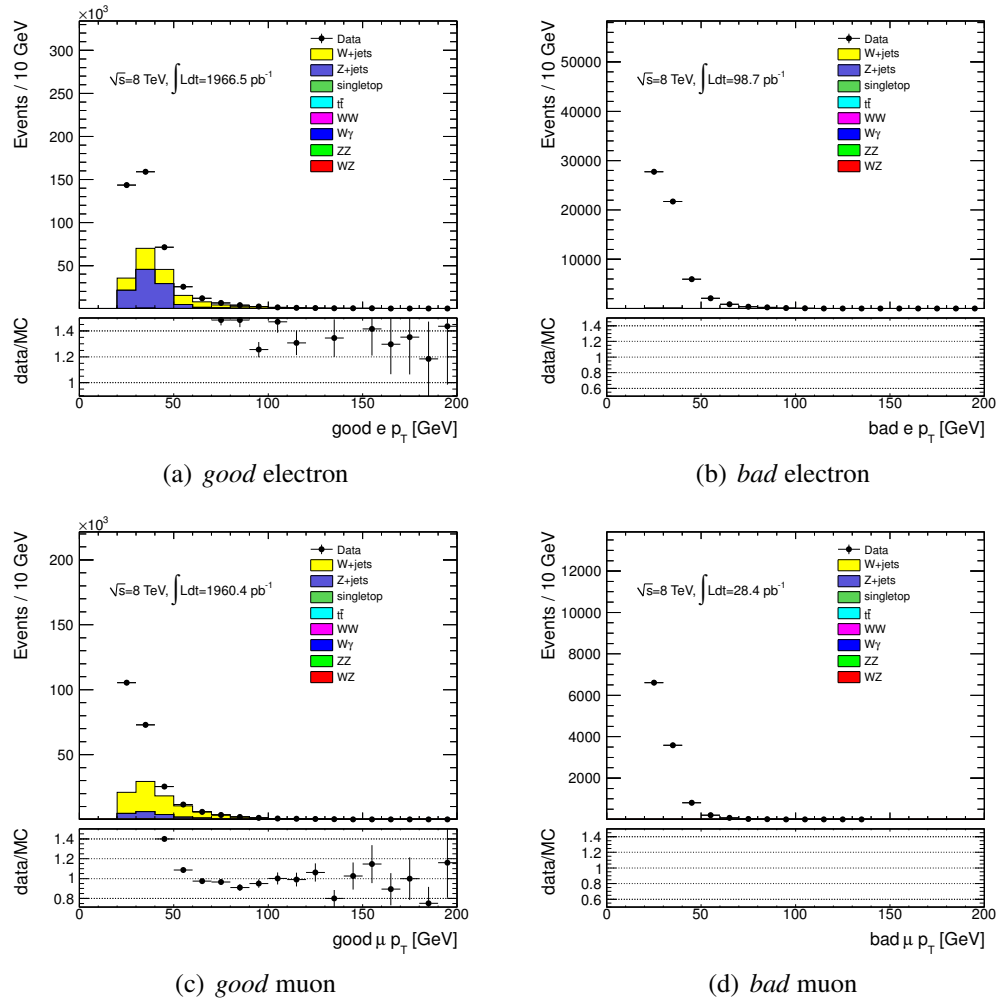
Figure 7.3: *Good* and *bad* lepton p_T distribution in dijet events. The overlaid MC indicates the predicted amount of real lepton contamination. The contributions from all non-fake backgrounds are subtracted distributions before computing the fake rate ratio.

Uncertainty	Estimation method	Computed Uncertainty	
		Electron FR	Muon FR
Trigger Bias	Loosened the trigger requirements upon the *good* and *bad* lepton events		
Tag-jet p_T	The tagged jet p_T thresholds are varied up and down by 5 GeV		
Jet kinematics/ HF composition	The nominal FR is compared to the rates computed with a b-tagged jet$_{probe}$ and excluding a b-tagged jet$_{probe}$		
MC subtraction	The uncertainty on all *real* lepton SM contributions is conservatively set to 10% enveloping uncertainties associated to the backgrounds acceptances		

Table 7.V: Methods used to estimate the uncertainties associated to the measurement of the fake rate (equation (7.7)) in **dijet** events. The results for both the electron and muon FR are given in the figures.

176

Combining in quadrature these uncertainties, we arrive at the measured fake rates for specified p_T binned regions. The final results for the electron FR are given in table 7.VI while the results for the muon FR are presented in table 7.VII.

p_T range [GeV]	Measured Electrons FR
[25,30[	$0.196 \pm 0.001^{+0.029}_{-0.027}$
[30,35[	$0.205 \pm 0.001^{+0.036}_{-0.027}$
[35,40[	$0.209 \pm 0.001^{+0.042}_{-0.030}$
[40,45[	$0.221 \pm 0.002^{+0.072}_{-0.051}$
[45,55[	$0.227 \pm 0.002^{+0.083}_{-0.046}$
[55,70[	$0.232 \pm 0.002^{+0.060}_{-0.045}$
[70,100]	$0.256 \pm 0.004^{+0.103}_{-0.077}$

Table 7.VI: The final measured electron fake fates as a function of p_T [GeV] with the statistical and systematic uncertainties.

p_T range [GeV]	Measured Muon FR
[25,30[	$0.185 \pm 0.001^{+0.030}_{-0.047}$
[30,35[	$0.183 \pm 0.001^{+0.024}_{-0.043}$
[35,40[	$0.161 \pm 0.001^{+0.026}_{-0.041}$
[40,50[	$0.130 \pm 0.001^{+0.039}_{-0.035}$
[50,70[	$0.037 \pm 0.001^{+0.101}_{-0.037}$
[70,100]	$0.001 \pm 0.001^{+0.114}_{-0.001}$

Table 7.VII: The final measured muon fake fates as a function of p_T [GeV] with the statistical and systematic uncertainties.

7.5.2 FAKE RATE ESTIMATION IN Z-TAGGED EVENTS

Turning to the estimation of the fake rate (equation (7.7)) in Z+jets events, recall that the requirement on *good* and *bad* leptons are tabulated 7.IV. This *good* and *bad* selection applies only to the third lepton, while the first two must pass the nominal criteria and satisfy equation (7.2).

From there, events satisfying the requirements

- $E_T^{\text{miss}} < 25$ GeV,

- $m_T(\ell_{3^{\text{rd}}}, E_T^{\text{miss}}) < 40$ GeV, and

- The invariant mass of the three leptons in the event has $|m(\ell,\ell,\ell) - m(Z)| > 20$ GeV,

shall be used to compute the yields of *good* and *bad* **electrons**. The low E_T^{miss} selection ensures the enrichment of the sample in Z+jet events and assures the orthogonality of the sample, while the second attempts to mitigate the contributions from real leptons coming from SM WZ events. The third selection criteria is necessary to remove QED FSR of the type Z+jet $\to \ell\ell + \gamma$+jet when the photon is mis-identified as an electron.

For muons, the single requirement $\left|\frac{d_0}{\sigma_{d_0}} > 3\right|$ is used to extract a sample dominated by non-prompt[5] muon.

With these selections defined, we obtained the p_T distributions of *good* and *bad* leptons as seen in figure 7.4 where the Z+jets MC is added for comparison. Given the significantly smaller statistics in comparison with the dijet estimation, a single FR for electrons and muons (one for each) shall be calculated, i.e. without any p_T dependence.

As was done for the measurement in dijet events, a variety of systematics uncertainties were considered in the estimation of the FR in Z+jet events. These uncertainties are summarized by the following.

- Biases associated to the differences in trigger efficiencies.

- Uncertainties originating from the assumption that the kinematics of the *good* leptons are identical to those of *bad* leptons.

- Differences that arise from the fact that the FR is measured in a region with low missing E_T, whereas it is applied in a region with high missing E_T.

- For the muon FR, it is measured in a region with high d_0 significance, i.e. $\left|\frac{d_0}{\sigma_{d_0}}\right| >$ 3, but applied in a region with low d_0 significance. This constitutes two sources of biases, one for the fake rate itself, and the other for kinematical differences in the *good*/*bad* lepton p_T's. Both will need to be assessed separately.

The methods used to estimate these uncertainties along with the final result is presented in table 7.VIII.

---

5. Originating from heavy flavour decays.

(a) *good* electron

(b) *bad* electron

(c) *good* muon

(d) *bad* muon
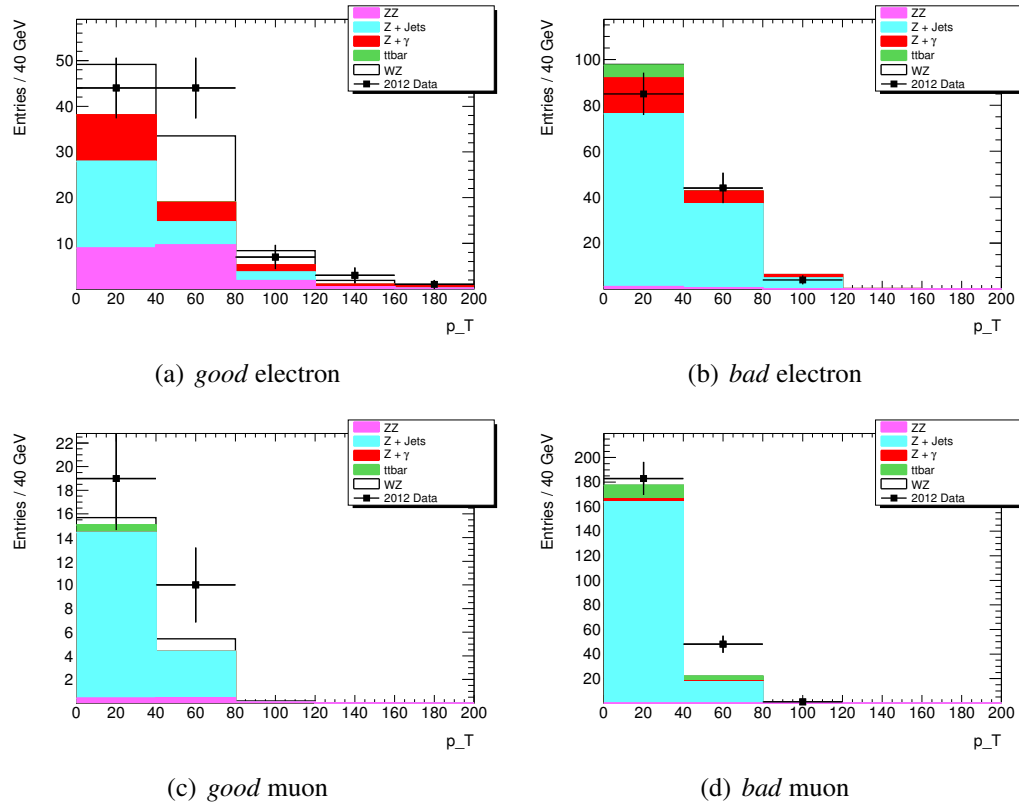
Figure 7.4: *Good* and *bad* lepton p_T distribution in Z+jets events as defined in the text. The overlaid MC gives an indication of the fake rate had we relied purely on MC. The contributions from all non-fake backgrounds (i.e. not including Z+jets) are subtracted to the data distributions before computing the fake rate ratio.

Uncertainty	Estimation method	Computed Uncertainty	
		Electron FR	Muon FR
Trigger Bias	The electron (muon) FR was computed using only muon (electron) triggers in $\mu\mu e\nu$ ($ee\mu\nu$) events	Effects found were negligible: **< 1 %**	Effects found were negligible: **< 1 %**
Good versus *bad* lepton kinematics	Compared the p_T distribution of *good* and *bad* lepton in Z+jets MC. The differences per-bin are assessed as a systematic uncertainty		
Low versus high E_T^{miss} FR	In Z+jets MC, the measured FR in low $E_T^{\mathrm{miss}} < 25$ GeV is compared to the FR in high $E_T^{\mathrm{miss}} > 25$ GeV	The difference in the FR: **5%**	N.A.
Electron kinematics in low versus high E_T^{miss} region	Compared the p_T distribution of electrons in Z+jets MC in a low and high E_T^{miss} regions. The differences per-bin are assessed as a systematic uncertainty		N.A.
Low versus high d_0 significance FR	In Z+jets MC, the measured FR in low d_0 significance is compared to the FR in high d_0 significance	N.A	Assign a correction factor: 35% Uncertainty: 15%
Muon kinematics in low versus high d_0 significance regions	Compared the p_T distribution of muons in Z+jets MC in a low and high d_0 significance regions. The differences per-bin are assessed as a systematic uncertainty	N.A.	

Table 7.VIII: Methods used to estimate the uncertainties associated to the measurement of the fake rate (equation (7.7)) in Z-**tagged** events. The results for both the electron and muon FR are give in the figures.

Using these systematic uncertainty estimates, we arrive at the resulting fake factors:

$$f(\text{electrons}) = 0.300 \pm 0.129 \text{ (stat.)} \pm 0.035 \text{ (syst.)} \qquad (7.8)$$

$$f(\text{muons}) = 0.174 \pm 0.039 \text{ (stat.)} \pm 0.029 \text{ (syst.)} \qquad (7.9)$$

In both cases, we find that statistical uncertainties dominate.

7.5.3 COMPARISON OF THE METHODS AND FINAL $\ell\ell$+JET EXPECTED YIELDS

After constructing a data template consisting of 2 *good* leptons + 1 *bad* lepton, the FR is then applied to these events just as if it were a reweighting scheme. The end result provides an estimate of the expected yields for the $\ell\ell$+jet background.

The predicted yields of mis-identified leptons between the two DD calculations and MC are shown in table 7.IX in each of the four lepton decay channels.

Region of interest	Estimation type	$e\nu ee$	$ee\mu\nu$	$e\nu\mu\mu$	$\mu\nu\mu\mu$
WZ Control Region	DD Z-jets using **dijet** events	$6.1 \pm 1.3^{+1.3}_{-1.0}$	$13.6 \pm 1.6^{+3.3}_{-3.7}$	$7.8 \pm 1.5^{+2.1}_{-1.5}$	$17.7 \pm 1.8^{+3.8}_{-4.6}$
	DD Z-jets using Z-**tagged** events	$8.85 \pm 1.45^{+3.98}_{-3.98}$	$15.19 \pm 1.59^{+4.18}_{-4.18}$	$11.78 \pm 1.67^{+5.25}_{-5.25}$	$19.22 \pm 1.78^{+5.29}_{-5.29}$
	MC Z+jets	7.6 ± 3.8	1.8 ± 1.5	6.8 ± 3.6	3.8 ± 2.7
	MC top	0.2 ± 0.2	1.2 ± 0.7	1.6 ± 0.5	1.7 ± 0.7
Signal Region	DD Z-jets using **dijet** events	$4.0 \pm 1.0^{+1.1}_{-0.8}$	$6.6 \pm 1.1^{+2.0}_{-1.8}$	$11.0 \pm 1.7^{+3.0}_{-2.2}$	$8.0 \pm 1.2^{+2.4}_{-2.3}$
	DD Z-jets using Z-**tagged** events	$5.36 \pm 1.17^{+2.39}_{-2.39}$	$7.99 \pm 1.15^{+2.20}_{-2.20}$	$15.16 \pm 2.14^{+6.75}_{-6.75}$	$10.04 \pm 1.28^{+2.76}_{-2.76}$
	MC Z+jets	4.8 ± 3.3	0.0 ± 0.0	8.6 ± 3.8	3.0 ± 3.0
	MC top	0.1 ± 0.1	0.1 ± 0.1	0.4 ± 0.2	0.3 ± 0.2

Table 7.IX: Comparison between the data-driven predictions of the $\ell\ell$+jet background using dijet and Z-tagged event samples for the fake rate measurement together with MC prediction in both the WZ control region and signal region.

Separating out the predicted yields in each of the channels enables one to notice that the expected rate of fakes from MC is significantly smaller in the case where the third lepton is a muon while the prediction of MC in the case where the third lepton is an electron is decent. This is perhaps a little unexpected although the isolation criteria

in the context of heavy flavour decays may probably not be well represented by MC simulation.

The agreement between the dijet and Z-tagged methods for predicting the rate of Z+jets events lends confidence to the final prediction of $\ell\ell$+jet.

Because of its smaller uncertainties, the dijet method is chosen for the nominal prediction of Z+jets. However, an additional systematic constructed from the differences between the dijet and Z-tagged predictions shall be taken into account when interpreting the final results in section 7.9.

As a final crosscheck, figure 7.5 presents the inclusive distributions for $m(Z)$, $m_T(W)$, $p_T(Z)$, $p_T(W)$, and $m(WZ)$ in the Z+jets control region [6], defined by

- $E_T^{\mathrm{miss}} < 25$ GeV, and
- $m_T(W(\ell, \nu)) < 25$ GeV.

These selection criteria both serve to increase the proportion of Z+jets in three lepton events.

7.6   EVALUATION OF THE SYSTEMATIC UNCERTAINTIES

7.6.1   BACKGROUND NORMALIZATION UNCERTAINTIES

All major backgrounds backgrounds modelled by MC were ascribed, as is ordinary, the following uncertainties on their cross section

- $\sigma(WZ) = 18.5 \pm 1.3$ pb or a 7% uncertainty [231],
- $\sigma(ZZ) = 5.96 \pm 0.30$ pb or a 5% uncertainty [232],
- $\sigma(Z\gamma) = 14.7 \pm 1.2$ pb or a 8% uncertainty [233].

However in light of recent approximate NNLO calculations [234] for high p_T observables, an additional 5% uncertainties was added in quadrature to $\sigma(WZ)$ yielding a total uncertainty of $\frac{\delta\sigma}{\sigma} = 0.085$.

---

6. Under the specific circumstances where the one of the jets is mis-identified as an electron.

(a) $m(Z)$

(b) $m_T(W)$

(c) $p_T(Z)$

(d) $p_T(W)$

(e) $p_T(W)$
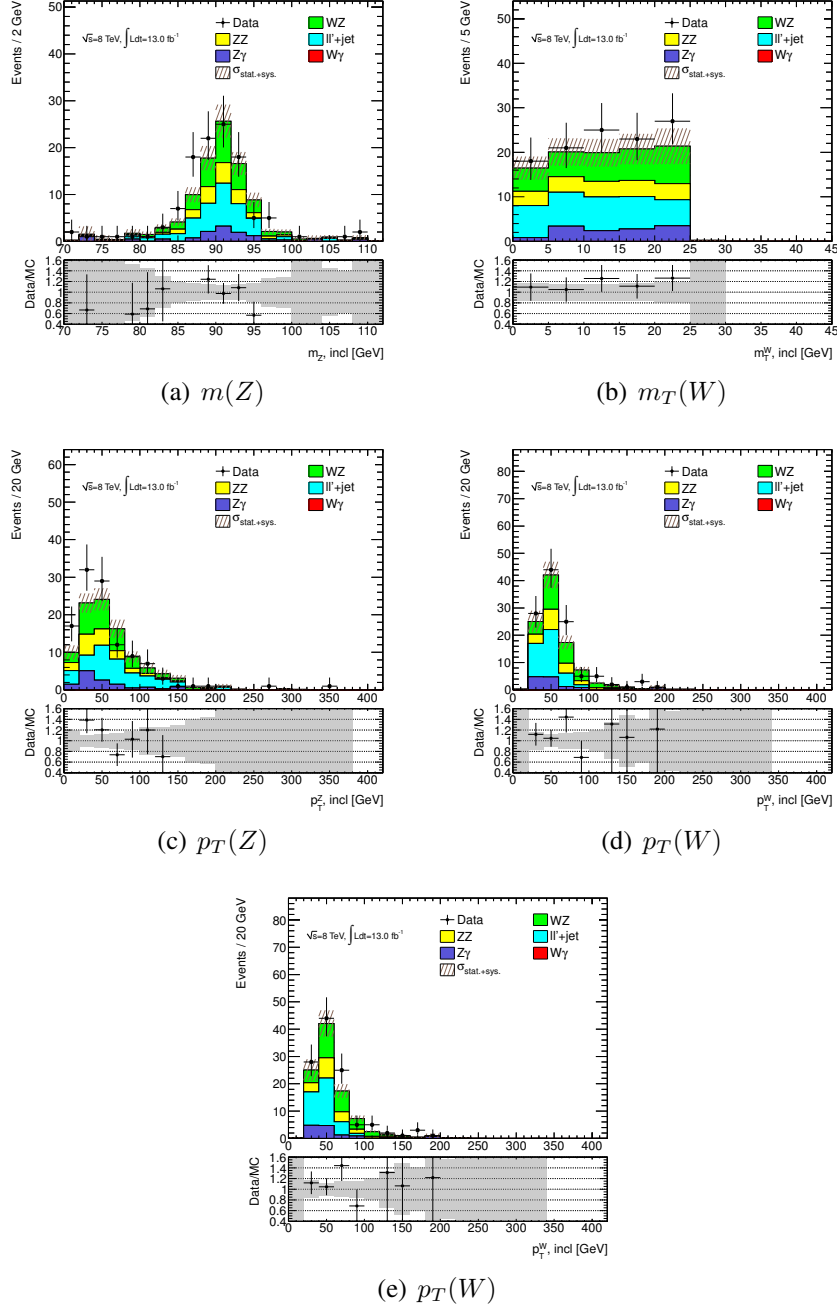
Figure 7.5: Observation versus prediction for several important physical quantities, namely, the $m(Z)$, $m_T(W)$, $p_T(Z)$, $p_T(W)$, and lastly the $m(WZ)$. The hashed error bars include all systematic uncertainties as discussed in section 7.6.

7.6.2 BACKGROUND SHAPE UNCERTAINTIES

Due to low statistics of all backgrounds in the high $m(WZ)$ mass region, an extrapolation method was devised. It consists of fitting the SM WZ background in the region $[500, \infty)$ with a single exponential function

$$N_{WZ}(x) = c_1 e^{k_1 x} \qquad (7.10)$$

and fitting the sum of all non-WZ backgrounds in the region $[300, \infty[$ with the sum of two exponentials

$$N_{\text{non-}WZ}(x) = c_2 e^{k_2 x} + c_3 e^{k_3 x}, \qquad (7.11)$$

where c_i and k_3 are independent parameters. This fitting procedure is repeated in each of the four channels separately yielding the results found in figure 7.6 for the fit to the SM WZ background and in figure 7.7 for the fit to the non-WZ backgrounds. At high mass, the background extrapolation fit uncertainties dominate with a 50% uncertainty at $m(WZ) = 800$ GeV and 200% at $m(WZ) = 1200$ GeV.

In this analysis, a good understanding of the irreducible SM WZ background is critical simply because its prediction shall be the basis upon which a potential excess will be judged. The goal here is therefore to determine whether different SM WZ generators predict varying shapes for the $m(WZ)$ invariant mass distribution in the signal region. To this end, the three generators: POWHEG [225–227], SHERPA [175], and MADGRAPH [177], are each compared to each other after normalizing all three to the yields predicted by POWHEG (which is our nominal choice). In an attempt to disentangle the statistical uncertainties from possible shape differences between the generators, three different types of binning choices were made. The first choice having bin delimitation at 0, 200, 300, 600, and 1600 GeV is shown in figure 7.8, with the other two showing very similar outcomes. Focusing on the ratio plots shown in this figure, no clear shape difference is observed between POWHEG and the other two generators, SHERPA and MADGRAPH, beyond statistical uncertainties. Hence, no additional shape systematic based on generator differences is applied in this analysis.

(a) $e\nu ee$

(b) $ee\mu\nu$

(c) $e\nu\mu\mu$

(d) $\mu\nu\mu\mu$
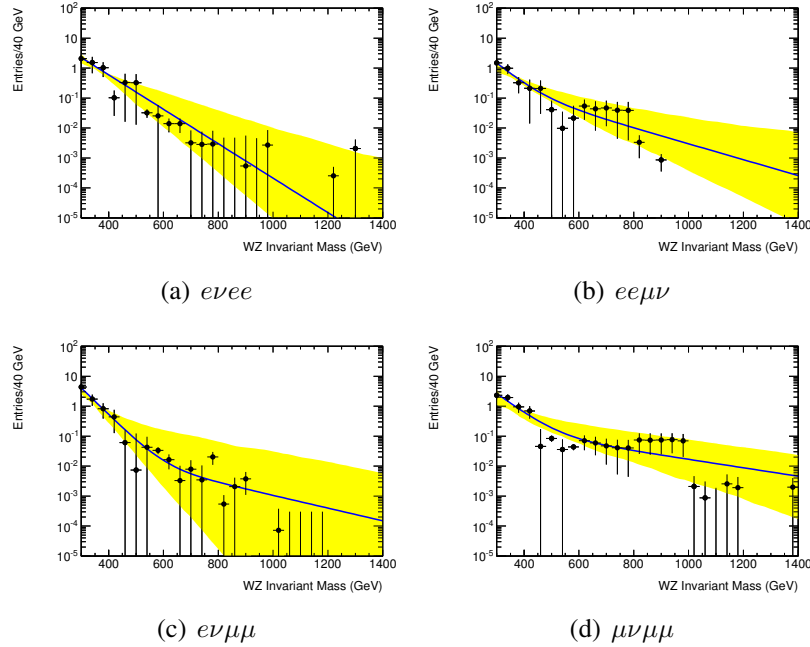
Figure 7.6: Double exponential fits to non-WZ backgrounds in the region $m(WZ) = [300, \infty)$ with uncertainties (yellow bands) obtained in each of the four WZ decay channels.

7.6.3 SIGNAL NORMALIZATION UNCERTAINTIES

The signal acceptances are heavily dependent on the experimentally measured parton distribution function parameters. The uncertainties associated to these parameters translate into uncertainties on the signal acceptances.

As mentioned previously, both the W' and ρ_T/a_T signals were generated using PYTHIA with the PDF set MRST2007 [224]. To estimate the PDF uncertainty, the PDF set MSTW2008 [235] was used as it supersedes MRST2007 and includes 20 independent parameters together with their associated uncertainties. The fiducial acceptance is calculated individually for each upward and downward variation of the parameters by one standard deviation. The total uncertainty on the acceptance is thus derived using

$$\Delta A = \frac{1}{2}\sqrt{\sum_i^{n_{\text{para.}}} \left(A_i^+ - A_i^-\right)^2},\tag{7.12}$$

185

(a) $e\nu ee$ (b) $ee\mu\nu$

(c) $e\nu\mu\mu$ (d) $\mu\nu\mu\mu$
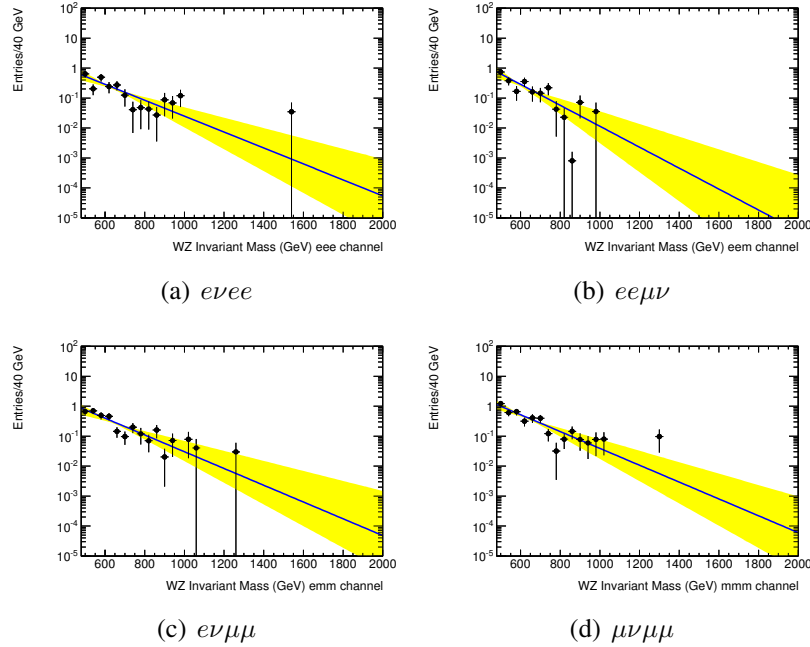
Figure 7.7: Exponential fits to the SM WZ background in the region $m(WZ) = [500, \infty)$ with uncertainties (yellow bands) obtained in each of the four WZ decay channels.

where A_i^+ and A_i^- are respectively the one sigma upward and downward deviations. Computing the uncertainties in this manner essentially averages out the differences between the upward and downward uncertainties. Because MSTW2008 was not used for the generation of the signal samples, a cross-check with the PDF set CT10 [183] was additionally performed. The nominal acceptance difference between the two sets is taken as a systematic although the differences observed were smaller than 0.5%.

The acceptance computations was repeated for each available W' and ρ_T/a_T mass samples. The final results on the PDF uncertainties are summarized in table 7.X.

7.6.4 ENERGY SCALE, RESOLUTION, AND OBJECT IDENTIFICATION UNCERTAINTIES

Using the performance tools listed in section 7.4.2, an event-by-event calculation on various uncertainties is computed. For conciseness, the results of this calculation are presented for SM WZ production in table 7.XI, and for a 800 GeV W' in table 7.XII. Note
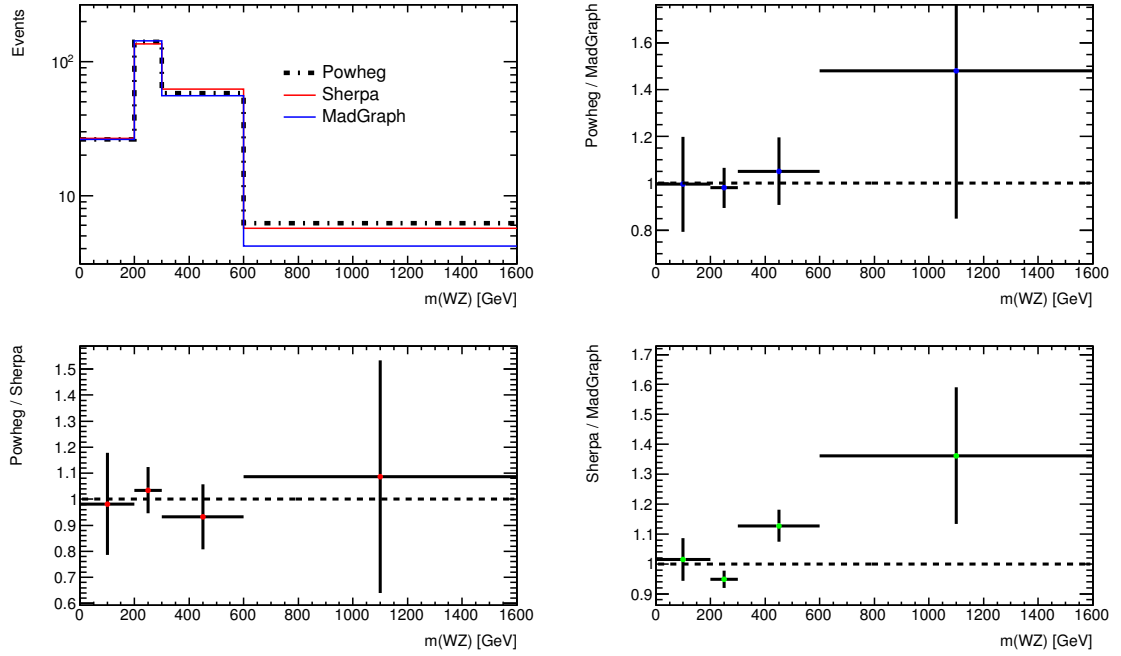
Figure 7.8: Shape comparison between POWHEG, SHERPA, and MADGRAPH with bin delimitation at 0, 200, 300, 600, and 1600 GeV. Uncertainties shown are statistical only.

that all energy scale and resolution variations are propagated to the E_T^{miss} computation.

7.7 *WZ* CONTROL REGION

It is critically important to verify the modelling of the WZ background by POWHEG. Accordingly, the figures in 7.9 show several distributions for important physical variables. The $m(Z)$, $m_T(W)$, $p_T(Z)$, $p_T(W)$, $m_T(WZ)$, and $m(WZ)$ distributions all display very good agreement between prediction and observation providing confidence in the modelling of SM WZ production.

7.8 SIGNAL INTERPOLATION

The W' fully-simulated PYTHIA samples have mass spacings larger than their respective resolutions. It is therefore possible that, using only these samples to extract a limit, the presence of a signal may be hidden from the limit procedure. To make sure

187

W' mass [GeV]	Total Uncertainty [%]
200	2.3
400	0.6
600	0.4
1000	0.3
1400	0.2
1800	4.3
ρ_T mass [GeV]	Total Uncertainty [%]
250	0.82
450	0.83
600	0.84
800	0.85
1000	0.86

Table 7.X: Signal acceptance uncertainties upon the W' and ρ_T/a_T signals directly related to the estimation of the uncertainties associated to the PDF set MSTW2008 [235]. A selected subset of the available signals samples are shown for brevity.

that a potential signal shall not be overlooked, a set of signal templates with masses in between the existing ones, spaced by 50 GeV one from each other, were created and their acceptances extracted from the simulated samples as explained below.

To construct these templates, the invariant WZ mass of each available fully simulated signal sample was fitted to a Crystal Ball (CB) function, which is a Gaussian with a power-law tail. The CB function is implemented in ROOFIT [14] and has 4 parameters along with its absolute normalization N. The function is defined as

$$\text{CB}(x; m, \sigma, a, n) = N \cdot \begin{cases} e^{-\frac{(x-m)^2}{2\sigma^2}} & \text{for } \frac{x-m}{\sigma} > -a \\ \left(\frac{n}{n-a^2-\frac{|a|(x-m)}{\sigma}}\right)^n e^{-\frac{a^2}{2}} & \text{for } \frac{x-m}{\sigma} \leq -a \end{cases} \tag{7.13}$$

Once the CB fits are performed on the available fully simulated samples as seen in figure 7.10, the mean m, the width σ, the delimiting value a, and the exponential factor n are then extracted from the fits to the simulated distributions and their trends, as a func-

tion of $m_{W'}$, are themselves fitted to polynomial functions. Good agreement has been observed for all mass points. The step size was chosen such that each signal has sufficient overlaps with the following one. For the mean m, a polynomial of degree 3 was used, whereas for the width and the n parameter, a polynomial of degree 5 was chosen, and finally, for the a parameter a polynomial of degree 6 was used. Figure 7.11 shows the fit to the crystal ball parameters used in the $e\nu ee$ channel (chosen as an example). The parameter fits were then used to interpolate the form of the signal for mass points between 200 and 2000 GeV in steps of 50 GeV. For the interpolated shapes between 200 and 400 GeV, the relative size of the power-law tails are expected to be small with respect to the Gaussian component of the CB. Furthermore, because the sign of the a parameter changes between 200 GeV and 400 GeV, the tail can be either be on the low or high mass side of the signal. Consequently, if the interpolation of the parameter a, derived from the parameter fit, finds a negative value for a within this interpolated mass range of 200 to 400 GeV, a tail of the size of the 200 GeV signal (its a value) is conservatively used. Similarly, if the fit to the parameter a is found to be positive, a tail of the size of the 400 GeV mass point was chosen conservatively. In other words, the fits to the parameter a determines which of the two a values between the 200 and 400 GeV mass points was chosen for the interpolated shapes of 250, 300, and 350 GeV.

Once the interpolated template shapes acquired, figure 7.12, a systematic uncertainty is computed to take into account the statistical uncertainties (including PRW) of the original simulated signal shapes. This was done in such a fashion as to obtain a systematic uncertainty that mirrored the statistical uncertainties found in the available fully simulated samples. For the other systematic uncertainties, each set of upward and downward fluctuated shapes were fitted and normalized independently. In other words, the above interpolation procedure was reproduced for each systematic uncertainty separately, thus reproducing all possible shape uncertainties across all interpolated mass points. To decipher whether or not the parametrization procedure is stable against the removal of a mass point, a comparison between the fitted shape and the interpolated shape for the 1000 GeV signal has been performed when the parameter fits do not use the ones from the very same 1000 GeV fit. Figure 7.13 shows this comparison in each channel.

To compute the normalization for these interpolated signal shapes, the acceptances were also interpolated from the fully simulated samples channel-by-channel using a spline[7] fit of degree 3. Figure 7.14 shows the fits and acceptance values obtained in each channel, whereas table 7.XIII shows the signal cross section and interpolated acceptances used for all channels. Given that the acceptances start to drop significantly after ~ 1.1 TeV, signal shapes beyond 1.6 TeV have large statistical uncertainties, thereby making the interpolation method less reliable in that region. For these reasons, production cross section limits shall be computed up to signal masses of 1.6 TeV only.

Putting together the different components of this interpolation procedure produces robust shape and yield predictions for WZ resonance signal hypotheses.

7.9 RESULTS

7.9.1 SIGNAL REGION

Applying the signal region selections as listed in section 7.4 upon the data and MC/DD predictions, we arrive at the final $m(WZ)$ distribution shown in figure 7.15, which includes the background extrapolation as discussed in section 7.6.2.

The yields per lepton decay channel and predicted background source are presented in table 7.XIV.

Complementing these results, figure 7.16 reveals the inclusive $m(Z)$, $m_T(W)$, $p_T(W)$, and $p_T(Z)$ distributions in the signal region breaking down the differences in shapes between signal (overlaid) and pure background expectation.

For the 16 highest $m(WZ)$ events, detailed object information can be found in appendix VII.

7.9.2 BUMP HUNTING

Although no large localized excess is apparent in the $m(WZ)$ distributions 7.15, to quantify this assertion, the p-values (see equation (III.22) in appendix V) for each interpolated signal mass points were computed and tabulated in 7.XV.

---

7. Piecewise-defined polynomials that remain smooth where the pieces connect.

The smallest p-value found is for the 350 GeV mass point with a p-value $= 0.0087$, equivalent to a $2.4\,\sigma$ deviation from the background-only expectation. Although not very large, the fluctuation is concentrated in the $e\nu\mu\mu$ channel, while the other channels have very background consistent p-values. Furthermore, as seen in table 7.XIV and in the full $m(WZ)$ distribution, the data overshoots expectation by roughly 1.3σ independently of $m(WZ)$ indicating perhaps that either the SM WZ is underestimated, the $|\Delta y(W, Z)|$ and $|\Delta\phi(W, Z)|$ variables are not perfectly modelled by POWHEG (since the yields in the WZ control region matchup very nicely), or we are simply witnessing a statistical fluctuation. Putting these ideas together leads one to believe that the small excess near 350 GeV is definitely not significant enough to get excited. Therefore, we now turn to extracting limits on the production cross section of W' and ρ_T.

7.9.3 LIMIT SETTING

Using the CL$_s$ method as outlined in appendix III, the expected and observed limits on the W' cross section times branching ratio are computed using the full background and signal shapes at 95% C.L. The calculation includes all mentioned systematics uncertainties as nuisance parameters and the signal shapes from the interpolation method. The final observed W' limits are

$$m(W') > 1.18 \text{ TeV}, \tag{7.14}$$

while the expected limit was $m(W') > 1.30$ TeV. As a function of $m(W')$, the observed and expected limits on $\sigma \times BR(W' \to WZ)$ are presented in figure 7.17. The expected limit is seen to rise beyond 1.2 TeV due to the lepton isolation criteria. High resonance masses naturally produce boosted W and Z bosons which in turn bring about collinear leptonic decays. The isolation cone of $R = 0.3$ (see table 7.II and 7.III for electrons and muons respectively) them becomes prohibitive and causes the signal acceptance to drop as observed in figure 7.14.

7.9.4 RE-INTERPRETATION FOR DIFFERENT MASSES OF π_T

Due to the fact that in LSTC, the decay

$$\rho_T/a_T \to W\pi_T \tag{7.15}$$

is allowed as long as $m(\rho_T/a_T) \geq m(W) + m(\pi_T)$, the limits already presented for $m(W')$ can be utilized to computed limits on $m(\rho_T)$ as a function of $m(\pi_T)$, as shown in figure 7.18. In terms of the observed mass limits, they read

$$m(\rho_T) > 920 \text{ GeV} \tag{7.16}$$

for both assumptions on $m(a_T)$, i.e. $m(a_T) = 1.1\,m(\rho_T)$ or $m(a_T) \gg m(\rho_T)$, while the expected limits are $m(\rho_T) > 1073$ GeV and $m(\rho_T) > 1068$ when $m(a_T) = 1.1\,m(\rho_T)$ and $m(a_T) \gg m(\rho_T)$ respectively.

As a final note, appendix II presents ATLAS event displays of the highest $WZ \to \ell\nu\ell\ell$ invariant mass events in each of the 4 lepton channels.

Uncertainty	$e\nu ee$ Channel	$ee\mu\nu$ Channel	$e\nu\mu\mu$ Channel	$\mu\mu\mu\nu$ Channel
Statistics	3.1%	2.7%	2.3%	2.0%
Luminosity	3.6%	3.6%	3.6%	3.6%
Electron trigger	0.01%	0.02%	0.06%	0.00%
Muon trigger	0.00%	0.01%	0.03%	0.19%
Electron identification	2.91%	1.88%	1.03%	0.00%
Electron reconstruction	1.99%	1.33%	0.66%	0.00%
Electron energy resolution	0.80%	0.56%	0.37%	0.00%
Electron energy scale	0.84%	0.92%	0.26%	0.00%
Electron isolation	1.88%	1.25%	0.63%	0.00%
Muon identification	0.00%	0.31%	0.62%	0.93%
Muon isolation	0.00%	0.30%	0.60%	0.90%
Muon momentum resolution from MS	0.00%	0.06%	0.14%	0.10%
Muon momentum resolution ID	0.00%	0.11%	0.04%	0.15%
Muon momentum scale	0.00%	0.00%	0.07%	0.23%
Jet energy scale	1.51%	2.20%	1.32%	1.19%
Jet energy resolution	0.14%	0.30%	0.43%	0.08%
E_T^{miss} resolution from soft terms	0.59%	0.46%	0.89%	0.19%
E_T^{miss} scale from soft terms	1.20%	0.80%	1.33%	1.25%
Total (with statistical uncertainty)	6.63%	5.85%	5.06%	4.66%

Table 7.XI: Enumeration of event-based systematic uncertainties for the SM WZ process.

Uncertainty	$e\nu ee$ Channel	$ee\mu\nu$ Channel	$e\nu\mu\mu$ Channel	$\mu\mu\mu\nu$ Channel
Statistics	2.9%	2.7%	2.6%	2.5%
Luminosity	3.6%	3.6%	3.6%	3.6%
Electron trigger	0.00%	0.01%	0.08%	0.00%
Muon trigger	0.00%	0.00%	0.01%	0.23%
Electron identification	2.35%	1.53%	0.82%	0.00%
Electron reconstruction	2.01%	1.34%	0.67%	0.00%
Electron energy resolution	0.43%	0.20%	0.39%	0.00%
Electron energy scale	0.22%	0.24%	0.25%	0.00%
Electron isolation	1.84%	1.23%	0.61%	0.00%
Muon identification	0.00%	0.37%	0.76%	1.14%
Muon isolation	0.00%	0.30%	0.60%	0.90%
Muon momentum resolution MS	0.00%	0.04%	0.04%	0.09%
Muon momentum resolution ID	0.00%	0.00%	0.03%	0.11%
Muon momentum scale	0.00%	0.00%	0.10%	0.04%
Jet energy scale	0.27%	0.37%	0.05%	0.47%
Jet energy resolution	0.74%	0.40%	0.06%	0.45%
E_T^{miss} resolution from soft terms	0.39%	0.33%	0.20%	0.24%
E_T^{miss} scale from soft terms	0.67%	0.16%	0.47%	0.02%
PDF	1%	1%	1%	1%
Total (with statistical uncertainty)	6.06%	5.26%	4.85%	4.78%

Table 7.XII: Listing of the systematic uncertainties involved for the W' signal process with $m(W') = 800$ GeV.

(a) $m(Z)$

(b) $m_T(W)$

(c) $p_T(Z)$

(d) $p_T(W)$

(e) $m_T(WZ)$

(f) $m(WZ)$
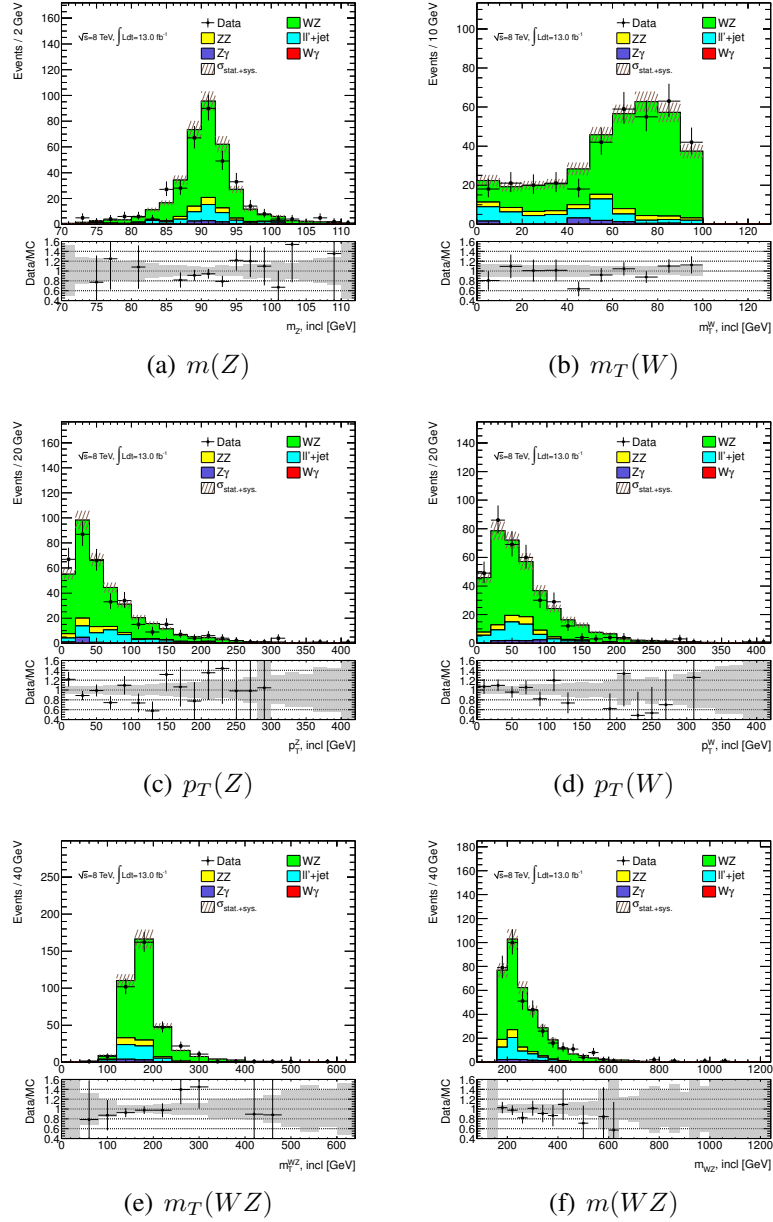
Figure 7.9: Data versus expectation comparisons for the $m(Z)$, $m_T(W)$, $p_T(Z)$, $p_T(W)$, $m_T(WZ)$, and $m(WZ)$ distributions in the WZ control region. The shaded errors bar include all systematic uncertainties details in section 7.6, and the $\ell\ell$+jet background is computed via the DD dijet technique as explained in section 7.5.

195
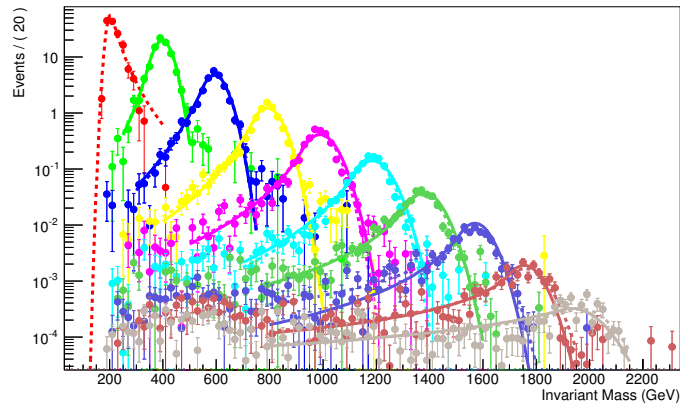
Figure 7.10: Comparison of the CB function fits (dotted lines) to the simulated W' samples with masses 200, 400, 600, 800, 1000, 1200, 1400, 1600, 1800, and 2000 GeV in $e\nu ee$ channel. Similar results were obtained in the other channels. The CB fits are individually compared to the *interpolated* signal shapes obtained from the parameter fits (full lines).
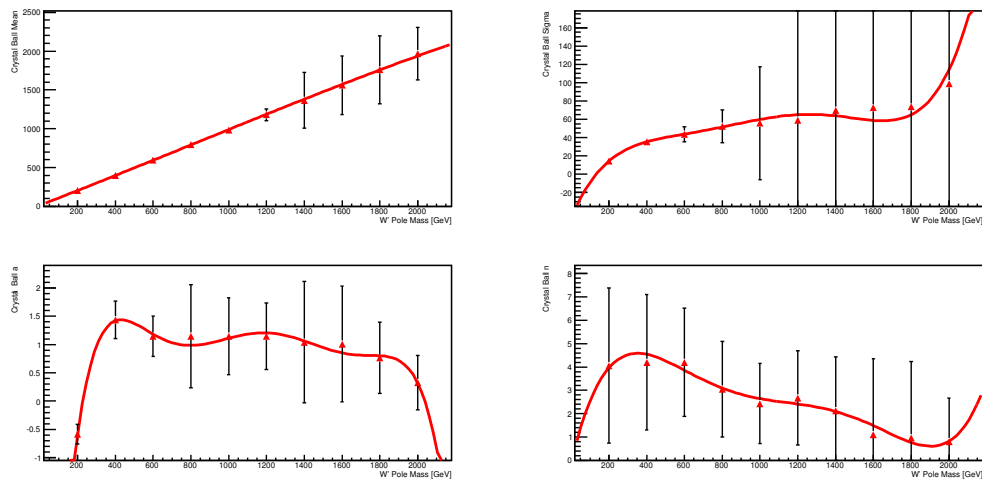
Figure 7.11: Parameter fits of the CB function, itself fitted to the fully-simulated W' samples with masses 200 to 2000 GeV in steps of 200 GeV. These parameter fits enable the interpolation of CB shapes for any signal mass between 200 and 2000 GeV.
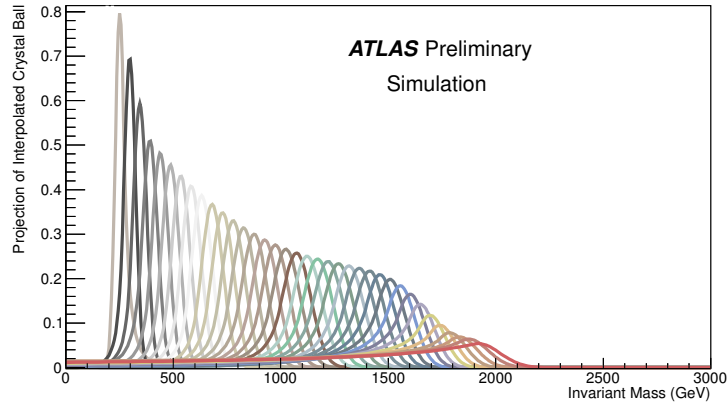
Figure 7.12: Templates of W' signal with masses between 200 and 2000 GeV in steps of 50 GeV, obtained from interpolating the full-simulated sample distributions as explained in the text, for the $e\nu ee$ channel.

(a) $e\nu ee$ channe

(b) $\mu\nu ee$ channe

(c) $e\nu\mu\mu$ channe

(d) $\mu\nu\mu\mu$ channe
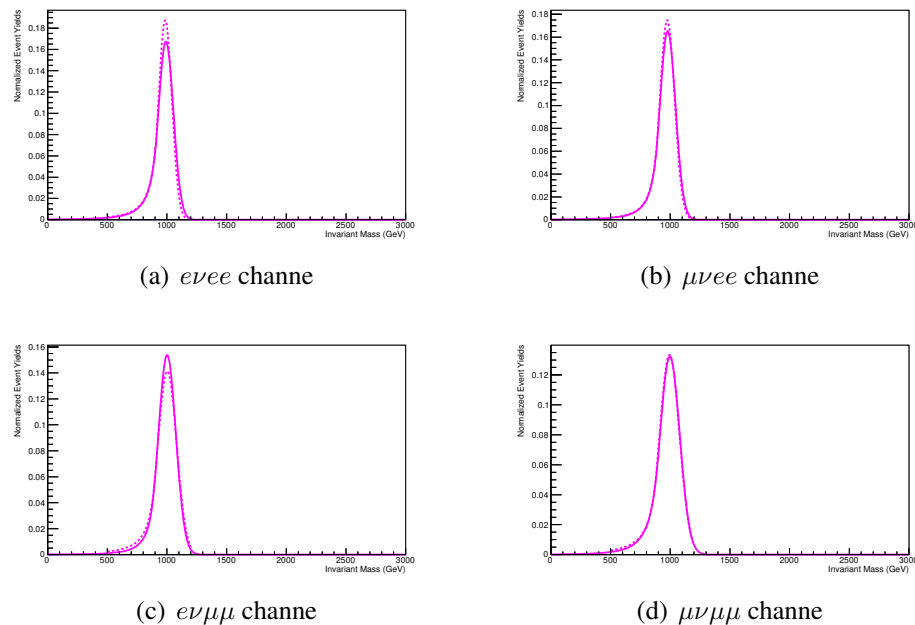
Figure 7.13: Comparison of the CB function fit (dotted lines) to the interpolated W' shape (full line) of the 1000 GeV signal where the interpolated shape was *not* derived using the parameters values obtained from the 1000 GeV fit itself. Hence, only the other mass points between 200 and 2000 GeV were used to extract the shown interpolated shape. The four lepton decay channel types are shown separately.

(a) *eνee* channe

(b) *μνee* channe

(c) *eνμμ* channe

(d) *μνμμ* channe
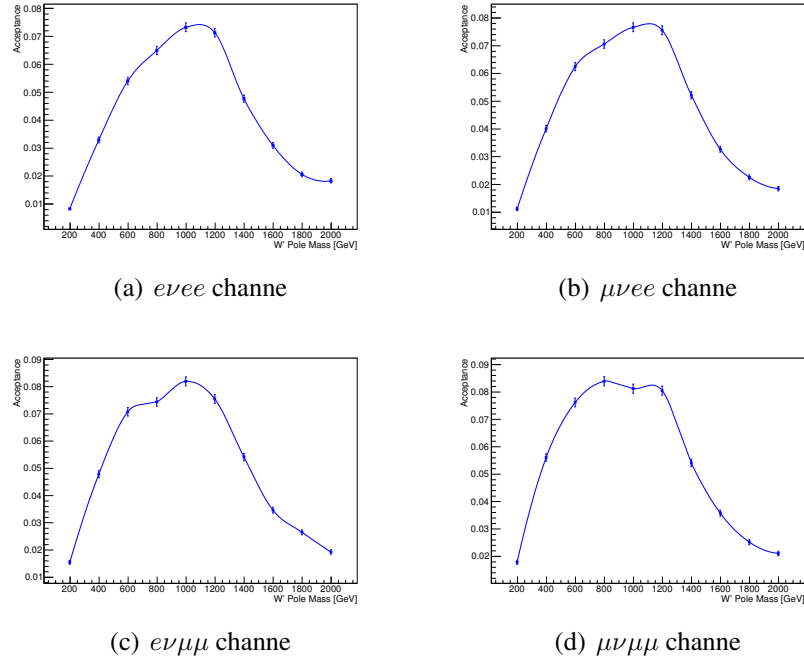
Figure 7.14: Degree 3 spline fits of the simulated samples in each decay channel separately.

(a) Log plot

(b) Linear plot
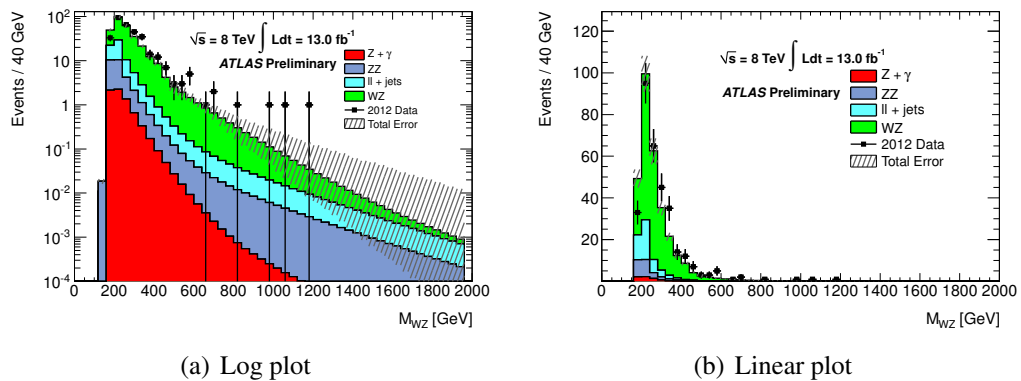
Figure 7.15: Comparison of the data with the expected background estimation for events in the signal region, i.e. with all selections applied, and with the extrapolated backgrounds. We find the $m(WZ)$ invariant mass in log scale on the left and linear scale on the right.

W' mass	$\sigma \times$BR	Acceptance $\times$ Efficiency *per* channel				
[GeV]	[pb]	$e\nu ee$	$e\nu \mu\mu$	$\mu\nu ee$	$\mu\nu \mu\mu$	Average
200	1.099	0.033	0.045	0.061	0.071	0.053
250	0.9353	0.056	0.073	0.093	0.118	0.085
300	0.5294	0.081	0.102	0.126	0.159	0.117
350	0.2959	0.106	0.131	0.159	0.194	0.148
400	0.1746	0.131	0.160	0.191	0.224	0.177
450	0.1074	0.156	0.187	0.220	0.250	0.203
500	6.939×10^{-2}	0.178	0.211	0.247	0.271	0.227
550	4.644×10^{-2}	0.199	0.233	0.268	0.289	0.247
600	3.243×10^{-2}	0.216	0.250	0.283	0.305	0.264
650	2.269×10^{-2}	0.230	0.262	0.290	0.317	0.275
700	1.641×10^{-2}	0.241	0.270	0.293	0.326	0.283
750	1.212×10^{-2}	0.251	0.276	0.294	0.333	0.289
800	9.281×10^{-3}	0.259	0.282	0.297	0.335	0.293
850	6.940×10^{-3}	0.269	0.288	0.304	0.333	0.299
900	5.352×10^{-3}	0.278	0.294	0.313	0.330	0.304
950	4.154×10^{-3}	0.286	0.300	0.322	0.326	0.309
1000	3.293×10^{-3}	0.293	0.306	0.328	0.325	0.313
1050	2.582×10^{-3}	0.298	0.311	0.328	0.327	0.316
1100	2.057×10^{-3}	0.299	0.314	0.324	0.330	0.317
1150	1.646×10^{-3}	0.296	0.311	0.315	0.330	0.313
1200	1.349×10^{-3}	0.285	0.302	0.301	0.321	0.302
1250	1.076×10^{-3}	0.266	0.284	0.284	0.302	0.284
1300	8.773×10^{-4}	0.242	0.261	0.262	0.275	0.260
1350	7.197×10^{-4}	0.216	0.234	0.240	0.245	0.234
1400	5.996×10^{-4}	0.191	0.208	0.217	0.216	0.208
1450	4.859×10^{-4}	0.170	0.185	0.194	0.192	0.185
1500	4.019×10^{-4}	0.152	0.164	0.173	0.171	0.165
1550	3.335×10^{-4}	0.137	0.146	0.154	0.156	0.148
1600	2.795×10^{-4}	0.123	0.130	0.138	0.142	0.133

Table 7.XIII: Cross section times branching ratios and acceptances per channel used to derive cross section limits at intermediate $m_{W'}$ mass values up to W' masses of 1600 GeV.

Sample	$e\nu ee$ Channel	$ee\mu\nu$ Channel	$e\nu\mu\mu$ Channel	$\mu\nu\mu\mu$ Channel	inclusive
Backgrounds:					
WZ	$39.1 \pm 1.2 \pm 4.0$	$52.0 \pm 1.4 \pm 5.2$	$60.2 \pm 1.4 \pm 5.8$	$81.5 \pm 1.6 \pm 7.7$	$232.8 \pm 2.8 \pm 22.4$
ZZ	$3.7 \pm 0.1 \pm 0.3$	$3.3 \pm 0.1 \pm 0.2$	$3.6 \pm 0.1 \pm 0.3$	$4.4 \pm 0.1 \pm 0.3$	$15.0 \pm 0.2 \pm 0.9$
$Z\gamma$	$2.4 \pm 1.0 \pm 0.9$	$negl.$	$6.0 \pm 1.8 \pm 0.8$	$negl.$	$8.4 \pm 2.1 \pm 1.2$
$\ell\ell$+jet (DD)	$4.0 \pm 1.0^{+1.7}_{-1.6}$	$6.6 \pm 1.1^{+2.5}_{-2.3}$	$11.0 \pm 1.7^{+5.2}_{-4.7}$	$8.0 \pm 1.2^{+3.2}_{-3.1}$	$29.6 \pm 2.6^{+6.8}_{-6.3}$
Sum of Backgrounds	$49.2 \pm 1.9 \pm 4.4$	$61.9 \pm 1.8 \pm 5.8$	$80.8 \pm 2.8 \pm 7.8$	$93.9 \pm 2.0 \pm 8.3$	$285.8 \pm 4.4 \pm 23.5$
Data	55	73	98	98	324
$W' \to WZ$ $m(W') = 600$ GeV	22.8 ± 0.7	26.3 ± 0.8	29.8 ± 0.8	32.1 ± 0.8	111.0 ± 1.6
$W' \to WZ$ $m(W') = 800$ GeV	7.8 ± 0.2	8.5 ± 0.2	9.0 ± 0.2	10.1 ± 0.2	35.4 ± 0.4
$W' \to WZ$ $m(W') = 1000$ GeV	3.1 ± 0.1	3.3 ± 0.1	3.5 ± 0.1	3.5 ± 0.1	13.4 ± 0.2
$\rho_T \to WZ$ $m(\rho_T) = 400$ GeV	14.2 ± 0.7	17.8 ± 0.7	22.3 ± 0.8	25.0 ± 0.8	79.3 ± 1.6
$\rho_T \to WZ$ $m(\rho_T) = 600$ GeV	4.9 ± 0.2	5.8 ± 0.2	6.7 ± 0.2	7.3 ± 0.2	24.7 ± 0.4
$\rho_T \to WZ$ $m(\rho_T) = 800$ GeV	2.0 ± 0.1	1.9 ± 0.1	2.3 ± 0.1	2.6 ± 0.1	8.8 ± 0.2

Table 7.XIV: Predicted background yields per channel in comparison with the observed yields. The yields of a selected set of W' and ρ_T signal masses are also displayed for comparison purposes.

(a) $m(Z)$ (b) $m_T(W)$

(c) $p_T(W)$ (d) $p_T(Z)$
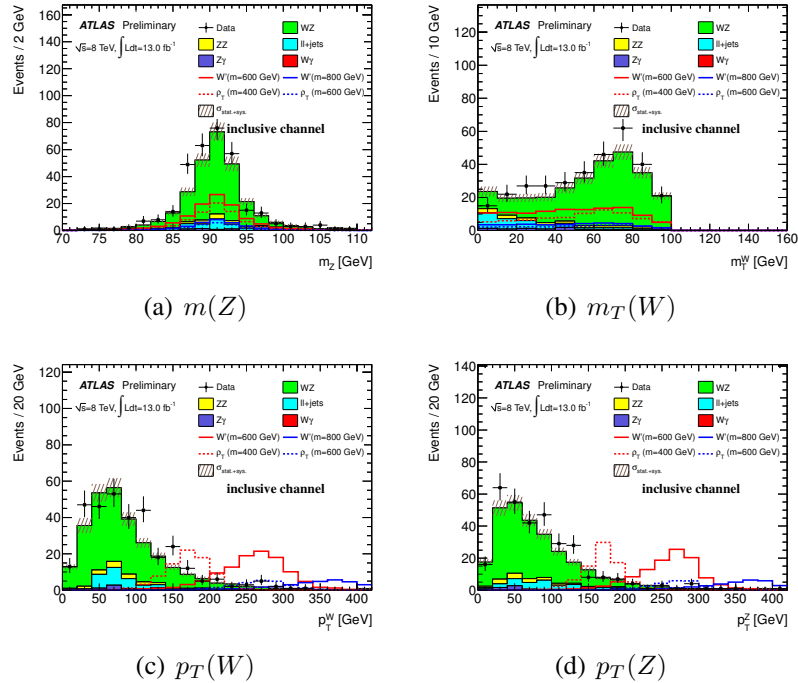
Figure 7.16: Comparison of the data with the background estimation for events with all signal region selection cuts applied. A W' signal of 800 GeV along with a 600 GeV ρ_T signal are overlaid indicating the nature of the shape differences such signals would induce in these distributions.

W' Mass [GeV]	$e\nu ee$	$\mu\nu ee$	$e\nu\mu\mu$	$\mu\nu\mu\mu$	Combination
200	0.86	0.29	0.47	0.84	0.71
250	0.36	0.31	0.14	0.63	0.31
300	0.056	0.22	0.0067	0.48	0.032
350	**0.057**	**0.21**	**0.00073**	**0.36**	**0.0087**
400	0.27	0.23	0.018	0.067	0.012
450	0.64	0.28	0.11	0.0082	0.035
500	0.39	0.53	0.14	0.0046	0.029
550	0.18	0.77	0.14	0.014	0.05
600	0.13	0.71	0.14	0.049	0.061
650	0.29	0.48	0.37	0.088	0.17
700	0.34	0.32	0.61	0.18	0.28
750	0.19	0.31	0.65	0.3	0.32
800	0.14	0.37	0.29	0.5	0.28
850	0.14	0.38	0.23	0.59	0.29
900	0.19	0.39	0.072	0.62	0.22
950	0.22	0.41	0.03	0.64	0.19
1000	0.17	0.42	0.023	0.68	0.15
1050	0.11	0.43	0.022	0.66	0.099
1100	0.052	0.44	0.03	0.66	0.078
1150	0.018	0.43	0.052	0.66	0.076
1200	0.012	0.57	0.12	0.62	0.089
1250	0.028	0.44	0.13	0.65	0.12
1300	0.035	0.45	0.14	0.65	0.17
1350	0.045	0.45	0.15	0.64	0.24
1400	0.052	0.41	0.15	0.57	0.28
1450	0.051	0.46	0.14	0.63	0.28
1500	0.049	0.47	0.14	0.62	0.28
1550	0.054	0.47	0.14	0.62	0.28
1600	0.063	0.5	0.16	0.56	0.35

Table 7.XV: The p-value probabilities $\equiv 1 - \mathrm{CL}_b$, that the background fluctuates to or above the data in each channel. Systematic uncertainties are included
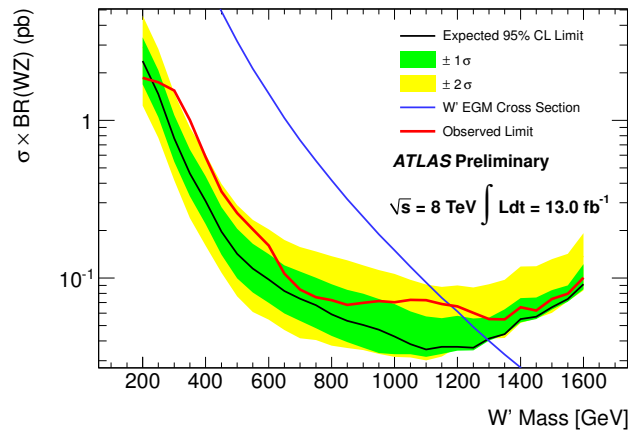
Figure 7.17: The expected (black line) and observed (red line) excluded production cross section limit at 95% C.L. multiplied by the branching fraction of the combined $e\nu ee$, $\mu\nu ee$, $e\nu\mu\mu$, and $\mu\nu\mu\mu$ final states assuming $W' \to WZ$.
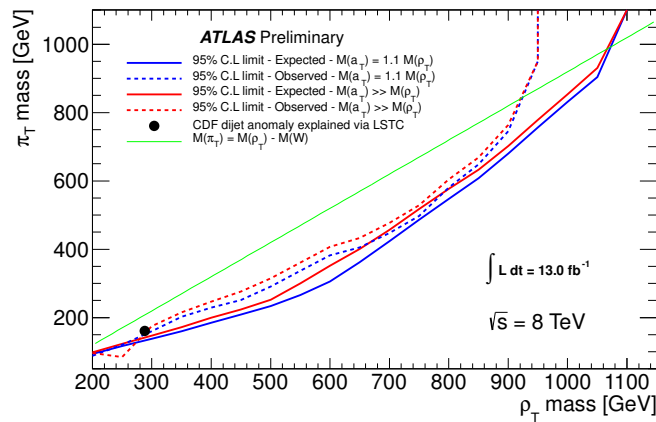
Figure 7.18: The 95% C.L. expected and observed excluded mass regions in the $m(\rho_T)$ versus $m(\pi_T)$ plane, using the combined $e\nu ee$, $ee\mu\nu$, $e\nu\mu\mu$, and $\mu\nu\mu\mu$ final states assuming the $\rho_T \to WZ$ signal. At the time of ATLASapproval, the CDF excess **??** in W+two jets events had yet to be explained.

CHAPTER 8

CONCLUSIONS AND OUTLOOK

> *If you don't like the way the world works, go somewhere else, another Universe perhaps.*
>
> Richard P. Feynman

The particle searches featured in this thesis have provided new benchmark points for theories purporting to extend or alter the SM of particle physics. Theories or models such as Little Higgs [131–133], Composite Higgs [31, 34, 134, 135], or Technicolor [36, 37, 39, 188], have seen some of their respective parameter spaces excluded by the results of chapters 5 and 7. Of course, these models are still quite viable, and future searches of the kind presented in this thesis must be carried out with more data and at higher center of mass energy.

In terms of mass limits on the benchmarks models LSTC, and EGM, as well as on the model independent VLQ doublets, the results are summarized in table 8.I.

Particle	Model	Observed (Expected) mass limit [GeV] at 95% C.L.
$\rho_T \left(m(a_T) \gg m(\rho_T) \right)$	LSTC	920 (1068)
$\rho_T \left(m(a_T) \gg 1.1 \, m(\rho_T) \right)$		920 (1073)
W'	EGM	1180 (1300)
$U^{2/3}$-type VLQ	Model Independent [172]	1080 (1090)*
$D^{-1/3}$-type VLQ		1180 (1360)*
$T^{5/3}$-type VLQ		1420 (1570)*

*Assuming $\tilde{\kappa}_{uU} = \tilde{\kappa}_{uD} = \tilde{\kappa}_{uT} = 1$.

Table 8.I: Summary of the mass limits obtained in chapters in the analyses presented in this thesis.

8.1 POSSIBLE IMPROVEMENTS

For the VLQ analysis, the first obvious improvement is to perform the search with 2012 data. Beyond that, the sensitivity of the search may be improved if, rather than using the VLQ invariant mass $m(VLQ)$ as the discriminating variable, the BDT classifier variable is used instead. For this to be done correctly however, the multijet background must also be part of the BDT training samples in order to produce a classifier variable distribution that is capable of matching the data. Perhaps even more importantly, for there to be good agreement between prediction and observation in the classifier distribution, there must also be an improved MC modelling of W/Z+jet background, which, as was shown in appendix VI, models rather poorly $m(VLQ)$.

Within the $WZ \to \ell\nu\ell\ell$ resonance search, two important facets can readily be improved upon. The first relates to the isolation criteria imposed on both electrons and muons. As was shown in figure 7.14, the signal acceptance drops substantially after ~ 1.1 TeV in signal mass, and this is due almost exclusively to the $\Delta R = 0.3$ isolation criteria. Hence, a mass dependent isolation or simply a smaller cone size would procure greater sensitivity at high mass. Furthermore, the observation of an apparent non-localized surplus (through the $m(WZ)$ region) of $\sim 1.3\sigma$ with respect to prediction in the signal region, in contrast to the observed agreement in the WZ control region, is *perhaps* indicative of a mis-modelling of the WZ background. These two regions are separated by the $\Delta y(W, Z)$ and $\Delta \phi(W, Z)$ selections (equations (7.3) through (7.6)) and are perhaps not sufficiently well-modelled to accurately predict the total yields. Thus, other MC simulations by different generators (other than POWHEG, SHERPAand LO MAD-GRAPH) must be considered in ongoing and future $WZ \to \ell\nu\ell\ell$ resonance searches.

8.2 OUTLOOK

Perhaps the most obvious of facts is that the analyses put forth in this thesis have presented null results. Although this may be uninteresting for some, in the larger picture of understanding the structures that *need* to exist beyond the SM, for the reasons outlined in chapter 2, the recent boson discovery [17, 18] cannot reasonably be the final story. In

this exciting perspective, a continued search for VLQ and WZ resonances shall remain key in our understanding of EWSB and shall help in differentiating between theories with composite Higgs and those where the Higgs is an elementary particle.

BIBLIOGRAPHY

[1] K. Assamagan, G. Azuelos, S. Bahinipati, P. Banerjee, A. B. Galtieri, J. Collot, M. Davies, A. Gaponenko, A. Haas, J. Kraus, G. Lima, W. Lockman, A. Solodkov, G. Unal, A. Watson, and Y. Zhu, "Overlay for ATLAS simulation," Tech. Rep. ATL-COM-SOFT-2011-013, CERN, Geneva, Jun 2011.

[2] S. A. *et al.*, "Geant4 - A Simulation Toolkit," *Nuclear Instruments and Methods in Physics Research Section A: Accelerators, Spectrometers, Detectors and Associated Equipment*, vol. 506, no. 3, pp. 250 – 303, 2003.

[3] M. Dührssen, "The Fast Calorimeter Simulation FastCaloSim," Tech. Rep. ATL-PHYS-INT-2008-043. ATL-COM-PHYS-2008-093, CERN, Geneva, Jul 2008.

[4] S. Hamilton, E. Kneringer, W. Lukas, E. Ritsch, A. Salzburger, K. Sliwa, S. Todorova, J. Wetter, and S. Zimmermann, "The ATLAS Fast Track Simulation Project," Tech. Rep. ATL-SOFT-PROC-2011-038, CERN, Geneva, Mar 2011.

[5] S. Hamilton, E. Kneringer, W. Lukas, E. Ritsch, A. Salzburger, K. Sliwa, S. Todorova, J. Wetter, and S. Zimmermann, "The ATLAS Fast Track Simulation Project (FATRAS)," Oct 2010.

[6] E. Boos *et al.*, "CompHEP 4.4: Automatic computations from Lagrangians to Events," *Nucl.Instrum.Meth.*, vol. A534, pp. 250–259, 2004.

[7] A. Belyaev, N. D. Christensen, and A. Pukhov, "CalcHEP 3.4 for collider physics within and beyond the Standard Model," 2012.

[8] ATLAS Collaboration, "Search for Single Production of Vector-like Quarks Coupling to Light Generations in 4.64 fb^{-1} of Data at $\sqrt{s} = 7$ TeV," Tech. Rep. ATLAS-COM-CONF-2012-167, CERN, Geneva, Aug 2012.

[9] ATLAS Collaboration, "Search for resonant $WZ \to 3l\nu$ production in $\sqrt{s} = 8$ TeV pp collisions with 13 fb^{-1} at ATLAS," Tech. Rep. ATLAS-COM-CONF-2013-001, CERN, Geneva, Jan 2013.

[10] ATLAS Collaboration, "Search for heavy vector-like quarks coupling to light quarks in proton-proton collisions at $\sqrt{s} = 7$ TeV with the ATLAS detector," *Phys.Lett.*, vol. B712, pp. 22–39, 2012.

[11] ATLAS Collaboration, "Search for resonant WZ production in the $WZ \to \ell\nu\ell'\ell'$ channel in $\sqrt{s} = 7$ TeV pp collisions with the ATLAS detector," *Phys.Rev.*, vol. D85, p. 112012, 2012.

[12] A. Höcker, J. Stelzer, F. Tegenfeldt, H. Voss, K. Voss, A. Christov, S. Henrot-Versillé, M. Jachowski, A. Krasznahorkay, Y. Mahalalel, X. Prudent, and P. Speckmayer, "TMVA - Toolkit for Multivariate Data Analysis with ROOT: Users guide," Tech. Rep. CERN-OPEN-2007-007, CERN, Geneva, Mar 2007.

[13] I. Antcheva, M. Ballintijn, B. Bellenot, M. Biskup, R. Brun, N. Buncic, P. Canal, D. Casadei, O. Couet, V. Fine, L. Franco, G. Ganis, A. Gheata, D. Gonzalez Maline, M. Goto, J. Iwaszkiewicz, A. Kreshuk, D. Marcos Segura, R. Maunder, L. Moneta, A. Naumann, E. Offermann, V. Onuchin, S. Panacek, F. Rademakers, P. Russo, and M. Tadel, "ROOT — A C++ framework for petabyte data storage, statistical analysis and visualization," *Comput. Phys. Commun.*, vol. 182, no. 6, pp. 1384–1385, 2011.

[14] W. Verkerke and D. Kirkby, "The RooFit toolkit for data modeling," *ArXiv Physics e-prints*, June 2003.

[15] C. Burgess and G. Moore, *The Standard Model: A Primer*. Cambridge University Press, 2007.

[16] J. B. et al. (Particle Data Group), "The Review of Particle Physics," *Phys. Rev.*, vol. **D86**, 2012.

[17] ATLAS Collaboration, "Observation of a new particle in the search for the Standard Model Higgs boson with the ATLAS detector at the LHC," *Phys.Lett.*, vol. B716, pp. 1–29, 2012.

[18] CMS Collaboration, "Observation of a new boson at a mass of 125 GeV with the CMS experiment at the LHC," *Phys.Lett.*, vol. B716, pp. 30–61, 2012.

[19] J. Valle, "Neutrino physics overview," *J.Phys.Conf.Ser.*, vol. 53, pp. 473–505, 2006.

[20] A. G. Riess *et al.*, "Observational evidence from supernovae for an accelerating universe and a cosmological constant," *Astron.J.*, vol. 116, pp. 1009–1038, 1998.

[21] ATLAS Collaboration, "Search for down-type fourth generation quarks with the ATLAS detector in events with one lepton and hadronically decaying W bosons," *Phys.Rev.Lett.*, vol. 109, p. 032001, 2012.

[22] ATLAS Collaboration, "Combined measurements of the mass and signal strength of the Higgs-like boson with the ATLAS detector using up to 25 fb^{-1} of proton-proton collision data," Tech. Rep. ATLAS-CONF-2013-014, CERN, Geneva, Mar 2013.

[23] Altarelli, Guido and Mele, B. and Ruiz-Altaba, M., "Searching for New Heavy Vector Bosons in $p\bar{p}$ Colliders," *Z.Phys.*, vol. C45, p. 109, 1989.

[24] Lykken, Joseph D., "Introduction to supersymmetry," pp. 85–153, 1996.

[25] Nastase, Horatiu, "Introduction to Supergravity," 2011.

[26] Aitchison, Ian J.R., "Supersymmetry and the MSSM: An Elementary introduction," 2005.

[27] N. Arkani-Hamed, A. G. Cohen, and H. Georgi, "Electroweak symmetry breaking from dimensional deconstruction," *Phys.Lett.*, vol. B513, pp. 232–240, 2001.

[28] H.-C. Cheng, I. Low, and L.-T. Wang, "Top partners in little Higgs theories with T-parity," *Phys.Rev.*, vol. D74, p. 055001, 2006.

[29] H.-C. Cheng and I. Low, "TeV symmetry and the little hierarchy problem," *JHEP*, vol. 0309, p. 051, 2003.

[30] H.-C. Cheng and I. Low, "Little hierarchy, little Higgses, and a little symmetry," *JHEP*, vol. 0408, p. 061, 2004.

[31] P. Lodone, "Vector-like quarks in a composite Higgs model," *JHEP*, vol. 0812, p. 029, 2008.

[32] Hooper, Dan and Profumo, Stefano, "Dark matter and collider phenomenology of universal extra dimensions," *Phys.Rept.*, vol. 453, pp. 29–115, 2007.

[33] Kakuda, Takuya and Nishiwaki, Kenji and Oda, Kin-ya and Watanabe, Ryoutaro, "Universal extra dimensions after Higgs discovery," *Phys.Rev.*, vol. D88, p. 035007, 2013.

[34] Agashe, Kaustubh and Contino, Roberto and Pomarol, Alex, "The minimal composite Higgs model," *Nucl.Phys.*, vol. B719, pp. 165–187, 2005.

[35] J. L. Hewett and T. G. Rizzo, "Low-energy phenomenology of superstring-inspired e_6 models," *Phys. Rep.*, vol. 183, p. 193. 509 p, Nov 1988.

[36] E. Farhi and L. Susskind, "Technicolor," *Phys.Rept.*, vol. 74, p. 277, 1981.

[37] K. D. Lane, "An Introduction to Technicolor," 1993.

[38] E. Eichten and K. Lane, "Low-scale technicolor at the Tevatron and LHC," *Phys.Lett.*, vol. B669, pp. 235–238, 2008.

[39] R. Foadi, M. T. Frandsen, T. A. Ryttov, and F. Sannino, "Minimal Walking Technicolor: Set Up for Collider Physics," *Phys.Rev.*, vol. D76, p. 055005, 2007.

[40] P. Langacker, "Structure of the Standard Model," 1995.

[41] P. W. Higgs, "Broken symmetries, massless particles and gauge fields," *Phys.Lett.*, vol. 12, pp. 132–133, 1964.

[42] A. Ringwald, "Exploring the Role of Axions and Other WISPs in the Dark Universe," 2012.

[43] Wikipedia, "Standard Model." `http://en.wikipedia.org/wiki/Standard_Model`, 2013.

[44] M. E. Peskin and D. V. Schroeder, *An Introduction to Quantum Field Theory (Frontiers in Physics)*. Perseus Books, 2008.

[45] S. Weinberg, *The Quantum Theory of Fields*. The Quantum Theory of Fields, Cambridge University Press, 1995.

[46] M. Kaku, *Quantum field theory: a modern introduction*. Oxford University Press, 1993.

[47] E. Torrente-Lujan, "A Review on neutrino physics, mass and oscillations," 1999.

[48] D. Roy, "Neutrino mass and oscillation: An Introductory review," *Pramana*, vol. 54, pp. 3–20, 2000.

[49] Álvarez-Gaumé, Luis and Ellis, John, "Eyes on a prize particle," *Nature*, vol. 7, pp. 2–3, 2011.

[50] S. R. Coleman and E. J. Weinberg, "Radiative Corrections as the Origin of Spontaneous Symmetry Breaking," *Phys.Rev.*, vol. D7, pp. 1888–1910, 1973.

[51] "International Conference on High Energy Physics." `https://indico.cern.ch/conferenceDisplay.py?confId=181298`, 2012.

[52] ATLAS Collaboration, "Study of the spin of the new boson with up to 25 fb^{-1} of ATLAS data," Tech. Rep. ATLAS-CONF-2013-040, CERN, Geneva, Apr 2013.

[53] CMS Collaboration, "Measurement of wz production rate," Tech. Rep. CMS-PAS-SMP-12-006, CERN, Geneva, 2013.

[54] CMS Collaboration, "Measurement of the electroweak production cross section of the Z boson with two forward-backward jets in pp collisions at 7 TeV," Tech. Rep. CMS-PAS-FSQ-12-019, CERN, Geneva, 2012.

[55] ATLAS Collaboration, "Measurement of the inclusive W and Z/γ^* cross sections in the e and μ decay channels in pp collisions at $\sqrt{s} = 7$ TeV with the ATLAS detector," *Phys. Rev. D*, vol. 85, p. 072004, Apr 2012.

[56] ATLAS Collaboration, "A measurement of the ratio of the W and Z cross sections with exactly one associated jet in pp collisions at $\sqrt{s} = 7$ TeV with ATLAS," *Phys.Lett.*, vol. B708, pp. 221–240, 2012.

[57] K. Abe and al., "Solar neutrino results in Super-Kamiokande-III," *Phys. Rev. D*, vol. 83, p. 052010, Mar 2011.

[58] T. Kirsten, "Retrospect of GALLEX/GNO," *J.Phys.Conf.Ser.*, vol. 120, p. 052013, 2008.

[59] F. Zhang, "Recent results of SNO experiment," *Int.J.Mod.Phys.*, vol. A23, pp. 3352–3357, 2008.

[60] C. D. Anderson, "The Apparent Existence of Easily Deflectable Positives," *Science*, vol. 76, pp. 238–239, 1932.

[61] E. Hubble, "A relation between distance and radial velocity among extra-galactic nebulae," *Proc.Nat.Acad.Sci.*, vol. 15, pp. 168–173, 1929.

[62] K. Abe and al., "Search for Antihelium with the BESS-Polar Spectrometer," *Phys. Rev. Lett.*, vol. 108, p. 131301, Mar 2012.

[63] J. Christenson, J. Cronin, V. Fitch, and R. Turlay, "Evidence for the 2 pi Decay of the k(2)0 Meson," *Phys.Rev.Lett.*, vol. 13, pp. 138–140, 1964.

[64] M. Gavela, P. Hernandez, J. Orloff, and O. Pene, "Standard model CP violation and baryon asymmetry," *Mod.Phys.Lett.*, vol. A9, pp. 795–810, 1994.

[65] T. Hambye, "CP violation and the matter–antimatter asymmetry of the Universe," *Comptes Rendus Physique*, vol. 13, no. 2, pp. 193 – 203, 2012. Flavour physics and CP violation / Physique de la saveur et violation de CP.

[66] V. C. Rubin and J. Ford, W. Kent, "Rotation of the Andromeda Nebula from a Spectroscopic Survey of Emission Regions," *Astrophys.J.*, vol. 159, pp. 379–403, 1970.

[67] D. Clowe, M. Bradac, A. H. Gonzalez, M. Markevitch, S. W. Randall, *et al.*, "A direct empirical proof of the existence of dark matter," *Astrophys.J.*, vol. 648, pp. L109–L113, 2006.

[68] R. Massey, T. Kitching, and J. Richard, "The dark matter of gravitational lensing," *Rept.Prog.Phys.*, vol. 73, p. 086901, 2010.

[69] P. Ade *et al.*, "Planck 2013 results. I. Overview of products and scientific results," 2013.

[70] M. Milgrom, "A Modification of the Newtonian dynamics as a possible alternative to the hidden mass hypothesis," *Astrophys.J.*, vol. 270, pp. 365–370, 1983.

[71] ATLAS Collaboration, "Search for dark matter candidates and large extra dimensions in events with a jet and missing transverse momentum with the ATLAS detector," Tech. Rep. ATLAS-CONF-2012-084, CERN, Geneva, Jul 2012.

[72] ATLAS Collaboration, "Search for dark matter candidates and large extra dimensions in events with a photon and missing transverse momentum in pp collision data at $\sqrt{s} = 7$ TeV with the ATLAS detector," Tech. Rep. ATLAS-CONF-2012-085, CERN, Geneva, Jul 2012.

[73] CMS Collaboration, "Search for dark matter and large extra dimensions in mono-jet events in pp collisions at $\sqrt{s} = 7$ TeV," *Submitted to JHEP*, 2012.

[74] S. Carroll, *Spacetime and Geometry: An Introduction to General Relativity*. Addison Wesley, 2004.

[75] P. Milonni, *The quantum vacuum: an introduction to quantum electrodynamics*. Academic Press, 1994.

[76] G. Degrassi, S. Di Vita, J. Elias-Miro, J. R. Espinosa, G. F. Giudice, *et al.*, "Higgs mass and vacuum stability in the Standard Model at NNLO," *JHEP*, vol. 1208, p. 098, 2012.

[77] J. Elias-Miro, J. R. Espinosa, G. F. Giudice, G. Isidori, A. Riotto, *et al.*, "Higgs mass implications on the stability of the electroweak vacuum," *Phys.Lett.*, vol. B709, pp. 222–228, 2012.

[78] K. G. Wilson, "Renormalization Group and Critical Phenomena. II. Phase-Space Cell Analysis of Critical Behavior," *Phys. Rev. B*, vol. 4, pp. 3184–3205, Nov 1971.

[79] K. Huang, "Triviality of the Higgs field," *Int.J.Mod.Phys.*, vol. A4, p. 1037, 1989.

[80] CERN, *The CERN Large Hadron Collider: Accelerator and Experiments*, vol. 1. Journal of Instrumentation, 2009.

[81] A. Collaboration, *ATLAS Detector and Physics Performance - Technical Design Report*. CERN, 1999.

[82] S. Myers, "The LEP Collider." `http://sl-div.web.cern.ch/sl-div/history/lep_doc.html`, 1990.

[83] CERN. `http://www.atlas.ch/photos/`, 2012. ATLAS public images.

[84] CERN, "Incident in LHC sector 3-4." `http://press.web.cern.ch/press/PressReleases/Releases2008/PR09.08E.html`, September 2008.

[85] ATLAS Collaboration, "Luminosity Public Results." `https://twiki.cern.ch/twiki/bin/view/AtlasPublic/LuminosityPublicResults`, 2013.

[86] CERN, "LHC energy consumption." `http://lhc-machine-outreach.web.cern.ch/lhc-machine-outreach/faq/lhc-energy-consumption.htm`, 2007.

[87] G. Antchev, P. Aspell, I. Atanassov, V. Avati, J. Baechler, *et al.*, "First measurement of the total proton-proton cross section at the LHC energy of $\sqrt{s}$=7 TeV," *Europhys.Lett.*, vol. 96, p. 21002, 2011.

[88] M. Aleksa, F. Bergsma, L. Chevalier, P. Giudici, J. Hart, *et al.*, "Results of the ATLAS solenoid magnetic field map," *J.Phys.Conf.Ser.*, vol. 110, p. 092018, 2008.

[89] M. Arnaud, J. Bardoux, F. Bergsma, G. Bobbink, A. Bruni, *et al.*, "Commissioning of the magnetic field in the ATLAS muon spectrometer," *Nucl.Phys.Proc.Suppl.*, vol. 177-178, pp. 265–266, 2008.

[90] A. Boldyrev, V. Bondarenko, V. Bychkov, B. Dolgoshein, O. Fedin, *et al.*, "The ATLAS transition radiation tracker," *Instrum.Exp.Tech.*, vol. 55, pp. 323–334, 2012.

[91] V. Ginzburg and I. Frank, "Radiation of a uniformly moving electron due to its transition from one medium into another," *J.Phys.(USSR)*, vol. 9, pp. 353–362, 1945.

[92] P. Goldsmith and J. V. Jelley, "Optical transition radiation from protons entering metal surfaces," *Philosophical Magazine*, vol. 4, no. 43, pp. 836–844, 1959.

[93] A. Andronic and J. Wessels, "Transition Radiation Detectors," *Nucl.Instrum.Meth.*, vol. A666, pp. 130–147, 2012.

[94] Y.-S. Tsai, "Pair Production and Bremsstrahlung of Charged Leptons," *Rev.Mod.Phys.*, vol. 46, p. 815, 1974.

[95] C. Fabjan, "Liquid ionization calorimetry: Review and preview," *Nucl.Instrum.Meth.*, vol. A360, pp. 228–236, 1995.

[96] J. Archambault, A. Artamonov, M. Cadabeschi, V. Epshteyn, C. Galt, *et al.*, "Energy calibration of the ATLAS liquid argon forward calorimeter," *JINST*, vol. 3, p. P02002, 2008.

[97] ATLAS Collaboration, "Probing the measurement of jet energies with the atlas detector using z+jet events from proton-proton collisions at $\sqrt{s} = 7$ tev," Tech. Rep. ATLAS-CONF-2012-053, CERN, Geneva, May 2012.

[98] ATLAS Collaboration, "Probing the measurement of jet energies with the atlas detector using photon+jet events in proton-proton collisions at $\sqrt{s} = 7$ tev," Tech. Rep. ATLAS-CONF-2012-063, CERN, Geneva, Jul 2012.

[99] ATLAS Collaboration, "Jet energy measurement with the ATLAS detector in proton-proton collisions at $\sqrt{s} = 7$ TeV," 2011.

[100] ATLAS Collaboration, *ATLAS tile calorimeter: Technical Design Report*. Technical Design Report ATLAS, Geneva: CERN, 1996.

[101] T. Kamon, K. Kondo, A. Yamashita, T. Shimizu, and L. Nodulman, "A new scintillator and wavelength shifter," *Nuclear Instruments and Methods in Physics Research*, vol. 213, no. 2-3, pp. 261 – 269, 1983.

[102] F. Bosi, S. Burdin, V. Cavasinni, D. Costanzo, T. Del Prete, *et al.*, "A Device to characterize optical fibers," *Nucl.Instrum.Meth.*, vol. A485, pp. 311–321, 2002.

[103] C. Clement, L. Fiorini, V. Rossetti, A. Succurro, and M. Tylmad, "Tilecal plots for approval : 7tev collision events," Jun 2010.

[104] E. Fullana, J. Castelo, V. Castillo, C. Cuenca, A. Ferrer, E. Higon, C. Iglesias, A. Munar, J. Poveda, A. Ruiz-Martinez, B. Salvachua, C. Solans, R. Teuscher, and J. Valls, "Digital signal reconstruction in the atlas hadronic tile calorimeter," in *Real Time Conference, 2005. 14th IEEE-NPSS*, p. 4 pp., june 2005.

[105] E. Diehl, "ATLAS Muon Detector Commissioning," 2009.

[106] M. Curatolo, "The monitored drift tube (MDT) chambers for the muon precision tracking in the ATLAS spectrometer," *Nuclear Physics B - Proceedings Supplements*, vol. 78, no. 1-3, pp. 422 – 425, 1999. Advanced Technology and Particle Physics.

215

[107] S. Schuh, "Precision aspects of ATLAS muon chamber design and construction," *Nuclear Instruments and Methods in Physics Research Section A: Accelerators, Spectrometers, Detectors and Associated Equipment*, vol. 572, no. 1, pp. 135 – 138, 2007. Frontier Detectors for Frontier Physics.

[108] J. Wotschack, "Atlas muon chamber construction parameters for csc, mdt, and rpc chambers," Tech. Rep. ATL-MUON-PUB-2008-006. ATL-COM-MUON-2008-008, CERN, Geneva, Apr 2008. Back-up document for the ATLAS Detector Paper.

[109] J. Wotschack, "ATLAS Muon Chamber Construction Parameters for CSC, MDT, and RPC chambers," Tech. Rep. ATL-MUON-PUB-2008-006. ATL-COM-MUON-2008-008, CERN, Geneva, Apr 2008. Back-up document for the ATLAS Detector Paper.

[110] ATLAS Collaboration, "Performance of the ATLAS Trigger System in 2010," *Eur.Phys.J.*, vol. C72, p. 1849, 2012.

[111] R. Blair, J. Dawson, G. Drake, W. Haberichter, J. Schlereth, *et al.*, "The ATLAS High Level Trigger Region of Interest Builder," *JINST*, vol. 3, p. P04001, 2008.

[112] e. t. I. Bird, *LHC Computing Grid*. CERN, 2005.

[113] ATLAS Collaboration. `https://twiki.cern.ch/twiki/bin/view/AtlasPublic/ElectronGammaPublicCollisionResults`, 2009. ATLAS public images.

[114] ATLAS Collaboration, "Expected electron performance in the ATLAS experiment," 2011.

[115] ATLAS Collaboration, "Electron performance measurements with the ATLAS detector using the 2010 LHC proton-proton collision data," *Eur.Phys.J.*, vol. C72, p. 1909, 2012.

[116] ATLAS Collaboration, "A measurement of the muon reconstruction efficiency in 2010 ATLAS data using J/ψ decays," Tech. Rep. ATLAS-CONF-2012-125, CERN, Geneva, Aug 2012.

[117] ATLAS Collaboration, "Atlas public results," 2010.

[118] G. C. Blazey, J. R. Dittmann, S. D. Ellis, V. D. Elvira, K. Frame, *et al.*, "Run II jet physics," tech. rep., 2000.

[119] S. D. Ellis and D. E. Soper, "Successive combination jet algorithm for hadron collisions," *Phys.Rev.*, vol. D48, pp. 3160–3166, 1993.

[120] S. Ellis, J. Huston, and M. Tonnesmann, "On building better cone jet algorithms," *eConf*, vol. C010630, p. P513, 2001.

[121] Y. L. Dokshitzer, G. Leder, S. Moretti, and B. Webber, "Better jet clustering algorithms," *JHEP*, vol. 9708, p. 001, 1997.

[122] M. Wobisch and T. Wengler, "Hadronization corrections to jet cross-sections in deep inelastic scattering," 1998.

[123] S. Catani, Y. L. Dokshitzer, M. Seymour, and B. Webber, "Longitudinally invariant K_t clustering algorithms for hadron hadron collisions," *Nucl.Phys.*, vol. B406, pp. 187–224, 1993.

[124] M. Cacciari, G. P. Salam, and G. Soyez, "The Anti-k(t) jet clustering algorithm," *JHEP*, vol. 0804, p. 063, 2008.

[125] G. P. Salam, "A Practical seedless infrared safe cone algorithm," 2007.

[126] ATLAS Collaboration, "Performance of Missing Transverse Momentum Reconstruction in ATLAS with 2011 Proton-Proton Collisions at $\sqrt{s} = 7$ TeV," Tech. Rep. ATLAS-CONF-2012-101, CERN, Geneva, Jul 2012.

[127] T. Sjostrand, S. Mrenna, and P. Z. Skands, "PYTHIA 6.4 Physics and Manual," *JHEP*, vol. 0605, p. 026, 2006.

[128] J. Kang, P. Langacker, and B. D. Nelson, "Theory and Phenomenology of Exotic Isosinglet Quarks and Squarks," *Phys.Rev.*, vol. D77, p. 035003, 2008.

[129] J. Aguilar-Saavedra, R. Benbrik, S. Heinemeyer, and M. Perez-Victoria, "A handbook of vector-like quarks: mixing and single production," 2013.

[130] Y. Okada and L. Panizzi, "LHC signatures of vector-like quarks," 2012.

[131] N. Arkani-Hamed, A. Cohen, E. Katz, A. Nelson, T. Gregoire, *et al.*, "The Minimal moose for a little Higgs," *JHEP*, vol. 0208, p. 021, 2002.

[132] N. Arkani-Hamed, A. Cohen, E. Katz, and A. Nelson, "The Littlest Higgs," *JHEP*, vol. 0207, p. 034, 2002.

[133] T. Han, H. E. Logan, B. McElrath, and L.-T. Wang, "Phenomenology of the little Higgs model," *Phys.Rev.*, vol. D67, p. 095004, 2003.

[134] R. Contino, Y. Nomura, and A. Pomarol, "Higgs as a holographic pseudoGoldstone boson," *Nucl.Phys.*, vol. B671, pp. 148–174, 2003.

[135] R. Barbieri, B. Bellazzini, V. S. Rychkov, and A. Varagnolo, "The Higgs boson from an extended symmetry," *Phys.Rev.*, vol. D76, p. 115008, 2007.

[136] G. Giudice, C. Grojean, A. Pomarol, and R. Rattazzi, "The Strongly-Interacting Light Higgs," *JHEP*, vol. 0706, p. 045, 2007.

[137] T. Appelquist, H.-C. Cheng, and B. A. Dobrescu, "Bounds on universal extra dimensions," *Phys.Rev.*, vol. D64, p. 035002, 2001.

[138] C. T. Hill, "Topcolor: Top quark condensation in a gauge extension of the standard model," *Phys.Lett.*, vol. B266, pp. 419–424, 1991.

[139] F. Gursey, P. Ramond, and P. Sikivie, "A Universal Gauge Theory Model Based on E6," *Phys.Lett.*, vol. B60, p. 177, 1976.

[140] F. Gursey and M. Serdaroglu, "Basic fermion masses and mixings in the E(6) model," *Lett.Nuovo Cim.*, vol. 21, p. 28, 1978.

[141] K. Babu, J. C. Pati, and H. Stremnitzer, "A Hint from the interfamily mass hierarchy: Two vector - like families in the TeV range," *Phys.Rev.*, vol. D51, pp. 2451–2462, 1995.

[142] A. Davidson and K. C. Wali, "Family mass hierarchy from universal seesaw mechanism," *Phys.Rev.Lett.*, vol. 60, p. 1813, 1988.

[143] D. Guadagnoli, R. N. Mohapatra, and I. Sung, "Gauged Flavor Group with Left-Right Symmetry," *JHEP*, vol. 1104, p. 093, 2011.

[144] CDF Collaboration, "Measurement of the top quark forward-backward production asymmetry and its dependence on event kinematic properties," 2012.

[145] D. Choudhury, T. M. Tait, and C. Wagner, "Beautiful mirrors and precision electroweak data," *Phys.Rev.*, vol. D65, p. 053002, 2002.

[146] K. Kumar, W. Shepherd, T. M. Tait, and R. Vega-Morales, "Beautiful Mirrors at the LHC," *JHEP*, vol. 1008, p. 052, 2010.

[147] F. del Aguila and M. J. Bowick, "The Possibility of new fermions with $\Delta I = 0$ mass," *Nucl.Phys.*, vol. B224, p. 107, 1983.

[148] J. I. d. S. Marcos, *Enhancing CP violation, vector-like quarks and possible FCNC within warped extra dimensions*. UTL, Instituto Superior Técnico,, 2010.

[149] Y. Nir and D. J. Silverman, "Z mediated flavor changing neutral currents and their implications for CP asymmetries in B^0 decays," *Phys.Rev.*, vol. D42, pp. 1477–1484, 1990.

[150] N. Arkani-Hamed, A. G. Cohen, and H. Georgi, "Electroweak symmetry breaking from dimensional deconstruction," *Phys.Lett.*, vol. B513, pp. 232–240, 2001.

[151] N. Arkani-Hamed, A. G. Cohen, T. Gregoire, and J. G. Wacker, "Phenomenology of electroweak symmetry breaking from theory space," *JHEP*, vol. 0208, p. 020, 2002.

[152] F. del Aguila, M. Perez-Victoria, and J. Santiago, "Effective description of quark mixing," *Phys.Lett.*, vol. B492, pp. 98–106, 2000.

[153] F. del Aguila, J. de Blas, and M. Perez-Victoria, "Effects of new leptons in Electroweak Precision Data," *Phys.Rev.*, vol. D78, p. 013010, 2008.

[154] C. Csaki, J. Hubisz, G. D. Kribs, P. Meade, and J. Terning, "Big corrections from a little Higgs," *Phys.Rev.*, vol. D67, p. 115002, 2003.

[155] J. L. Hewett, F. J. Petriello, and T. G. Rizzo, "Constraining the littlest Higgs," *JHEP*, vol. 0310, p. 062, 2003.

[156] H.-C. Cheng and I. Low, "TeV symmetry and the little hierarchy problem," *JHEP*, vol. 0309, p. 051, 2003.

[157] H.-C. Cheng and I. Low, "Little hierarchy, little Higgses, and a little symmetry," *JHEP*, vol. 0408, p. 061, 2004.

[158] M. Perelstein, "Little Higgs models and T parity," *Pramana*, vol. 67, pp. 813–820, 2006.

[159] J. Hubisz, P. Meade, A. Noble, and M. Perelstein, "Electroweak precision constraints on the littlest Higgs model with T parity," *JHEP*, vol. 0601, p. 135, 2006.

[160] C. T. Hill and R. J. Hill, "T^- parity violation by anomalies," *Phys.Rev.*, vol. D76, p. 115014, 2007.

[161] C. T. Hill and R. J. Hill, "Topological Physics of Little Higgs Bosons," *Phys.Rev.*, vol. D75, p. 115009, 2007.

[162] D. Krohn and I. Yavin, "Anomalies in Fermionic UV Completions of Little Higgs Models," *JHEP*, vol. 0806, p. 092, 2008.

[163] A. Birkedal, A. Noble, M. Perelstein, and A. Spray, "Little Higgs dark matter," *Phys.Rev.*, vol. D74, p. 035002, 2006.

[164] M. E. Peskin and T. Takeuchi, "A New constraint on a strongly interacting Higgs sector," *Phys.Rev.Lett.*, vol. 65, pp. 964–967, 1990.

[165] M. Golden and L. Randall, "Radiative corrections to electroweak parameters in technicolor theories," *Nucl.Phys.*, vol. B361, pp. 3–23, 1991.

[166] J. Espinosa, C. Grojean, and M. Muhlleitner, "Composite Higgs Search at the LHC," *JHEP*, vol. 1005, p. 065, 2010.

[167] D. B. Kaplan, "Flavor at SSC energies: A New mechanism for dynamically generated fermion masses," *Nucl.Phys.*, vol. B365, pp. 259–278, 1991.

[168] R. Contino, T. Kramer, M. Son, and R. Sundrum, "Warped/composite phenomenology simplified," *JHEP*, vol. 0705, p. 074, 2007.

[169] C. Anastasiou, E. Furlan, and J. Santiago, "Realistic Composite Higgs Models," *Phys.Rev.*, vol. D79, p. 075003, 2009.

[170] F. del Aguila, M. Perez-Victoria, and J. Santiago, "Observable contributions of new exotic quarks to quark mixing," *JHEP*, vol. 0009, p. 011, 2000.

[171] A. Atre, M. Carena, T. Han, and J. Santiago, "Heavy Quarks Above the Top at the Tevatron," *Phys.Rev.*, vol. D79, p. 054018, 2009.

[172] A. Atre, G. Azuelos, M. Carena, T. Han, E. Ozcan, *et al.*, "Model-Independent Searches for New Quarks at the LHC," *JHEP*, vol. 1108, p. 080, 2011.

[173] A. Atre, M. Chala, and J. Santiago, "Searches for New Vector Like Quarks: Higgs Channels," 2013.

[174] A. Antonaki, G. Azuelos, S. Borroni, M. Davies, L. Liu, P. Loscutoff, M. Shapiro, Y. Wu, Z. Zhao, B. Zhou, and J. Zhu, "Search for resonant WZ production in the $WZ \to \ell\nu\ell\ell$ channel using the ATLAS detector," Tech. Rep. ATL-COM-PHYS-2012-1494, CERN, Geneva, Oct 2012.

[175] J. Archibald, S. Hoeche, F. Krauss, F. Siegert, T. Gleisberg, *et al.*, "Simulation of photon-photon interactions in hadron collisions with SHERPA," *Nucl.Phys.Proc.Suppl.*, vol. 179-180, pp. 218–225, 2008.

[176] ATLAS Collaboration, "Improved luminosity determination in pp collisions at $\sqrt{s} = 7$ TeV using the ATLAS detector at the LHC," 2013.

[177] J. Alwall, M. Herquet, F. Maltoni, O. Mattelaer, and T. Stelzer, "MadGraph 5 : Going Beyond," *JHEP*, vol. 1106, p. 128, 2011.

[178] M. L. Mangano, M. Moretti, F. Piccinini, R. Pittau, and A. D. Polosa, "ALPGEN, a generator for hard multiparton processes in hadronic collisions," *JHEP*, vol. 0307, p. 001, 2003.

[179] M. Bahr, S. Gieseke, M. Gigg, D. Grellscheid, K. Hamilton, *et al.*, "Herwig++ Physics and Manual," *Eur.Phys.J.*, vol. C58, pp. 639–707, 2008.

[180] J. Butterworth, J. R. Forshaw, and M. Seymour, "Multiparton interactions in photoproduction at HERA," *Z.Phys.*, vol. C72, pp. 637–646, 1996.

[181] S. Frixione and B. R. Webber, "Matching NLO QCD computations and parton shower simulations," *JHEP*, vol. 0206, p. 029, 2002.

[182] ATLAS Collaboration, "W/Z and Electroweak Common Topics (2011)." `https://twiki.cern.ch/twiki/bin/viewauth/AtlasProtected/WZElectroweakCommonTopics2011`, 2011-2013.

[183] P. M. Nadolsky, H.-L. Lai, Q.-H. Cao, J. Huston, J. Pumplin, *et al.*, "Implications of CTEQ global analysis for collider observables," *Phys.Rev.*, vol. D78, p. 013004, 2008.

[184] T. Aaltonen *et al.*, "Search for new particles decaying into dijets in proton-antiproton collisions at s**(1/2) = 1.96-TeV," *Phys.Rev.*, vol. D79, p. 112002, 2009.

[185] ATLAS Collaboration, "Search for New Particles in Two-Jet Final States in 7 TeV Proton-Proton Collisions with the ATLAS Detector at the LHC," *Phys.Rev.Lett.*, vol. 105, p. 161801, 2010.

[186] CMS Collaboration, "Search for Resonances in the Dijet Mass Spectrum from 7 TeV pp Collisions at CMS," *Phys.Lett.*, vol. B704, pp. 123–142, 2011.

[187] C. T. Hill, "Topcolor assisted technicolor," *Phys.Lett.*, vol. B345, pp. 483–489, 1995.

[188] K. Lane and A. Martin, "An Effective Lagrangian for Low-Scale Technicolor," *Phys.Rev.*, vol. D80, p. 115001, 2009.

[189] CDF Collaboration, "Invariant Mass Distribution of Jet Pairs Produced in Association with a W/Z boson in pp Collisions at CDF," no. 10973, 2013.

[190] R. Lewis, C. Pica, and F. Sannino, "Light Asymmetric Dark Matter on the Lattice: SU(2) Technicolor with Two Fundamental Flavors," *Phys.Rev.*, vol. D85, p. 014504, 2012.

[191] M. T. Frandsen and F. Sannino, "iTIMP: isotriplet Technicolor Interacting Massive Particle as Dark Matter," *Phys.Rev.*, vol. D81, p. 097704, 2010.

[192] A. Hietanen, C. Pica, F. Sannino, and U. I. Sondergaard, "Orthogonal Technicolor with Isotriplet Dark Matter on the Lattice," 2012.

[193] Y. Nambu, "Quasiparticles and Gauge Invariance in the Theory of Superconductivity," *Phys.Rev.*, vol. 117, pp. 648–663, 1960.

[194] J. Goldstone, "Field Theories with Superconductor Solutions," *Nuovo Cim.*, vol. 19, pp. 154–164, 1961.

[195] K. D. Lane, "Technicolor 2000," pp. 235–280, 2000.

[196] S. Dimopoulos and L. Susskind, "Mass Without Scalars," *Nucl.Phys.*, vol. B155, pp. 237–252, 1979.

[197] E. Eichten and K. D. Lane, "Dynamical Breaking of Weak Interaction Symmetries," *Phys.Lett.*, vol. B90, pp. 125–130, 1980.

[198] M. E. Peskin, "The Alignment of the Vacuum in Theories of Technicolor," *Nucl.Phys.*, vol. B175, pp. 197–233, 1980.

[199] S. Dimopoulos and J. R. Ellis, "Challenges for Extended Technicolor Theories," *Nucl.Phys.*, vol. B182, pp. 505–528, 1982.

[200] K. D. Lane and E. Eichten, "Natural topcolor assisted technicolor," *Phys.Lett.*, vol. B352, pp. 382–387, 1995.

[201] C. T. Hill and E. H. Simmons, "Strong dynamics and electroweak symmetry breaking," *Phys.Rept.*, vol. 381, pp. 235–402, 2003.

[202] K. D. Lane, "A New model of topcolor assisted technicolor," *Phys.Lett.*, vol. B433, pp. 96–101, 1998.

[203] M. E. Peskin and T. Takeuchi, "Estimation of oblique electroweak corrections," *Phys. Rev. D*, vol. 46, pp. 381–409, Jul 1992.

[204] T. Appelquist, G. T. Fleming, and E. T. Neil, "Lattice study of the conformal window in QCD-like theories," *Phys.Rev.Lett.*, vol. 100, p. 171607, 2008.

[205] K. Yamawaki, M. Bando, and K.-i. Matumoto, "Scale Invariant Technicolor Model and a Technidilaton," *Phys.Rev.Lett.*, vol. 56, p. 1335, 1986.

[206] T. W. Appelquist, D. Karabali, and L. Wijewardhana, "Chiral Hierarchies and the Flavor Changing Neutral Current Problem in Technicolor," *Phys.Rev.Lett.*, vol. 57, p. 957, 1986.

[207] T. Akiba and T. Yanagida, "Hierarchic Chiral Condensate," *Phys.Lett.*, vol. B169, p. 432, 1986.

[208] T. Appelquist and F. Sannino, "The Physical spectrum of conformal SU(N) gauge theories," *Phys.Rev.*, vol. D59, p. 067702, 1999.

[209] T. Appelquist, P. Rodrigues da Silva, and F. Sannino, "Enhanced global symmetries and the chiral phase transition," *Phys.Rev.*, vol. D60, p. 116007, 1999.

[210] K. D. Lane and E. Eichten, "Two Scale Technicolor," *Phys.Lett.*, vol. B222, p. 274, 1989.

[211] E. Eichten, K. D. Lane, and J. Womersley, "Finding low scale technicolor at hadron colliders," *Phys.Lett.*, vol. B405, pp. 305–311, 1997.

[212] K. D. Lane, "Technihadron production and decay in low scale technicolor," *Phys.Rev.*, vol. D60, p. 075007, 1999.

[213] K. Lane and S. Mrenna, "The Collider phenomenology of technihadrons in the technicolor straw man model," *Phys.Rev.*, vol. D67, p. 115011, 2003.

[214] E. Eichten, K. Lane, and A. Martin, "A Higgs Impostor in Low-Scale Technicolor," 2012.

[215] t. Aaltonen, T., "Invariant mass distribution of jet pairs produced in association with a w boson in $p\bar{p}$ collisions at $\sqrt{s} = 1.96$ TeV," *Phys. Rev. Lett.*, vol. 106, p. 171801, Apr 2011.

[216] E. J. Eichten, K. Lane, and A. Martin, "Technicolor Explanation for the CDF W_{jj} Excess," *Phys.Rev.Lett.*, vol. 106, p. 251803, 2011.

[217] D. D. Dietrich, F. Sannino, and K. Tuominen, "Light composite Higgs from higher representations versus electroweak precision measurements: Predictions for CERN LHC," *Phys.Rev.*, vol. D72, p. 055001, 2005.

[218] F. Sannino, "Dynamical Stabilization of the Fermi Scale: Phase Diagram of Strongly Coupled Theories for (Minimal) Walking Technicolor and Unparticles," 2008.

[219] E. Witten, "An SU(2) Anomaly," *Phys.Lett.*, vol. B117, pp. 324–328, 1982.

[220] J. Andersen, O. Antipin, G. Azuelos, L. Del Debbio, E. Del Nobile, *et al.*, "Discovering Technicolor," *Eur.Phys.J.Plus*, vol. 126, p. 81, 2011.

[221] A. Belyaev, R. Foadi, M. T. Frandsen, M. Jarvinen, F. Sannino, *et al.*, "Technicolor Walks at the LHC," *Phys.Rev.*, vol. D79, p. 035006, 2009.

[222] ATLAS Collaboration, "Search for high-mass resonances decaying to dilepton final states in pp collisions at $\sqrt{s} = 7$ TeV with the ATLAS detector," *JHEP*, vol. 1211, p. 138, 2012.

[223] A. Collaboration, "Search for resonant diboson production in the $WW/WZ \to l\nu jj$ decay channels with the ATLAS detector at $\sqrt{s} = 7$ TeV," 2013.

[224] A. Sherstnev and R. Thorne, "Different PDF approximations useful for LO Monte Carlo generators," p. 149, 2008.

[225] P. Nason, "A New method for combining NLO QCD with shower Monte Carlo algorithms," *JHEP*, vol. 0411, p. 040, 2004.

[226] S. Frixione, P. Nason, and C. Oleari, "Matching NLO QCD computations with Parton Shower simulations: the POWHEG method," *JHEP*, vol. 0711, p. 070, 2007.

[227] S. Alioli, P. Nason, C. Oleari, and E. Re, "A general framework for implementing NLO calculations in shower Monte Carlo programs: the POWHEG BOX," *JHEP*, vol. 1006, p. 043, 2010.

[228] T. Binoth, M. Ciccolini, N. Kauer, and M. Kramer, "Gluon-induced W-boson pair production at the LHC," *JHEP*, vol. 0612, p. 046, 2006.

[229] J. Pumplin, D. Stump, J. Huston, H. Lai, P. M. Nadolsky, *et al.*, "New generation of parton distributions with uncertainties from global QCD analysis," *JHEP*, vol. 0207, p. 012, 2002.

[230] B. P. Kersevan and E. Richter-Was, "The Monte Carlo event generator AcerMC version 2.0 with interfaces to PYTHIA 6.2 and HERWIG 6.5," 2004.

[231] ATLAS Collaboration, "Measurement of WZ production in proton-proton collisions at $\sqrt{s} = 7$ TeV with the ATLAS detector," *Eur.Phys.J.*, vol. C72, p. 2173, 2012.

[232] ATLAS Collaboration, "Measurement of ZZ production in pp collisions at $\sqrt{s} = 7$ TeV and limits on anomalous ZZZ and $ZZ\gamma$ couplings with the ATLAS detector," *JHEP*, vol. 1303, p. 128, 2013.

[233] ATLAS Collaboration, "Measurement of $W\gamma$ and $Z\gamma$ production in proton-proton collisions at $\sqrt{s} = 7$ TeV with the ATLAS Detector," *JHEP*, vol. 1109, p. 072, 2011.

[234] F. Campanario and S. Sapeta, "WZ production beyond NLO for high-pT observables," *Phys.Lett.*, vol. B718, pp. 100–104, 2012.

[235] A. Martin, W. Stirling, R. Thorne, and G. Watt, "Parton distributions for the LHC," *Eur.Phys.J.*, vol. C63, pp. 189–285, 2009.

[236] ATLAS Collaboration, "The TGC Parameter Book," 2009.

[237] F. Feroz, *Bayesian methods for astrophysics and particle physics*. PhD thesis, University of Cambridge, Oct. 2008.

[238] R. Cousins, "Treatment of nuisance parameters in high energy physics, and possible justifications and improvements in the statistics literature," *Conf.Proc.*, vol. C050912, pp. 75–85, 2005.

[239] B. Mistlberger and F. Dulat, "Limit setting procedures and theoretical uncertainties in Higgs boson searches," 2012.

[240] J. Neyman and E. S. Pearson, "On the problem of the most efficient tests of statistical hypotheses," *Philosophical Transactions of the Royal Society of London. Series A, Containing Papers of a Mathematical or Physical Character*, vol. 231, pp. pp. 289–337, 1933.

[241] G. Zech, "Upper limits in experiments with background or measurement errors," *Nuclear Instruments and Methods in Physics Research Section A: Accelerators, Spectrometers, Detectors and Associated Equipment*, vol. 277, no. 2 to 3, pp. 608 – 610, 1989.

[242] G. Cowan, K. Cranmer, E. Gross, and O. Vitells, "Asymptotic formulae for likelihood-based tests of new physics," *Eur.Phys.J.*, vol. C71, p. 1554, 2011.

[243] A. Wald, "Tests of statistical hypotheses concerning several parameters when the number of observations is large," *Transactions of the American Mathematical Society*, vol. 54, No. 3, pp. 426–482, 1943.

[244] S. S. Wilks, "The large-sample distribution of the likelihood ratio for testing composite hypotheses," *The Annals of Mathematical Statistics*, vol. 9, no. 1, pp. pp. 60–62, 1938.

[245] G. Choudalakis, "On hypothesis testing, trials factor, hypertests and the bumphunter georgios choudalakis," p. 39, 2011.

[246] K. Agashe, R. Contino, L. Da Rold, and A. Pomarol, "A custodial symmetry for Zb anti-b," *Phys.Lett.*, vol. B641, pp. 62–66, 2006.

[247] ATLAS Collaboration, "Luminosity Determination in pp Collisions at $\sqrt{s} = 7$ TeV Using the ATLAS Detector at the LHC," *Eur.Phys.J.*, vol. C71, p. 1630, 2011.

[248] ATLAS Collaboration, "ATLAS search for a heavy gauge boson decaying to a charged lepton and a neutrino in pp collisions at $\sqrt{s} = 7$ TeV," *Eur.Phys.J.*, vol. C72, p. 2241, 2012.

[249] CMS Collaboration, "Search for leptonic decays of W' bosons in pp collisions at $\sqrt{s} = 7$ TeV," *JHEP*, vol. 1208, p. 023, 2012.

[250] R. Hamberg, W. van Neerven, and T. Matsuura, "A complete calculation of the order α_s^2 correction to the Drell-Yan K-factor," *Nuclear Physics B*, vol. 359, no. 2-3, pp. 343 – 405, 1991.

Appendix I

ATLAS DETECTOR - MISCELLANEOUS FEATURES

Table I.I shows in details the granularity of the EM and hadronic calorimeters.

Barrel Calorimeters

Detector	η coverage	Granularity $\Delta\eta \times \Delta\phi$
Presampler	$\|\eta\| < 1.52$	0.025×0.1
EM barrel calorimeter - 1st layer	$\|\eta\| < 1.4$	$0.025/8 \times 0.1$
	$1.4 < \|\eta\| < 1.475$	0.025×0.025
EM barrel calorimeter - 2nd layer	$\|\eta\| < 1.4$	0.025×0.025
	$1.4 < \|\eta\| < 1.475$	0.075×0.025
EM barrel calorimeter - 3rd layer	$\|\eta\| < 1.35$	0.05×0.025
Tile barrel calorimeter	$\|\eta\| < 1.0$	0.1×0.1
Tile extended barrel calorimeter	$0.8 < \|\eta\| < 1.7$	0.1×0.1

End-cap Calorimeters

Detector	η coverage	Granularity $\Delta\eta \times \Delta\phi$
Presampler	$1.5 < \|\eta\| < 1.8$	0.025×0.1
EMEC - 1st layer	$1.375 < \|\eta\| < 1.425$	0.05×0.1
	$1.425 < \|\eta\| < 1.5$	0.025×0.1
	$1.5 < \|\eta\| < 1.8$	$0.025/8 \times 0.1$
	$1.8 < \|\eta\| < 2.0$	$0.025/6 \times 0.1$
	$2.0 < \|\eta\| < 2.4$	$0.025/4 \times 0.1$
	$2.4 < \|\eta\| < 2.5$	0.025×0.1
	$2.5 < \|\eta\| < 3.2$	0.1×0.1
EMEC - 2nd layer	$1.375 < \|\eta\| < 1.425$	0.05×0.025
	$1.425 < \|\eta\| < 2.5$	0.025×0.025
	$2.5 < \|\eta\| < 3.2$	0.1×0.1
EMEC - 3rd layer	$1.5\|\eta\| < 2.5$	0.05×0.025
HEC	$1.5 < \|\eta\| < 2.5$	0.1×0.1
	$2.5 < \|\eta\| < 3.2$	0.2×0.2
FCAL - 1st	$3.15 < \|\eta\| < 4.30$	$\sim 0.8 \times 0.7$
	$3.15 < \|\eta\| < 4.30$	3.0×2.6
	$4.30 < \|\eta\| < 4.83$	$\sim 0.8 \times 0.7$
FCAL - 2nd	$3.20 < \|\eta\| < 3.24$	$\sim 0.9 \times 1.1$
	$3.24 < \|\eta\| < 4.5$	3.3×4.2
	$4.5 < \|\eta\| < 4.81$	$\sim 0.9 \times 1.1$
FCAL - 3rd	$3.29 < \|\eta\| < 3.32$	$\sim 1.3 \times 1.2$
	$3.32 < \|\eta\| < 4.6$	5.4×4.7
	$4.6 < \|\eta\| < 4.75$	$\sim 1.3 \times 1.2$

Table I.I: $\Delta\eta \times \Delta\phi$ granularity of ATLAS' barrel and end-cap calorimeters [80].

Table I.II provides information on the granularity, size, and η range of the muon

subdetectors.

Detector	Function	Region	η range	Number of output channels	Size [m^2]
MDT	Tracking	barrel+endcap	$\|\eta\| < 2.7$	3.54×10^5	5500
CSC	Tracking	endcap	$2.0 < \|\eta\| < 2.7$	3.07×10^4	27
RPC	Trigger	barrel	$\|\eta\| < 1.0$	3.73×10^5	3650
TGC	Trigger	endcap	$1.0 < \|\eta\| < 2.4$	3.18×10^5	2900

Table I.II: Muon spectrometer subdetector layout, function, number of output channels, and area size [105].

The general RPC and TGC operational specificities are presented in table I.III.

Parameter	RPC	TGC
Gas composition	$C_2H_2F_4$/Iso-C_4H_{10}/SF_6 (94.7/5/0.3)	CO_2/n-pentane (55/45)
Intrinsic operation time	10 ns	25 ns
Nominal operating voltage	9800 V	2900 V
η coverage	$\|\eta\| < 1.05$	$1.05 < \|\eta\| < 2.4$

Table I.III: The muon triggering detector specificities, comparing the gas composition, intrinsic operation time, nominal operating voltage, and η coverage between the RPC and TGC [80, 109, 236].

Appendix II

ATLAS EVENT DISPLAYS

The following figures present the highest invariant mass candidate events in each of the studied decay channels for both the VLQ and WZ resonance searches. Figures II.1 through II.4 show these candidate events for the VLQ search while figures II.5 through II.8 illustrate those in the WZ resonance search.
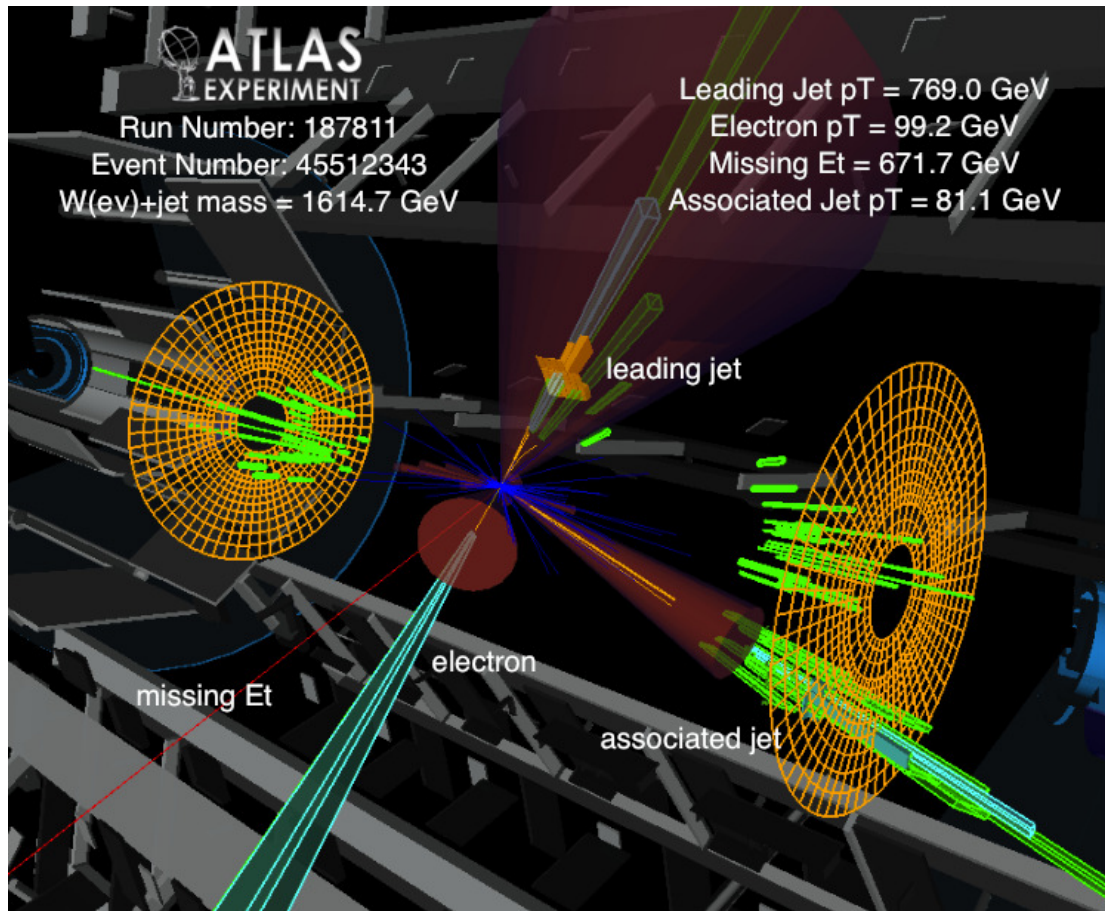
Figure II.1: Event display of a vector-like quark candidate in the CC decay channel with $W \rightarrow e\nu$ that had the highest invariant mass. The leading p_T jet combined with the electron and E_T^{miss} together formed an 1610 GeV invariant mass candidate.
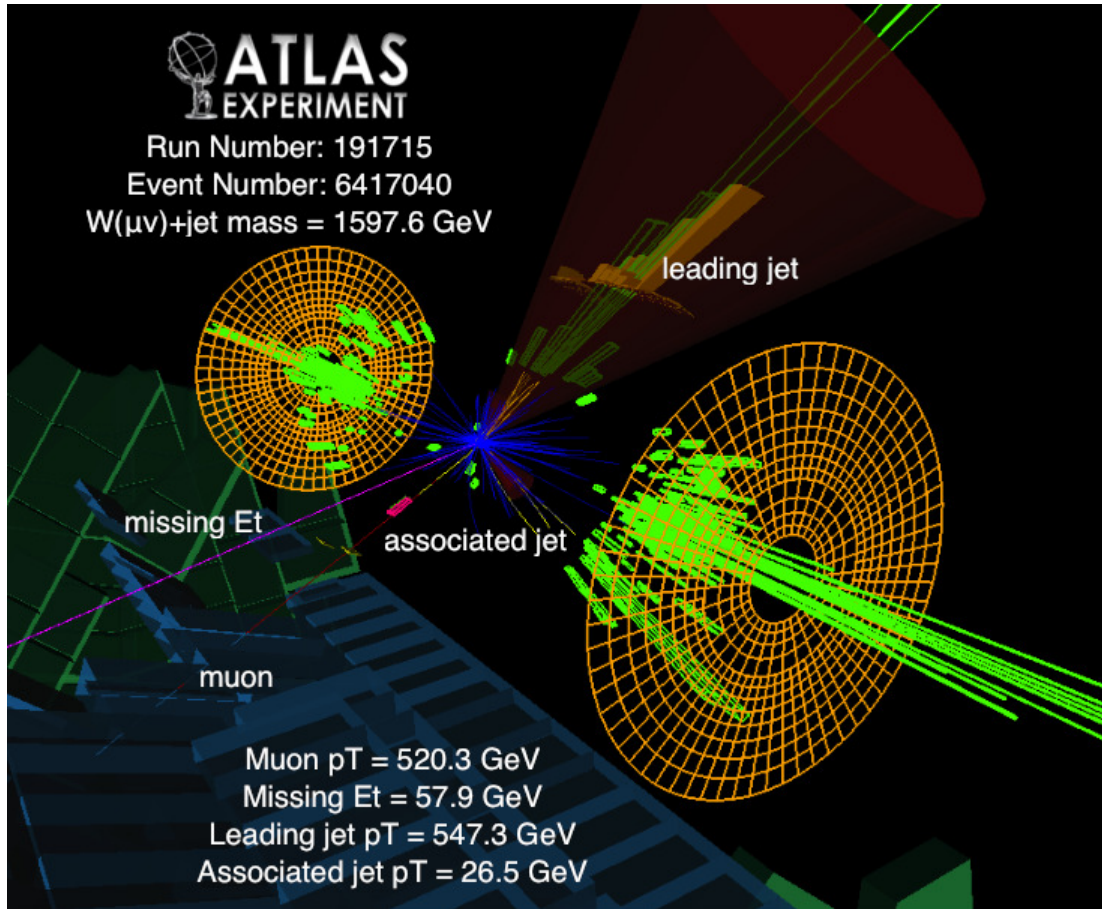
Figure II.2: Event display of a vector-like quark candidate in the CC decay channel with $W \rightarrow \mu\nu$ that had the highest invariant mass. The leading p_T jet combined with the muon and E_T^{miss} together formed an 1600 GeV invariant mass candidate.
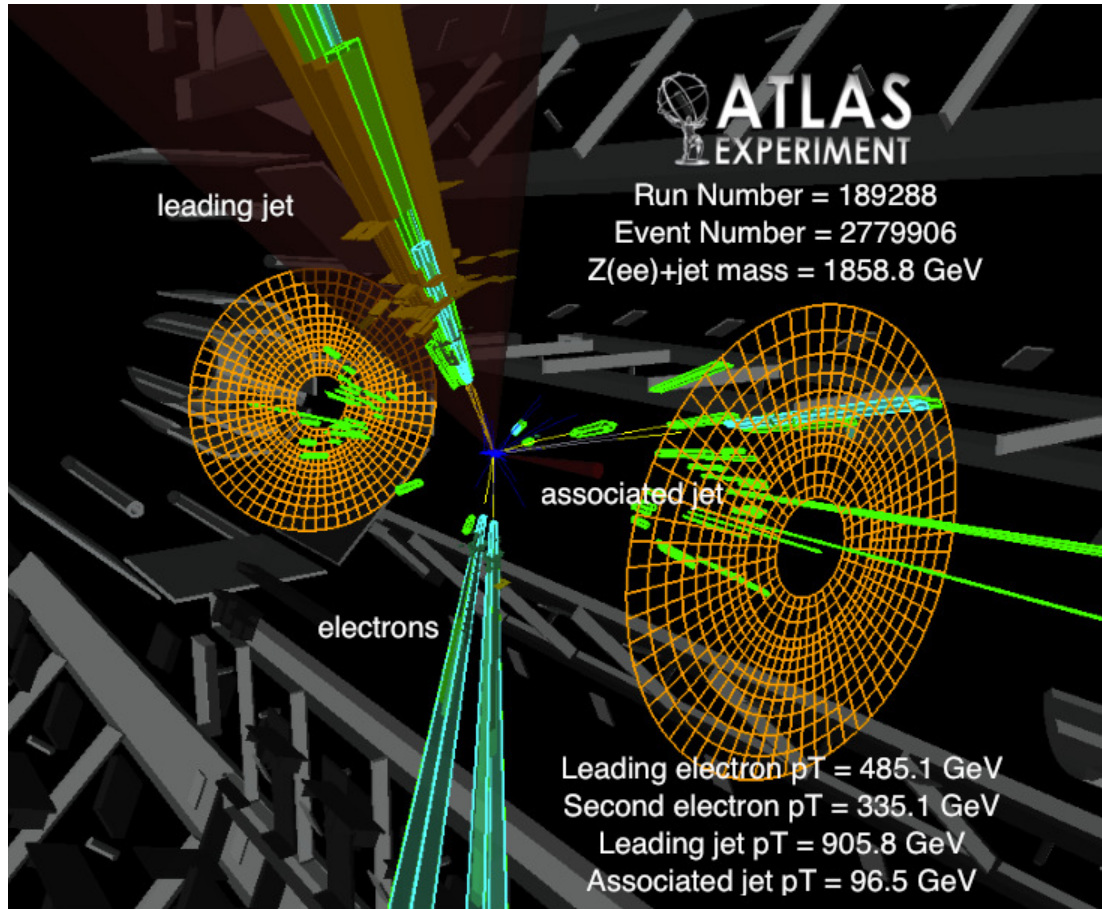
Figure II.3: Event display of a vector-like quark candidate in the NC decay channel with $Z \to ee$ that had the highest invariant mass. The leading p_T jet combined with the two electrons formed an 1860 GeV invariant mass candidate.
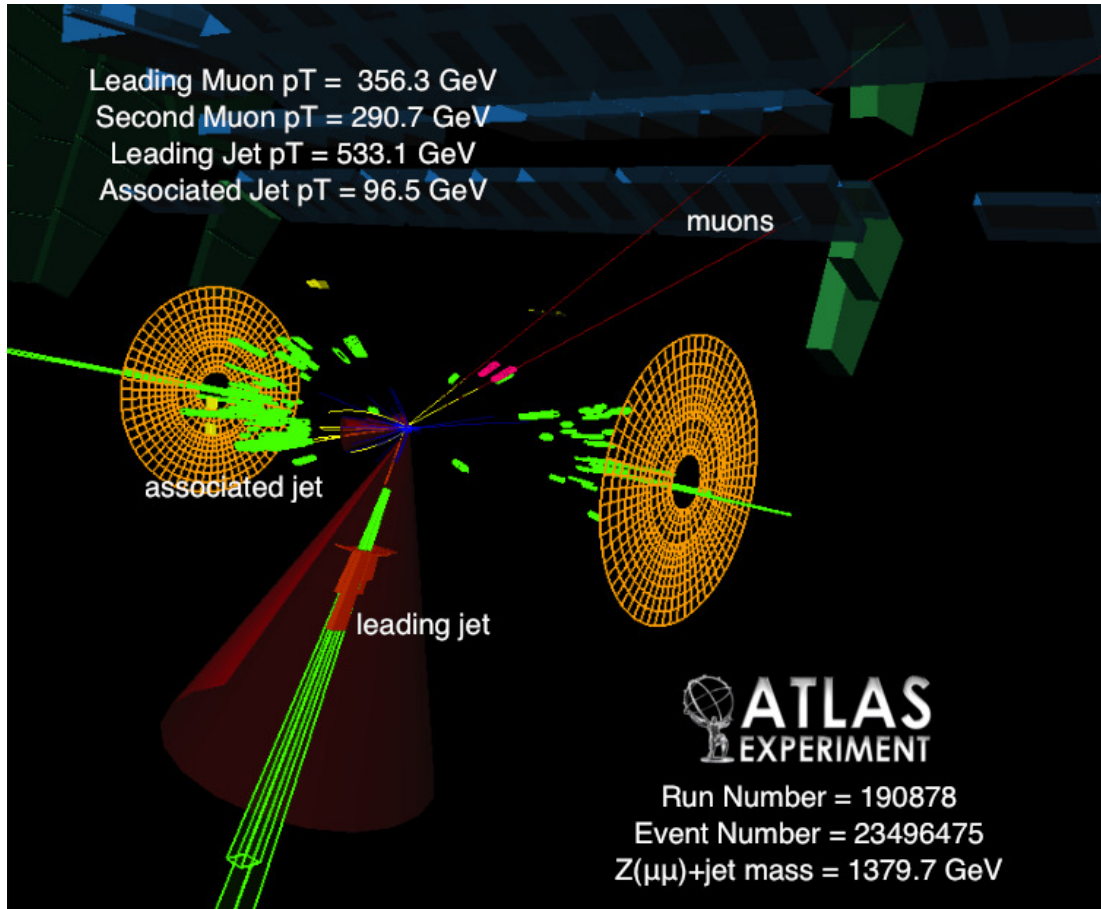
Figure II.4: Event display of a vector-like quark candidate in the NC decay channel with $Z \to \mu\mu$ that had the highest invariant mass. The leading p_T jet combined with the two muons formed an 1380 GeV invariant mass candidate.
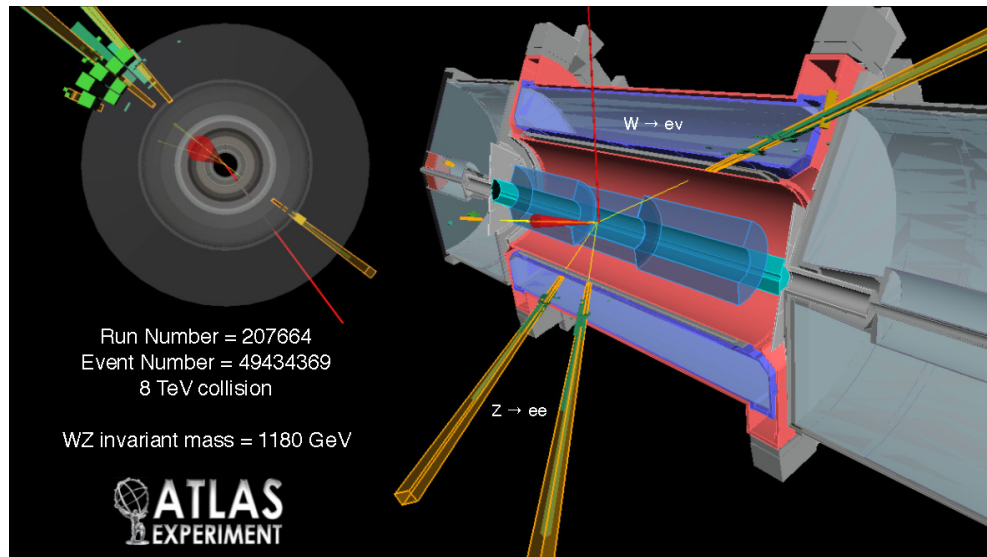
Figure II.5: Event display of the highest WZ invariant mass candidate in the triple electron channel. The reconstructed electron tracks are colored yellow while the direction of the missing transverse energy is indicated by the red line. The event has a WZ invariant mass of 1180 GeV.
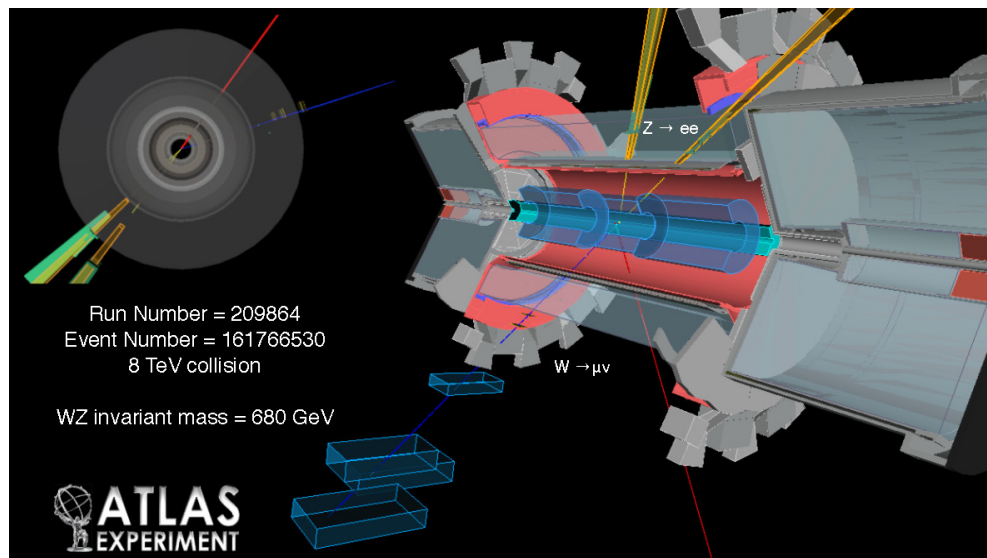
Figure II.6: Event display of the highest WZ invariant mass candidate in the one muon plus two electron channel. The reconstructed electron tracks are colored yellow while the reconstructed muon track is illustrated by the blue line. The direction of the missing transverse energy is indicated by the red line. The event has a reconstructed WZ invariant mass of 680 GeV.
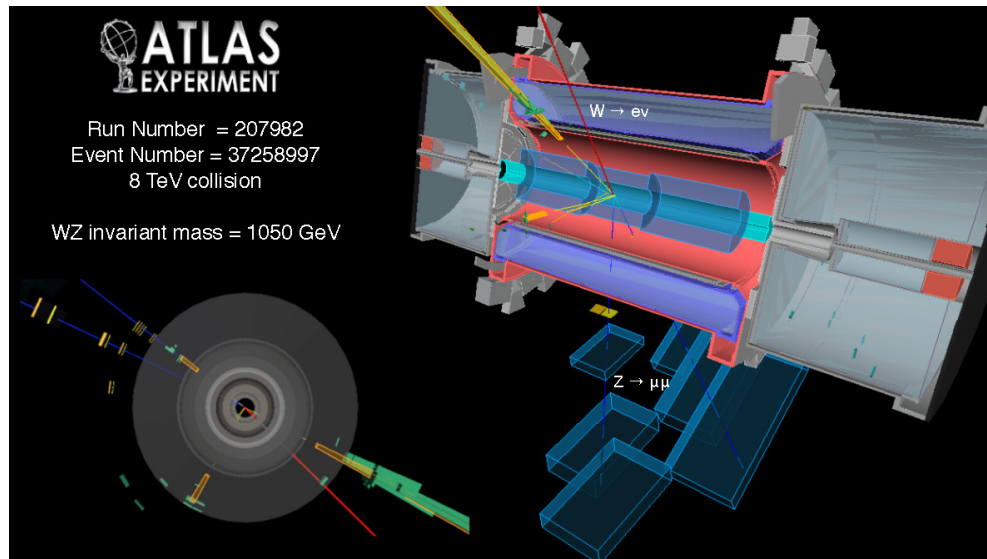
Figure II.7: Event display of the highest WZ invariant mass candidate in the one electron plus two muon channel. The reconstructed electron track is colored yellow while the reconstructed muon tracks are illustrated by the blue lines. The direction of the missing transverse energy is indicated by the red line. The event has a reconstructed WZ invariant mass of 1050 GeV.
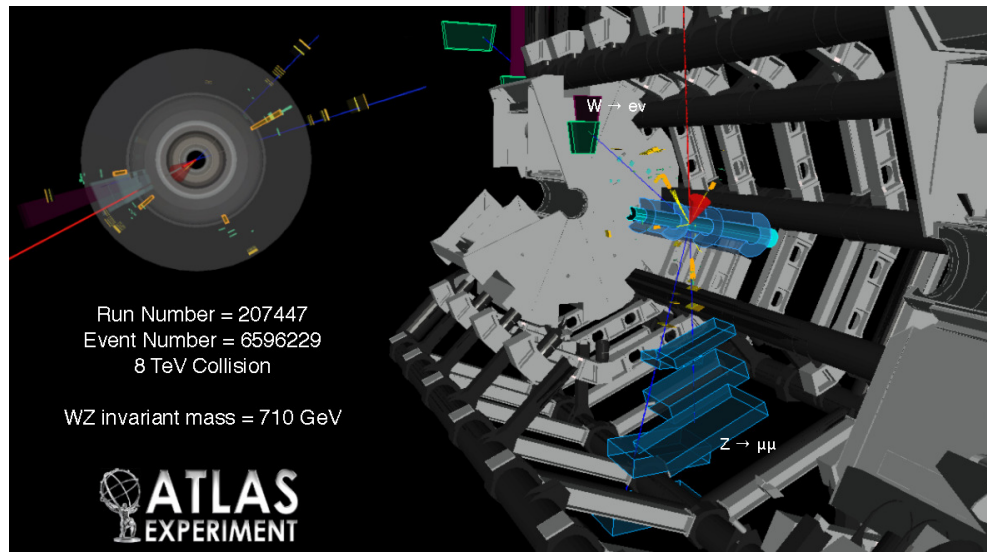
Figure II.8: Event display of the highest WZ invariant mass candidate in the triple muon channel. The reconstructed muon tracks are colored blue while the direction of the missing transverse energy is indicated by the red line. The event has a reconstructed WZ invariant mass of 710 GeV.

Appendix III

LIMIT SETTING TECHNIQUES

This annex discusses and explains the statistical methods and tools used in the search for vector-like quarks and WZ resonances.

III.1 ATLAS: FREQUENTIST OR BAYESIAN?

As with any scientific endeavour, one would like to make a probabilistic statement relating the hypothesis and the outcome of an experiment (the data). Two distinct possibilities then come about regarding how one wants to frame the results. The first being a statement about the probability of a hypothesis H given the data D:

$$p(H|D), \tag{III.1}$$

This is known as the Bayesian approach. The second is a statement about the probability of the data assuming the hypothesis were true, or

$$p(D|H). \tag{III.2}$$

The is the frequentist approach. It is associated to the frequency interpretation of probability which views D as outcomes of repeatable experiments. The Bayesian method on the other hand, defined by equation (III.1), has the advantage of being closely related to the intuitive notion of probability. However, to arrive at such a probability, one needs to use Bayes' theorem:

$$p(\theta|D) = \frac{p(D|\theta)p(\theta|A)}{\int p(D|\theta')p(\theta'|A)\,d\theta'} \tag{III.3}$$

where A refers to all *prior* knowledge obtained before experiment D took place, where θ and θ' are the parameters one would wish to measure (thus defining H), and where the law of total probability was used to replace $p(D)$ in the denominator. The difficulty in employing the Bayesian method is how one defines the prior $p(\theta|A)$, which is not

straight forward. The prior probability distribution often depends on unmeasurable variables or parameters, such as the prior *belief* in SUSY, thus consequently rendering an objective assessment of its value more difficult to achieve. Despite some recent advancements [237], the Bayesian method is less frequently used by the ATLAS Collaboration in favor of Frequentist methods.

III.2 THE LOG-LIKELIHOOD RATIO AS TEST STATISTIC

The probability in (III.2) is a function of H, the hypothesis choice, itself possibly dependent on a number of parameters. Experiments almost always concentrate on a single parameter of interest, and in the case of new particle resonances, it is nominally the signal strength μ. The set of variables affecting the precision of measurements of μ are called the nuisance parameters ν_j. These are directly related to the systematic uncertainties and are a reflection of the uncertainties in the background model and the signal itself. A detailed treatment of nuisance parameters is found in the literature [238]. In what ensues here, we will content ourselves with a description of how they were treated in the analyses presented in the main text.

Given a set $X = X_i$ of N measured values, where X_i are the number of events in a defined region (bin), the probability $p(D|\theta)$ can thereby be written as [239]:

$$p(\text{Data}|\mu, \nu_j) = p(X|\mu, \nu_j) \tag{III.4}$$

$$= \prod_i^N p(X_i|\mu, \nu_j) \tag{III.5}$$

$$= L(\mu, \nu_j|X), \tag{III.6}$$

where $L(\mu, \nu_j|X)$ is the binned-likelihood of a signal of strength μ, and nuisance parameters ν_j given X_i. From probability theory, $p(X_i|\mu, \nu_j)$ are distributed following the Poisson distribution (assuming low-statistics):

$$p(X_i|\mu, \nu_i) = \frac{e^{-\lambda(\mu;\nu_j)}\lambda(\mu, \nu_j)^{X_i}}{X_i!}, \tag{III.7}$$

where $\lambda(\mu; \nu_j)$ is the expected value given the hypothetical signal. The nomenclature $\lambda(\mu; \nu_j)$ signifies that $\lambda(\mu; \nu_j)$ is a function of μ and gaussian convoluted with the nuisance parameters ν_j. The actual dependence however of λ on ν_j is non-analytical and often intractable, hence the notation. The background+signal hypothesis, and background-only hypothesis, in terms of their likelihoods, can be written as:

$$L(\mu, \nu_j | X) = L(b + \mu s | X) = \prod_i^N \frac{\lambda(\mu, \nu_j)^{X_i} e^{-\lambda_i(\mu, \nu_j)}}{X_i!}, \text{ and} \qquad \text{(III.8)}$$

$$L(\mu = 0, \nu_j | X) = L(b | X) = \prod_i^N \frac{\lambda(\mu = 0, \nu_j)^{X_i} e^{-\lambda_i(\mu = 0, \nu_j)}}{X_i!}, \qquad \text{(III.9)}$$

where it is assumed that b_i and s_i are convolutely dependent on ν_j. The functions s_i (b_i) encode the shape of the signal (background) across each bin i. All of this in hand, the log-likelihood ratio (LLR) test statistic can now be defined:

$$LLR(X) = -2 \ln \frac{L(b + \mu s | X)}{L(b + \hat{\mu} s | X)} \qquad \text{(III.10)}$$

$$= -2 \ln \prod_i^N \frac{\frac{(b_i + \mu s_i)^{X_i} e^{-(b_i + \mu s_i)}}{X_i!}}{\frac{(b_i + \hat{\mu} s_i)^{X_i} e^{-(b_i + \hat{\mu} s_i)}}{X_i!}}$$

$$= -2 \ln \left[\prod_i^N \left(\frac{b_i + \mu s_i}{b_i + \hat{\mu} s_i} \right)^{X_i} e^{(\hat{\mu} - \mu) s_i} \right] \qquad \text{(III.11)}$$

for $\mu \geq \hat{\mu} \geq 0$, otherwise $LLR(X) = 0$. $\hat{\mu}$ is the value of μ that maximizes unconditionally (irrespective of ν_j) the likelihood. Under some circumstances, as in the asymptotic approximation method, the criteria $\hat{\mu} > 0$ may be loosened to allow negative signal strengths [1] in order to describe $\hat{\mu}$ as Gaussian distributed variable (more on this in section III.4). The -2 factor is inserted in the LLR to link it to the χ^2 test in the limit of high statistics where the Poisson distribution becomes a Gaussian distributed one. With the simplifications $\mu = 1$, and $\hat{\mu} = 0$, the LLR becomes

$$LLR(X) = -2 \ln \frac{L(b + s | X)}{L(b | X)} = 2 \left[s_i - X_i \ln \left(1 + \frac{s_i}{b_i} \right) \right]. \qquad \text{(III.12)}$$

---

1. This while always keeping $b_i + \mu s_i$ positive.

A number of different types of test statistics exist, however the LLR has the highest statistical power according to the Neyman-Pearson lemma [240]. For this reason, the LLR is the foremost used test statistic in particle physics. Finally, the dependencies of s_i and b_i on ν_j are treated in a manner explained in the next section.

III.3 THE CL$_s$ METHOD

The LLR test is performed only once using the data, i.e. $LLR(X = \text{Data})$. Then, to decipher its statistical significance, its value is compared to the probability density function

$$\mathcal{P}(LLR(X = \text{Pseudo-data})), \tag{III.13}$$

where the pseudo-data is generated according to the following prescription:

- 1) Set μ to a value between $]0, \infty[$. This value will be varied iteratively [2].
- 2) For each nuisance parameter ν_j, or equivalently each systematic uncertainty, generate a random number r_j from a normalized Gaussian distribution with the variance of ν_j. If the systematic uncertainties are asymmetric, extract the random number from a pair of bifurcated Gaussian distributions.
- 3) Adding together the contributions of each background type k and signal, compute the total yield to bin i with

$$b_i^k = b_i^{k,0} \left(1 + \sum_j^{N_{\text{Syst}}} |b_i^{k,0} - b_{j,i}^{k,1}| r_j \right) \tag{III.14}$$

$$s_i = s_i^0 \left(1 + \sum_j^{N_{\text{Syst}}} |s_i^0 - s_{j,i}^1| r_j \right), \tag{III.15}$$

where N_{Syst} are the number of systematic uncertainties, $b^{k,0}$ and s^0 are the nominal background k and signal yields in bin i, and where $b_{j,i}^{k,1}$ and $s_{j,i}^{k,1}$ are the $\pm 1\sigma$ variations in the yields due to systematic uncertainty j in bin i for background k and signal respectively. Here, each systematic is treated in a fully correlated bin-by-

---

2. Generally begin with $\mu = 1$.

bin fashion. In other words, only one random number is required and used for all bins i as equations (III.14) and (III.15) indicate. Note however, that the systematic uncertainties amongst themselves are assumed to be completely uncorrelated, that is, the r_j are independent from one another.

- 4) Extract values from a Poisson distribution under hypotheses $b_i + s_i$ and b_i

$$D_i^{b+s} = \text{Poisson}\left(\sum_k^{N_{\text{Back}}} b_i^k\right) + \text{Poisson}(s_i) \qquad \text{(III.16)}$$

$$D_i^b = \text{Poisson}\left(\sum_k^{N_{\text{Back}}} b_i^k\right), \qquad \text{(III.17)}$$

with means equal to the sum of all backgrounds $\sum_k^{N_{\text{Back}}} b_i^k$ or signal s_i.

- 5) Compute the LLR with $X = D^{b+s}$ and $X = D^b$.
- 6) Repeat operations 2) to 5) to obtain the probability density distributions $\mathcal{P}(LLR(D^{b+s}))$ and $\mathcal{P}(LLR(D^b))$.

With sufficient statistics, these probability densities are then compared to $LLR(X = \text{Data})$, the LLR value for data, thereby defining in the same step the confidence levels

$$\text{CL}_{b+s} = \int_{LLR(X=\text{Data})}^{\infty} \mathcal{P}(LLR(D^{b+s})) \qquad \text{(III.18)}$$

for the background plus signal hypothesis and

$$\text{CL}_b = \int_{-\infty}^{LLR(X=\text{Data})} \mathcal{P}(LLR(D^b)) \qquad \text{(III.19)}$$

for the background-only hypothesis. These quantities are interpreted as the frequency or probability that the data results from either background plus signal or background-only hypotheses. Both are fundamental in indicating the reliability of the predictions. They are also deeply related to the premise of the frequentist approach, which views D, or the data, as a single sample of a larger set of outcomes of repeatable experiments.

Although CL$_{b+s}$ and CL$_b$ are well defined statistical quantities, they are heavily dependent on the background modelling. To extract a statement about the presence of a

signal, the ratio

$$\mathrm{CL}_s = \frac{\mathrm{CL}_{b+s}}{\mathrm{CL}_b} \tag{III.20}$$

becomes valuable. By definition, it defines the confidence level in the signal hypothesis. For example, if

$$\mathrm{CL}_s \leq 0.05, \tag{III.21}$$

then the signal is excluded at 95% C.L. [3] The objective is hence to vary the signal strength μ and repeat the pseudo-experiments until the CL_s value approaches 0.05 at which point the μ parameter can be translated to a 95% C.L. upper limit on the signal cross section.

First proposed by G. Zech in 1989 [241], the CL_s method was first put into practice during the LEP experiment. A clear definite interpretation of the CL_s value however remains somewhat out of reach since it is a *ratio* of probabilities, and therefore its precise meaning is hard to circumscribe. It remains nonetheless the most frequently used technique for extracting limits in particle physics simply because it makes a quantifiable statement about the signal strength that is disentangled from background hypotheses.

Lastly, for completeness, it is convenient to defined here the p-value:

$$p = 1 - \mathrm{CL}_b = \int_{t(X)}^{\infty} \mathcal{P}(t(D^{b+s})), \tag{III.22}$$

where $t(X)$ is some test statistic (generalizing slightly equation (III.19) where $t(X) = LLR(X)$). It is interpreted as the probability that the data agrees with or is less signal-like than the background-only hypothesis. It is often quoted in standard deviation σ. A 5σ discovery for examples can be translated to a p-value of $p = 4.3 \times 10^{-7}$.

III.4   ASYMPTOTIC APPROXIMATION FOR LLR BASED TESTS

The amount of computing time necessary for generating the myriads of pseudo-experiments can sometimes be a burden difficult to circumvent. However, there exist asymptotic approximations [242] that offer simplifications to the procedure outlined in

---

3. Since CL_b is less than unity, the exclusion based on CL_s is more conservative than exclusion on CL_{b+s}.

the previous section in the limit of high statistics. Namely, the LLR test statistic for a single parameter of interest μ has been shown to follow [243]

$$LLR(\mu, \nu_j | X) = \frac{\mu - \hat{\mu}}{\sigma^2} + \mathcal{O}(1/\sqrt{N}), \tag{III.23}$$

where N is the size of the sample, $\hat{\mu} \leq \mu$ are those defined in equation (III.10), and where σ is the standard deviation of $\hat{\mu}$ obtained from the covariance matrix of all parameters, i.e. both μ and the nuisance parameters (see [242] for more details). Assuming $\mathcal{O}(1/\sqrt{N})$ is negligible, it has also been shown that the probability density distribution follows a χ^2 distribution with one degree of freedom μ [244]. If the LLR does indeed follow a χ^2 distribution, one can use (III.23) and the definition the CL$_s$ 95% confidence level exclusion to solve for μ:

$$\frac{1 - \Phi\sqrt{LLR(\mu, \nu_i | X)}}{\Phi\left(\sqrt{LLR(\mu = 0, \nu_i | X)} - \sqrt{LLR(\mu, \nu_i | X)}\right)} = 0.05 \tag{III.24}$$

where Φ is the cumulent of a standard Gaussian with mean and variance equal to 1. Using equation (III.24), a simple numerical scan of μ renders the desired result, and in doing so, no pseudo-experiment was required saving precious computation time.

III.5   BUMP HUNTING METHODS

The CL$_s$ method is extremely useful for excluding various regions of BSM parameter regions. However, if a real signal appears, one would like a more flexible tool for scrutinizing the signal region than the CL$_s$ method, which can be quite cumbersome given that it requires a specific signal shape for every mass point considered. To this end, the ATLAS BUMPHUNTERtool was developed [245]. Its only requirement on the test statistic is that it be monotonically increasing as a function of signal content. For simplicity, one can therefore use instead of the usual log-Likelihood ratio

$$t(X) = \sum_i \left(\frac{X_i - b_i}{\sqrt{b_i}}\right)^2, \tag{III.25}$$

which is the χ^2 test statistic. Notice from equation (III.25) that the BUMPHUNTERtool concerns itself exclusively with background-only hypotheses, and in particular with p-values as defined in equation (III.22). The BUMPHUNTERalgorithm constructs a set $K = \{p - \text{value}_i\}$ of p-values by computing the probability density distributions $\mathcal{P}(t(X))$ in a restricted window within the distribution of interest I [4] and finds the smallest p-value within this set K by sliding the window across all bins of the distribution.

More thoroughly, The BUMPHUNTERprocedure works as follows. With a given set of data D and expected background B, one must first set

- 1) The minimum and maximum widths of the search window. This choice follows naturally from the detector resolution of the variable of interest I and the chosen binning of its distribution (whose widths should also ideally be equivalent to the detector's resolution).

- 2) The width of the sidebands (optional) if one desires to impose that B does not exceed D in the sideband region. This is useful for eliminating possible normalization issues between the expected B and D.

From there, the BUMPHUNTERtool counts the number of data D in the window D_W as well as the number in the left and right sideband regions D_L and D_R, and does the same for the background, thereby obtaining the three real values B_W, B_L, and B_R. Then it extends the definition of the test statistic in equation (III.25) to account for sidebands [245]:

$$
t(X) = \begin{cases} 0 & \text{if } D_W \leq B_W \text{ or } F(D_L, B_L) \leq a \text{ or } F(D_R, B_R) \leq a \\ \sum_i^{\text{window}} \left(\frac{X_i - b_i}{\sqrt{b_i}} \right)^2 & \text{otherwise} \end{cases}
$$

(III.26)

where

$$
F(D, B) = \begin{cases} \sum_{n=D}^{\infty} \frac{B^n}{n!} e^{-B} & \text{if } D \geq B, \\ \sum_{n=0}^{D} \frac{B^n}{n!} e^{-B} & \text{if } D < B, \end{cases}
$$

(III.27)

and where the χ^2 test statistic was chosen here without loss of generality. Therefore,

---

4. This can be the invariant mass distribution of $t\bar{t}$, for example.

the parameter a in (III.26) controls how strict one wants B to match D in the sideband regions. Using the well-known convergence formulas for these sums, one finds

$$\sum_{n=D}^{\infty} \frac{B^n}{n!} e^{-B} = \frac{1}{\Gamma(D)} \int_0^B x^{D-1} e^{-x}\, dx = \Gamma(D, B) \tag{III.28}$$

$$\text{and} \quad \sum_{n=0}^{D} \frac{B^n}{n!} e^{-B} = \frac{1}{\Gamma(D)} \int_B^{\infty} x^{D-1} e^{-x}\, dx, \tag{III.29}$$

$$\tag{III.30}$$

where $\Gamma(D) = \int_0^{\infty} x^{D-1} e^{-x}\, dx$ is the standard gamma function. These identities facilitate the calculation of the p-values since they side step the computationally intensive pseudo-experiments. Finally, as mentioned before, the p-value calculation is then repeated for every possible window within I yielding the set K of p-values from which the smallest is chosen to give

$$h = -\ln(\min(K)). \tag{III.31}$$

This p-value h carries information about the whole I spectrum and describes where the background-only hypothesis is least probable. In other words, it points to the region within I where a false-discovery is least probable, signifying by the same token where a possible signal may lie.

The BUMPHUNTERmethod just describes was used in the search for vector-like quarks (see chapter 5) and is a powerful tool for clearly quantifying whether a distribution contains a significantly discrepant region or not. In the advent the smallest p-value is above a certain predetermined threshold [5] (say 0.005 for example), then the usual CL$_s$ may then be safely employed to place limits on the processes' cross section.

---

5. This arbitrary threshold is set at a point where one does not trust that the background-only hypothesis.

Appendix IV

SEARCH FOR VECTOR-LIKE QUARKS COUPLING TO LIGHT GENERATIONS WITH 1.04 FB^{-1} OF 2011 DATA AT $\sqrt{s} = 7$ TEV WITH ATLAS

In this annex, an overview of the ATLAS paper searching for heavy vector-like quarks coupling to light quarks with 1.04 fb^{-1} of 7 TeV 2011 data will be presented [10]. The extended and refined version of the analysis using the full 2011 dataset is presented in chapter 5.

Vector-like quarks have, by definition, the property that both chiralities transform identically under $SU(2)$ and are found in many SM extensions. Focusing on a model-independent approach [172] with a set of two VLQ doublets, the single production of a VLQ Q is known to outweigh pair production given that its coupling to light quarks may be as large as

$$\kappa_q Q = \frac{v}{m_Q} \tilde{\kappa}, \tag{IV.1}$$

where $\tilde{\kappa}$ contains the model dependence and can be of $\mathcal{O}(1)$. This is made possible by the fact that VLQ evade many electroweak constraints [16]. Hence, under such conditions, the analysis searched for the processes

$$pp \to Qq \to Vq'q, \tag{IV.2}$$

where $V = W, Z$ subsequently decay leptonically. Within the model-independent Lagrangian of two VLQ doublets, the four VLQ have charges $5/3, 2/3, -1/3$, and $-4/3$ [172]. However, for simplicity reasons, only VLQs with charges $2/3$, denoted by U, and $-1/3$, denoted by D are used as benchmark signals. The possible multiplet structure that may go beyond two doublets (see chapter 4) are therefore ignored. Furthermore, the LHC being a proton-proton collider, the production of the D quark dominates in the charge current (CC) channel and the U quark dominates in the neutral current (NC) channel. The events of interest include one high p_T jet, one forward jet originating the t-channel process, and two leptons either coming from the W in the CC channel or the Z in the

NC channel. The observables of interest are therefore

$$m(\ell, E_T^{\text{miss}}, \text{leading jet}); \quad \text{CC channel, and} \qquad\qquad \text{(IV.3)}$$

$$m(\ell, \ell, \text{leading jet}); \quad \text{NC channel}, \qquad\qquad \text{(IV.4)}$$

where the leading jet refers to the highest p_T jet. To obtain the *invariant* mass in the CC channel, the missing p_Z is extracted by fixing the invariant mass of the $(\ell, E_T^{\text{miss}})$ system to be precisely the mass of the W.

IV.1 EXPECTED BACKGROUND AND SIGNAL MODELLING

The VLQ signal samples were generated with MADGRAPH [177] using the model parameters developed in Refs. [171, 172, 246] and interfaced with PYTHIA [127] to simulate particle hadronization. The parton distribution function (PDF) CTEQ6L1 [229] was used for all signal samples generated with masses ranging from 225 GeV to 1 TeV in steps of 100 GeV starting from 300 GeV in both the CC and NC channels.

In each of the channels, W/Z+jets is the anticipated dominant background, however the nature and mixture of the subdominant backgrounds are quite different. Table IV.I presents the backgrounds considered and the generators used to simulated them. As

Backgrounds	Event generator	Parton Shower	CC Backgrounds in order of importance	NC Backgrounds in order of importance
W+jets	ALPGEN [178]	HERWIG [179] (Jimmy [180] underlying event)	1	*negli.*
Z+jets	ALPGEN [178]	HERWIG [179] (Jimmy [180] underlying event)	5	1
$t\bar{t}$	MC@NLO [181]	MC@NLO	2	2
Single top	ACERMC [230]	PYTHIA	3	*negli.*
Diboson	NC: alpgen CC: HERWIG	CC and NC: HERWIG	6	3
Multijet	data-driven estimated	N.A.	4	negli.

Table IV.I: List of backgrounds considered and the generators through which their events types were generated.

one can notice from the table, the multijet background was estimated using data-driven methods, which will be described in section IV.3. Before that however, a description of the event selections is needed.

IV.2 EVENT SELECTION AND SIGNAL REGION DEFINITION

The event selection begins with the requirement of having at least one reconstructed vertex defined by the intersection of three reconstructed tracks. Among such reconstructed vertices, the vertex with the highest total transverse momentum $\sum_{\text{tracks}} |p_T|$ designates the primary vertex (PV). Two trigger types were considered for electron and muon events respectively. The EM trigger required at least one cluster with $E_T > 20$ GeV, while the muon trigger required one reconstructed track pointing to the primary vertex with $p_T > 18$ GeV.

The essential requirements imposed on electron and muon reconstructed candidates are given in table IV.II. For jet reconstruction, the anti-k_T algorithm with cone size of

Quantity	Electrons	Muons
Transverse Momentum	$p_T > 25$ GeV	$p_T > 25$ GeV
Pseudo-rapidity	$\|\eta\| < 1.37$ OR $1.52 < \|\eta\| < 2.47$	$\|\eta\| < 2.4$
Lepton Reconstruction quality	`tight`	Combined muons
Isolation	$E_T^{\not{e}}$ in $\Delta R = 0.2 < 4$ GeV	$\frac{p_T^{\not{\mu}}}{p_T^{\mu}} < 0.1$ in $\Delta R = 0.2$
Pile-up/Cosmics Suppression	—	$\|z_o\| < 5$ mm $\|d_0\| < 0.1$ mm

Table IV.II: Basic lepton selection criteria for electrons and muons in the 2011 VLQ search [10]. $E_T^{\not{e}}$ ($p_T^{\not{\mu}}$) signifies the transverse energy (momentum) not associated to the reconstructed electron (muon). The distances with respect to the PV along the beam axis, denoted z_o, and in the tangential plane, denoted d_0, are used to quantify how compatible the reconstructed object is to the PV. No such requirement however is imposed on electrons.

$R = 0.4$ was chosen. These jets were required to have $p_T > 25$ GeV and $|\eta| < 4.5$. Thus, the entire fiducial region of the detector is utilized to gain as much information as possible on the expected forward jet produced by the single production of a VLQ. To minimize the impact of jets arising from pile-up interactions, 75% of the jet's tracks need to point to the PV. E_T^{miss} is computed as the negative vector of the energy deposits in the calorimeters (`MET_HadLocTopo`, see section 3.8.4) up to an $|\eta| < 4.5$.

Although the basic object selection are the same for the CC and NC channels, their respective events selections differ due to the nature of W and Z leptonic decays. In the

CC channel, the event specifications are:

- CC.1 - Exactly one electron or muon,
- CC.2 - $E_T^{\text{miss}} > 50$ GeV,
- CC.3 - One jet with $p_T > 50$ GeV,
- CC.4 - A second jet with $p_T > 25$ GeV,
- CC.5 - A pseudo-rapidity separation of $|\eta| > 1.0$ between the highest p_T jet and the second or third jet.
- CC.6 - $m^{\ell, E_T^{\text{miss}}} = \sqrt{2 E_T^\ell E_T^{\text{miss}} (1 - \cos \Delta\phi_{\ell, E_T^{\text{miss}}})} > 40$ GeV. This is the transverse momentum of the candidate W.
- CC.7 - $\phi_{\ell, E_T^{\text{miss}}} < 2.4$ rad.

For the NC channel, the selections are:

- NC.1 - Exactly two opposite sign same flavour electrons or muons with an invariant of mass between $66 < m(\ell, \ell) < 116$ GeV.
- NC.2 - The p_T of the candidate Z must be greater than $p_T(\ell, \ell) > 50 GeV$.
- NC.3 - At least two jets with $p_T > 25$ GeV.
- NC.4 - A pseudo-rapidity separation of $|\eta| > 1.0$ between the highest p_T jet and the second or third jet.

The above selection criteria together define the signal regions. The $p_T > 50$ GeV selection on the candidate Z performs a similar function as the CC.7 selection upon the opening angle between the single lepton and E_T^{miss} which would both result from boosted W. In that sense, the CC and NC channels define equivalent selections.

IV.3 MULTIJET BACKGROUND ESTIMATION

The multijet background in the NC channel was found to be negligible by comparing the total yields of the data and other backgrounds in an adjacent region of phase space to the signal region.

In the CC channel, the E_T^{miss} distribution is the guiding kinematical variable used to estimate the multijet background. With an E_T^{miss} between $0 < E_T^{\text{miss}} < 100$ GeV, and imposing only selection criteria 1) and 5) (from the previous section), the E_T^{miss} distri-

bution from data is then compared to the total simulated non-multijet backgrounds plus a multijet template E_T^{miss} distribution, which is constructed as follows. For electrons, the contribution to the multijet background is expected to come primarily from misidentified electrons. Consequently, the E_T^{miss} template is built upon an enriched sample of `medium` and not `tight` electrons (see section 3.8.1). In the case of muons, since the main source of misidentified muons is expected to arise from heavy-flavour decays, the E_T^{miss} template is constructed from a $b\bar{b}$ PYTHIA generated sample. In both lepton channels, the E_T^{miss} distribution is fitted to the sum of the non- and multijet components which were both left to float. The result was then tested in an orthogonallow E_T^{miss} region $10 < E_T^{\mathrm{miss}} < 30$ GeV, and the agreement with data was observed to be within statistical error, giving confidence in the data-driven method at hand.

IV.4   SYSTEMATICS: AN OVERVIEW

In both the NC and CC channels, the dominant systematic uncertainty was JES with roughly a 20% uncertainty in the tails of the m^{Wj} and m^{Zj} invariant mass distributions. A number of other systematic uncertainties were considered and are tabulated in IV.III. None of the systematics were shown to affect the shape of the background or signal.

Type	Average Normalization Uncertainty in m^{Wj} (%)	Average Normalization Uncertainty in m^{Zj} (%)	NC signal eff. (%)	CC signal eff. (%)
JES	20	20	5	5
JER	1	1	1	1
LES	$\ll 1$	$\ll 1$	$\ll 1$	$\ll 1$
LER	$\ll 1$	$\ll 1$	$\ll 1$	$\ll 1$
Reconstruction and identification eff.	$\ll 1$	$\ll 1$	1-2*	1-2*
PDF (CTEQ66 [183])	N.A.	N.A	3-4.4*	3-4.4*
Factorization Renormalization scales	5-7	5-7	4-12*	4-12*
ISR and FSR	N.A.	N.A.	1	1

* Depends on the signal mass.

Table IV.III: Main systematics and their average uncertainty over the VLQ mass distribution. These systematics include jet energy scale (JES), jet energy resolution (JER), lepton energy scale (LES), lepton energy resolution (LER), parton distribution function (PDF), factorization and renormalization scales, initial and final state radiation (ISR and FSR). Note that all uncertainties related to energy measurements, their uncertainties are all propagated to the E_T^{miss} calculation.

Other uncertainties included luminosity, 3.7% [247], and Monte-Carlo statistical uncertainty, 3 to 5%.

IV.5 RESULTS AND DISCUSSION

Once the signal region selections described in IV.2 are imposed, the VLQ invariant mass distributions with 1.04 fb^{-1} are obtained. These are shown in figure IV.1 for the CC channel, and in figure IV.2 for the NC channel. A VLQ signal would appear simply
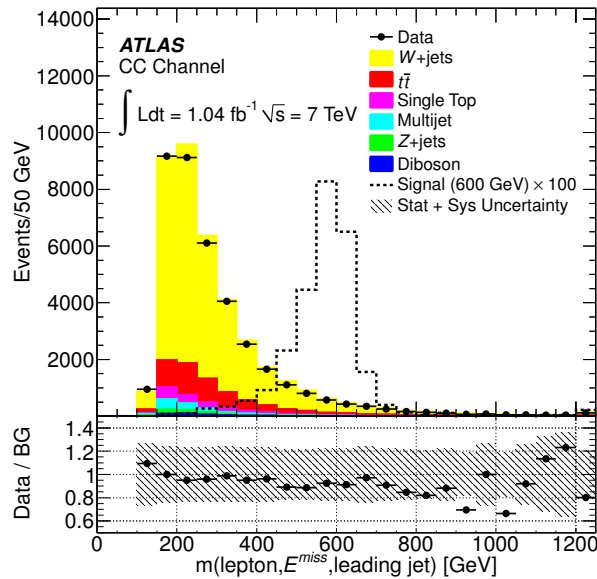
Figure IV.1: Invariant mass distribution of the lepton plus E_T^{miss} plus jet system [10]. A hypothetical signal of mass 600 GeV is overlaid on top of the expected background and data with a cross section 100 times its leading order theoretical estimate with $\tilde{\kappa} = 1$.

as a resonance, or peak, on top of the smooth background, but no such localized excess is seen in these invariant mass spectrums. Despite this last fact and before continuing ahead with the limits setting procedure, the correct background shape and normalization must be observed throughout. From the distributions shown, a slight discrepancy in the shape does reveal itself. Although the background is left to float within the chosen limit setting method, this small shape deviation may cause biases, especially in the
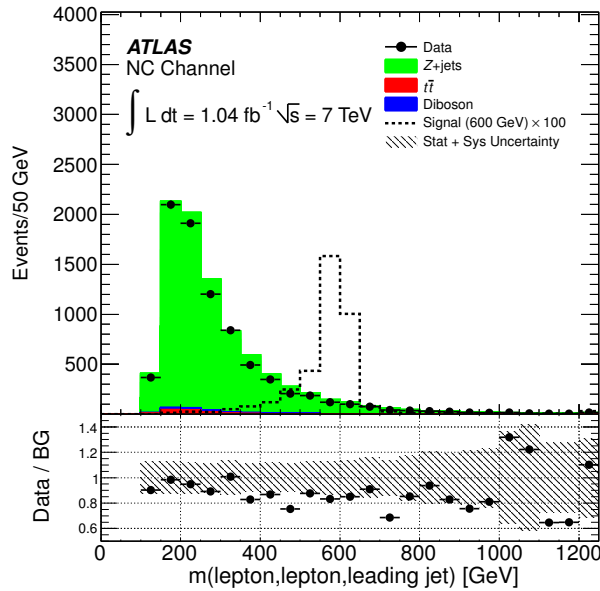
Figure IV.2: Invariant mass distribution of the dilepton plus jet system [10]. A hypothetical signal of mass 600 GeV is overlaid on top of the expected background and data with a cross section 100 times its leading order theoretical estimate with $\tilde{\kappa} = 1$.

high mass region. To cure this issue, a *linear*[6] correction is applied in each of the four channels independently, slightly rescaling the tails of the background model upwards and the low-end downwards. The errors of the fit are of course propagated into the limit setting procedure. To remove the possible influence of a hypothetical signal of mass M in this background correction, the linear fit is performed while excluding the region $[M - 200, M + 100]$ GeV. The asymmetric choice in the exclusion band stems from the observed nature of the signal shapes which have low mass tails.

Once the background correction applied, the exclusion limits on the VLQ production cross section $\sigma(pp \rightarrow Qq) \times \mathrm{BR}(Q \rightarrow Vq)$ as a function of the VLQ mass up to 1 TeV were obtained using the asymptotic formula (III.24) to compute CL_s limits at 95% C.L. for both the expected and observed yields. In figure IV.3, the upper limit on $\sigma \times \mathrm{BR}(D \rightarrow Wq)$ of a hypothetical vector-like D-quark are presented. The observed limit is 900 GeV while the expected was 840 GeV. In a similar fashion, figure IV.4

---

6. A linear fit to the ratio Data/(Expected Background) is computed and its resulting parameters are used to re-weight the background and have its shape match the data.
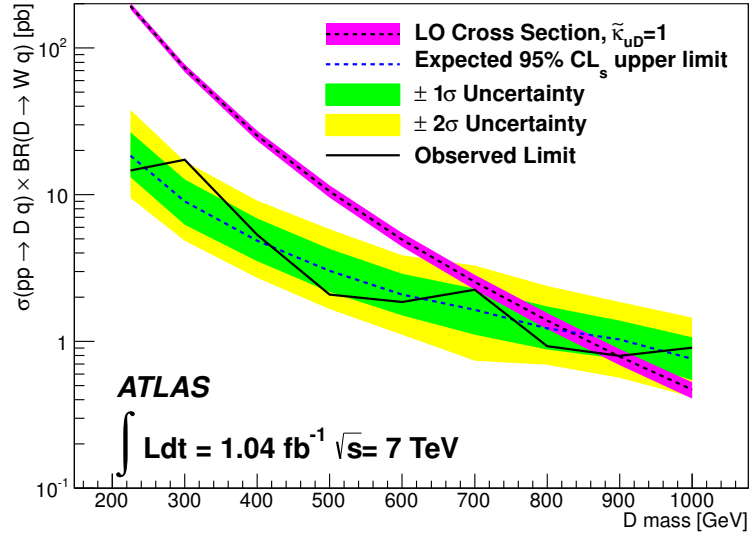
Figure IV.3: Expected and observed limits at 95% C.L. on the CC single production cross section of a Down-type VLQ D times its branching ratio to Wq [10]. The observed (expected) limit is 900 (840) GeV.

presents the obtained upper limits on $\sigma \times \mathrm{BR}(U \to Zq)$ in the case of a hypothetical vector-like U-quark. The obtained expected upper limit on such a process is 820 GeV while the observed is 760 GeV. In terms of the coupling $\tilde{\kappa}$ between either the u and D (CC channel), or the u and U (NC channel) quarks, table IV.IV presents limits on these couplings . The table also shows the upper limit on $\sigma \times \mathrm{BR}(D \to Wq)$ in the special case when one requires the additional cut: CC.8 - Lepton Charge = -1.
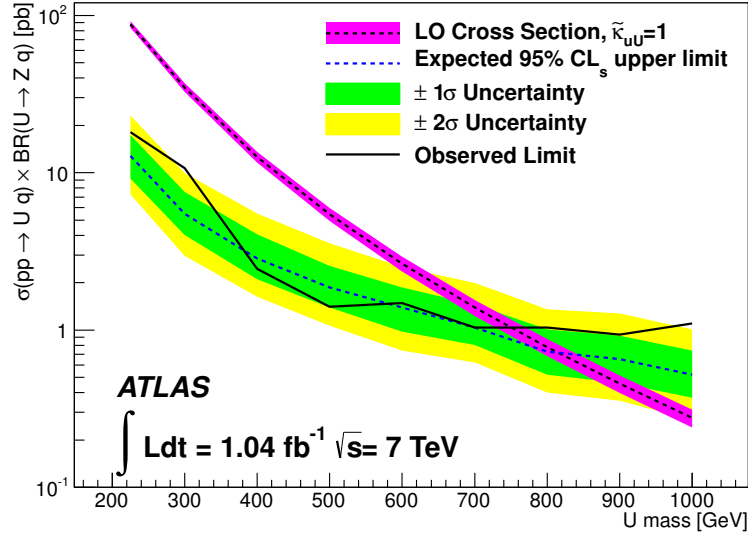
Figure IV.4: Expected and observed limits at 95% C.L. on the NC single production of an Up-type VLQ U times its branching ratio to Zq [10]. the observed (expected) limit is 760 (820) GeV.

Signal Mass [GeV]	CC $\sigma \times$ BR($D \to Wq$) [pb]	NC $\sigma \times$ BR($U \to Zq$) [pb]	$\tilde{\kappa}_{uD}^2$	$\tilde{\kappa}_{uU}^2$	CC$^-$ $\sigma \times$ BR($D \to Wq$) [pb]
225	15	18	0.075	0.21	12
300	17	11	0.24	0.31	5.6
400	5.3	2.4	0.21	0.19	3.8
500	2.1	1.4	0.19	0.26	1.1
600	1.9	1.5	0.37	0.56	1.9
700	2.2	1.0	0.86	0.75	2.2
800	0.93	1.0	0.66	1.33	0.97
900	0.80	0.9	1.0	2.1	0.70
1000	0.91	1.1	1.9	4.0	0.50

Table IV.IV: Upper limits on the VLQ production cross section $\sigma(pp \to Qq) \times$ BR($Q \to Vq$), where $V = W, Z$. These are translated into limits on $\tilde{\kappa}$ which controls the model dependence of the search. The last column presents the upper limits for negative charge leptons in the CC channel [10].

SEARCH FOR WZ RESONANCE WITH 1.02 FB^{-1} OF 2011 DATA AT $\sqrt{s} = 7$ TEV WITH ATLAS

In the present annex, an overview of the search for WZ resonances with 1.02 fb^{-1} of 2011 data at $\sqrt{s} = 7$ with the ATLAS detector will be presented [11]. The more complete and larger search that was performed in 2012 with 13 fb^{-1} is presented in chapter 7.

The chosen observable used to test the potential presence of a signal is the transverse mass of the WZ system, written as m_T^{WZ} and computed from three reconstructed leptons and E_T^{miss} :

$$m_T^{WZ} = \sqrt{(E_T^Z + E_T^W)^2 - (p_x^Z + p_x^W)^2 - (p_y^Z + p_y^W)^2}, \tag{V.1}$$

where E_T^Z, p_x^Z, and p_y^Z are calculated from the two lepton Z decay products, and where the W boson variables are computed from the remaining 3$^{\text{rd}}$ lepton and the E_T^{miss} , which serves as a measure of the neutrino transverse momentum.

V.1 WZ RESONANCE SIGNAL PROVENANCES AND SIMULATION

Two independent signal types formed the basis of this search. The first signal type arises from the extended gauge model (EGM) W' whose coupling strength to WZ is defined by

$$g_{W'WZ} = g_{WWZ} \frac{m_W^2}{m_{W'}^2}, \tag{V.2}$$

where m_W, m_Z, and $m_{W'}$ are the masses of the W, Z, and W' bosons respectively. It is important to emphasize here, as it was in chapter 7, that this search is complementary yet independent to $W' \to l\nu$ searches because in those single lepton plus E_T^{miss} searches [248, 249], a SSM W' is used as the benchmark model and its coupling to WZ does not follow (V.2) and is in fact deeply suppressed. The second signal type emerges

from Low-Scale Technicolor (LSTC)[7] where narrow width techni-mesons are predicted to decay to WZ. These resonances are the techni-rho ρ_T, and its axial-vector partner, the techni-a a_T.

Both signals were simulated at LO with the PYTHIA [127] event generator, itself using the parton distribution function (PDF) set MRST2007 [224] at modified LO*. Both the EGM and LSTC are hence implemented in PYTHIA. However, in the LSTC decay chain $\rho_T \to WZ \to l\nu l'l'$ the spin polarization correlations were not fully propagated yielding kinematic distributions that are approximate at best[8]. Thankfully, given that both the ρ_T and the W' are narrow width signals, it is expected that the decay kinematics of the two signal types to be very similar if not identical. Under this assumption, an extra set of cross section limits on the ρ_T were calculated based upon the measured W' detector acceptances.

The LSTC samples were generated using identical input parameters as the ones later used in the 2012 analysis (see section 7.2 for more details). Two hypotheses for the mass of the a_T were considered. The first being $m(\rho_T) = 1.1\, m(a_T)$ and the second $m(a_T) >> m(\rho_T)$.

Finally, a mass-dependent k-factor was used to rescale the generated LO signals to NNLO. The calculation was performed with the ZWPRODprogram [250] with values ranging from 1.08 at high mass (1 TeV) up to 1.17 at low mass resonances (200 GeV). The computed k-factors are independent of resonance type and therefore were applied to both the W' and ρ_T, a_T signals.

V.2 EVENT AND LEPTON SELECTION CRITERIA

Single leptons triggers with baseline thresholds of 20 GeV in E_T for electrons and 18 GeV in p_T for muons were required for the online data-taking, and offline Monte-Carlo simulation.

After imposing primary vertex (PV) requirements, the general electron and muon selection criteria are applied as described in table V.I.

---

7. For more details on this model, see chapter 6.
8. See chapter 7 for a more thorough discussion on this issue

Quantity	Electrons	Muons
Transverse Energy or Momentum	$E_T > 25$ GeV	$p_T > 25$ GeV
Pseudo-rapidity	$|\eta| < 1.37$ OR $1.52 < |\eta| < 2.47$	$|\eta| < 2.4$
Lepton Reconstruction quality	`medium` or better	Combined muons
Isolation	$E_T^{\not e}$ in $\Delta R = 0.3 < 4$ GeV	$\frac{p_T^{\not \mu}}{p_T^{\mu}} < 0.1$ in $\Delta R = 0.2$
Pile-up/Cosmics Suppression	$|z_o| < 10$ mm $|d_0|/\sigma_{d_0} < 10$	$|z_o| < 10$ mm $|d_0|/\sigma_{d_0} < 10$

Table V.I: Basic lepton selection criteria for electrons and muons in the 2011 WZ resonance search [11]. $E_T^{\not e}$ ($p_T^{\not \mu}$) signifies the transverse energy (momentum) not associated to the reconstructed electron (muon). The distances with respect to the PV along the beam axis, denoted z_o, and in the tangential plane, denoted d_0, are used to quantify how compatible the reconstructed object is to the PV.

The decay of the W to leptons presents the challenging task of measuring missing transverse energy, E_T^{miss}, which is calculated based upon carefully calibrated inputs from the detector up to an $\eta < 4.5$ (see section 3.8.4). The final selection imposes $E_T^{\mathrm{miss}} > 25$ GeV.

The Z reconstruction necessitates the presence of two opposite sign same flavour leptons with an invariant mass within 20 GeV of the PDG Z boson mass. The W, on the other hand, is reconstructed together with the third remaining lepton and E_T^{miss}. The transverse mass of W, defined as $\sqrt{2p_T^l E_T^{\mathrm{miss}}(1 - \cos\Delta\phi)}$, where $\Delta\phi$ represents the opening angle between the third lepton and the direction of the E_T^{miss}, is required to be greater than 15 GeV thereby suppressing misidentified jet backgrounds.

Lastly, the candidate events with exactly three lepton event and $E_T^{\mathrm{miss}} > 25$ GeV are used to computed m_T^{WZ} as defined in equation (V.1). The combination of these selections defines the signal region.

V.3 BACKGROUND MODELLING AND CONTROL REGIONS

The main irreducible background to this search is SM WZ production, and was simulated by MC@NLO [181]. The second background in importance is the result of misidentified jets faking the detection signature of leptons in Z+jets events. For a solid modelling of such backgrounds, data-driven techniques were employed. Using dijets

events, the tag-and-probe method was utilized, where the lepton-like qualities of the probed jet was varied in order to ascertain the lepton fake rate by jets as a function then p_T. The fake factor that describes the rate at which a *bad* lepton fakes a *good* lepton can be written as

$$f(p_T) = \frac{\# \text{ good } leptons}{\# \text{ bad } leptons}, \tag{V.3}$$

where *bad* and *good* lepton refers to the quality of the objects reconstruction. The *good* lepton definition simply means leptons that have passed the basic object selection as presented in table V.I. *Bad* leptons however fail some of the selection requirements. For *bad* electrons, they must fail the `medium` quality definition, but pass the `loose` definition, whereas for *bad* muons, they must simply fail the isolation criteria.

This fake rate was then applied to an independent data region defined by $Z + 1$ *bad* lepton, thus rendering a prediction on the number of events with $Z + 1$ *good* lepton after applying the fake factor calculated in dijet events. In the ll'+jets control region, defined by reversing the missing transverse energy selection: $E_T^{\text{miss}} < 25$ GeV, but keeping all other selections intact. The prediction of the data-driven estimate for this background is presented in figure V.1 along with the sum of all the other backgrounds in the $m(Z)$ distribution showing the sum of the two $Z \to ee$ and $Z \to \mu\mu$ channels. Comparing these
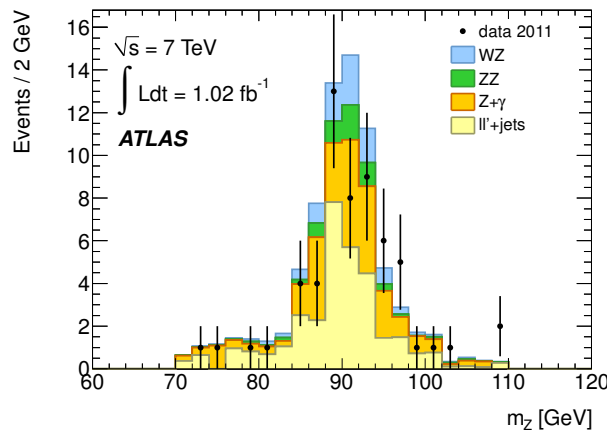
Figure V.1: Dilepton invariant mass spectrum e in the ll'+jet control region as defined in the text and within ± 20 GeV of the Z boson mass [11].

with the observed yields, one finds that prediction is in good agreement with observation,

validating the method's prediction of fakes.

The WZ control region, which simply looks at events that have one well recon-structed Z and W boson as defined above, but with $m_T^{WZ} < 300$ GeV, is necessary to gain insight in the accurateness of the SM WZ background modelling. Figure V.2 puts forward the results as seen through the W transverse mass distribution (both leptons channels summed). Dropping the selection $m_T^{WZ} < 300$ GeV yields the definition of the signal region. Although the definition of the WZ control region is not orthogonal to the
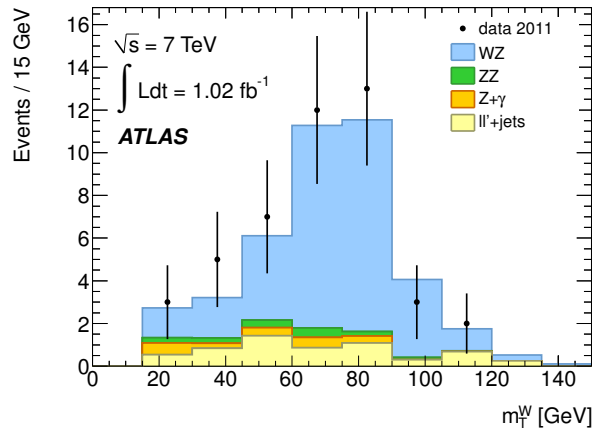
Figure V.2: Transverse mass of the 3$^{\mathrm{rd}}$ lepton + E_T^{miss} system as defined in the text [11].

signal region (it is simply a subset), examining these events within the m_T^W distribution is nonetheless a good test of non-resonant contributions to WZ production. Finally, given the very good agreement seen in figure V.2, one can be confident in the predictions of Monte-Carlo WZ production in the signal region.

V.4 A HANDLE ON SYSTEMATICS UNCERTAINTIES

Various sources of systematics uncertainties were considered in each aspect of the analysis. To enumerate them succinctly, the following details those considered and their contribution to the total uncertainty.

- Lepton trigger efficiency: 1%.
- Electron reconstruction/identification and isolation efficiencies are respectively: 1.2% and 2%.

- Muon reconstruction/identification and isolation efficiencies are respectively: 0.5% and 1%.

- Electron 4-momenta resolution: $\sim 0.1\%$.

- Muon 4-momenta resolution: $\sim 0.1\%$.

- Total E_T^{miss} uncertainty (from all source including JES): 2-3%.

- Theoretical SM WZ cross section: 7%.

- Theoretical SM $Z\gamma$ and ZZ cross sections: 8% and 5% respectively.

- Total uncertainty on the ll'+jets background estimation: $\sim 50\%$.

- Signal acceptance due to the choice of PDF: 0.6%.

- Luminosity uncertainty: 3.7%.

All of these systematics uncertainty are taken as uncorrelated when came the time to compute limits.

V.5 RESULTS AND DISCUSSION

The final tally of events found in the signal region in each of the lepton channels and the total combined sum is found in table V.II.

Event Type	$e\nu ee$	$\mu\nu ee$	$e\nu\mu\mu$	$\mu\nu\mu\mu$	Combined
WZ	6.2 ± 0.7	7.6 ± 0.7	9.2 ± 0.8	11.6 ± 1.0	34.6 ± 3.1
ZZ	$0.25^{+0.07}_{-0.11}$	$0.48^{+0.14}_{-0.11}$	$0.37^{+0.15}_{-0.11}$	$0.63^{+0.16}_{-0.11}$	$1.7^{+0.5}_{-0.3}$
$Z\gamma$	1.3 ± 0.7	-	1.0 ± 0.9	-	2.3 ± 1.1
ll'+jets	$1.1 \pm 0.4 \pm 0.7$	$1.3 \pm 0.5^{+0.6}_{-0.8}$	$3.0 \pm 0.7^{+1.6}_{-1.9}$	$1.0 \pm 0.4^{+0.5}_{-0.6}$	$6.4 \pm 1.0^{+4.6}_{-4.0}$
Total backgrounds	$8.9 \pm 0.4 \pm 1.2$	$9.4 \pm 0.5^{+0.6}_{-0.8}$	$13.6 \pm 0.7^{+2.0}_{-2.3}$		$45.5 \pm 1.2^{+3.1}_{-3.6}$
Data	9	7	16	16	48
$W' \to WZ$ ($m_{W'} = 750\,\mathrm{GeV}$)	0.74 ± 0.07	0.82 ± 0.06	0.97 ± 0.06	1.10 ± 0.08	3.64 ± 0.21
$\rho_T \to WZ$ ($m_{\rho_T} = 500\,\mathrm{GeV}$)	0.68 ± 0.08	0.79 ± 0.08	0.97 ± 0.09	1.11 ± 0.10	3.55 ± 0.24

Table V.II: Integrated number of events in the signal region for the major backgrounds, their combined total, and the observed count are shown. In addition to these, the predicted W' and ρ_T boson yields are shown with masses of 750 and 500 GeV respectively. In the case of the ρ_T, the yields were computed with the assumption $m_{a_T} = 1.1 \times m_{\rho_T}$ between the masses of the techni-a and techni-rho. The total statistical and systematic uncertainties are also given. If only one error is given, it is the combination of statistical and systematics errors [11].

Comparing the overall background and the data in table V.II, along with its associated distribution shown in figure V.3, no evidence of a clear localized excess is seen.

Therefore, confidence levels for the background plus signal hypothesis CL$_{b+s}$ and back-
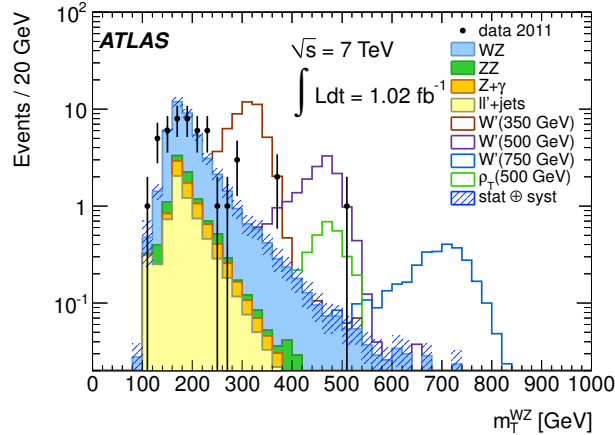
Figure V.3: Transverse mass of the WZ system whose reconstructed components are described in the text. Shown overlaid with the background are hypothetical signals of various masses [11]. This background modelling shown here together with the observed data-points form the basis upon which the limits are computed.

ground only hypothesis CL$_b$ were computed utilizing the methods described in annex III. However, before detailing the limit results, a word about the differences in acceptances between the W' and ρ_T signals is necessary. Both the extended gauge and LSTC models are implemented in PYTHIA [127]. Unfortunately, in the special case of the ρ_T decaying to $WZ \rightarrow \ell\nu\ell\ell$, the spin polarizations of the final state leptons are not propagated properly rendering only very approximate final reconstructed kinematical distributions. Consequently, the signal acceptances for the simulated ρ_T need to be taken skeptically. Thankfully, the PYTHIA implementation of the $W' \rightarrow WZ \rightarrow \ell\nu\ell\ell$ decay chain does fully handle the spin polarizations. Additionally, it is expected that the ρ_T's decay kinematics be very similar, if not identical, to those of the W'. Hence, limits on ρ_T production was computed for both acceptance scenarios, taking into account of course their respective cross section. The acceptance times efficiency $A \times \epsilon$ differences between the PYTHIA implementation of the two signals is given in table V.III [11].

Computing the ratio CL$_s = \frac{\text{CL}_{b+s}}{\text{CL}_b}$ for both the ρ_T and W' signal types, the upper limits on their respective cross section times branching ratio were obtained and are given in figures V.4 and V.5 respectively. The observed (expected) W' limits on

Mass [GeV]	$A \times \epsilon$ for W' (%)	$A \times \epsilon$ for ρ_T (%)
200	6.2 ± 0.2	5.7 ± 0.2
250	8.2 ± 0.4	6.1 ± 0.2
300	10.0 ± 0.5	7.6 ± 0.3
350	11.6 ± 0.3	9.4 ± 0.3
400	13.2 ± 0.5	10.8 ± 0.3
450	14.5 ± 0.6	11.8 ± 0.3
500	15.9 ± 0.3	12.6 ± 0.3
550	16.9 ± 0.6	—
600	17.9 ± 0.6	13.8 ± 0.3
650	18.7 ± 0.6	—
700	19.4 ± 0.7	15.6 ± 0.4
750	19.9 ± 0.3	—
800	20.3 ± 0.7	16.1 ± 0.4
850	20.6 ± 0.7	—
900	20.6 ± 0.7	—
950	20.6 ± 0.7	—
1000	20.5 ± 0.3	—

Table V.III: Signal acceptance times efficiency comparison between the W' and ρ_T signal resonances decaying to $WZ \to \ell\nu\ell'\ell'$, where both signals were simulated with PYTHIA. Statistical uncertainties are shown.

$\sigma \times \mathrm{BR}(W' \to WZ$ is 760 (776) GeV. For the ρ_T signal, the observed (expected) limits on $\sigma \times \mathrm{BR}(\rho_T, a_T \to WZ)$ is 467 (506) GeV under the assumption that the axial vector a_T is related in mass to the ρ_T via $m_{a_T} = 1.1\, m_{\rho_T}$. The cross section for such a resonance is given by the blue line in figure V.5. Alternatively, under the assumption that a_T is very massive and beyond on-shell production at 7 TeV, the observed (expected) limits on the process $\rho_T \to WZ$ is 456 (482) GeV. Assuming the W' acceptance approximates well the LSTC ρ_T production and subsequent decay to WZ, the observed (expected) limits become 483 (553) GeV and 469 (507) for $m_{a_T} = 1.1\, m_{\rho_T}$ and $m_{a_T} \gg m_{\rho_T}$ respectively.

The simulation of the W' signal were performed in steps of 150 to 250 GeV. To obtain resonance signal shapes in 50 GeV steps, an interpolation procedure was devised. It consisted of fitting each of the available signal shapes with a crystal ball function as implemented in ROOFIT [14]. The four parameters of the crystal ball were then extracted and themselves fitted with simple functions. This enabled to gather the necessary in-
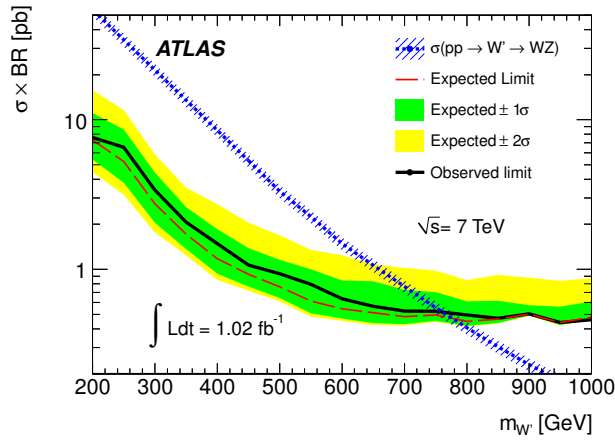
Figure V.4: Expected (dotted red line) and observed (black solid line) upper limits on $\sigma \times BR(W' \to WZ)$ as a function of W' mass [11]. The EGM W' is exclude at 95% C.L. for masses below 760 GeV while the expectation was for it to be excluded for masses below 776 GeV.

formation for constructing signal shapes at any intermediate point between the available simulated shapes. A 50 GeV was chosen purely because it covered adequately the m_T^{WZ} distribution given the larger signal resolution.

Within LSTC, the π_T mass has an impact on the $\rho_T \to WZ$ branching ratio if $m_{\pi_T} \lesssim m_{\rho_T} + m_W$ in which case the process $\rho_T \to Wm_{\pi_T}$ becomes possible. In this manner, the limits on $\sigma \times \mathrm{BR}(\rho_T, a_T \to WZ)$ were recomputed in the mass plane m_{π_T} versus m_{ρ_T}. Figures V.6 and V.7 present the results assuming $m(a_T) >> m(\rho_T)$ and $m(\rho_T) = 1.1\, m(a_T)$ respectively.

To conclude, this 1.02 fb^{-1} analysis of 2011 data provided the ground work upon which the 2012 analysis, presented in chapter 7, was able to push further the search for leptonic WZ resonances.
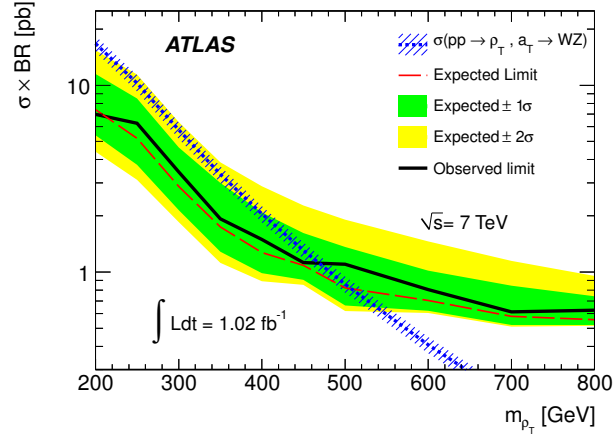
Figure V.5: Expected (dotted red line) and observed (black solid line) upper limits on $\sigma \times BR(W' \to WZ)$ as a function of ρ_T mass [11]. The Shaded blue line represents the expected LSTC cross section of the process $pp \to \rho_T, a_T \to WZ$ when the ρ_T and a_T masses are related by $m(\rho_T) = 1.1\, m(a_T)$.
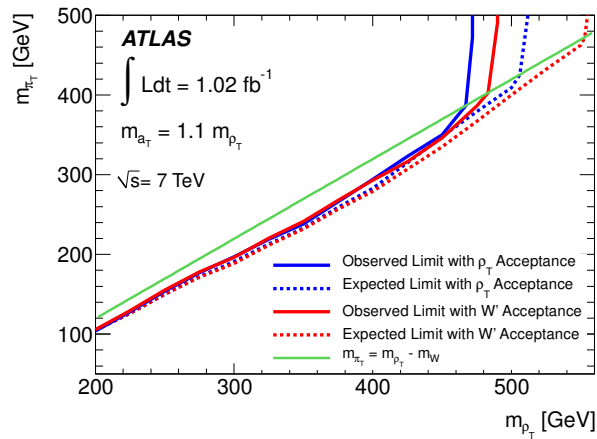
Figure V.6: The 95% expected and observed excluded regions in the $m(\rho_t, \pi_T)$ plane when $m(a_T) >> m(\rho_T)$ [11]. Both assumptions on the resonance acceptance are presented as detailed in the text. To guide the eye, the green line represents the $m(\rho_T) = m(\pi_T) + m_W$ mass threshold beyond which the branching ratio $BR(\rho_T \to WZ) = 1$.
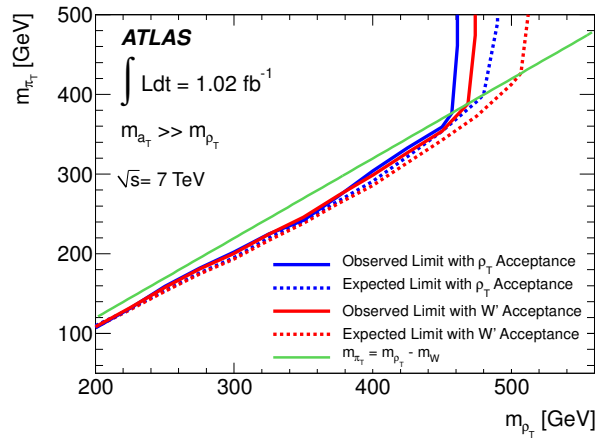
Figure V.7: The 95% expected and observed excluded regions in the $m(\rho_t, \pi_T)$ plane when $m(\rho_T) = 1.1\, m(a_T)$ [11]. Both assumptions on the resonance acceptance are presented as detailed in the text. To guide the eye, the green line represents the $m(\rho_T) = m(\pi_T) + m_W$ mass threshold beyond which the branching ratio $BR(\rho_T \to WZ)$ is 100%.

Appendix VI

MONTE-CARLO SAMPLES

This annex tabulates the cross sections, generator efficiencies, k-factors for each of the Monte-Carlo datasets used for understanding the backgrounds and potential signals within the searches presented in the main chapters.

VI.1 MONTE-CARLO SAMPLE INFORMATION: VLQ SEARCH

The following sections present a series of tables enumerating the Monte-Carlo datasets utilized in the search detailed in chapter 5.

VI.1.1 SIGNAL MONTE-CARLO SPECIFICATIONS

Table VI.I and VI.II provide the basic information for the NC and CC channel VLQ signal datasets used to understand their expected kinematical topologies.

In figures VI.1 and VI.2, a comparison of the main kinematical variables between the CC D VLQ production and the CC $T^{5/3}$ production (labelled as X in figures) are given. In both of these figures, the mass of the VLQ resonances is 600 GeV.

VI.1.2 BACKGROUND MONTE-CARLO SPECIFICATIONS

The modelling of the electroweak W/Z+jets backgrounds are of considerable concern within the VLQ searches. Tables VI.III and VI.IV enumerate the ALPGEN datasets used for the understanding of W+jets and Z+jets production respectively. Lastly, the parameters related to the subdominant backgrounds that are $t\bar{t}$, single *top*, and diboson production are shown in table VI.V.
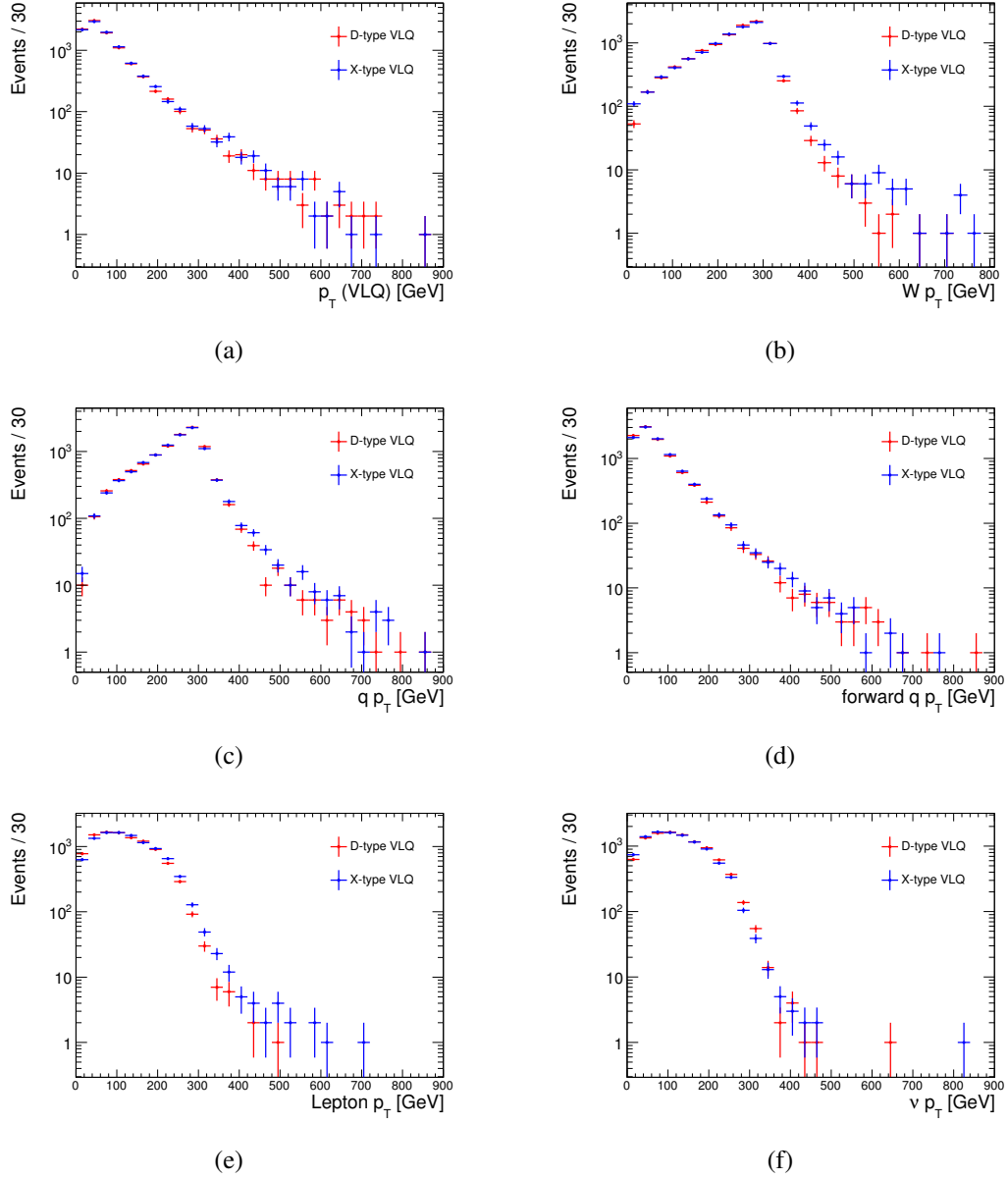
Figure VI.1: Kinematical comparisons between the relevant objects in VLQ single production for the D-type VLQ and the $T^{5/3}$ VLQ denoted as X in the above legends.
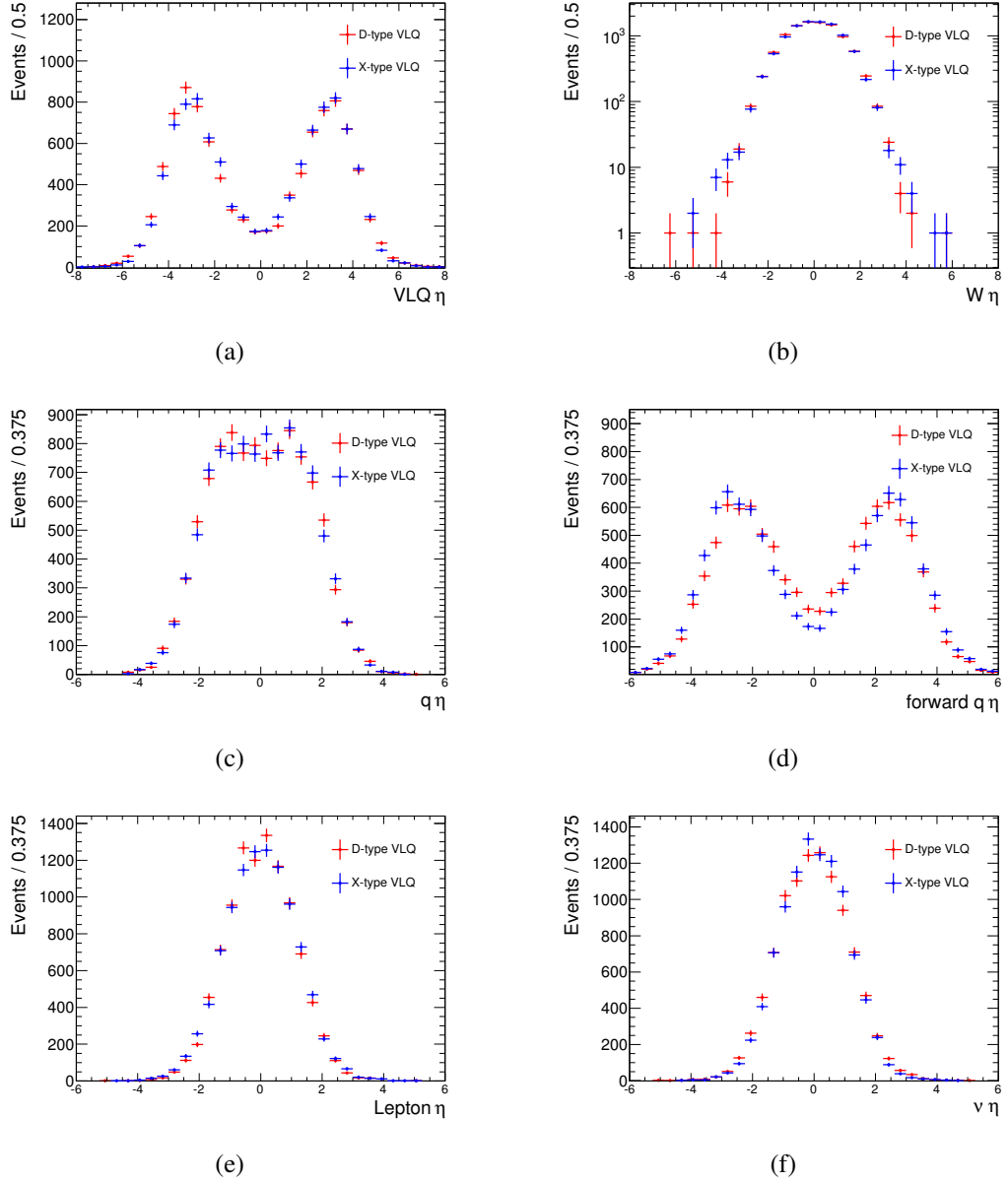
Figure VI.2: Pseudo-rapidity η comparisons between the relevant objects in VLQ single production for the D-type VLQ and the $T^{5/3}$ VLQ denoted as X in the above legends.

Generator PDF	Parton Shower	Process	Dataset Number	Signal Mass [GeV]	Generator Efficiency	$\sigma \times$BR [pb]
MADGRAPH CTEQ6L1	PYTHIA		115522	400	1.0	0.849
			115526	500		0.367
			115527	600		0.178
			115528	700		0.0938
			115529	800		0.0525
			115530	900		0.0307
			115531	1000		0.0186
			145092	1100		0.0115
			145093	1200		0.00738
			145094	1300		0.00478
			145095	1400		0.00314
			145096	1500		0.00209
			145097	1600		0.00140
			145098	1700		0.00095
			145099	1800		0.00065
			145100	1900		0.000442
			145101	2000		0.000305
			145104	400		0.481
			145105	500		0.200
			145106	600		0.0929
			145107	700		0.0481
			145108	800		0.0260
			145109	900		0.0143
			145110	1000		0.00841
			145111	1100		0.00514
			145112	1200		0.00313
			145113	1300		0.00198
			145114	1400		0.00126
			145115	1500		0.000813
			145116	1600		0.000528
			145117	1700		0.000347
			145118	1800		0.000229
			145119	1900		0.000151
			145120	2000		0.000101

Table VI.I: Shown here are the primary parameters for the VLQ samples in the NC channel. These include the signal cross section, the generator efficiency, and the k-factors as a function of signal mass. The cross sections were computed assuming $\tilde{\kappa} = 1$. Note that the dataset numbers referred to in these tables are for ATLAS internal reference.

Generator PDF	Parton Shower	Process	Dataset Number	Signal Mass [GeV]	Generator Efficiency	$\sigma \times$BR [pb]	$T^{-5/3}$ Signal $U \to T$ $\sigma \times$BR [pb]
MADGRAPH CTEQ6L1	PYTHIA		115513	400	1.0	5.47	7.78
			115514	500		2.28	3.42
			115515	600		1.07	1.72
			115516	700		0.551	0.916
			115517	800		0.299	0.528
			115518	900		0.170	0.312
			115519	1000		0.101	0.194
			145082	1100		0.0610	0.122
			145083	1200		0.0379	0.0794
			145084	1300		0.0242	0.0517
			145085	1400		0.0153	0.0348
			145086	1500		0.0101	0.0234
			145087	1600		0.00667	0.0158
			145088	1700		0.00441	0.0109
			145089	1800		0.00293	0.00754
			145090	1900		0.00196	0.00522
			145091	2000		0.00132	0.00364
			145123	400		4.509	N.A.
			145124	500		1.888	
			145125	600		0.883	
			145126	700		0.461	
			145127	800		0.255	
			145128	900		0.143	
			145129	1000		0.0850	
			145130	1100		0.0525	
			145131	1200		0.0328	
			145132	1300		0.0209	
			145133	1400		0.0135	
			145134	1500		0.00886	
			145135	1600		0.00583	
			145136	1700		0.00389	
			145137	1800		0.00260	
			119898	1900		0.00176	
			119899	2000		0.00119	
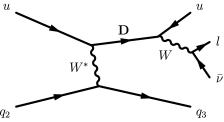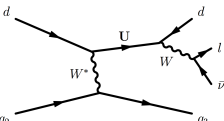
Table VI.II: Shown here are the primary parameters for the VLQ samples in the CC channel. These include the signal cross section, the generator efficiency, and the k-factors as a function of signal mass. The cross sections were computed assuming $\tilde{\kappa} = 1$. Additionally, the T VLQ of charge $5/3$ cross sections are presented here since the signal shape from the regular U VLQ are used to approximate the expected signal kinematics of the T-quark (see chapter 5 for details). Note that the dataset numbers referred to in these tables are for ATLAS internal reference.

Generator	Parton Shower	Process	Dataset Number	Generator Efficiency	k-factor	$\sigma \times$BR [pb]
ALPGEN	HERWIG + JIMMY	$W(e\nu)$ + jets 0-5 partons	107680			6.9×10^3
			107681			1.3×10^3
			107682			3.8×10^2
			107683			1.0×10^2
			107684			26
			107685			7.0
		$W(\mu\nu)$ + jets 0-5 partons	107690			6.9×10^3
			107691			1.3×10^3
			107692	1.0	1.2	3.8×10^2
			107693			1.0×10^2
			107694			26
			107695			6.9
		$W(\tau\nu)$ + jets 0-5 partons	107700			6.9×10^3
			107701			1.3×10^3
			107702			3.8×10^2
			107703			1.0×10^2
			107704			26
			107705			7.0

Table VI.III: W+jets production is the foremost important background in the CC channel VLQ search. Presented here are the ALPGEN datasets that were used to model this crucial background. Included in the table are the cross sections, k-factors, and generator efficiency for the 0-5 partons samples in each of the lepton W decay modes. Note once again that the dataset numbers referred to in these tables are for ATLAS internal reference.

Generator	Parton Shower	Process	Dataset Number	Generator Efficiency	k-factor	$\sigma \times$BR [pb]
ALPGEN	HERWIG + JIMMY	$Z(ee)$ + jets 0-5 partons	107650	1.0	1.2	6.7×10^2
			107651			1.3×10^2
			107652			41
			107653			11
			107654			2.9
			107655			0.83
		$Z(\mu\mu)$ + jets 0-5 partons	107660			6.7×10^2
			107661			1.3×10^2
			107662			41
			107663			22
			107664			2.9
			107665			0.77
		$Z(\tau\tau)$ + jets 0-5 partons	107670			6.7×10^2
			107671			1.3×10^2
			107672			40
			107673			11
			107674			2.8
			107675			0.77

Table VI.IV: Z+jets production, like W+jets, is a crucially important background in the NC channel VLQ search. Therefore, presented here are the ALPGEN datasets that were used to model this essential background. Included in the table are the cross sections, k-factors, and generator efficiency for the 0-5 partons samples in each of the lepton Z decay modes. Again, note that the dataset numbers are for ATLAS internal reference only.

Generator	Parton Shower	Process	Dataset Number	Generator Efficiency	k-factor	$\sigma \times$BR [pb]
MC@NLO	HERWIG + JIMMY	$t\bar{t}$	105200	0.56	1.0	1.6×10^2
		Single Top	117360	1.0		6.9
			117361			6.8
			117362			7.3
			117363			0.50
			117364			0.50
			117365			0.50
			105500			16.
			117363			0.50
HERWIG	HERWIG + JIMMY	Diboson	105985	0.39	1.5	30
			105986	0.21	1.4	4.6
			105987	1.0	1.6	3.4

Table VI.V: Parameters of interest for the subdominant backgrounds that are $t\bar{t}$, single *top*, and diboson production are presented. These included their respective cross sections, generator efficiencies, and k-factors. Note once more that the dataset numbers are intended for ATLAS reference purposes.

VI.2 MONTE-CARLO SAMPLE INFORMATION: WZ RESONANCE SEARCH

The following sections present a series of tables enumerating the Monte-Carlo datasets utilized in the search detailed in chapter 7.

VI.2.1 SIGNAL MONTE-CARLO SPECIFICATIONS

Tabulated in VI.VI are the W' and ρ_T signal sample particulars.

Generator PDF	Process	Dataset Number	Signal Mass [GeV]	Generator Efficiency	$\sigma \times$ BR [pb]	Effective Luminosity [fb^{-1}]
PYTHIA [9] MRST2007 LO* [224]		15922	200		1.01	29.7
		159228	400		0.174	172
		159229	600		0.0323	929
		159230	800		9.13×10^{-3}	3.29×10^3
		159231	1000		3.29×10^{-3}	9.12×10^3
		159232	1200		1.35×10^{-3}	2.22×10^4
		159233	1400		5.95×10^{-4}	5.04×10^4
		159234	1600		2.78×10^{-4}	1.08×10^5
		159235	1800		1.35×10^{-4}	2.22×10^5
		159236	2000		6.85×10^{-5}	4.38×10^5
		158129	250	1.0	0.133	150
		158130	300		0.0767	261
		158131	350		0.0460	435
		158132	400		0.0288	694
		158133	450		0.0191	1.05×10^3
		158134	500		0.0130	1.54×10^3
		158135	550		9.10×10^{-3}	2.20×10^3
		158136	600		6.54×10^{-3}	3.06×10^3
		158137	650		4.79×10^{-3}	4.18×10^3
		158138	700		3.56×10^{-3}	5.62×10^3
		158139	750		2.70×10^{-3}	7.41×10^3
		158140	800		2.06×10^{-3}	9.71×10^3
		158141	850		1.59×10^{-3}	1.26×10^4
		158142	900		1.25×10^{-3}	1.60×10^4
		158143	950		9.78×10^{-4}	2.04×10^4
		158144	1000		7.77×10^{-4}	2.57×10^4
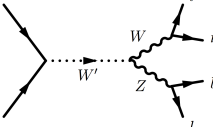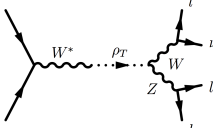
Table VI.VI: EGM W' and LSTC ρ_T signal sample parameters. Their respective filter efficiency, cross section times branching ratio to leptons, effective luminosity, and dataset number (for ATLAS internal use only).

VI.2.2   BACKGROUND MONTE-CARLE SAMPLES

Generator PDF set	Parton Shower	Process	Dataset Number	Generator Efficiency	k-factor	$\sigma \times$BR [pb]
POWHEG CT10 [183]	PYTHIA		129477	0.29456	1.0	1.407
			129478	0.35211		0.9382
			129479	0.16682		0.1746
			129480	0.29351		1.399
			129481	0.35132		0.9537
			129482	0.16863		0.1746
			129483	0.14289		1.399
			129484	0.18256		0.9382
			129485	0.058517		0.1719
			129486	0.29694		0.9795
			129487	0.35302		0.639
			129488	0.15969		0.1125
			129489	0.29766		0.9359
			129490	0.35414		0.6488
			129491	0.16023		0.1125
			129492	0.14803		0.9359
			129493	0.18657		0.639
			129494	0.056651		0.1107
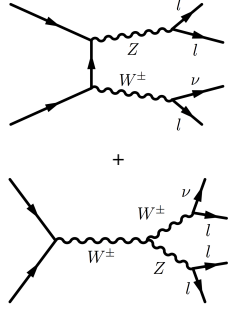
Table VI.VII: WZ+jets production is the fundamental irreducible background for the WZ resonance search. Presented here are the NLO POWHEG datasets that were used to model this essential background. Included in the table are the cross sections, k-factors, and generator efficiencies. Once more, note that the dataset numbers are for ATLAS internal reference only.

Used in the comparison with the DD Z+jets estimation, shown in table VI.VIII are the MC Z+jets POWHEG samples.

Table VI.IX shows the equivalent ALPGEN datasets for comparison.

Generator	Parton Shower	Process	Dataset Number	Generator Efficiency	k-factor	$\sigma \times$ BR [pb]
POWHEG	PYTHIA	$Z(ee)$ + jets	147806	1.0	1.104	1.1098×10^3
		$Z(\mu\mu)$ + jets	147807			
		$Z(\tau\tau)$ +jets	147808			

Table VI.VIII: Z+jets MC production, although modelled via DD techniques, shall remain important for understanding the lepton-fakes it produces. Shown here are the POWHEG [225–227] dataset specifications. Included in the table are the cross sections, k-factors, and generator efficiency in each of the lepton Z decay modes. Again, note that the dataset numbers are for ATLAS internal reference only.

Generator	Parton Shower	Process	Dataset Number	Generator Efficiency	k-factor	$\sigma \times$ BR [pb]
ALPGEN	HERWIG + JIMMY	$Z(ee)$ + jets 0-5 partons	107650	1.0	1.23	7.1×10^2
			107651			1.6×10^2
			107652			49
			107653			14
			107654			3.8
			107655			1.1
		$Z(\mu\mu)$ + jets 0-5 partons	107660			7.1×10^2
			107661			1.5×10^2
			107662			49
			107663			14
			107664			3.8
			107665			1.1
		$Z(\tau\tau)$ + jets 0-5 partons	107670			7.1×10^2
			107671			1.6×10^2
			107672			49
			107673			14
			107674			3.8
			107675			1.1

Table VI.IX: Z+jets MC production, although modelled via DD techniques, shall remain important for understanding the lepton-fakes it produces. Shown here are the ALPGEN [178] datasets specifications. Included in the table are the cross sections, k-factors, and generator efficiency for the 0-5 partons samples in each of the lepton Z decay modes. Again, note that the dataset numbers are for ATLAS internal reference only.

Appendix VII

WZ Resonance: 16 Highest Mass Event Details

Tables VII.I, VII.II, VII.III, and VII.IV found in this annexe tabulate the relevant event information for the 16 events with $m(WZ) > 500$ GeV in the signal region.

Run # / Event #	$m(WZ)$	E_T^{miss}	$e\,p_T$	$e\,\eta$	$e\,\phi$	$\Delta\phi(e, E_T^{\text{miss}})$	$j\,p_T$	$\Delta\phi(j, E_T^{\text{miss}})$	$Z\,p_T$	$m(Z)$	$W\,p_T$	$m_T(W)$
203602 89063495	518.8	111.2	197.6	-1.353	-2.347	2.943	128.1	0.1879	294.2	101.1	202.8	82.23
			107.6	-1.074	1.366	0.7706						
			97.78	-0.6633	-2.535	3.13						
207332 71471042	576.9	87.59	224.4	-1.116	1.845	2.608			276.5	89.91	260.3	75.76
			183.5	-0.8404	-1.37	0.6069						
			61.23	-1.577	2.465	3.055						
207664 49434369	1184	201.5	257.8	1.356	-2.49	0.2877	57.29	2.821	405.6	91.77	454.6	65.33
			249.6	-0.2005	0.8695	3.072						
			157.5	-0.6258	0.6944	2.897						
207620 40445722	593.2	34.19	264.9	-0.5082	-1.263	1.021	31.36	2.235	211.6	93.42	284.2	92.98
			174.8	-1.689	1.923	2.165						
			43.01	-0.8185	2.527	2.769						
209736 139060645	835	228.5	394	-0.3597	0.2761	2.922	263.9	0.1618	567.4	94.31	294.3	30.41
			181.2	-0.3846	0.6301	3.008	30.33	0.8475				
			67.3	-0.728	-2.4	0.2458						

Table VII.I: Details of the 5 events with $m(WZ) > 500$ GeV in the $e\nu ee$ channel.

Run # / Event #	$m(WZ)$	E_T^{miss}	$\ell\,p_T$	$\ell\,\eta$	$\ell\,\phi$	$\Delta\phi(\ell, E_T^{\text{miss}})$	$Z\,p_T$	$m(Z)$	$W\,p_T$	$m_T(W)$
209864 161766530	682.7	229.5	257.9 (e)	-0.3676 (e)	-0.7698 (e)	2.956 (e)	303.3	90.57	271.4	69.63
			45.98 (e)	-1.162 (e)	-0.9345 (e)	3.121 (e)				
			50.68 (μ)	0.8554 (μ)	2.844 (μ)	0.6574 (μ)				

Table VII.II: Details of the single events with $m(WZ) > 500$ GeV in the $ee\mu\nu$ channel. The event has 0 jets passing the object selection.

Run # Event #	$m(WZ)$	E_T^{miss}	$\ell\,p_T$	$\ell\,\eta$	$\ell\,\phi$	$\Delta\phi(\ell, E_T^{\text{miss}})$	$j\,p_T$	$\Delta\phi(j, E_T^{\text{miss}})$	$Z\,p_T$	$m(Z)$	$W\,p_T$	$m_T(W)$
202991 46767590	595.8	95.18	118.4 (e) 156.9 (μ) 52.96	-1.572 (e) 0.5278 (μ) -0.3515	1.449 (e) -1.698 (μ) -2.081	0.2496 (e) 2.898 (μ) 3.002			207	89.73	211.9	26.43
203277 8024898	976.2	264.7	75.52 (e) 465.3 (μ) 157.5 (μ)	0.1934 (e) -0.8322 (μ) -0.7649 (μ)	1.672 (e) -1.868 (μ) -2.184 (μ)	0.3634 (e) 3.107 (μ) 2.791 (μ)	411.2 173.4 48.49	0.1801 3.093 1.52	616.9	87.04	336.4	51.11
207982 37258997	1050	37.09	451.3 (e) 280.3 (μ) 173.9 (μ)	-0.9526 (e) -0.1598 (μ) 0.1999 (μ)	-2.663 (e) 0.4377 (μ) 0.651 (μ)	0.2984 (e) 2.802 (μ) 3.015 (μ)			451.7	92.65	486.9	38.46
210308 180720096	533.2	248.6	69.72 (e) 110.3 (μ) 42.68 (μ)	-0.5231 (e) 0.1762 (μ) 1.393 (μ)	-0.4707 (e) 2.764 (μ) 2.964 (μ)	0.646 (e) 2.589 (μ) 2.789 (μ)	128.3 37.78	2.991 1.127	152.4	89.82	307.2	83.57
209161 94994229	571.5	37.46	130.4 (e) 249.5 (μ) 114.4 (μ)	-2.261 (e) -1.225 (μ) -0.8867 (μ)	-2.604 (e) 0.4869 (μ) 0.971 (μ)	0.2954 (e) 2.896 (μ) 2.412 (μ)	418.2 188.6 64.88 49.95	0.224 3.129 1.572 2.325	354.8	99.28	166.6	20.57

Table VII.III: Details of the 5 events with $m(WZ) > 500$ GeV in the $e\nu\mu\mu$ channel.

Run # Event #	$m(WZ)$	E_T^{miss}	$\mu\,p_T$	$\mu\,\eta$	$\mu\,\phi$	$\Delta\phi(\mu, E_T^{\text{miss}})$	$j\,p_T$	$\Delta\phi(j, E_T^{\text{miss}})$	$Z\,p_T$	$m(Z)$	$W\,p_T$	$m_T(W)$
204240 94726109	562.6	111.9	226.1 61.89 30.97	1.135 1.512 0.6294	2.319 2.895 -0.07024	2.736 2.971 0.3467	88.45 61.25	0.2647 0.7716	280.1	80.85	141.4	20.3
205055 49327421	550.8	168	116.3 103.4 66.07	-1.549 -0.2629 -0.5591	2.943 0.2459 2.976	3.089 0.4968 3.056	164.8 148.5 65.71 48.24 46.88	2.703 0.6594 2.158 0.8789 2.26	182.3	90.45	263.5	64.8
207447 65969229	706.5	192	192.5 147.8 88.6	0.1779 0.4115 1.639	2.822 2.335 -0.2787	2.96 2.837 0.2231	50.01 25.29	0.1396 0.1705	330.4	90.31	279.1	29.05
208970 124423139	533.7	130.2	118.9 79.67 53.6	2.215 0.7832 -0.137	-1.866 0.5344 1.499	0.6422 3.043 2.276	142.8 135.2	1.76 2.416	118.7	86.9	236.4	78.53
209864 94603127	663.8	86.37	184.7 165.5 130.4	0.3312 -0.6381 -1.16	0.3592 -2.465 -2.19	0.3592 2.809 3.085			293.1	87.34	267.2	45.11

Table VII.IV: Details of the 5 events with $m(WZ) > 500$ GeV in the $\mu\nu\mu\mu$ channel.